STUDY OF TURBULENT FLOW CONTROL USING SERPENTINE PLASMA ACTUATOR

By

ARNOB DAS GUPTA

A DISSERTATION PRESENTED TO THE GRADUATE SCHOOL
OF THE UNIVERSITY OF FLORIDA IN PARTIAL FULFILLMENT
OF THE REQUIREMENTS FOR THE DEGREE OF
DOCTOR OF PHILOSOPHY

UNIVERSITY OF FLORIDA

2017

To my mom and dad

ACKNOWLEDGMENTS

I would like to thank my advisor and chair Dr. Subrata Roy for his immense support and guidance. He has helped me not only to prosper as a student but also to adjust into this new environment. I admire his patience and dedication towards me as well and his students in Applied Physics Research Group. I would also like to thank my lab members Ankush, Tomas, Pengfei, Jignesh, Sherlie, Navya, Mark, Ariel, Moses, Bhaswati and Nick for providing me with the support and encouragement I needed. I appreciate the guidance and suggestions provided by my doctoral committee members Dr. William Lear, Dr. Sivaramakrishnan Balachandar and Dr. William Hager in improving my dissertation.

I also acknowledge the support and inspiration my mom, dad, my brother Aritro, my family and my friend Shaleen gave throughout my life and career.

TABLE OF CONTENTS

page

LIST OF TABLES

LIST OF FIGURES

Abstract of Dissertation Presented to the Graduate School
of the University of Florida in Partial Fulfillment of the
Requirements for the Degree of Doctor of Philosophy

STUDY OF TURBULENT FLOW CONTROL USING SERPENTINE PLASMA ACTUATOR

By

Arnob Das Gupta

December 2017

Chair: Subrata Roy
Major: Mechanical Engineering

The current work involves the numerical study of plasma actuators and their applications for flow control. A parallel time explicit discontinuous Galerkin (DG) formulation suitable for compressible turbulent flow problems has been implemented due to its advantage to solve equation systems on an element by element basis with high-order accuracy and capability of highly efficient parallelization. This research incorporates the implicit large eddy simulation model into our in-house DG augmented multi-scale ionized gas flow codes for flow simulations with practical Reynolds numbers.

A study involving vectored momentum and energy addition is performed since they play a crucial role in flow control. The method used mimics the actual plasma actuation process where momentum is induced by the electric field and energy is added by the thermal energy generated at the electrodes of the actuator. Specifically, an in-depth study of the flow structures generated by serpentine shaped plasma actuators is done to understand how they alter the neighboring laminar or turbulent flow field.

The analysis of serpentine actuator shows that the transition mechanism for a finite amplitude perturbation generated by the actuator resembles oblique wave transition. The actuator generates subharmonic sinuous streaks which break down due to nonlinear interactions and

undergoes bypass transition. The different geometries of the serpentine actuator follow similar transition process. The frequency and amplitude of the actuator are crucial in order to avoid decay of disturbances. The important parameter governing the transition process by the serpentine actuator is the ratio of the maximum mean velocity magnitude of the actuator in quiescent condition to the freestream velocity. For specific ranges of temperature generated by the actuator and the flow regime, only localized impact on the flow field is obtained. The transition behavior is found to be similar regardless of the orientation (co-flow or counter-flow) of the actuator. Collocation of two serpentine actuators is found to favorably manipulate turbulent streaks to accentuate or mitigate turbulence for aerodynamic applications. It is found that the orientation, as well as the location of the second actuator, also called the control actuator, is crucial to obtain the maximum impact on the flow field.

CHAPTER 1
INTRODUCTION

1.1 Background

The field of fluid dynamics has an inexhaustible range of practical applications ranging from microscopic scales in biological systems to astronomical scales found in interstellar events. Although fluid dynamics concerns itself with only continuum mechanics, where physical scales are large compared to the distances between individual molecules, applications such as blood flow through capillary beds, water flow through common house pipes, air flow around airplanes, weather phenomenon, movement of molten magma inside earth's core, solar wind of charged particles, spacecraft propulsion etc. apply this field of study. The maturity of this field comes from the well-established governing equations (Navier-Stokes) and approximations which provide a fundamental understanding of the system. Despite all the applications and centuries of research, persistent challenges remain and are still being investigated. Among all the challenges, one that stands out as an interesting phenomenon is turbulent flow. Turbulent flow is associated with wide space and time scales in addition to the nonlinear governing equations. This makes it extremely challenging to precisely predict and reproduce the behavior of a turbulent flow field.

To appreciate the concept of turbulence, one must understand what type of flow can be termed turbulent. The three integral and necessary characteristics of a turbulent flow field are disorders or chaotic behaviors which makes it unpredictable, highly efficient mixing and random vortical structures in three spatial dimensions. Despite their chaotic behavior, the mean flow characteristics of turbulence are reproducible which makes it a tractable problem.

Although turbulence is a commonly occurring phenomenon, other types of flow regimes exist alongside it. Any given flow can be broadly categorized as either laminar or turbulent. The famous pipe flow experiment [1] conducted by Osborne Reynolds, showed that the key parameter which relates to the type of flow regime is Reynolds number, Re (more details in Chapter 4). There exists a critical Reynolds Number, Re_c above which naturally occurring perturbations grow and cause the transition to turbulence. In most applications these perturbations decay, if the Reynolds numbers are below Re_c. The value of Re_c varies for different problems. There are scenarios where finite nonlinear perturbations added to a flow field can result in the growth of disturbances even below Re_c. This dissertation focuses on using these types of nonlinear perturbations to control the turbulent flow field for applications such as drag reduction, noise mitigation, flow mixing, improving heat transfer etc.

1.2 Flow Control Methods

Understanding turbulent flow provides information on how vehicle experiences drag during motion, how noise vibrations can impact an airplane landing gear system, how fuel and air mix in an internal combustion engine, the behavior of separated flow behind a semi-trailer truck and much more. This information can be utilized for developing flow control methods to improve efficiency and reliability of a system. Depending on the application, suppressing turbulence can lead to a reduction in skin friction drag or mitigate flow-induced noise, while enhancing it can result in mitigation of flow separation. Due to this, flow control has been a major topic of research in fluid mechanics. Following the work of Prandtl [2] in control of boundary layer and free shear flows, flow control has progressed from defense industry applications to everyday civilian applications. The history of flow control over the 20th century has been well summarized by Gad-el-Hak [3] as five eras of flow control.

In general, flow control methods can be categorized based on the applied location or mechanism of energy expenditure. For the first category, the method can be applied either in the highly viscous region of a boundary layer near a wall or away from it where flow becomes more nearly inviscid. The latter category focuses on whether the method falls under active or passive flow control [3], [4]. Here passive control methods are defined as flow control methods which influence the flow field without using a continuously monitoring external energy signal and generally requires geometric modification. Whereas, active control involves the use of a continuous external energy signal to alter the background flow field. For the present work, the second category is chosen to classify the flow control methods. Figure 1-1 gives the classification of commonly used flow control methods and devices [5].

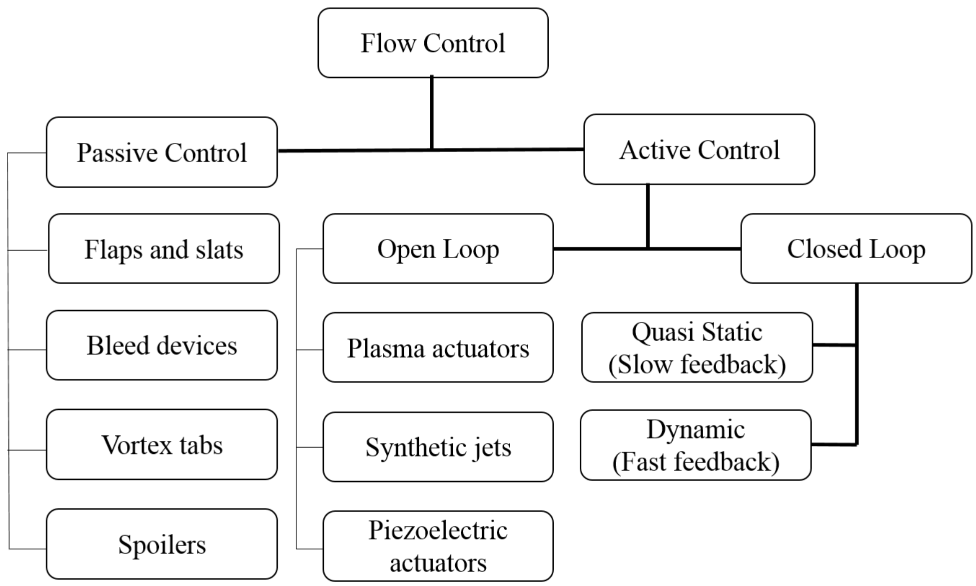

Figure 1-1. Classification of flow control devices and few examples [5].

Some passive devices [3] have found real-world applications. For example, bleed devices and spoilers [6], [7], [8] have been used to control noise generated in an aircraft weapons bay and landing gear system. They work on the principle of manipulating the incoming boundary layer or by distributing the energy present in the flow. Airfoil slats and flaps [9] were studied to reduce the separation bubble formed around it. Riblets [10] were designed to diminish turbulent drag over a flat plate. A reduction of drag up to 8% was reported depending on the height and shape of the Riblets. Both numerical and experimental work was performed to understand the flow structures around the Riblets which lead to drag reduction [11], [12]. Other techniques include vortex generator tabs which have been used in a variety of applications such as backward facing ramp [13], supersonic shock-induced separation [14] and flat plate boundary layer [15], [16]. Some of the passive control methods are depicted in Figure 1-2. Despite their popularity, near wall manipulation of boundary layer using passive control remains a difficult task since they do not perform well over a wide range of operating conditions and are not adaptable to variations in the incoming flow.

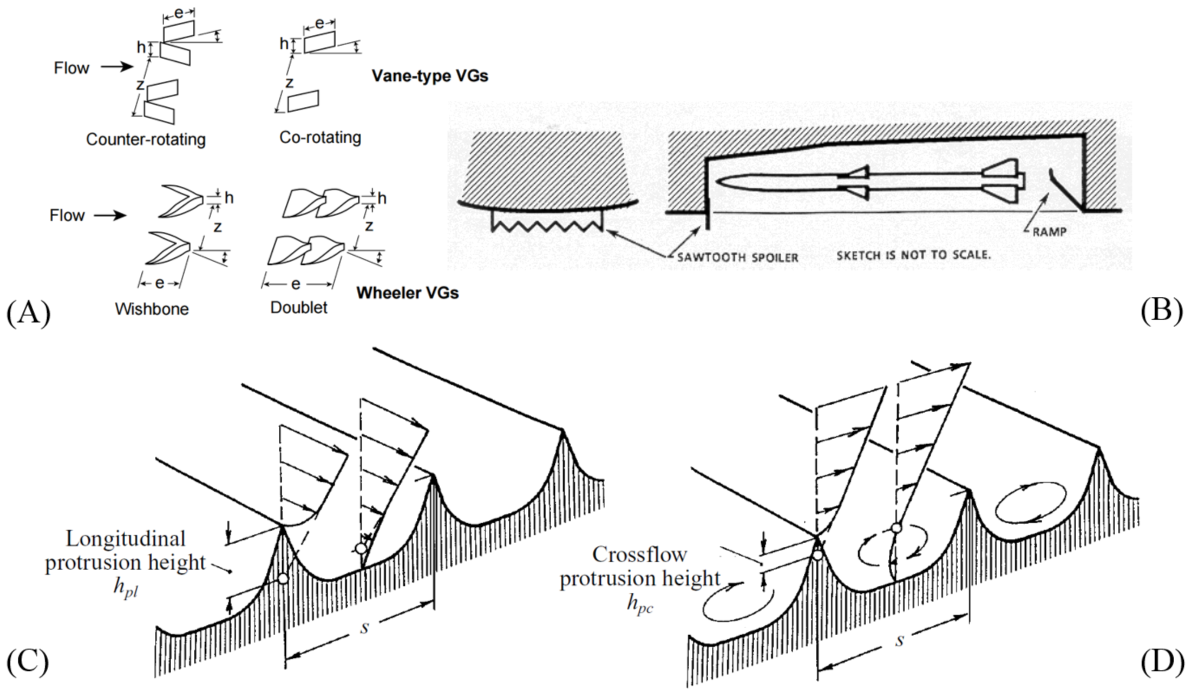

Figure 1-2. Passive flow control devices. (A) Vortex Generator Tabs [17], (B) saw tooth spoiler [18] and (C) Riblets [11].

Contrarily, active control devices have shown reasonable promise in flow control applications even when the flow conditions vary. Representative active flow control devices are shown in Figure 1-3. Examples include synthetic jets, piezoelectric actuators, plasma actuators, resonance tubes, resonating rods etc. Synthetic jets are like pulsed flow actuators but are based on reusing the same fluid by the process of suction and injection which results in zero net mass flux addition. They have been applied in a variety of applications such as flow control around bluff bodies [19], [20], airfoils [21] and reduction of skin friction drag on a flat plate [22]. A detailed analysis of synthetic jets has been discussed and reviewed by Glezer and Amitay [23]. Piezoelectric actuators have also been studied for airfoil flow control [24], [25]. For noise control in aircraft weapons bay and landing gear systems different active control strategies have been employed such as synthetic jets and pulsed blowing [26], [27], piezoelectric actuators [28], and plasma actuators [29], [30]. MHD actuators have been implemented mostly for high-speed flow control applications such as in hypersonic flow around a cylinder [31]. A review of different kinds of active control actuators can be found in Cattafesta & Sheplak [4].

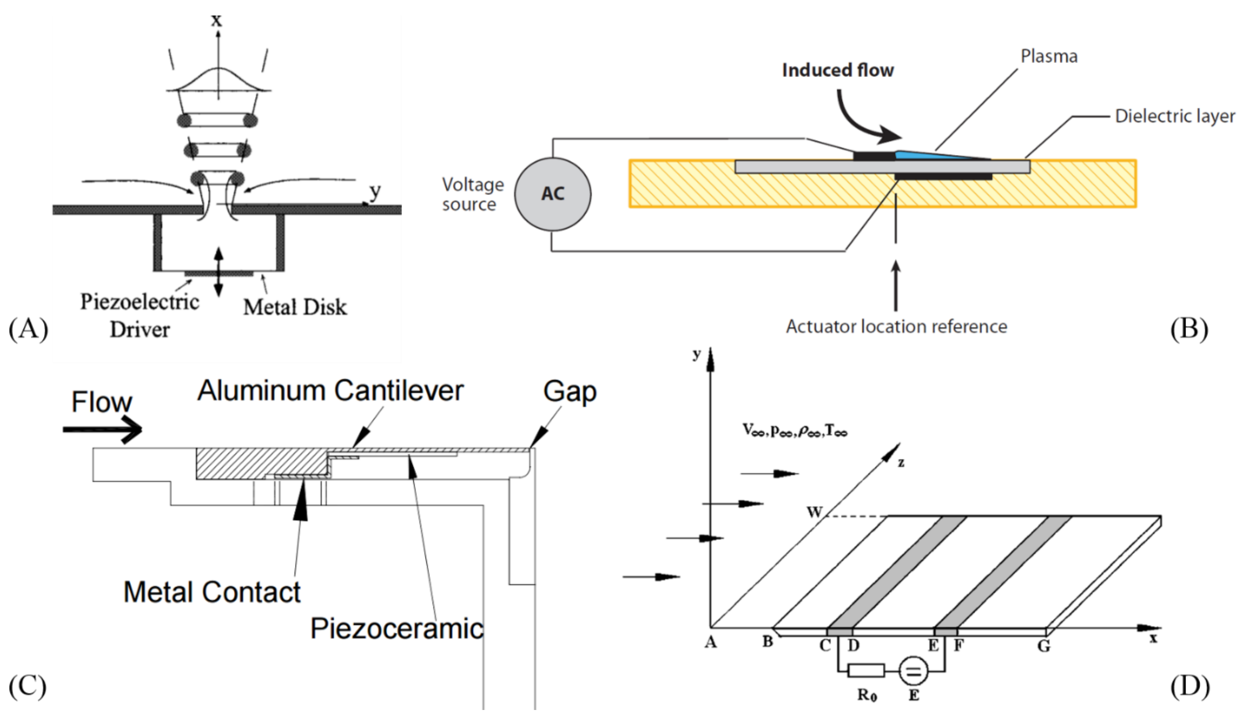

Figure 1-3. Active flow control devices. (A) Synthetic Jets [32], (B) piezoelectric Actuator [28], (C) plasma Actuator [33], [34] and (D) MHD actuators [31].

1.3 Plasma Actuators as Active Flow Control Device

Plasma actuators have increased in prevalence as active flow control devices over the last three decades [35]. In general, plasma actuators can be classified into three main categories based on their discharge characteristics [36]. These are dark discharge, glow discharge, and arc discharge. Dark discharge is associated with low current and high voltage while arc discharge has high current and low voltages. Glow discharge falls in between the dark and arc discharge regimes. These actuators can be operated using direct current (DC) or alternating current (AC) signals to create surface or volume plasmas. Most of the plasma actuators developed for flow control operate in one of these three regimes. Corona discharge actuators fall under the dark discharge regime. Arc filament and spark-jet actuators operate in the arc discharge regime. Surface dielectric barrier discharge (SDBD) plasma actuators operate in the glow discharge regime. These actuators work by the principles of electrohydrodynamics (EHD). They control the background flow field by adding thermal energy and inducing a wall jet type fluid motion also called ionic wind. Unlike most flow control devices, plasma actuators do not have any moving parts and are cheap to design. Since they are EHD devices, they directly convert electrical energy to kinetic energy and provides fast response time. Most flow control methods do not provide the flexibility of controlling the direction of energy added to the flow. Plasma actuators on the other hand can easily manipulate the direction of the wall jet by alteration of the input signal. Additionally, these actuators are surface compliant and can be applied at receptive locations for optimal flow control. However, these actuators are highly inefficient in converting electrical energy to kinetic energy. This can result in greater power consumption compared to power saved by controlling the flow. Nonetheless, for low-speed applications, these actuators can easily overcome this drawback.

1.3.1 Dark Discharge Actuators

Corona discharge actuators have been used to reduce drag, improve heat transfer, control flow separation and create thrust. Early use of these actuators involved delaying transition to turbulence for a flat plate boundary layer [37]. Velkoff and Godfrey [38] also showed improvement in heat transfer at low velocities. Van Rosendale et al. [39] numerically simulated the impact of ionic wind on skin friction in channel flow as well as flow over a flat plate. Léger et al. [40] and Moreau et al. [41] conducted an experimental study of corona discharge actuators to show separation control over an inclined flat plate. Moreau et al. [42] also showed improvement in thruster effectiveness using corona discharge actuators. Zhao et al. [43] used needle plasma actuators to show improvement in convective cooling over a flat surface.

1.3.2 Arc Discharge Actuators

Arc discharge actuators have numerous applications, especially in high-speed flows. These actuators utilize either high thermal energy addition or shock propagation to control the background flow field. These actuators are generally referred by different names such as arc filament actuators [44], spark-jet actuators [45], [46] or pulsed plasma jet actuators [47]. Leonov et al. [48] showed that these actuators can be used to suppress instabilities in supersonic flow. A pulsed arc filament plasma actuator was used to enhance mixing for a supersonic jet (M = 1.3) [49]. Noise reduction of almost 20 dB in cavity flow [29] was achieved by placing the arc filament actuators at the leading edge of the cavity. Arc discharge actuators have been also used in underwater applications [50], [51] but most of them do not fall under flow control.

1.3.3 Glow Discharge Actuators

The most frequently used glow discharge plasma actuators are surface dielectric barrier discharge (SDBD) actuators. The standard design of an SDBD actuator is depicted in Figure 1-3 (B). It involves two asymmetrically placed electrodes, one exposed and the other encapsulated, separated by a dielectric material. A high voltage (~ kV) alternating current (~kHz) is applied to the electrodes across the dielectric material, which ionizes the air surrounding the exposed electrode. Due to an asymmetry of the electrodes, the electric field accelerates the ionized particles in the required direction, generating a wall jet via a collisional mechanism. This can be used to manipulate the background flow field. Depending on the input signal waveform or geometry of the electrodes, all SDBD actuators can be categorized as standard linear SDBD actuators [34], [33], nanosecond pulsed discharge (NPD) actuators [52], [53], sliding discharge actuators [54], [55], serpentine plasma actuators [56], [57], [58] or plasma synthetic jet actuators [59], [60]. From here on all actuators operating on sinusoidal AC waveform will be called SDBD actuators distinguishing them from NPD actuators.

NPD actuators have been applied to both low-speed and high-speed flows. These actuators use nanosecond width pulsed signal instead of sinusoidal AC signal. Similar to arc filament actuators, NPD actuators generate compression waves [61]. Rouopassov et al. [52] and Little et al. [61] showed flow attachment for an airfoil at different angles of attack and Mach numbers ranging from subsonic to transonic regimes using NPD actuators. Nishihara et al. [62] used these actuators to alter the shock standoff distance for a Mach 5 air flow. A comparative numerical study [63] between the NPD and standard linear SDBD actuators showed the difference in mechanism of flow control between the two actuator types. They showed that SDBD actuators act as a momentum source by creating wall jet, whereas NPD actuators act as an aero-acoustic source by generating micro-shock waves. The EHD effects dominate in SDBD actuators while thermal heating is dominant in NPD actuators. Due to this, NPD actuators have found applications in high-speed flows while SDBD actuators are mainly used in low subsonic flows.

The first detailed study using SDBD plasma actuator as a flow control device was conducted by Roth et al. [34]. They placed arrays of SDBD actuators in streamwise and spanwise orientation to study their impact on the coefficient of drag for a flat plate. Since then SDBD actuators have been used for separation control, drag reduction, improving lift in aircraft wings, reducing flow-induced noise etc. In a standard SDBD actuator, plasma forms along the straight edge of the exposed electrode. These actuators can be either applied individually or in a parallel array arrangement. A single SDBD actuator was shown to control flow separation and pitching moment around a NACA 0015 airfoil [64], [65]. Since the last two decades, these actuators have been experimentally studied to control flow around airfoils to improve stability as well as lift to drag ratio [66], [67], [68]. SDBD actuators have also been used to control flow separation around low-pressure turbine blades [69], [70]. Li et al. [71] studied the effect of SDBD actuators on broadband noise levels for a flow over a cylinder. Huang and Zhang [72] conducted a similar study on noise levels for a cavity flow. Figure 1-4 shows one of the applications of SDBD actuator to control flow separation behind a cylinder [33].

(A) 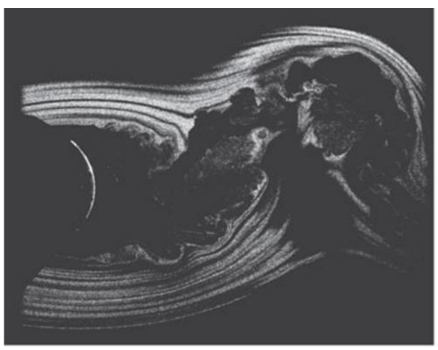 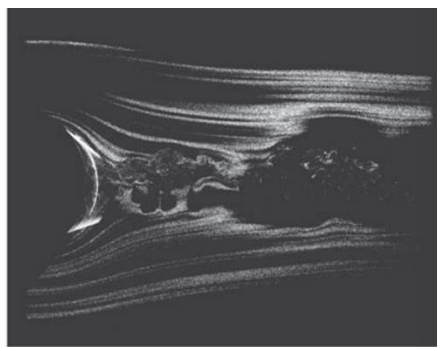 (B)

Figure 1-4. Particle image velocimetry images for a flow around a cylinder at Re = 33,000. (A) Plasma off (B) Plasma on [33].

Along with experimental studies, numerical simulations of SDBD actuators have also been performed and validated with experimental data. Numerical investigations provide detailed information about the control methodology of SDBD actuators which is difficult to obtain experimentally. Different plasma body force models were developed based on first principles and compared to the experimentally obtained data [73, 74, 75]. These models were incorporated in flow simulations to mimic the behavior of these actuators. Numerical studies have shown the benefits of using plasma actuators to delay transition in flow over airfoils [76, 77]. They have been also used for controlling flow separation around turbine blades [78, 79]. SDBD actuators [30] were also used along with a geometric modification at the trailing edge of a cavity to reduce the acoustic tones. It involved the use of plasma actuators along with a passive receptive channel, which allowed up to a 15dB reduction in sound pressure levels (SPL).

To improve the efficiency of these actuators, the geometry or orientation of these actuators need to be altered. This allows vectoring of the plasma jet at an angle to the wall. This led to the development of SDBD actuators such as traveling wave actuators [80], plasma synthetic jet actuator [59, 60] and serpentine plasma actuators [56, 57]. Although the fundamental mechanism of momentum generation is through EHD force, these actuators have completely different flow structures when compared to standard SDBD actuators. Just by changing the orientation and input signal of the standard actuators, Choi et al. [80] showed almost 45% skin friction reduction on a turbulent flat plate using traveling wave actuators. Caruana et al. [60] used plasma synthetic jet actuators to reduce separation near the trailing edge of a NACA 0015 airfoil. These actuators generally have annular electrodes to generate wall-normal jets. The present study focuses on using active, shaped plasma actuation for turbulent flow control. Different types of serpentine plasma actuators fall under this category and will be the focus of the current work.

1.4 Need for Studying Serpentine Plasma Actuators

Despite all the applications of SDBD actuators, their use has generally been limited to low-speed incompressible flows. This is due to the low induced velocity of the wall jet (maximum induced velocity recorded ~11 m/s [81]) generated by these actuators. Therefore, a novel design of the SDBD actuator was required to improve the control authority, while keeping the input signal waveform the same as the standard SDBD actuator. This led to the development of serpentine plasma actuators. These actuators can be categorized by differences in geometry of the electrodes. It should be noted that traveling wave actuators also fall under this category. Various designs of serpentine actuators are depicted in Figure 1-5. All the serpentine actuators can be related to the standard SDBD actuator in Figure 1-5 (B) by their amplitude A and wavelength λ. It should be noted that traveling wave actuators are similar to comb actuators and sawtooth [82] or zig-zag [83] actuators are similar to a triangular serpentine actuator.

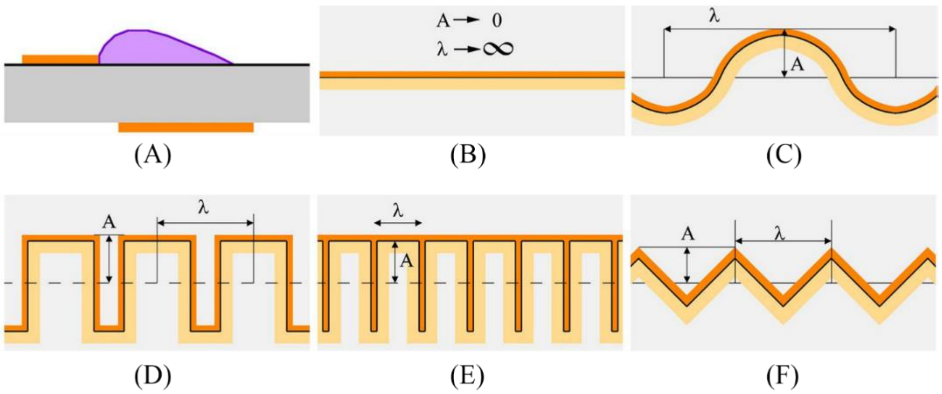

Figure 1-5. Schematic of different shaped serpentine plasma actuators. (A) Schematic of plasma formation on a standard SDBD actuator. (B) Linear, (C) Circular serpentine, (D) Square serpentine, (E) Comb and (E) triangular serpentine actuator [84].

The improvement in efficiency of these actuators in turbulent flow control comes from their transient growth based vortex generation. Turbulent flows involve three-dimensional vortices and streaks which can be controlled to manipulate turbulence production and achieve better flow control authority. The turbulence production is associated with these three-dimensional vortices in a turbulent flow field. In a wall-bounded turbulent flow, these vortices bring fast-moving fluid towards the wall (sweeping event) and slow-moving fluid away from the wall (ejection event). These events are generally associated with streamwise vortices which are closely related to elongated low-speed streaks near the wall [85]. These streaks also called Klebanoff modes [86], are fluctuations in the turbulent boundary layer with low frequencies, generally arising due to low frequency filtering of free stream perturbations [87, 88] by the boundary layer. In a transitional flow, these streaks exhibit algebraic or transient growth [89] and lead to bypass transition due to their nonmodal nature [90]. This type of mechanism is commonly found in pipe flow [91] and turbomachinery applications [92]. The two significant mechanisms by which streaks break down are via sinuous and varicose modes [85], which can be either fundamental or subharmonic in nature. One of the ways to promote the break down is to amplify the sinuous streak waviness (nonlinear Streak Transient Growth) [85]. The use of serpentine geometry plasma actuator allows this kind of amplification. One of the examples for this amplification is clearly visible in Figure 1-6 [84]. The standard linear geometry actuators are compared with serpentine geometry [56, 57] actuators. The transition from laminar to turbulent for the serpentine actuator is more rapid when compared to the linear actuator. Although the structures at the end of the airfoil look similar, the tubular structures also called Tollmien – Schlichting (TS) waves are more sinuous for serpentine actuators, indicating secondary instabilities. The early formation of secondary instabilities allows better near wall three-dimensional flow control and advance transition to turbulence [84].

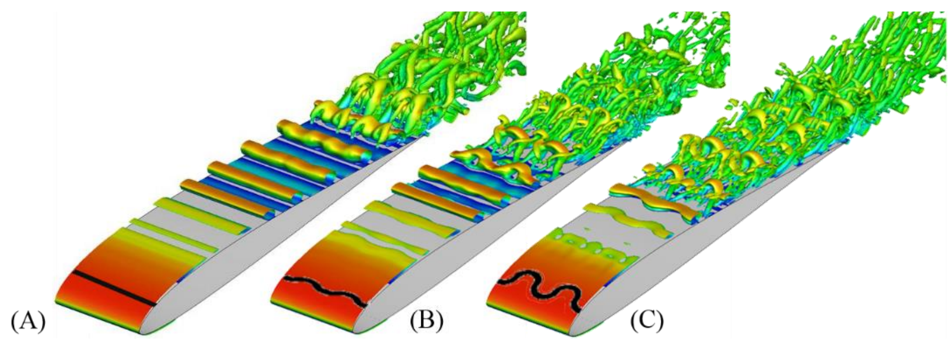

Figure 1-6. Increase in the sinuous streak waviness with the application of serpentine actuators (shown in black lines) causing advancement of turbulent transition. [84]

In accordance with the space act agreement (SAA1-23461) between NASA Langley and APRG, UF, experiments were conducted at NASA Langley (Mr. Stephen Wilkinson) for drag reduction on a flat plate using serpentine and linear actuators. A drag reduction of almost 29% could be achieved using serpentine geometry actuators when compared to 12% for linear actuators. Figure 1-7 shows the effect of linear and serpentine actuators on the skin friction and drag over a flat plate. PIV study on a backward step using comb actuators were conducted and are shown in Figure 1-8 [93]. This measurement was carried out at a velocity of 13.5 m/s and the actuators were operated in an amplitude modulated mode and a continuous mode showing a reduction in reattachment length by almost 15%. Further applications include testing these actuators on bluff bodies like semi-trailer trucks. A 1:60 scale model of the truck was tested in a wind tunnel at 31.2 m/s (70 mph) and 26.8 m/s (60 mph) and was found to give almost 13% and 15% drag reduction respectively [94]. The data on drag collected at various voltages for the 26.8 m/s case is shown in Figure 1-9. All these benefits make these actuators highly versatile for flow control applications.

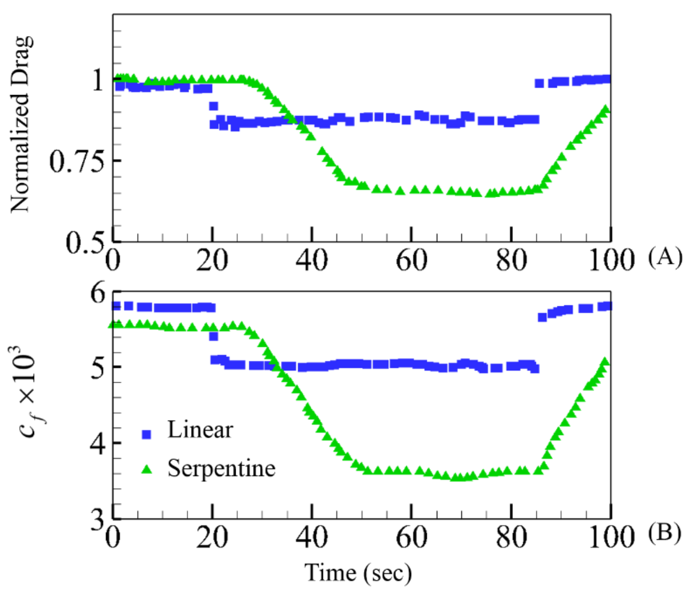

Figure 1-7. Experimental study on the drag reduction obtained using different linear and circular serpentine actuators. (A) Normalized drag and (B) skin friction obtained from drag measurement (Data extracted from NASA Langley report with permission).

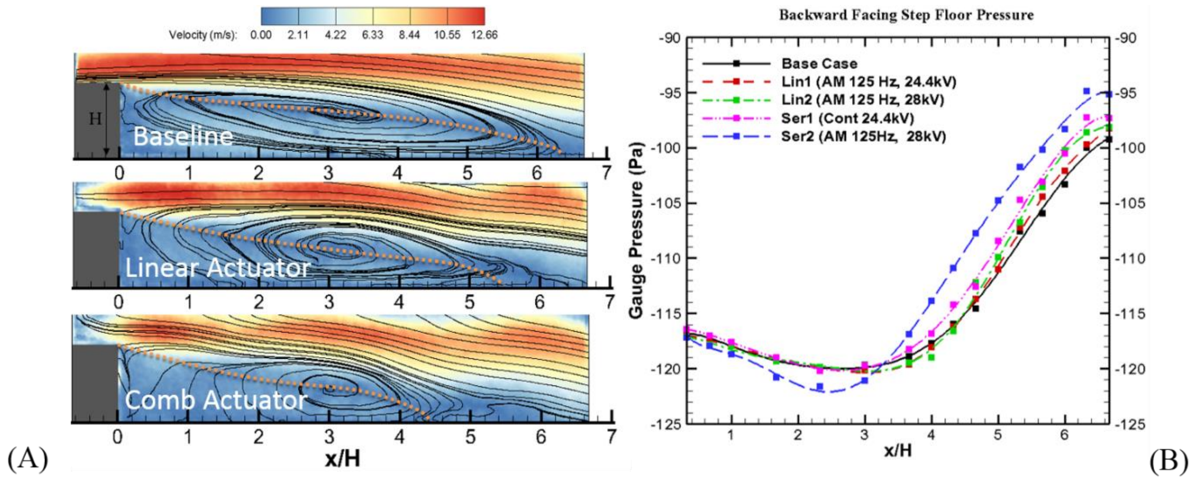

Figure 1-8. Experimental data for flow control around backward facing step using linear and comb actuators [93]. (A) Contour of time averaged velocity magnitude along with actuators run at 28kVpp in AM mode (B) Variation of pressure along the floor after the step for different actuators and actuation methods.

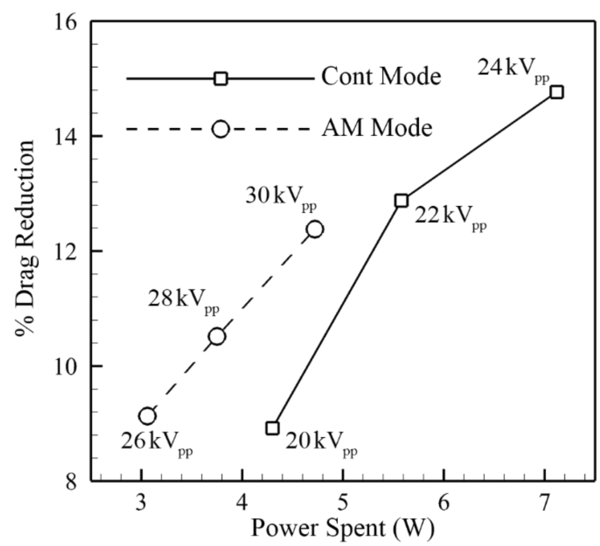

Figure 1-9. Relation between power consumption and drag reduction under continuous mode and amplitude modulated mode [94].

Despite all the efforts of using serpentine plasma actuators as a flow control device, underlying fundamental questions remain unanswered. Questions such as what is the inherent transition mechanism caused by these actuators? How do the structures generated by these actuators interact and break down? What is the optimal design and configuration of these actuators to maximize efficiency in control authority? Can multiple arrays of these actuators be used to control transitional or turbulent flow as for a traveling wave actuator? All of these questions are addressed in this current study by conducting numerical simulations of serpentine shaped plasma actuators.

This work is organized as follows: In Chapter 2, the numerical method used for all simulations is described. This includes implementation of discontinuous Galerkin method with different types of inviscid and viscous numerical fluxes along with different time discretization. Chapter 3 covers the governing equations used to perform this study along with a description of different methods to solve turbulent flow. In Chapter 4, the relevant flow physics for laminar, transitional and turbulent flow are discussed. Chapter 5 provides benchmarking and validation of the implemented numerical scheme for two types of turbulence problem. Chapter 6 provides an in-depth analysis of the transition mechanism for a square serpentine actuator. The breakdown of flow structures as well as the behavior of coherent flow structures are discussed to show how the flow transitions to turbulence. The effect of different parameters on flow transition such as geometry, the frequency of operation, amplitude and thermal heating of the actuator are discussed in Chapter 7. The influence of these parameters on instantaneous and mean flow properties are explained for optimal operation of these actuators. Chapter 8 describes the use of collocation of square serpentine actuators as a method to modify turbulent streaklines and thereby control drag as well as heat transfer. Finally, a summary and conclusions along with the future work and expected impact of this research are presented in Chapter 9.

CHAPTER 2
NUMERICAL METHOD

2.1 Background

To simulate practical problems which involve partial differential equations, different numerical methods have been used over the past century. These include finite difference method, finite element method, finite volume method, discontinuous Galerkin (DG) method etc. However, this study only covers DG finite element method due to its advantage to solve equation systems on an element by element basis with high-order accuracy and capability of highly efficient parallelization. This method was first proposed by Reed and Hill [95] to solve the linear system of neutron transport equations. However, the fundamental challenge is to solve the nonlinear systems of equations such as the hyperbolic conservation laws which govern most physical systems. For this an explicit version of DG method was devised [96] which employed the use of Runge – Kutta time discretization with a total variation diminishing in the means (TVDM) and total variation bounded (TVB) slope limiter. This method was called the RKDG method. This was extended to high order RKDG methods [97] which showed $P+1$ order of convergence for P order space discretization.

The development of DG method for nonlinear hyperbolic systems occurred rapidly over the last two decades. However, the need to solve problems both hyperbolic and elliptic in nature led to the extension of this method to convection-diffusion problems. A generic convection-diffusion equation is given in Eq. (2-1).

$$\frac{\partial \vec{U}}{\partial t}+\nabla\cdot\vec{F}^{inv}\left(\vec{U}\right)-\nabla\cdot\vec{F}^{v}\left(\vec{U},\nabla\vec{U}\right)=0 \tag{2-1}$$

The first study of this form of equations was conducted on hydrodynamic models for semiconductor device simulations [98], [99]. This was further studied for compressible Navier-

Stokes equations [100] to achieve a higher order of accuracy. It involved the simple break down of the second order equation into two first-order equations with U and ∇U as independent variables and then solving the system using the original RKDG method. This method, also known as the first Bassi – Rebay (BR1) method [100] was further extended to achieve higher stability. This incorporated the explicit evaluation of the term dU without making it a new variable. This is also known as the second Bassi – Rebay (BR2) method [101]. There are numerous other methods [102] to tackle these type of equation systems and can also be generalized as the local discontinuous Galerkin (LDG) methods [103]. It should also be noted that different methods have been implemented on DG framework. Some of these methods include Spectral DG method and *hp*-adaptive methods. The first DG spectral method was conducted for elliptic problems [104] and linear hyperbolic problems [105]. It was further studied for advection-diffusion problems, compressible flow and complex geometries [106], [107], [108]. Implementation of adaptive methods in DG is straightforward. This is because there is no inter-element continuity requirement which allows changing the order of the element based on the gradient simple. Lower orders are achieved by making the higher order terms zero. This method has been applied to both hyperbolic conservation laws [109] and convection-diffusion problems [110], [111].

The entire DG framework was implemented in an in-house code called the Multiscale Ionized Gas (MIG) flow code. This is a FORTRAN 90 modular code which can be used to solve various problems like plasma drift-diffusion equations [112], hypersonic Non-Equilibrium flow [113] and magnetohydrodynamic equations [114].

Although the MIG code has been used for a variety of problems, it has been limited to laminar flow physics. Therefore, a capability of simulating three-dimensional turbulent flow physics using DG method was added into the code as a part of this research. To utilize the method's ease of parallelization and high order of accuracy, a fully explicit modal DG method was implemented. Simulating turbulent flow physics requires many computations and parallelization becomes necessary to make the problem tractable. The fully explicit approach allows matrix free computations and reduces inter-element communications, thereby improving the parallel efficiency. The modal approach allows higher order spatial accuracy by simply adding higher order basis functions. Therefore, high-fidelity simulations can be conducted without altering the mesh or expanding the stencil. The Sections 2.2 through 2.5 ahead will describe different methods for space and time discretization of Discontinuous Galerkin finite element framework, convergence study, and parallelization of the code.

2.2 Discontinuous Galerkin Space Discretization

To understand the discretization process for convection-diffusion problems, a generic scalar equation is chosen which can be extended to any equation system. This is given by

$$\frac{\partial U}{\partial t}+\nabla\cdot\vec{F}^{inv}\left(U\right)-\nabla\cdot\vec{F}^{v}\left(U,\nabla U\right)=0 \tag{2-2}$$

$$U\left(x,0\right)=U_0\left(x\right) \tag{2-3}$$

Where U denotes the conserved scalar variable, F^{inv} and F^{v} denote the inviscid and viscous fluxes respectively and $x \in \Omega$, which is the multidimensional domain. All the boundaries are considered periodic in this section. For an element, the approximate solution $U_h\left(x,t\right)$ is represented by Eq. (2-4).

$$U_h\left(x,t\right)=\sum_{l=0}^{P}U_K^l\left(t\right)\varphi_l\left(x\right) \tag{2-4}$$

Where subscript K denotes the element, U_K^l denotes the modal degrees of freedom of that element, φ_l denotes the basis function. Legendre polynomials are chosen as local basis functions because of their property of L^2 – orthogonality, which leads to a diagonal mass matrix and is beneficial when performing explicit calculations. The list of basis functions for a transformed coordinate system of $x, y, z \in [-1,1]$ are provided in Table 2-1.

Table 2-1. Basis functions

Order	$\varphi_l(x)$	$\varphi_l(x,y)$	$\varphi_l(x,y,z)$
0	1	1	1
1	x	x, y	x, y, z
2	$3x^2-1$	$3x^2-1, 3y^2-1, xy$	$3x^2-1, 3y^2-1, 3z^2-1, xy, yz, xz$
3	$5x^3-3x$	$5x^3-3x, 5y^3-3y,$ $(3x^2-1)y, (3y^2-1)x$	$5x^3-3x, 5x^3-3x, 5x^3-3x, (3x^2-1)y, (3x^2-1)z,$ $(3y^2-1)x, (3y^2-1)z, (3z^2-1)x, (3z^2-1)y$

To obtain the weak form of the equation, the variable U is replaced by U_h and Eq. (2-2) is multiplied with the basis function φ_l. After integration by parts, Eq. (2-5) is obtained.

$$\begin{aligned}&\frac{d}{dt}\int_K U_h\varphi(x)\,dx-\int_K \vec{F}^{inv}\cdot\nabla\varphi(x)\,dx+\sum_{e\in\Gamma}\int_e \vec{F}^{inv}\cdot\vec{n}_{e,K}\varphi(x)\,d\Gamma\\&+\int_K \vec{F}^{v}\cdot\nabla\varphi(x)\,dx-\sum_{e\in\Gamma}\int_e \vec{F}^{v}\cdot\vec{n}_{e,K}\varphi(x)\,d\Gamma=0\end{aligned} \tag{2-5}$$

In Eq. (2-5), $n_{e,K}$ denotes the outward unit normal for the edge e (it can be a face or an edge) of element K. Figure 2-1 shows a representation of these elements. The element boundary space is denoted by Γ. For the terms in summation, where fluxes are to be evaluated at the element interfaces, the solution U_h is discontinuous and cannot be uniquely defined. Thus, the terms must be replaced by a locally Lipschitz, consistent, monotone flux to maintain the stability and convergence properties of the scheme with a higher order of accuracy [97]. In Eq. (2-5),

$\vec{F}^v$ is a function of both U and ∇U, which implies that either ∇U needs to be evaluated as a new variable or treated explicitly. Detailed descriptions of the numerical integration, inviscid numerical fluxes, and viscous numerical fluxes are provided in Sections 2.2.1, 2.2.2 and 2.2.3 respectively.

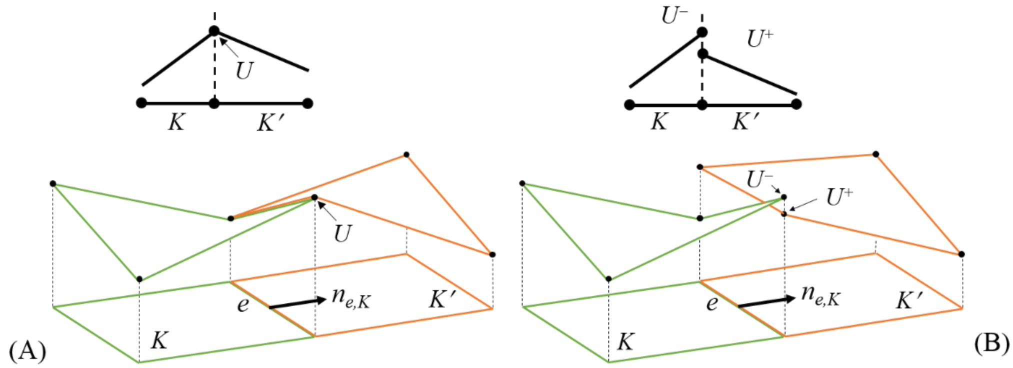

Figure 2-1. Comparison between continuous and discontinuous Galerkin method. (A) Continuous element with interface solution U for element K and K' and (B) discontinuous element with interface solutions U^- and U^+ for element K and K' respectively sharing the edge e with an outward unit normal $n_{e,K}$.

2.2.1 Numerical Integration

All the integrals can be written in a discrete form using Gauss – Legendre quadrature rules.

$$\int_K f(x)dx = jac\int_{-1}^{1} f(x')dx' = jac\sum_{n=1}^{N} w_n f\left(x'_n\right)dx' \tag{2-6}$$

In Eq. (2-6) jac is obtained when transforming from global coordinate system to local coordinate system. Also for all the integrals shown, the basis functions vary with space, while the degrees of freedom vary in time as shown in Eq. (2-4). Since the basis functions are already in transformed space x'_n are the Gauss – Legendre points provided in Table 2-2. One should note that for multidimensional integration the single summation becomes multiple summations with quadrature points x'_n and weights w_n being obtained via the tensor product of one-dimensional weights and points.

Table 2-2. Gauss – Legendre Quadrature

n	1	2	3		4		5		
w_n	2	1	$\frac{8}{9}$	$\frac{5}{9}$	$\frac{18+\sqrt{30}}{36}$	$\frac{18-\sqrt{30}}{36}$	$\frac{128}{225}$	$\frac{322+13\sqrt{70}}{900}$	$\frac{322-13\sqrt{70}}{900}$
x'_n	0	$\pm\sqrt{\frac{1}{3}}$	0	$\pm\sqrt{\frac{3}{5}}$	$\pm\sqrt{\frac{3}{7}-\frac{2}{7}\sqrt{\frac{6}{5}}}$	$\pm\sqrt{\frac{3}{7}+\frac{2}{7}\sqrt{\frac{6}{5}}}$	0	$\pm\sqrt{\frac{5}{9}-\frac{2}{9}\sqrt{\frac{10}{7}}}$	$\pm\sqrt{\frac{5}{9}+\frac{2}{9}\sqrt{\frac{10}{7}}}$

2.2.2 Inviscid Fluxes

As mentioned earlier, the discontinuity at the element interfaces requires the use of numerical fluxes. There are a wide variety of numerical fluxes which satisfy the locally Lipschitz, monotone and consistent criteria [115]. However, the present work uses either Godunov flux or Local Lax-Friedrichs flux [116]. The later, also known as ENO-LLF, provides better shock capturing with improved accuracy. Although it is more diffusive than the Roe flux and the Godunov flux, its impact on the solution is insignificant for higher order approximations [115]. After replacing the inviscid flux in Eq. (2-5) with the numerical flux $h_{e,K}^{inv}$, the first summation term can be written as

$$\sum_{e\in\Gamma}\int_{e}\vec{F}^{inv}\cdot\vec{n}_{e,K}\varphi(x)\,d\Gamma=\sum_{e\in\Gamma}\int_{e}h_{e,K}^{inv}\left(U_h^-,U_h^+\right)\varphi(x)\,d\Gamma \tag{2-7}$$

The + and – states of the solution refer to the outside and inside solution along edge e as depicted in Figure 2-1. The Godunov flux is given by

$$h_{e,K}^{inv}\left(U^-,U^+\right)=\begin{cases}\min_{U^-\le U\le U^+} F^{inv}(U), & \text{if } U^-\le U^+\\ \max_{U^+\le U\le U^-} F^{inv}(U), & \text{otherwise}\end{cases} \tag{2-8}$$

Eq. (2-8) can be interpreted as, if the neighboring solution U^+ is bigger than the inside solution U^- then choose the minimum flux $\left(\min\left[F^{inv}\left(U^+\right),F^{inv}\left(U^-\right)\right]\right)$ otherwise choose the maximum of the two. The Lax – Friedrichs flux is given by

$$h_{e,K}^{inv}\left(U_h^+,U_h^-\right)=\frac{1}{2}\left[\vec{F}^{inv}\left(U_h^-\right)\cdot\vec{n}_{e,K}+\vec{F}^{inv}\left(U_h^+\right)\cdot\vec{n}_{e,K}-\alpha_{e,K}\left(U_h^+-U_h^-\right)\right] \tag{2-9}$$

In Eq. (2-9) $\alpha_{e,K}$ is obtained by evaluating the largest absolute eigenvalue of the Jacobian matrices for the outside and inside elements.

$$\begin{aligned}\alpha_{e,K}&=\max\left[\left\{abs\left(\boldsymbol{\lambda}^+\right)\right\},\left\{abs\left(\boldsymbol{\lambda}^-\right)\right\}\right]\\ \boldsymbol{\lambda}^+&=eigenvalue\left\{\frac{\partial F\left(\overline{U}^+\right)}{\partial U}\cdot n_{e,K}\right\}\\ \boldsymbol{\lambda}^-&=eigenvalue\left\{\frac{\partial F\left(\overline{U}^-\right)}{\partial U}\cdot n_{e,K}\right\}\end{aligned} \tag{2-10}$$

For Euler equations or Navier-Stokes equations, the eigenvalues are $u + a$, $u - a$ and u, where a is the speed of sound. In Eq. (2-10) $\overline{U}$ is the mean solution of the inside or outside element depending on the λ being evaluated.

2.2.3 Viscous Fluxes

The viscous terms in Eq. (2-5) can be modeled in numerous ways. Some of the common methods are Local Discontinuous Galerkin (LDG) [103], Bassi – Rebay (BR1 and BR2) [100], [101] method, Interior Penalty (IP) methods [117], Baumann – Oden [110] etc. A detailed comparison and insight on these methods can be found in Arnold et al. [102]. However, for brevity, only the LDG, BR1 and BR2 schemes are described here.

The viscous fluxes include ∇U as an unknown which must be evaluated either a priori or along with the equation system. To evaluate ∇U, Eq. (2-2) is first changed to Eq. (2-11) and Eq. (2-12).

$$\frac{\partial U}{\partial t}+\nabla\cdot\vec{F}^{inv}\left(U\right)-\nabla\cdot\vec{F}^{v}\left(U,\theta\right)=0 \tag{2-11}$$

$$\theta = \nabla U \tag{2-12}$$

The same procedure as mentioned before is followed and finally, equations like Eq. (2-5) are obtained.

$$\begin{aligned}&\frac{d}{dt}\int_K U_h \varphi(x)\,dx \;-\; \int_K \vec{F}^{inv}(U_h)\cdot\nabla\varphi(x)\,dx \;+\; \sum_{e\in\Gamma}\int_e \vec{F}^{inv}(U_h)\cdot\vec{n}_{e,K}\varphi(x)\,d\Gamma \\ &\quad+\int_K \vec{F}^{v}(U_h,\theta_h)\cdot\nabla\varphi(x)\,dx \;-\; \sum_{e\in\Gamma}\int_e \vec{F}^{v}(U_h,\theta_h)\cdot\vec{n}_{e,K}\varphi(x)\,d\Gamma = 0\end{aligned} \tag{2-13}$$

$$\int_K \theta_h\varphi(x)\,dx \;+\; \int_K U_h\nabla\varphi(x)\,dx \;-\; \sum_{e\in\Gamma}\int_e U_h\vec{n}_{e,K}\varphi(x)\,d\Gamma = 0 \tag{2-14}$$

It should be noted that in Eq. (2-13) and Eq. (2-14) θ_h denotes the approximate solution of θ like the definition given in Eq. (2-4). As discussed earlier, the discontinuous interface requires the fluxes in the summation terms to be evaluated using a locally Lipschitz, consistent and monotone flux. Therefore, the last terms in Eq. (2-13) and Eq. (2-14) are represented as Eq. (2-15) and Eq. (2-16).

$$\sum_{e\in\Gamma}\int_e \vec{F}^{v}(U_h,\theta_h)\cdot\vec{n}_{e,K}\varphi(x)\,d\Gamma = \sum_{e\in\Gamma}\int_e h^{v}_{e,K}\left(U_h^+,U_h^-,\theta_h^+,\theta_h^-\right)\cdot\vec{n}_{e,K}\varphi(x)\,d\Gamma \tag{2-15}$$

$$\sum_{e\in\Gamma}\int_e U_h\vec{n}_{e,K}\varphi(x)\,d\Gamma = \sum_{e\in\Gamma}\int_e h^{\theta}_{e,K}\left(U_h^+,U_h^-,\theta_h^+,\theta_h^-\right)\vec{n}_{e,K}\varphi(x)\,d\Gamma \tag{2-16}$$

The choice of numerical fluxes $h^{v}_{e,K}$ and $h^{\theta}_{e,K}$ gives rise to different methods.

Local discontinuous Galerkin method

The viscous numerical fluxes for this method can be written as

$$\begin{gathered}h\left(U_h^+,U_h^-,\theta_h^+,\theta_h^-\right) = \frac{1}{2}\left[\vec{F}^{v}\left(U_h^+,\theta_h^+\right)+\vec{F}^{v}\left(U_h^-,\theta_h^-\right)\right]+\boldsymbol{C}\left(\boldsymbol{U}^+-\boldsymbol{U}^-\right) \\ \boldsymbol{C} = \begin{bmatrix} c_{11} & c_{12} \\ -c_{12} & 0\end{bmatrix},\ \boldsymbol{U} = \{U,\theta\}\end{gathered} \tag{2-17}$$

Using Eq. (2-17) and since $\vec{F}^{v}$ for Eq. (2-12) is U, obtain the expressions for $h^{v}_{e,K}$ and $h^{\theta}_{e,K}$ are

$$h_{e,K}^{v}\left(U_h^+,U_h^-,\theta_h^+,\theta_h^-\right)=\frac{1}{2}\left[\vec{F}^{v}\left(U_h^+,\theta_h^+\right)+\vec{F}^{v}\left(U_h^-,\theta_h^-\right)\right]+c_{11}\left(U_h^+-U_h^-\right)+c_{12}\left(\theta_h^+-\theta_h^-\right)$$
$$h_{e,K}^{\theta}\left(U_h^+,U_h^-,\theta_h^+,\theta_h^-\right)=\frac{1}{2}\left(U_h^++U_h^-\right)-c_{12}\left(U_h^+-U_h^-\right) \quad (2\text{-}18)$$

A detailed discussion about the choice of constants c_{11} and c_{12}, as well as the extension to multidimensional problems have been described by Cockburn and Shu [103].

Bassi – Rebay method I

The numerical fluxes $h_{e,K}^{v}$ and $h_{e,K}^{\theta}$ are obtained by averaging the fluxes at the edge of the element and its neighbor. This is provided in Eq. (2-19) and Eq. (2-20).

$$h_{e,K}^{v}\left(U_h^+,U_h^-,\theta_h^+,\theta_h^-\right)=\frac{1}{2}\left[\vec{F}^{v}\left(U_h^+,\theta_h^+\right)+\vec{F}^{v}\left(U_h^-,\theta_h^-\right)\right] \quad (2\text{-}19)$$

$$h_{e,K}^{\theta}\left(U_h^+,U_h^-,\theta_h^+,\theta_h^-\right)=\frac{1}{2}\left[U_h^++U_h^-\right] \quad (2\text{-}20)$$

The above method describes the BR1 scheme. However due to the method's deficiencies, such as non-optimal accuracy for purely elliptic problems, spread stencil and increase in the number of degrees of freedom per element (specifically for an implicit algorithm) [101], lead to the implementation of the BR2 scheme.

Bassi – Rebay method II

This scheme uses the property that, the evaluation of solution gradient inside the element is trivial and can be obtained using the gradients of the basis functions. However, for $P = 0$ elements and at interface discontinuities it is not trivial. To obtain ∇U without adding an extra equation a correction term R is added. This is known as the lift operator. After few mathematical manipulations [101] Eq. (2-14) can be rewritten as Eq. (2-21).

$$\int_K \theta_h\varphi(x)\,dx=\int_K \varphi(x)\nabla U_h dx \;+\; \sum_{e\in\Gamma}\int_e \frac{1}{2}\left(U_h^+-U_h^-\right)\vec{n}_{e,K}\varphi(x)\,d\Gamma \quad (2\text{-}21)$$

Thus, we can write $\theta_h = \nabla U_h + R_h$, where R_h is defined like Eq. (2-4) and can be obtained using Eq. (2-22).

$$\int_K R_h \varphi(x)\,dx = \sum_{e\in\Gamma}\int_e \frac{1}{2}\left(U_h^+ - U_h^-\right)\vec{n}_{e,K}\varphi(x)\,d\Gamma \tag{2-22}$$

Using the global lifting operator leads to a non-compact stencil which can be avoided by using local lift operators r_h . This is defined by

$$\begin{gathered}\int_K r_h \varphi(x)\,dx = \int_e \frac{1}{2}\left(U_h^+ - U_h^-\right)\vec{n}_{e,K}\varphi(x)\,d\Gamma \\ R_h = \sum_{e\in\Gamma} r_h\end{gathered} \tag{2-23}$$

When performing volume integrals, global lift operators are used and for element boundary integrals, local lift operators are used. Using this scheme leads to the reduction in the number of degrees of freedom and making the stencil compact due to information exchange only between immediate neighbors.

2.3 Temporal Discretization

The choice of time integration depends on the problem in hand. For transient accuracy, high order time accurate scheme needs to be implemented. Problems involving acoustic wave propagation fall in this category. This section will describe some of the common time integration methods implemented and their advantages and disadvantages.

2.3.1 Explicit Time Integration

To solve the nonlinear hyperbolic conservation laws in DG framework led to the implementation of the explicit version of the method [118]. This overcame the issue of solving nonlinear problems on an element by element basis. However, a simple Euler explicit method is restricted by the CFL condition. To improve the stability of the scheme a TVDM slope limiter was implemented [119]. However, this method was only first order in time and the slope limiter affected the smooth regions of the solution reducing the spatial accuracy. This was finally overcome by using the RKDG method and a modified slope limiter which was second order in time and maintained the accuracy of the scheme in smooth regions [96]. This made the scheme stable for CFL ≤ 1/3. To show the explicit time integration Eq. (2-5) is written in a modified form given by Eq. (2-5).

$$\frac{d}{dt}\int_K U_h\left(x,t^n\right)\varphi(x)\,dx = L_h\left[U_h\left(x,t^n\right)\right]$$

$$\frac{d}{dt}\int_K U_K^l\left(t^n\right)\varphi_l(x)\varphi_l^T(x)\,dx = L_h\left[U_h\left(x,t^n\right)\right] \tag{2-24}$$

$$\frac{d}{dt}\left[U_K^l\left(t^n\right)\right]\int_K \varphi_l(x)\varphi_l^T(x)\,dx = \frac{d}{dt}\left[U_K^l\left(t^n\right)\right][M] = L_h\left[U_h\left(x,t^n\right)\right]$$

$$\frac{d}{dt}\left[U_K^l\left(t^n\right)\right] = L_h\left[U_h\left(x,t^n\right)\right][M]^{-1} \tag{2-25}$$

The mass matrix [*M*], is diagonal for the present choice of basis functions. For simple Euler explicit, Eq. (2-25) can be written as Eq. (2-26) which will give only first-order accurate in time.

$$\left[U_K^l\left(t^{n+1}\right)-U_K^l\left(t^n\right)\right] = (\Delta t)L_h\left[U_h\left(x,t^n\right)\right][M]^{-1} \tag{2-26}$$

Using the second order RKDG method the solution can be more time accurate. This is described in Eq. (2-27).

$$\begin{aligned}
\left[U_K^l\left(t^m\right)\right] &= \left[U_K^l\left(t^n\right)\right]+(\Delta t)L_h\left[U_h\left(x,t^n\right)\right][M]^{-1}\\
\left[U_K^l\left(t^{m+1}\right)\right] &= \left[U_K^l\left(t^m\right)\right]+(\Delta t)L_h\left[U_h\left(x,t^m\right)\right][M]^{-1}\\
\left[U_K^l\left(t^{n+1}\right)\right] &= \frac{1}{2}\left(\left[U_K^l\left(t^{m+1}\right)\right]+\left[U_K^l\left(t^n\right)\right]\right)
\end{aligned} \tag{2-27}$$

The RKDG method has been proven to give CFL ≤ 1/3 for P = 1 and CFL ≤ 1/5 for P = 2 case [96]. Although RKDG scheme has high parallelizability like any explicit scheme, it has CFL restrictions.

2.3.2 Implicit Time Integration

Since the problems studied are nonlinear in nature, Newton Raphson method is employed to solve the equation system. The goal here is to find a value iteratively, which would be closest to the actual solution. Thus, Eq. (2-25) is written as Eq. (2-28) for iteration q

$$f\left(U_k^l\left(t^{n,q}\right)\right)=\frac{d}{dt}\left[U_K^l\left(t^{n,q}\right)\right]-L_h\left[U_h\left(x,t^{n,q}\right)\right]\left[M\right]^{-1}\approx 0 \tag{2-28}$$

To get the next time step solution Eq. (2-28) is discretized in time using Euler Implicit algorithm to obtain Eq. (2-29).

$$f\left(U_k^l\left(t^{n+1,q}\right),U_k^l\left(t^{n+1,q-1}\right)\right)=\left[U_k^l\left(t^{n+1,q}\right)-U_K^l\left(t^{n+1,q-1}\right)\right]-\Delta t L_h\left[U_h\left(x,t^{n+1,q}\right)\right]\left[M\right]^{-1} \tag{2-29}$$

Therefore, for $q \geq 1$, Newton's method can be applied to Eq. (2-29). It should be noted that when q = 1 in Eq. (2-29), $U_K^l\left(t^{n+1,q-1}\right)=U_K^l\left(t^n\right)$.

$$\begin{aligned}&\left[\frac{\partial\left\{f\left(U_k^l\left(t^{n+1,q}\right),U_k^l\left(t^{n,q}\right)\right)\right\}}{\partial U_K^l\left(t^{n+1,q}\right)}\right]\left[U_k^l\left(t^{n+1,q+1}\right)-U_k^l\left(t^{n+1,q}\right)\right]=\\&-f\left(U_k^l\left(t^{n+1,q}\right),U_k^l\left(t^{n+1,q}\right)\right)\end{aligned} \tag{2-30}$$

2.4 Convergence Study

Most of the initial convergence studies for DG methods were done for problems with smooth exact solutions. The first analysis on convergence was carried out for generalized mesh and Cartesian mesh which gave P and P + 1 convergence respectively [120]. Further studies were carried out on the dependence of mesh on the rate of convergence [121]. Cockburn et al. [122] used a local post-processing to double the order of convergence of the method.

To test the convergence of the method, Navier-Stokes equations are solved for a Taylor Green vortex isotropic turbulence problem. The details of the governing equations, problem statement and boundary conditions will be provided in Chapter 5. For convergence study, the L_2 error estimates are obtained by comparing kinetic energy dissipation rate to the DNS solutions. Only the LDG scheme is analyzed here. Three different spatial order polynomials are studied namely P = 2 (quadratic), P = 3 (cubic) and P = 4 (quartic). The degrees of freedom (DOF) corresponding to a N^3 mesh is $N^3 \times (P+1)^3$. It can be seen in Figure 2-2 that the rate of convergence obtained for a polynomial of order P is P + 1.

2.5 Parallel Implementation

To parallelize the MIG code, open MPI was used and the code was tested at the University of Florida high-performance computing center. All the tests were run on servers with Intel E5-2698 v3 processors with the capability to achieve HPL R_{max} of 7.381×10^5 GFlops. The domain was decomposed lexicographically with equal elements in each processor. The solution time for Navier-Stokes equations was studied for processors 1, 8, 16, 32, 64, 128, 256 and 512. The parallel performance is studied by solving time explicit Navier-Stokes equations for Taylor Green vortex isotropic turbulence problem. Two cases were tested with a total number of elements, 32^3 (DOF = 5570560) and 64^3 (DOF = 44545480). The number of elements was chosen low, to have a significant inter-processor communication time with respect to the calculations performed. The problem is run for hundred time steps to average out the total time duration and the all the tests are repeated three times.

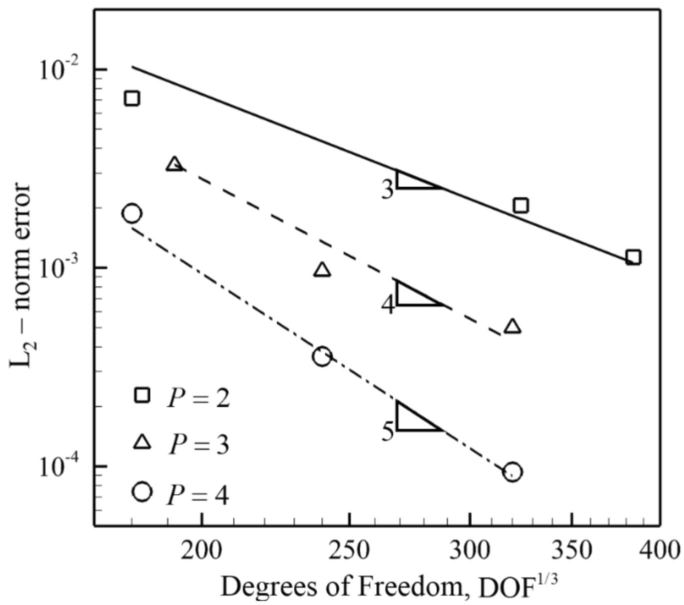

Figure 2-2. Comparison of rate of convergence for P = 2, P = 3 and P = 4 uniform rectangular elements using the LDG scheme to solve Navier-Stokes equations for isotropic turbulence problem.

Figure 2-3 (A) shows that the speedup on a log-log plot is similar for both 32^3 and 64^3 cases up to 512 processors. The power data fit to 32^3 case shows a speedup slope of 0.94 while for 64^3 it shows 0.95. Based on the data fit the parallel speedup (speedup/ideal) efficiency ranges from 99% for 8 processors to 63% for 512 processors. In Figure 2-3 (B) the speedup is plotted on a linear scale and the 32^3 case starts to plateau due to increase in communication time between processors while the 64^3 case maintains a linear slope. The processors show different performances for different runs since each case is not run on the same server, which gives a deviation in the speedup of up to 5%. The initial higher speedup for the 32^3 case compared to the 64^3 case is within this tolerance limit. Further improvements can be made by using non – blocking instead of blocking MPI send and receive commands. Also using better domain decomposition can allow lower communication time.

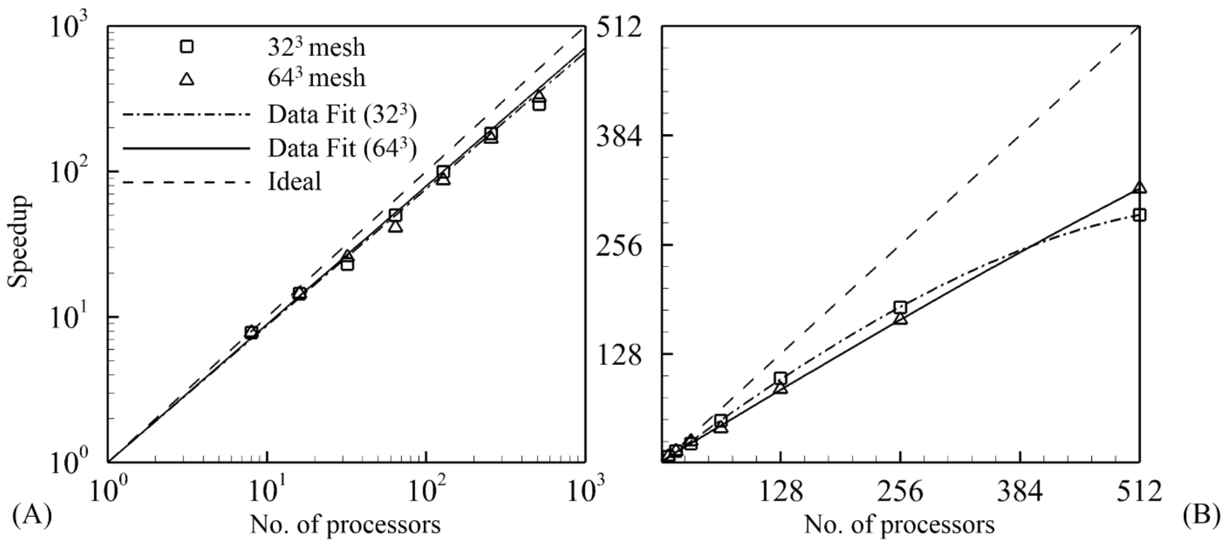

Figure 2-3. Parallel performance for different number of elements. (A) Comparison of speedup on a log-log plot with data fit using power curves and (B) speedup on a linear scale plot with data fit using quadratic polynomial.

CHAPTER 3
GOVERNING EQUATIONS

To understand the mechanics of fluid flow, one must appreciate the equations which govern this flow. This section describes these governing equations as well as other equations involved in this study.

3.1 Compressible Navier-Stokes Equations

For a compressible Newtonian fluid, the multi-dimensional Navier-Stokes equations in normalized conservative form can be written as

$$\frac{\partial \rho}{\partial t} + \nabla \cdot \left(\rho \mathbf{v}\right) = 0 \tag{3-1}$$

$$\frac{\partial \left(\rho \mathbf{v}\right)}{\partial t} + \nabla \cdot \left(\rho \mathbf{v}\mathbf{v}^t + p\mathbf{I} - \bar{\boldsymbol{\tau}}\right) = 0 \tag{3-2}$$

$$\frac{\partial \left(\rho E\right)}{\partial t} + \nabla \cdot \left[\left(\rho E + p\right)\mathbf{v} - k\nabla T - \mathbf{v} \cdot \bar{\boldsymbol{\tau}}\right] = 0 \tag{3-3}$$

$$\bar{\boldsymbol{\tau}} = \begin{bmatrix} \tau_{xx} & \tau_{xy} & \tau_{xz} \\ \tau_{yx} & \tau_{yy} & \tau_{yz} \\ \tau_{zx} & \tau_{zy} & \tau_{zz} \end{bmatrix}; \tau_{ij} = \mu\left(\frac{\partial \mathrm{v}_i}{\partial x_j} + \frac{\partial \mathrm{v}_j}{\partial x_i} - \frac{2}{3}\frac{\partial \mathrm{v}_k}{\partial x_k}\delta_{ij}\right) \tag{3-4}$$

$$p = \left(\gamma - 1\right)\left[\rho E - \frac{1}{2}\rho\left|\mathbf{v}\right|^2\right];\ T = \frac{p}{\rho R};\ R = \frac{1}{\gamma M^2};\ k = \frac{\mu c_p}{\mathrm{Pr}} \tag{3-5}$$

Here $\bar{\boldsymbol{\tau}}$ denotes the viscous stress tensor which is given by Eq. (3-4). The term μ in the viscous stresses is the dynamic viscosity of the fluid and Sutherland's law is used to define it. The term k denotes the thermal conductivity of the fluid with T being its temperature. This term comes from the Fourier's Law of heat conduction. The thermal conductivity is obtained using the dynamic viscosity μ, Prandtl number (Pr) and specific heat (c_p) of the fluid given by Eq. (3-5). The velocity vector is denoted by **v**, which includes the three components, *u*, *v* and *w* in streamwise, wall-normal and spanwise directions respectively.

3.2 Large Eddy Simulation

Although the governing equations mentioned in Section 3.1 can describe the flow physics behind a large variety of scientific problems, simulating turbulent flow physics is still a big challenge and remains one of the most difficult problems posed in physics [123]. One way of tackling this problem is to solve the compressible Navier-Stokes equations on a highly-resolved grid which resolves both the large-scale structures $\left(l_0, u_0, \tau_0\right)$ and the small-scale structures $\left(l_\eta, u_\eta, \tau_\eta\right)$. The Kolmogorov's scales for length, velocity and time are given by Eq. (3-6) [124].

$$\begin{aligned} \eta / l_0 &\sim \mathrm{Re}^{-3/4} \\ u_\eta / u_0 &\sim \mathrm{Re}^{-1/4} \\ \tau_\eta / \tau_0 &\sim \mathrm{Re}^{-1/2} \end{aligned} \tag{3-6}$$

This method of resolving all the scales is commonly known as Direct Numerical Simulation (DNS) [125]. For a numerical scheme to capture these structures encountered in real-world applications such as aircraft flow physics, atmospheric boundary layer, and astrophysics simulations need to be carried out over 10^{15} – 10^{18} grid points. However, due to limitations of computational resources and technological advancement, tackling such a huge problem is not practicable. This led to the introduction of Large – Eddy Simulation (LES) techniques.

LES exactly resolves the large scales when compared to the Reynolds-averaged Navier-Stokes methods and models the small-scale structures using a sub – grid scale (SGS) model. It is based on a low pass filtering operation which eliminates some of the small-scale structures with high frequencies and allows turbulent simulations to be practicable. It was first introduced by Smagorinsky [126] and designed to solve for large scale atmospheric and ocean flow problems.

The constant used in his modeling, also known as the Smagorinsky constant, had to be adjusted depending on the problem. It required trial and error and made the modeling unfavorable for some applications. The first successful implementation of this method for engineering applications was by Deardorff [127]. This model was further extended, to a Dynamic sub – grid scale (SGS) model by Germano et al. [128] and Moin et al. [129] which allowed the variation of Smagorinsky constant with space and time based on two filters. A dynamic global – coefficient SGS model was developed by You and Moin [130] to solve for flow involving complex geometries. For detailed information on different LES modeling techniques and trends, the author refers the reader to the book by Lesieur et al. [123]. Although extensive research has been done to model the small-scale structures, a universal SGS model is yet to be found.

To implement these models the variables in compressible Navier-Stokes equations need to be modified. This is done by using filtered variables and density – weighted Favre-averaged variables [131]. The filtered form of a variable ϕ is obtained using a spatial or temporal filtering function G as shown in Eq. (3-7)[124].

$$\bar{\phi}(\boldsymbol{x},t)=\int_{-\infty}^{\infty}\int_{-\infty}^{\infty}\phi\left(\boldsymbol{r},t'\right)G\left(\boldsymbol{x}-\boldsymbol{r},t-t'\right)dt'd\boldsymbol{r} \tag{3-7}$$

The density – weighted Favre – averaged variables are defined as Eq. (3-8).

$$\tilde{\phi}=\frac{\overline{\rho\phi}}{\bar{\rho}} \tag{3-8}$$

This modifies compressible N – S equations to Eq. (3-9) through Eq. (3-11) [123].

$$\frac{\partial\bar{\rho}}{\partial t}+\nabla\cdot\left(\bar{\rho}\tilde{\mathbf{v}}\right)=0 \tag{3-9}$$

$$\frac{\partial\left(\bar{\rho}\tilde{\mathbf{v}}\right)}{\partial t}+\nabla\cdot\left(\bar{\rho}\tilde{\mathbf{v}}\tilde{\mathbf{v}}^{t}+\varpi\mathbf{I}\ -\ \tilde{\boldsymbol{\tau}}-\boldsymbol{\tau}'\right)=0 \tag{3-10}$$

$$\frac{\partial\left(\bar{\rho}\tilde{E}\right)}{\partial t}+\nabla\cdot\left[\left(\bar{\rho}\tilde{E}+\varpi\right)\tilde{\mathbf{v}}-\tilde{\mathbf{v}}\cdot\tilde{\boldsymbol{\tau}}-\mathcal{L}\right]=0 \tag{3-11}$$

Here ϖ, $\tilde{\boldsymbol{\tau}}$, $\boldsymbol{\tau}'$ and $\mathcal{L}$ are defined by Eq. (3-12). The terms ϖ and υ are called the macro pressure and macro temperature [123].

$$\begin{gathered}
\tilde{\tau}_{ij}=\bar{\mu}\left(\frac{\partial\tilde{\mathrm{v}}_i}{\partial x_j}+\frac{\partial\tilde{\mathrm{v}}_j}{\partial x_i}-\frac{2}{3}\frac{\partial\tilde{\mathrm{v}}_k}{\partial x_k}\delta_{ij}\right)\\
\varpi=p-\frac{1}{3}\mathcal{T}_{ll}\\
\mathcal{T}_{ij}=-\bar{\rho}\left(\mathrm{v}_i\mathrm{v}_j-\tilde{\mathrm{v}}_i\tilde{\mathrm{v}}_j\right)\\
\tau'_{ij}=\mathcal{T}_{ij}-\frac{1}{3}\mathcal{T}_{ll}\delta_{ij}\\
\mathcal{L}=\left(\bar{k}+\bar{\rho}c_p\frac{\nu_t}{\mathrm{Pr}_t}\right)\nabla\upsilon\\
\upsilon=\tilde{T}-\frac{1}{2c_{\mathrm{v}}\bar{\rho}}\mathcal{T}_{ll}
\end{gathered} \tag{3-12}$$

In Eq. (3-12) ν_t and Pr_t are the eddy viscosity and turbulent Prandtl number and $\mathcal{T}_{ij}$ is the SGS tensor. For DNS simulations, $\boldsymbol{\tau}'\to 0$, $\mathcal{L}\to k$ and $\varpi\to p$ with all the variables replaced back to their original unfiltered form. The next two sections will describe the Smagorinsky and the Dynamic SGS models to determine the eddy viscosity and turbulent Prandtl number.

3.2.1 Smagorinsky Sub-Grid Scale Model

This model assumes that at small scales the turbulent kinetic energy produced is balanced by dissipation. It is a variation of Prandtl's mixing layer theory for SGS modeling. This model takes the eddy viscosity to be proportional to the SGS characteristic length Δx and to a SGS velocity. The final form of Smagorinsky eddy viscosity is given by Eq. (3-13).

$$\nu_t=\left(C_S\Delta x\right)^2\left|\tilde{S}\right| \tag{3-13}$$

Where $\left|\tilde{S}\right|$ is given by Eq. (3-14).

$$\left|\tilde{S}\right| = \sqrt{2\tilde{S}_{ij}\tilde{S}_{ij}}$$

$$\tilde{S}_{ij} = \frac{1}{2}\left(\frac{\partial \tilde{u}_i}{\partial x_j} + \frac{\partial \tilde{u}_j}{\partial x_i}\right) \tag{3-14}$$

$$C_{\mathrm{S}} \approx \frac{1}{\pi}\left(\frac{3C_{\mathrm{K}}}{2}\right)^{-3/4}$$

The expression for constant, C_{S} is determined if the filter cutoff wavenumber lies within the $k^{-5/3}$ Kolmogorov cascade. This gives a value of $C_{\mathrm{S}} \approx 0.18$ for Kolmogorov constant $C_{\mathrm{K}} \approx 1.4$. However, this value is modified to $C_{\mathrm{S}} \approx 0.1$ for free shear and wall bounded flows [132] due to the highly dissipative nature of this model in the presence of a wall.

3.2.2 Dynamic Smagorinsky Sub-Grid Scale Model

This model uses a double filtering method to obtain a time and space varying Smagorinsky constant. This is achieved by using the regular low pass filter of width Δx along with another test filter with larger width $\alpha\Delta x$ (for instance $2\Delta x$). This test filter is associated with test function $\hat{G}$ given in equation Eq. (3-15).

$$\hat{\phi}(\boldsymbol{x},t) = \int_{-\infty}^{\infty}\int_{-\infty}^{\infty}\phi\left(\boldsymbol{r},t'\right)\hat{G}\left(\boldsymbol{x}-\boldsymbol{r},t-t'\right)dt'd\boldsymbol{r} \tag{3-15}$$

The SGS tensor obtained using the double filter can be written as Eq. (3-16).

$$\mathrm{T}_{ij} = \left(\overline{\rho \mathrm{v}_i \mathrm{v}_j}\right) - \frac{1}{\hat{\bar{\rho}}}\left(\overline{\rho \mathrm{v}_i}\,\overline{\rho \mathrm{v}_j}\right) \tag{3-16}$$

Using Germano's Identity [128], Leonard's stresses are found.

$$L_{ij} = T_{ij} - \hat{\mathcal{T}}_{ij} = \bar{\rho}\tilde{\mathrm{v}}_i\tilde{\mathrm{v}}_j - \frac{1}{\hat{\bar{\rho}}}\bar{\rho}\tilde{\mathrm{v}}_i\bar{\rho}\tilde{\mathrm{v}}_j \tag{3-17}$$

The eddy viscosity coefficients can be obtained by assuming

$$\mathcal{T}_{ij} - \frac{1}{3}\mathcal{T}_{ll}\delta_{ij} = -2C_{\mathrm{S}}\rho\left(\Delta x\right)^2\left|\tilde{S}\right|\left(\tilde{S}_{ij} - \frac{1}{3}\tilde{S}_{ll}\delta_{ij}\right)$$
$$\mathcal{T}_{ll} = 2C_{\mathrm{I}}\bar{\rho}\left(\Delta x\right)^2\left|\tilde{S}\right|^2 \tag{3-18}$$

Using Eq. (3-17) and Eq. (3-18), the normal stress constant C_{I} is obtained after a spatial averaging $(\langle\ .\ \rangle)$ along directions in which flow may be homogeneous. This is done to avoid ill conditioned model coefficients.

$$C_{\mathrm{I}} = \frac{\left\langle \bar{\rho}\tilde{\mathrm{v}}_l\tilde{\mathrm{v}}_l - \frac{1}{\hat{\bar{\rho}}}\bar{\rho}\tilde{\mathrm{v}}_l\bar{\rho}\tilde{\mathrm{v}}_l \right\rangle}{\left\langle 2\bar{\rho}\left(\alpha\Delta x\right)^2\left|\tilde{S}\right|^2 - 2\left(\Delta x\right)^2\bar{\rho}\left|\tilde{S}\right|^2 \right\rangle}$$
$$C_{\mathrm{S}} = \frac{\left\langle \left(L_{ij} - \frac{1}{3}L_{ll}\delta_{ij}\right)M_{ij} \right\rangle}{\left\langle \left(\Delta x\right)^2 M_{ij}M_{ij} \right\rangle} \tag{3-19}$$
$$M_{ij} = -2\alpha^2\hat{\bar{\rho}}\left|\hat{\tilde{S}}\right|\left(\hat{S}_{ij} - \frac{1}{3}\hat{S}_{ll}\delta_{ij}\right) + 2\rho\left|\tilde{S}\right|\left(\tilde{S}_{ij} - \frac{1}{3}\tilde{S}_{ll}\delta_{ij}\right)$$

For the energy flux, the turbulent Prandtl number is given by Eq. (3-20) [133]

$$\Pr_t = C_{\mathrm{S}}\left(\Delta x\right)^2\frac{\left\langle N_iN_i \right\rangle}{\left\langle -K_iN_i \right\rangle}$$
$$K_i = \bar{\rho}\tilde{\mathrm{v}}_i\tilde{T} - \frac{1}{\hat{\bar{\rho}}}\bar{\rho}\tilde{\mathrm{v}}_i\bar{\rho}\tilde{T} \tag{3-20}$$
$$N_i = \alpha^2\hat{\bar{\rho}}\left|\hat{\tilde{S}}\right|\frac{\partial\hat{\tilde{T}}}{\partial x_i} - \bar{\rho}\left|\tilde{S}\right|\frac{\partial\tilde{T}}{\partial x_i}$$

3.3 Implicit Large Eddy Simulation

In the present work, the turbulent flow simulations have been carried out using implicit large eddy simulation (ILES) with a modal DG method. The ILES approach introduced by Boris [134], [135], does not require problem specific description of SGS model. The motivation came from flux corrected transport convection algorithm [136] which was developed to accurately capture dynamic convection of strong gradients such as shocks and contact discontinuities. It has been often called the monotone integrated LES (MILES) approach. From here on this will also be referred as ILES. The use of shock capturing schemes for LES has been discussed by Garnier et al. [137]. The ILES approach relies on the numerical dissipation to dampen the under – resolved high frequency waves present in the flow. The numerics of ILES is based on modified equation analysis introduced by Hirt [138], where the numerical scheme satisfies a modified partial differential equation (PDE) rather than the original PDE and the truncated terms due to the order approximation become the SGS model. Extensive studies were conducted for free shear flows [139] and wall bounded and free boundary problems using ILES [140]. Examples of methods used for ILES are flux corrected transport, piecewise parabolic method [141] and multi-dimensional positive definite advection transport algorithm [142], third order upwinding scheme [143], and a 6th order compact finite difference scheme with an 8th order filter [144]. Detailed analysis and formulation for ILES can be found in Grinstein et al. [145]. The ILES method can also use a flux limiter which maintains high order accuracy in smooth regions and reduces the scheme to a lower order accuracy when there are sharp gradients. For ILES, the truncation terms due to the numerical algorithm have similar properties as the SGS models [145]. The comparison of decaying isotropic turbulence problem using ILES, Smagorinsky Model and Dynamics Smagorinsky Model with the experimental work [146] is shown in Figure 3-1.

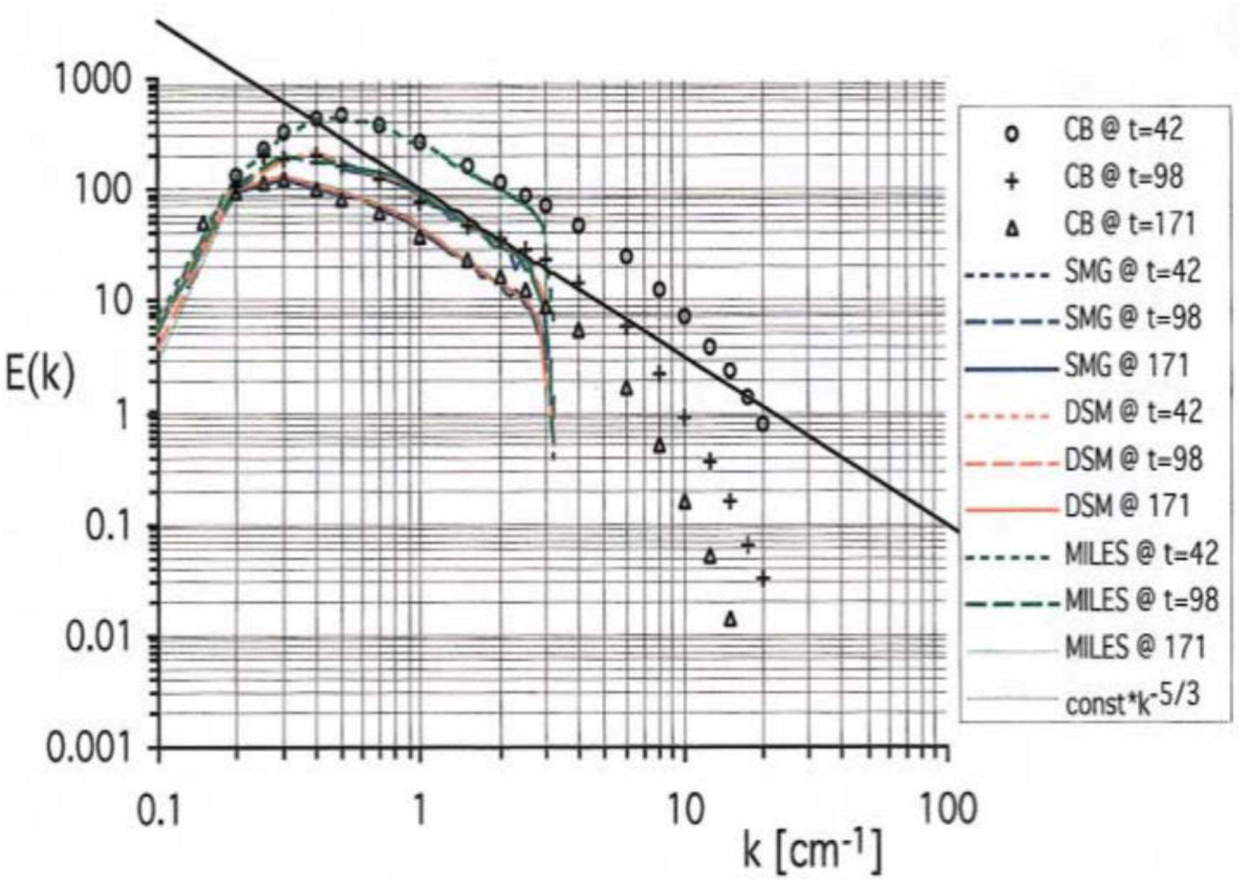

Figure 3-1. Three-dimensional isotropic turbulence comparisons for one-dimensional energy spectrum using different LES methods for a 64^3 grid [140]

However, the question here would be the convergence of this method. This was studied for a helically perturbed circular jet using FCT based ILES with three different grids and was found to converge to a solution for each case [135]. Similar studies were conducted for two and three-dimensional turbulence using Euler equations and comparisons with Navier-Stokes solutions for an evolution of compressible turbulent flow containing strong shocks [147], [141]. The ILES approach was also applied to solve magnetohydrodynamic equations for the 2D Orszag tang vortex problem [148] using second order accurate DG method with different grids and the solution was found to converge with increasing mesh resolution [114]. Figure 3-2 depicts this behavior. However, as the resolution is increased, ILES approaches DNS where all the structures are resolved.

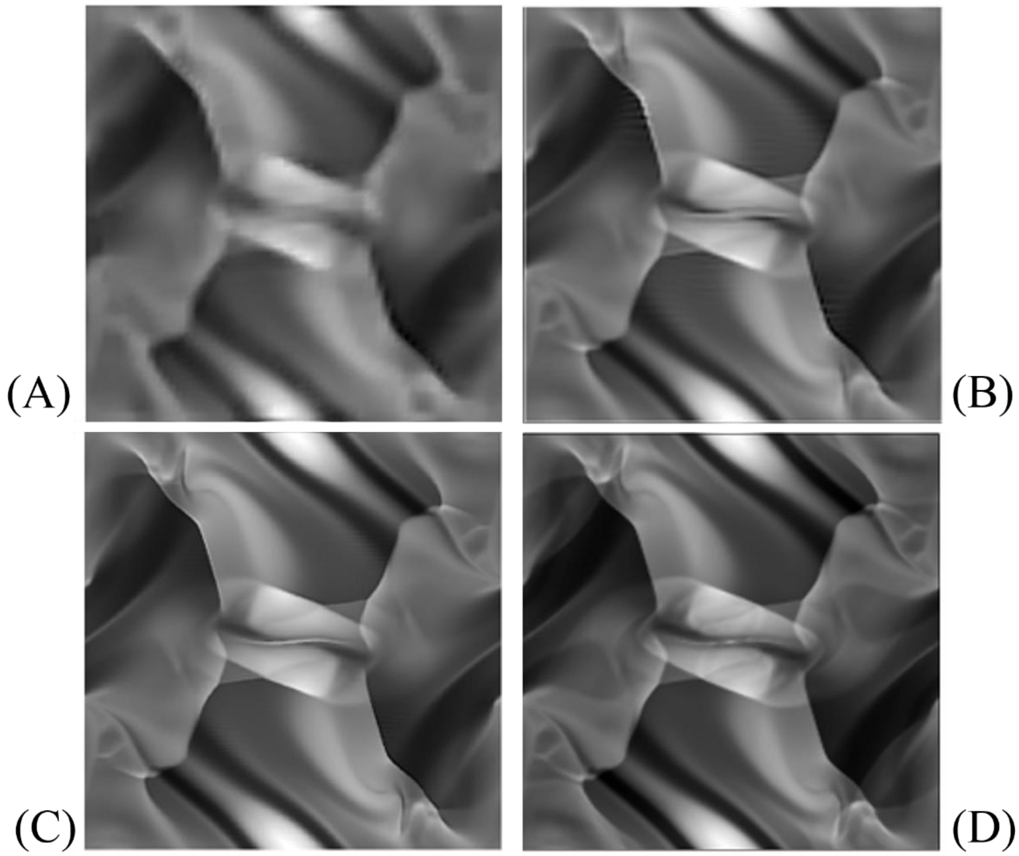

Figure 3-2. Comparison of compressible Orszag Tang vortex at t = 0.5. Solution with (A) 64^2, (B) 128^2, (C) 256^2 elements and (D) solution obtained using a Princeton open source Athena code for 256^2 elements.

To simulate turbulent flow physics in DG MIG an implicit large eddy simulation (ILES) code is implemented. As explained earlier this method relies on capturing the physics of the flow by resolving the large eddies and filtering the higher frequencies based on the high order monotone numerical scheme. DG ILES was applied in two-dimensional flow channel flow [149], [150]. Study on flow over an airfoil was conducted using the ILES approach in DG framework [151]. They used third order and fourth order accurate schemes to resolve the turbulent structures without applying any additional filter or limiter and showed good comparison with previously published work. To understand the effect of order *P*, on the dispersion and dissipation errors, an eigenvalue analysis is necessary. Figure 3-3 shows the numerical dispersion and dissipation for an upwind scheme DG method for one-dimensional advection equation using different spatial order polynomials. The results shown in Figure 3-3 follow the procedure given by Hu et al. [152]. They performed both one-dimensional and two-dimensional wavenumber analyses for an advection equation and a wave equation respectively. Based on their cutoff criteria the advection equation can be best captured by using a 6th order accurate scheme.

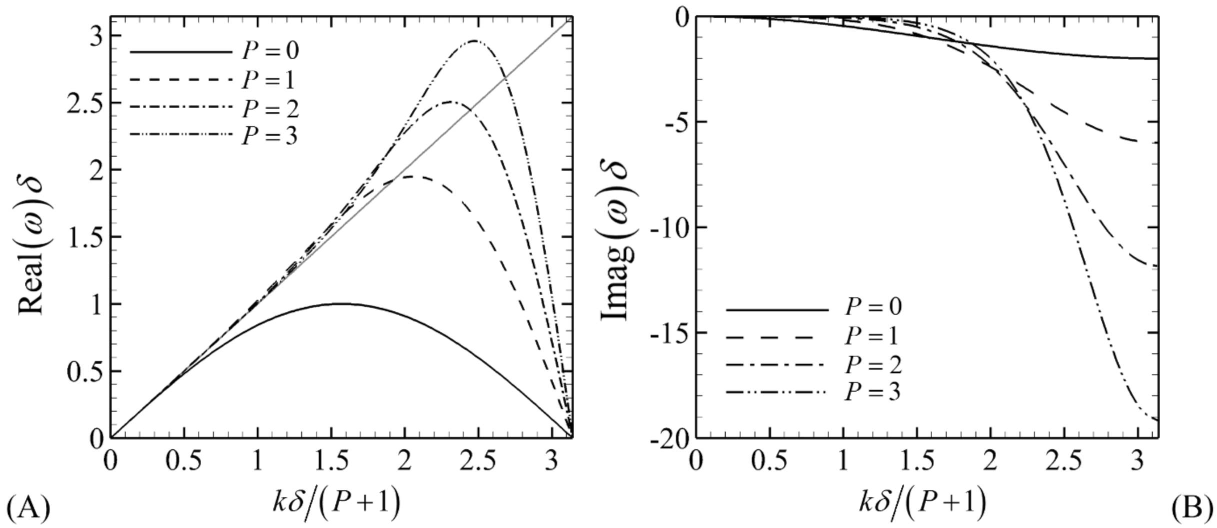

Figure 3-3. Wavenumber analysis for an upwind discontinuous Galerkin framework of an advection problem for different spatial orders of approximation. Numerical (A) dispersion and (B) dissipation.

CHAPTER 4
BACKGROUND OF RELEVANT FLOW PHYSICS

4.1 Relevant Flow Physics

Fluid flow can be classified into many categories, such as viscous or inviscid, internal or external, compressible or incompressible, laminar or turbulent, steady or unsteady, etc. Here we shall consider the laminar and turbulent category. A flow is considered laminar when the fluid is moving in a smooth, orderly and predictable fashion. However, turbulent flow is unpredictable and chaotic. To understand when a flow is laminar or turbulent one must study the nondimensional parameter also known as the Reynolds number (Re). The concept was briefly introduced in Chapter 1. This parameter denotes the ratio of inertial and viscous effects in a flow. The Reynolds number can be represented by Eq. (4-1).

$$\mathrm{Re}_L = \frac{\rho_\infty U_\infty L}{\mu} \tag{4-1}$$

It should be noted that Re_L is generally evaluated using the characteristic length scales L, freestream velocity U_∞, freestream density ρ_∞ and kinematic viscosity ν. The length scale is a very important parameter in determining Re_L and is problem specific. For example, the length scale for flow over a cylinder is the cylinder diameter, whereas the length scale for flow over a flat plate is the streamwise location on the plate or a boundary layer parameter. To study boundary layers, some of the relevant length scales are the boundary layer thickness (δ), displacement thickness (δ^*) and momentum thickness (θ). Their definitions are provided in Eq. (4-2). For a flat plate, the location on the plate is also a relevant length scale. Figure 4-1 shows how the flow changes from laminar to turbulent as we move along the plate toward downstream direction.

$$\begin{aligned}
\delta &= y\big|_{u=0.99U_\infty} \\
\delta^* &= \int_0^\infty \left(1-\frac{\rho u}{\rho_\infty U_\infty}\right) dy \\
\theta &= \int_0^\infty \frac{\rho u}{\rho_\infty U_\infty}\left(1-\frac{\rho u}{\rho_\infty U_\infty}\right) dy
\end{aligned} \tag{4-2}$$

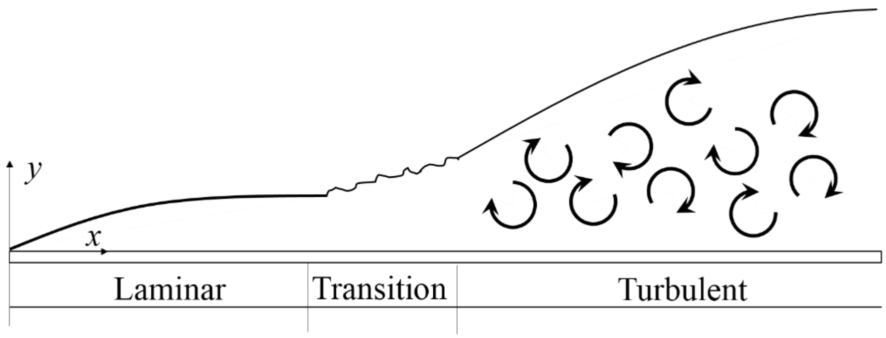

Figure 4-1. Schematic of a boundary layer for a flow over a flat plate with zero pressure gradient.

For any kind of flow involving boundary layers, there is an associated force on the object as the fluid flows past it. This force can have both detrimental effects such as drag on vehicle or aircraft and beneficial effects such as lift in aircrafts.

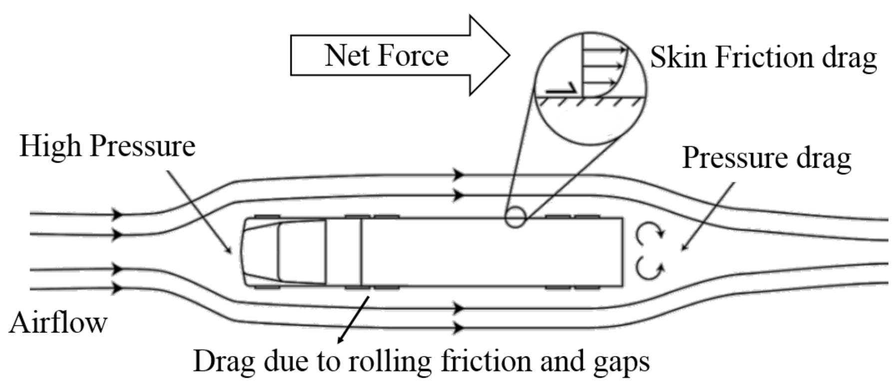

Figure 4-2. Different drag forces associated with a semi-trailer truck [153].

Drag on an object can occur due to pressure drag because of flow separation, friction drag due to boundary layers and roughness, and interference drag due to aerodynamic effects between surfaces. Figure 4-2 shows some of the drag forces associated with a semi-trailer truck. The focus of this study is on the skin friction drag. This along with pressure drag contributes to almost 50 % in a semi-trailer truck [153] at highway speeds. Drag can be associated with skin friction using Eq. (4-3).

$$F_D = c_f A \frac{1}{2} \rho U^2 \tag{4-3}$$

Here A denotes the effective surface area over which the drag is being calculated and c_f is the skin friction coefficient. Most flow control methods are designed to reduce this drag by manipulating the laminar or turbulent boundary layer. The focus of this study is on controlling the drag contributions resulting from skin friction and flow separation.

4.1.1 Laminar Boundary Layer

For a flow over a flat plate with zero pressure gradient, there are different length scales such as boundary layer thickness, momentum thickness, displacement thickness, plate length, etc. Since the boundary layer thickness is a difficult parameter to determine based on measurement, the integral length scales are more reliable. These length scales can be determined through similarity solutions for a zero pressure gradient laminar boundary layer (Blasius solution). Eq. (4-4) gives the relationship between different thicknesses obtained from the similarity solution.

$$\frac{\delta}{x} \approx 5\,\mathrm{Re}_x^{-1/2} \;\; ; \;\; \frac{\delta^*}{\delta} \approx 0.35 \; ; \;\; \frac{\theta}{\delta} \approx 0.14 \tag{4-4}$$

Another parameter relevant in boundary layer flows is given by the skin friction coefficient $\left(c_f\right)$ mentioned before. This parameter quantifies the increase in momentum deficit due to wall shear stress $\left(\tau_w\right)$. This is given by Eq. (4-5).

$$c_f = \frac{\tau_w}{\frac{1}{2}\rho U_\infty^2} = 2\frac{d\theta}{dy} \tag{4-5}$$

4.1.2 Turbulent Boundary Layer

A turbulent boundary layer can be divided into four regions: a viscous sublayer, buffer layer, log layer and a wake region. The mean turbulent velocity profile for a typical flat plate boundary layer at different Reynolds numbers based on displacement thickness is shown in Figure 4-3 [154]. The appropriate velocity, length and time scales for a turbulent boundary layer are defined in Eq. (4-6).

$$u_\tau = \sqrt{\frac{\tau_w}{\rho}} \;;\; \delta_\nu = \frac{\nu}{u_\tau} \;;\; y^+ = \frac{y}{\delta_\nu} \;;\; u^+ = \frac{u}{u_\tau} \;;\; \mathrm{Re}_\tau = \frac{u_\tau \delta}{\nu} \tag{4-6}$$

where u_τ is called the friction velocity and Re_τ is the friction Reynolds number. Close to the wall, viscosity ν and wall shear τ_w become important parameters and are more relevant for scaling than freestream parameters. The friction Reynolds number provides the ratio of the turbulent boundary layer thickness to the viscous length scale δ_ν.

To understand whether a flow will become turbulent or stay laminar, linearized Navier – Stokes equations need to be solved to determine the unstable eigenmodes. The linearized equations reduce to Orr-Sommerfeld and Squire equations. However, in some cases (Poiseuille Flow, pipe flow and Couette flow) the prediction using eigenvalue analysis for instability did not match with the experimental results. This was attributed to the nonlinear effects involved [156]. Different methods [156], [157], [158] were developed to tackle this problem. But the predictions using these methods were not consistent because the transition to turbulence is dependent on the path taken [154].

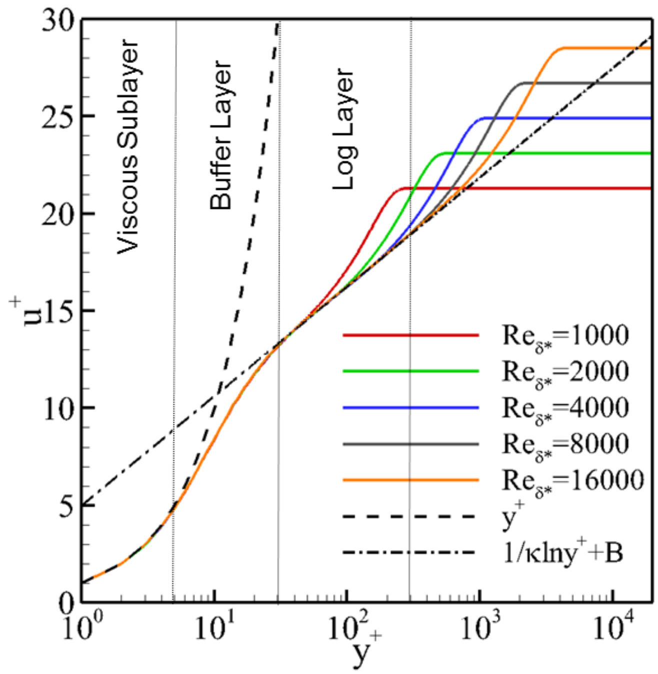

Figure 4-3. Turbulent Boundary layer profile for flow over a flat plate showing different regions in the turbulent boundary [154], [155]

This variability in the transition process can be defined by the term "receptivity" [159]. The receptivity determines the response of the flow to an added perturbation (such as from a plasma actuator). One of the most widely studied flow transition path in boundary layer flows is the TS (Tollmien-Schlichting) mode. It allows small perturbations to grow or decay exponentially along the length of boundary layer flow [160]. Figure 4-4 shows the streamwise and normal velocity components of a boundary layer TS wave and how they can extend way beyond the boundary layer with a rapid decay in magnitude away from the wall.

The growth of TS waves was found to depend on the shape factor (ratio of displacement thickness to the momentum thickness) which gives a critical Reynolds number. This was called the “universal correlation” [161]. It was also found through temporal [162] and spatial stability analysis [163] that there is a threshold magnitude of exponential growth required for the transition process to occur. This threshold is often called as the N-factor.

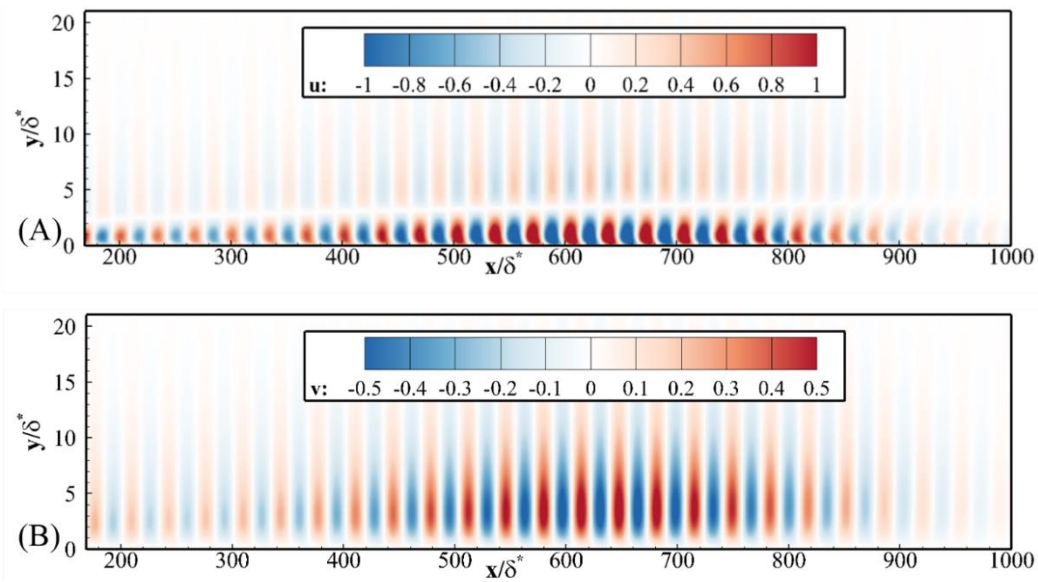

Figure 4-4. TS wave fluctuating velocity components. (A) Streamwise component and (B) wall-normal component [154]

$$A/A_0 = \exp\left(\int_{x_{crit}}^{x_{trans}} \omega_i dt\right)$$
$$A/A_0 = \exp\left(\int_{x_{crit}}^{x_{trans}} \alpha_i dx\right) \tag{4-7}$$

The ratio A/A_0 denotes the ratio of amplitude at a transition location (x_{trans}) to the initial amplitude where the instability begins (x_{crit}). The terms inside the integral are the temporal and spatial amplification rates. However, this analysis did not describe the conditions at the end of the transition process. There are secondary instabilities that form in TS mode after the frequencies reach a certain critical magnitude [164]. These lead to the formation of Λ (lambda) vortices which can form an H-type or K-type pattern as shown in Figure 4-5. The H-type pattern is found to be more stable than the K-type for the same perturbation amplitude [165]. These Λ vortices coalesce and the flow becomes fully turbulent containing hairpin shaped vortices as shown in Figure 4-6. These hairpin (named after their Ω shape) vortices have been studied extensively both numerically and experimentally [166], [167], [168], [169]. The structure is shown in Figure 4-7. It was determined that the regeneration of hairpin vortices occurs behind the hairpin head (spanwise) and the two legs (streamwise) with the vortex forming due to unsteady separation and roll up based on Kelvin – Helmholtz instability.

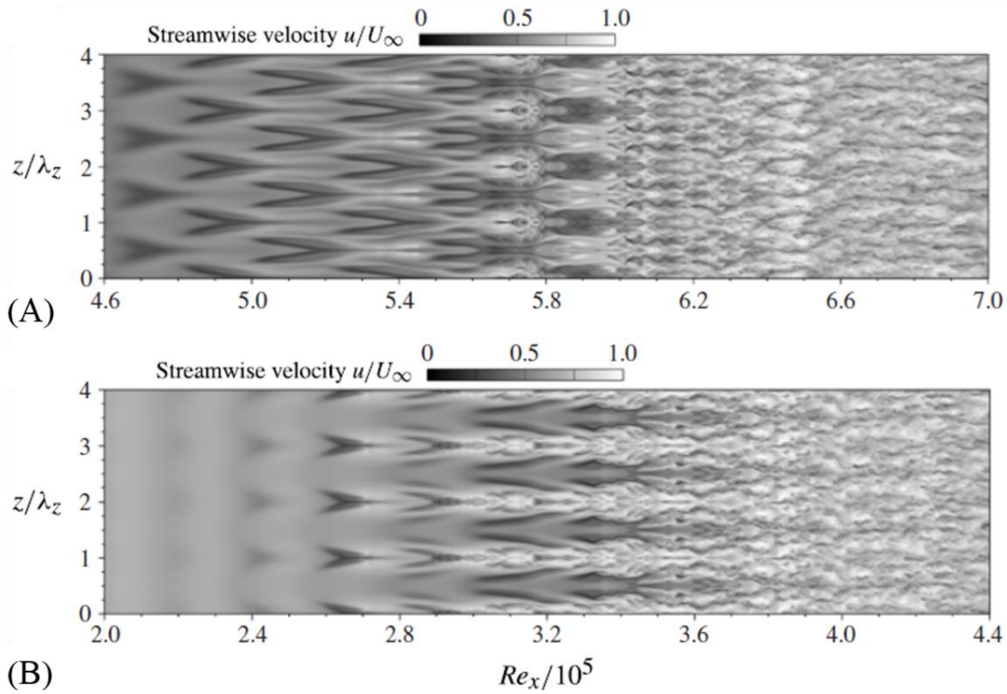

Figure 4-5. Instantaneous streamwise velocity contours showing Λ vortices formed during the transition process. (A) H – type and (B) K – type transition [165].

An illustration of near-wall turbulence region is given in Figure 4-8 (A) which shows the lifted streaks Figure 4-8 (B) and streamwise vortices. These lifted streaks cause a non-linear growth of instabilities. However, there is a threshold lift angle denoted by θ_{20} (angle at y^+ = 20) for these streaks to become unstable. This was found to be 56° as shown in Figure 4-8 (B) [85]. There is also a possibility that the lifted streaks crossing the threshold might not create instability if they are not present outside the viscous sublayer and are not elongated enough in streamwise direction to permit growth.

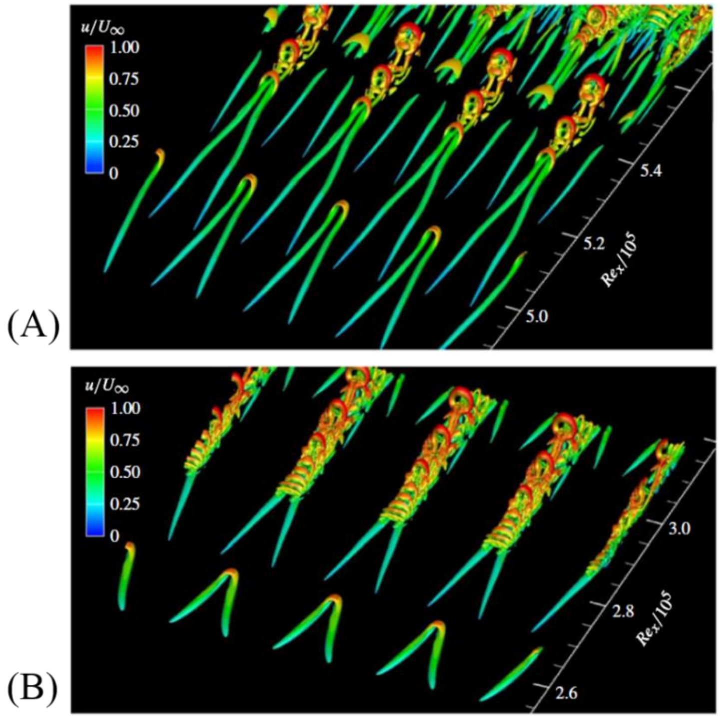

Figure 4-6. Instantaneous iso-surfaces of the second invariant of velocity gradient tensor showing the formation of hairpin vortices from Λ vortices. (A) H – type and (B) K – type transition [165]

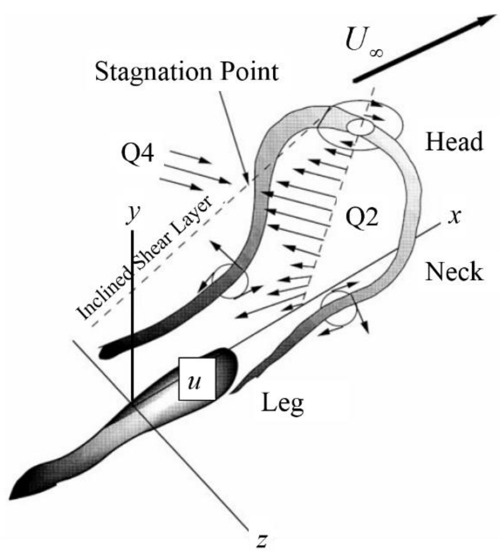

Figure 4-7. Schematic of a hairpin vortex structure showing head, neck, and legs [169]. Fonts have been edited for a clearer depiction.

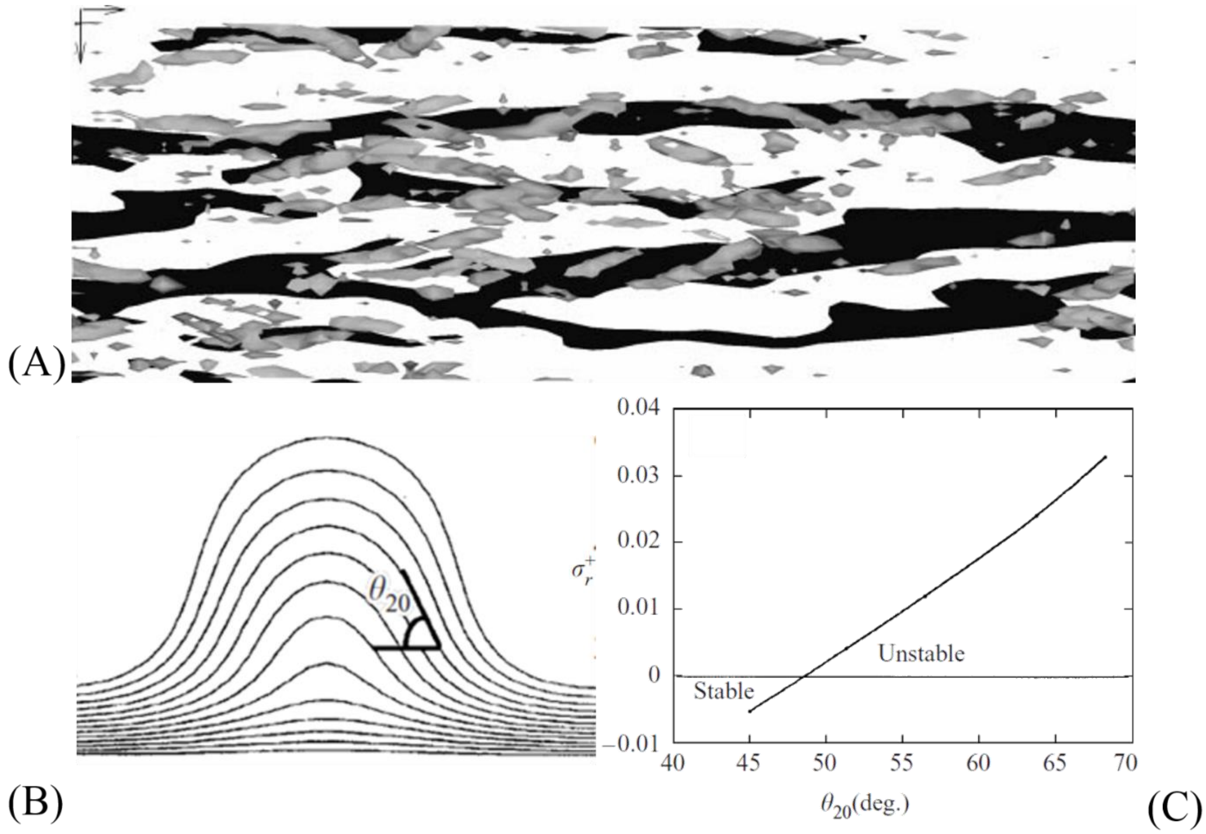

Figure 4-8. Turbulent streaks and stability curve based on lift angle [85]. (A) Top view of the lifted streaks (black regions) and streamwise vortices (grey region), (B) depiction of the streak lift angle and (C) stable and unstable regions.

Another type of transition mechanism known as the oblique wave transition was first investigated numerically using direct numerical simulation (DNS) by Schmid and Henningson [170]. They found that transition via oblique waves can be significantly faster compared to the standard secondary instability mechanism with similar disturbance amplitude. It involves a non-modal growth of disturbances and utilizes transient growth mechanism. Reddy et al. [171] conducted DNS studies for various transition mechanisms and found that transition initiated by streamwise vortices and oblique waves in a Poiseuille flow can occur at subcritical Reynolds numbers with threshold energy at least two orders of magnitude lower when compared to transition via TS waves. DNS of oblique transition was also conducted by Joslin et al. [172] and

Berlin et al. [173] for zero pressure gradient boundary layer flow. Berlin et al. speculated that the oblique transition occurs through three universal steps involving nonlinear streamwise vortex generation, non-modal transient streak growth, and finally streak breakdown. The oblique transition is generated using the superposition of a pair of oblique waves with equal magnitude and opposite sign wave angles. These have been experimentally tested using speakers and ribbons [174], [175] and with periodic suction and blowing [176]. Experiments for Blasius boundary layer as well as Poiseuille flow were conducted by Elofsson and Alfredsson [174], [175]. A depiction of transition via oblique wave transition is shown in Figure 4-9 [177]. The oblique transition has been widely studied for low Mach number supersonic flows since the most unstable mode in this flow regime is the oblique waves. Numerical studies have been conducted at different Mach numbers [178], [179] to show that oblique transition requires lower initial disturbance when compared to two-dimensional TS wave transition scenario.

The streamwise vortex generation involves nonlinear interaction between different wave number eddies which results in a distribution of the disturbance energy. Since the low wavenumber eddies contain higher energy in the energy spectrum, they are affected by the energy distribution. The transient growth of the streamwise oriented structures occurs due to this and when the disturbance reaches an amplitude higher than the threshold, the streaks may become unstable and the flow may break down. Since this transition scenario utilizes the transient growth mechanism, it is governed by an inviscid algebraic instability [180]. Therefore, the transition mainly arises from inviscid growth and viscous damping. The lift up mechanism due to the inviscid algebraic instability causes the streaks to become unstable and finally break down.

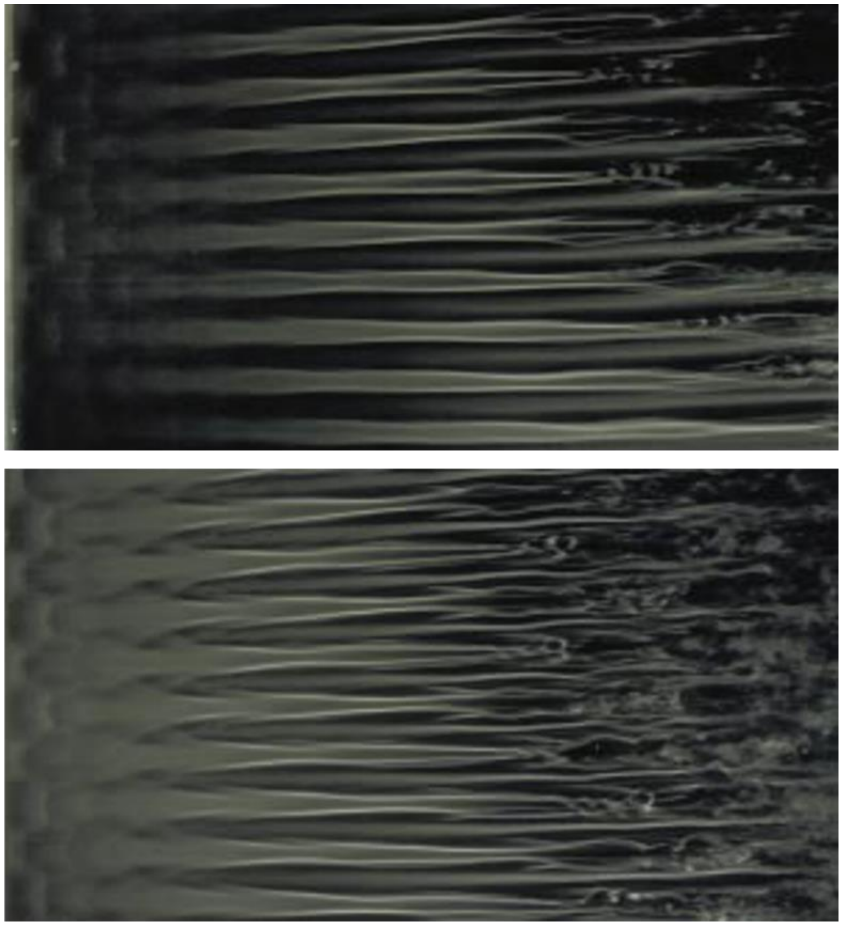

(A)

(B)

Figure 4-9. Flow visualization of oblique transition for a streamwise – spanwise plane with forcing frequency of 51 Hz. (A) Freestream velocity of 8.4 m/s and (B) freestream velocity of 7.0 m/s. [177].

CHAPTER 5
CODE VALIDATION AND BENCHMARKING

The three-dimensional parallel DG code is validated and benchmarked using three turbulent flow cases. The cases studied are the Taylor Green Vortex isotropic turbulence problem, turbulent channel flow, and zero pressure gradient turbulent boundary layer flow over a flat plate. The next three sections will describe these cases and provide comparative results.

5.1 Taylor Green Vortex

5.1.1 Background

This is one of the canonical problems studied for hydrodynamic turbulence. This has been extensively studied in literature to derive empirical and analytical relations in turbulent flow physics. Early in depth numerical investigation of this problem was done by Orszag [181] and Brachet et al. [182], [183]. This problem was also studied by Comte-Bellot and Corrsin [146] experimentally as a grid turbulence problem. These studies became the benchmark for turbulent code validation. Since then, different numerical methods [140], [184], [185], [186] have been used to improve or validate these studies. Results for different Reynolds number, mesh and spatial order of accuracy are compared and investigated. The domain size $\Omega = (2\pi \times 2\pi \times 2\pi)$ with periodic boundaries on all faces. The initial conditions for this problem are

$$\begin{aligned} u_0 &= \sin(x)\cos(y)\cos(z),\ v_0 = \sin(y)\cos(x)\cos(z), w_0 = 0, \\ p_0 &= 100 + \frac{1}{16}\left(\cos(2x)+\cos(2y)\right)\left(\cos(2z)+2\right),\ \rho_0 = 1 \end{aligned} \tag{5-1}$$

This problem is solved using the RKDG method, which involves RK2 time marching and LDG scheme for viscous flux. Two types of inviscid fluxes are tested, namely Godunov flux and LLF flux. The mesh is uniform in all directions and the DOFs for an N^3 mesh corresponds to

$N^3 \times (P+1)^3$. Although the cases can be run at different time step Δt, the solutions are obtained using $\Delta t = 2.5\times10^{-4}$, to have similar time diffusion. The time step is kept low since the Godunov flux requires more restrictive time stepping than the LLF flux. The simulations are run till $t = 10$. Three main parameters are used to study this case. These include the integrated kinetic energy E_k, kinetic energy dissipation rate ε and integrated enstrophy ζ. These parameters are given in Eq. (5-2). For incompressible flows, ε and ζ can be related using the relation given in Eq. (5-3). It should be noted that evaluation of $\varepsilon(\zeta)$ requires additional degrees of freedom to reach the correct ε levels when compared to $\varepsilon(E_k)$.

$$\begin{gathered} E_k = \frac{1}{\rho_0 \Omega}\int_{\Omega} \rho \frac{\mathbf{v}\cdot\mathbf{v}}{2} d\Omega ; \quad \varepsilon(E_k) = -\frac{\partial E_k}{\partial t} \\ \zeta = \frac{1}{\rho_0 \Omega}\int_{\Omega} \rho \frac{\boldsymbol{\omega}\cdot\boldsymbol{\omega}}{2} d\Omega \end{gathered} \tag{5-2}$$

$$\varepsilon(\zeta) = \frac{2\zeta}{\mathrm{Re}} \tag{5-3}$$

5.1.2 Effect of Reynolds Number

To study the effect of Reynolds number, the inviscid flux is kept as Godunov flux and a 60^3 (180^3 degrees of freedom) mesh size is used. The third order accurate $(P=2)$ spatial accuracy is chosen. The Reynolds numbers tested are 100, 200, 400, 800 and 1600. The normalized root mean square (RMS) error in $\varepsilon(E_k)$ in comparison with DNS data is given in Table 5-1. The norm error is evaluated using Eq. (5-4). Except Re = 1600, all the other Reynolds number have results are comparative to DNS results [183]. The profile of kinetic energy dissipation rate $\varepsilon(E_k)$ is shown in Figure 5-1. The dissipation rate is captured accurately by

MIG DG ILES. However, in Section 5.1.3 it will be seen that using LLF inviscid flux has slightly more error than the Godunov flux due to its higher dissipation.

Table 5-1. Norm RMS Error in dissipation rate at different Reynolds number

Re	Norm RMS Error
100	2.25×10^{-6}
200	2.85×10^{-6}
400	2.62×10^{-6}
800	3.14×10^{-5}
1600	3.43×10^{-4}

$$\text{Norm RMS Error} = \sqrt{\frac{\sum_{i=1}^{N}\left(\varepsilon_i - \varepsilon_{DNS}\right)^2}{N}} \tag{5-4}$$

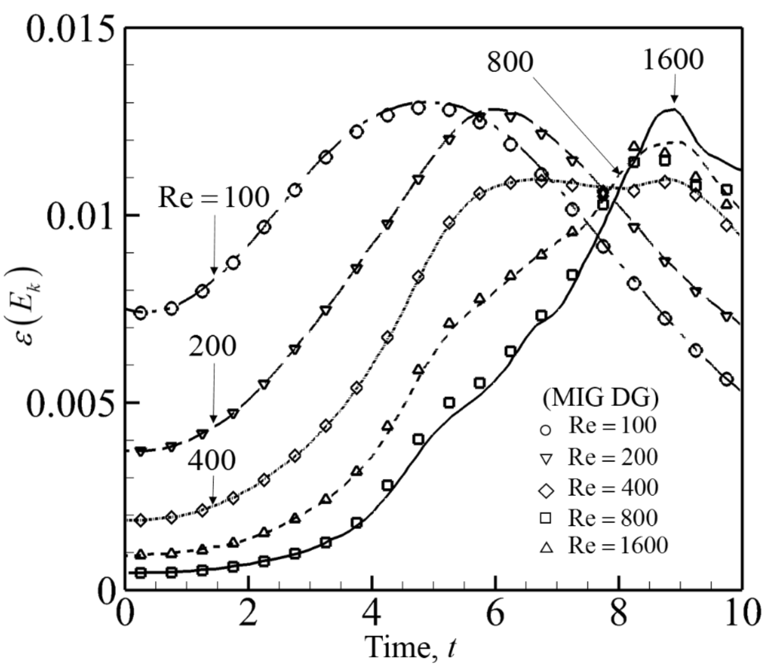

Figure 5-1. Energy dissipation rate at different Reynolds numbers using third order accurate DG solution on a 60^3 mesh compared with DNS results [183], [184].

5.1.3 Effect of Inviscid Numerical Flux

To study the effect of numerical fluxes, the Godunov flux and LLF flux are tested for a 60^3 with P = 2 (180^3 DOF), 45^3 with P = 3 (180^3 DOF) and 36^3 with P = 3 (180^3 DOF) mesh sizes. It should be noted that the total DOF is calculated by $N^3\times\left(P+1\right)^3$. The Reynolds number for the cases here is kept at Re = 1600. The normalized root mean square (RMS) error in $\varepsilon\left(E_k\right)$ in comparison with DNS data [184] is given in Table 5-2. The dissipation rate has higher errors when LLF flux is used. The greater diffusive nature of LLF flux was also observed by Beck et al. [187] when comparing with Roe flux. However, the differences are very low as the errors are two orders of magnitude lower than the variable value. It should be noted that although Godunov flux is more accurate due to its least dissipative nature, it creates larger oscillations which can result in backscatter and also requires lower time step. Therefore, although LLF has a higher diffusion it is preferable to be used with slightly higher degrees of freedom. For this problem, using around 1.4 times the DOF in each direction matches the solutions for both the fluxes at P = 2. For higher orders, the differences dissipation rate due to fluxes become negligible. This can be observed in Figure 5-2 which depicts the similarity in solutions for the two fluxes at different degrees of freedom for a P = 2 and P = 4 case.

Table 5-2. Norm RMS Error in dissipation rate for Godunov and LLF fluxes

Order	Godunov Flux	Local Lax – Friedrichs flux
2	3.43×10^{-4}	7.35×10^{-4}
3	9.38×10^{-5}	3.36×10^{-4}
4	7.83×10^{-4}	1.93×10^{-4}

5.1.4 Effect of Spatial Order of Accuracy

To study the effect of spatial order of accuracy LLF flux is chosen as the inviscid numerical flux. The problem is studied using orders P = 2, P = 3 and P = 4. The Reynolds number for the cases here is kept at Re = 1600. All the parameters mentioned in Eq. (5-2) and Eq. (5-3) are depicted in Figure 5-3. Both $\varepsilon\left(\zeta\right)$ and $\varepsilon\left(E_k\right)$ are compared to highlight the differences between ILES results and DNS results [184], as well as to show that capturing gradients in ILES requires more degrees of freedom. The DNS results are obtained using 13-point DRP scheme with 512^3 grid [184]. The solutions obtained using P = 2 have the largest error for the same DOF. This is a known property which is utilized in turbulent flow simulations using higher order methods. However, the differences between the fluxes are negligible.

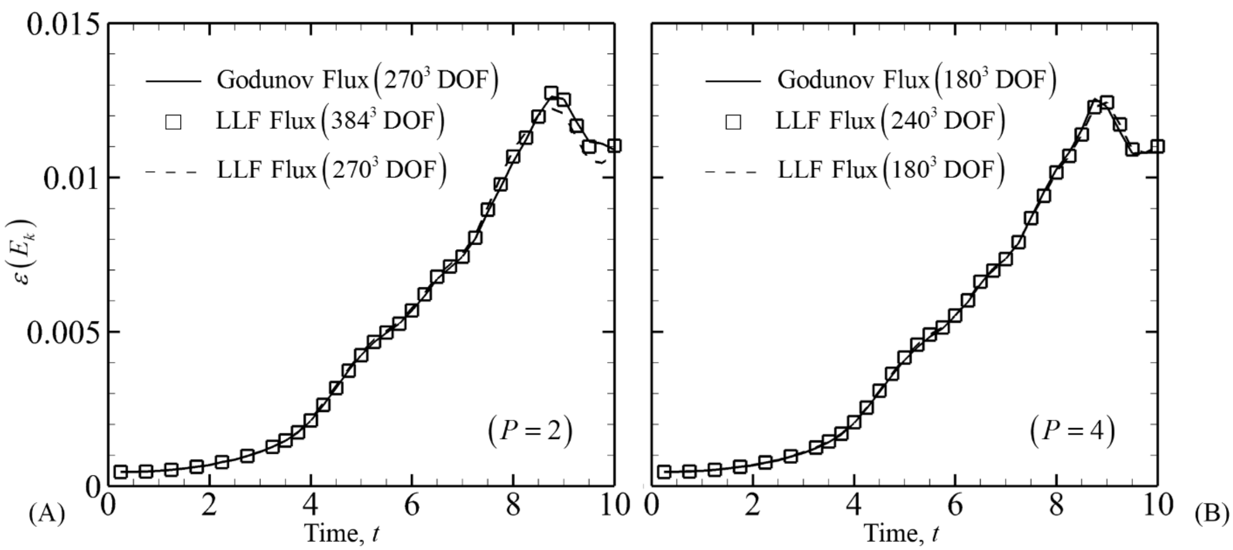

Figure 5-2. Comparison of energy dissipation rate for different inviscid numerical fluxes at different degrees of freedom and polynomial order. Dissipation rate for (A) P = 2 and (B) P = 4.

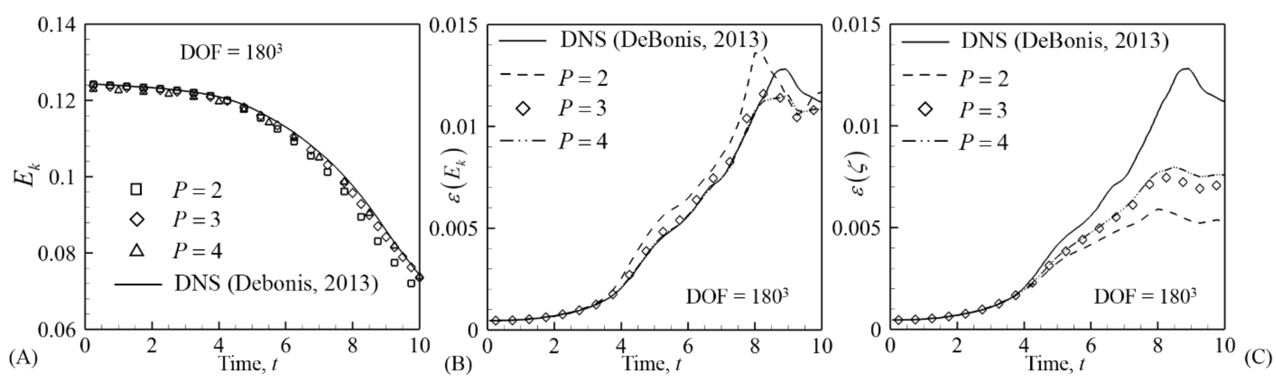

Figure 5-3. Comparison of MIG DG solution with published DNS results [184]. (A)Turbulent kinetic energy, (B) energy dissipation rate based on integral kinetic energy and (C) energy dissipation rate based on enstrophy.

To see if the solution converges, higher DOFs were compared to the DNS solution. This is depicted in Figure 5-4. Although $\varepsilon(E_k)$ has converged to the DNS solution, $\varepsilon(\zeta)$ has not converged yet. This behavior was also observed by DeBonis [184] who performed a comparison between 4th, 8th and 12th order central finite difference schemes with a 13-point DRP scheme (DNS). Similar behavior has been found for DNS [188] solutions using DG method.

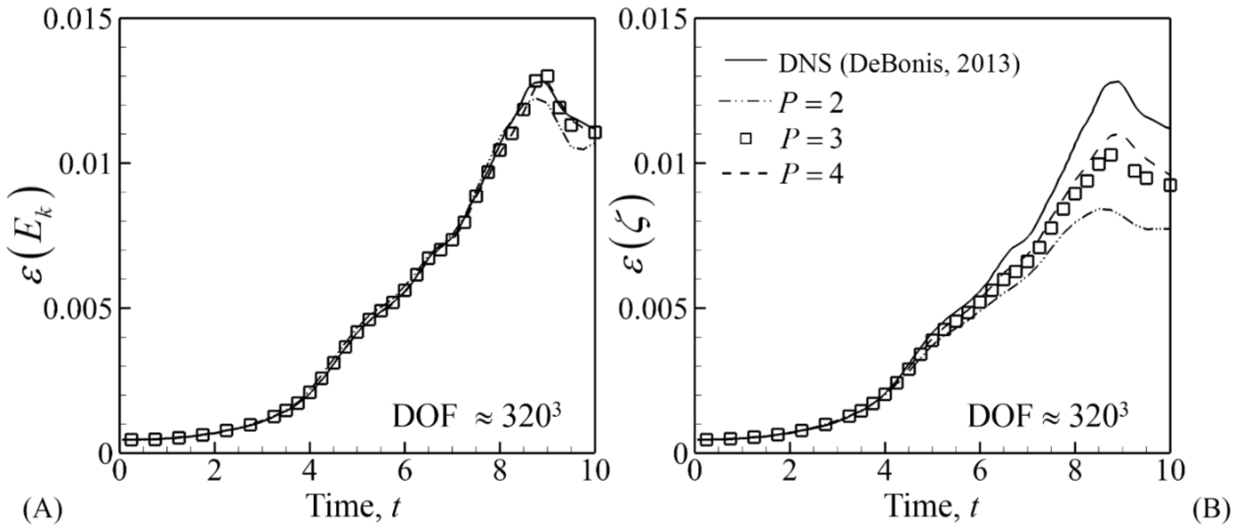

Figure 5-4. Comparison of turbulent kinetic energy dissipation rate for different orders of spatial accuracy at approximately 320^3 DOF. (A) Dissipation rate based on integral kinetic energy and (B) enstrophy.

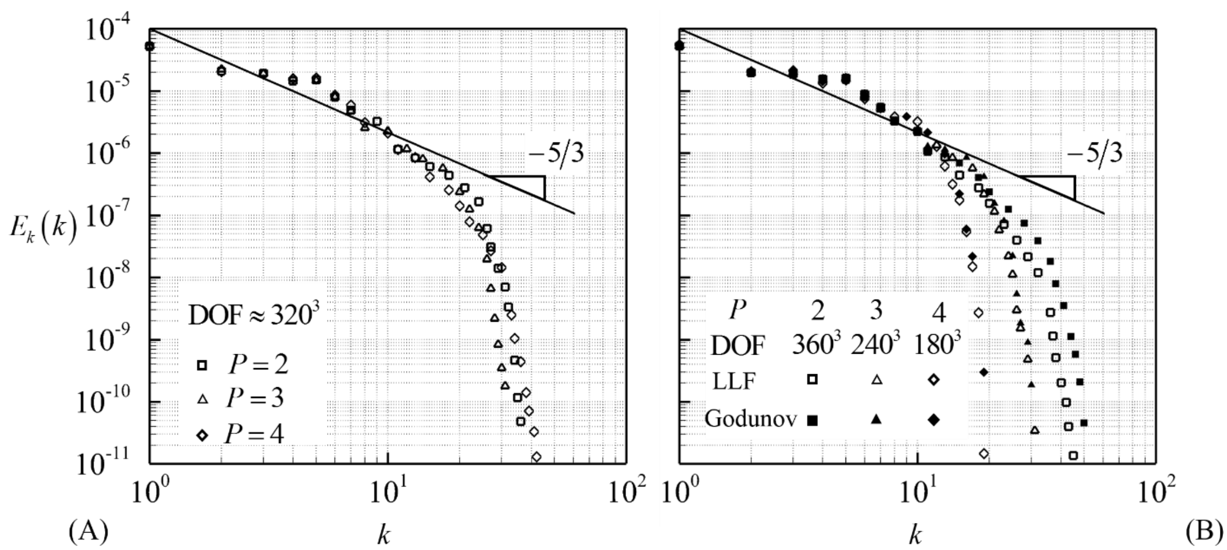

Figure 5-5. Kinetic energy spectrum for Taylor Green vortex problem at t = 10. (A) Effect of polynomial order and (B) effect of inviscid flux on energy spectrum.

5.1.5 Energy Spectrum

The kinetic energy spectrum for all the cases is plotted at t = 10 in Figure 5-5. All the curves follow the standard turbulent spectrum of −5/3 slope. The differences between the spectrums for different order polynomials depicted in Figure 5-5 (A) is negligible. Also, the effect of flux is not significant on the energy spectrum.

5.1.6 Flow Structures

The instantaneous iso-surface of Q – criterion (positive second scalar invariant of ∇u) colored with velocity magnitude is depicted in Figure 5-6. The equation defining Q – criterion is provided in Eq. (5-5). The data corresponds to the simulation with P = 3 (DOF = 320^3). The coherent structures keep breaking down into smaller structures as the time progresses and finally around t = 9 the flow becomes fully turbulent.

$$Q = \frac{1}{2}\left[\left|\boldsymbol{\Omega}\right|^2 - \left|\mathbf{S}\right|^2\right];\ \boldsymbol{\Omega} = \frac{1}{2}\left[\nabla\mathbf{v} - \left(\nabla\mathbf{v}\right)^T\right];\ \mathbf{S} = \frac{1}{2}\left[\nabla\mathbf{v} + \left(\nabla\mathbf{v}\right)^T\right] \tag{5-5}$$

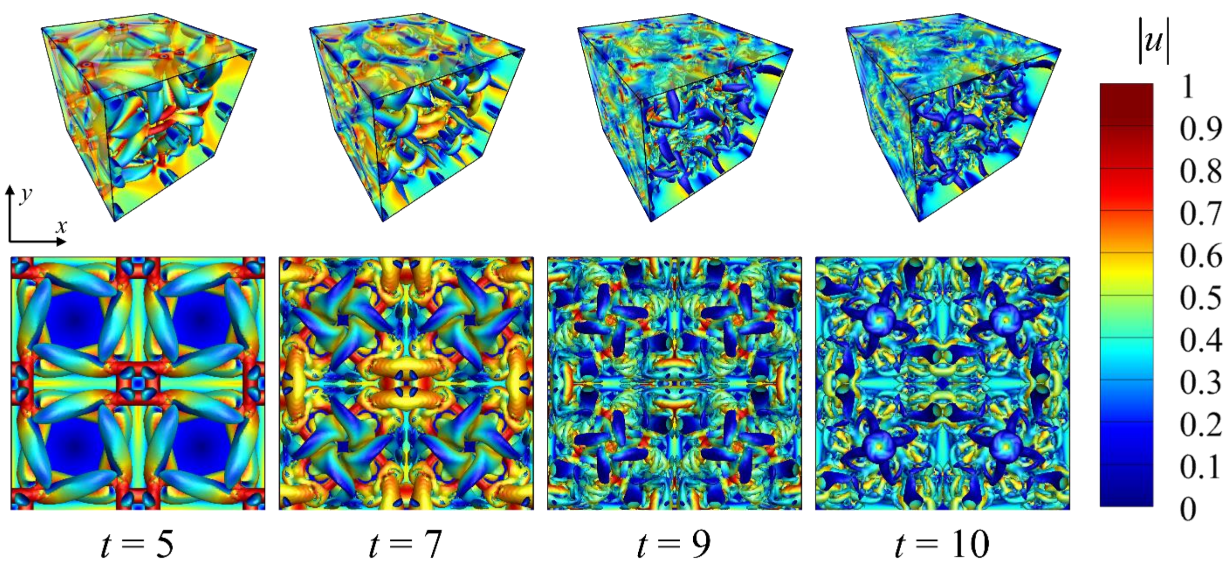

Figure 5-6. Instantaneous Q – criterion colored with instantaneous velocity magnitude showing breakdown of coherent structures with time for a Taylor Green vortex problem.

5.2 Zero Pressure Gradient Turbulent Boundary Layer

5.2.1 Background

A spatially developing zero pressure gradient turbulent boundary layer (ZPGTBL) flow over a flat plate is studied using numerical simulation. Turbulent flow over a flat plate has been extensively studied both experimentally and numerically to understand the fluid-fluid and fluid-structure interactions in various applications. The main objective has been to obtain better scaling laws and models for predicting quantities of practical relevance. Extensive experimental studies of the turbulent boundary layer were conducted by Klebanoff and Diehl [189], Coles [190], Kline et al. [191], Murlis et al. [192], Österlund [193], Degraaff and Eaton [194], Schlatter et al. [195] and Hutchins et al. [196]. Degraaff and Eaton provided data for a wide range of Reynolds numbers and different scaling parameters for predicting boundary layer characteristics at near wall and wake region. Hutchins et al. [196] conducted studies on large-scale coherent structures for atmospheric turbulence and compared them with the laboratory turbulent boundary layers. They found that the two-point correlations of velocity fluctuations are similar for both cases.

In practical applications, the friction Reynolds numbers $\left(\mathrm{Re}_{\tau} = u_{\tau}\delta/\nu\right)$ based on friction velocity u_{τ}, boundary layer thickness δ and kinematic viscosity ν, can go up to $O\ (10^6)$. This is challenging to obtain in laboratory experiments or simulation settings due to large length scales and prohibitive computational resource requirement. Therefore, better scaling laws and models are required to predict turbulent flow field at high Reynolds numbers. Due to the recent advances in computational technology, direct numerical simulation (DNS) has become feasible for simulating ZPGTBL at moderate Reynolds numbers. DNS for spatially developing ZPGTBL was conducted by Spalart [197] for Reynolds number based on momentum boundary layer thickness,

$\mathrm{Re}_\theta = U_\infty \theta / \nu$ up to 1410 and by Schlatter [195] for Re_θ up to 2500, which gave extensive benchmark data for this problem. Although DNS is a useful tool to accurately capture all the relevant scales in a flow of moderate Reynolds number, computational resource demands remain restrictive. As a remedy, large-eddy simulations (LES) have become increasingly popular as a simulation tool to understand turbulent flow physics.

Schlatter and Orlu [198] compared various DNS data for ZPGTBL and found inconsistencies in the integral quantities as well as mean and fluctuation profiles. They suggest that the variation of these quantities for similar freestream flow conditions reported by different authors is mainly due to the differences in prescribing inflow conditions, settling length and domain size. Therefore, a detailed study of ZPGTBL is documented in this paper to establish the capability of DG ILES in capturing turbulent flow physics. The first representative set of works on LES using DG started only a decade ago and was conducted by Collis and Chang [199]. They studied flow over a cylinder and inside a channel. Sengupta et al. [150] and Wei and Pollard [200] simulated turbulent channel flow using DG method. More recently Uranga et al. [151], Bassi et al. [201] and Fernandez et al. [202] conducted a simulation of turbulent flow over an airfoil. DG method was also tested for different types of problems including isotropic turbulence and channel flow by Wiart et al. [203].

This study involves the transition to turbulence using bypass mechanism. For all the cases here, the Reynolds number based on plate length, Re_x ranges from 2.5×10^5 to 6.25×10^5 and Re_θ ranges from 330 to 1250. This problem is studied using P = 2 order for spatial accuracy and RK2 method for temporal accuracy. The LLF flux is chosen as the inviscid flux and LDG scheme is used for the viscous fluxes.

5.2.2 Mesh Details

The different mesh sizes used have been tabulated in Table 5-3. The streamwise (*x*-direction), wall-normal (*y*-direction) and spanwise (*z*-direction) domain sizes, $\left(L_x^+,\ L_y^+ \text{ and } L_z^+ \text{ respectively}\right)$ are based on the inlet wall unit $\Delta y_i^+ = \Delta y_i u_{\tau,i} / \nu$, where $u_{\tau,i}$ is the friction velocity at the inlet and ν is the kinematic viscosity, which is held constant for all the mesh sizes. Although, the number of elements $\left(N_y\right)$ in the wall-normal direction is changed, Δy_i^+ does not change since more elements are packed in the log layer and the mesh is wall-resolved. This was done since studies conducted by Nagib et al. [204] found large variations of mean data for the log layer. The number of grid points in the boundary layer ranges over the domain from 40 at the inlet to 44 at the outlet for the coarse mesh, 50 to 60 for the medium mesh, 80 to 90 for the fine mesh of case I and 40 to 44 for case II. The mesh is stretched [205] in the wall-normal direction using

$$y(j) = L_y \frac{C\eta}{1+C-\eta}\ ,\ \eta = \frac{j-1}{N_y - 1} \tag{5-6}$$

In Eq. (5-6), L_y is the height of the domain in wall-normal direction and *j* is the grid point. The choice of constant *C* gives $\Delta y_i^+ = 0.9$. The mesh is uniform in *x* and *z* directions. However, near the streamwise and wall-normal outflow boundaries, the mesh is geometrically expanded and the outlet velocities are relaminarized to Blasius profile using a sink term, like a sponge region [206], [207], to avoid any reflections. It should be noted that the mesh parameters chosen here correspond to the grid requirements for wall resolved LES provided by Choi and Moin [208].

Table 5-3. Computational mesh details

Case	N_x	N_y	N_z	Δx_i^+	Δy_i^+	Δz_i^+	L_x^+	L_y^+	L_z^+
coarse	700	48	32	26.5	0.9	24	18 600	4200	750
z_fine	700	48	64	26.5	0.9	12	18 600	4200	750
medium	700	64	64	26.5	0.9	12	18 600	4200	750
fine	950	96	64	13	0.9	12	18 600	4200	750

5.2.3 Flow Field Parameters

The Mach number for all the cases studied here is set to 0.5, which is weakly compressible. The inlet freestream conditions are applied with static pressure (P_∞) of 10132.5 Pa and static temperature (T_∞) of 273 K. The freestream velocity $U_\infty = 165.61\,\text{m/s}$ and the viscosity (μ_∞) based on Sutherland's law for T_∞ is 1.716×10^{-5} Ns/m^2. A Blasius profile corresponding to $\mathrm{Re}_x = 2.5\times10^5$ is used for the streamwise and wall-normal velocity at the inlet. Based on this, the incoming Re_θ is 330. The inlet boundary layer thickness δ_i based on $0.99U_\infty$ is 6.2×10^{-3} and inlet displacement thickness $\delta_i^* = 6.7\times10^{-4}$. The wall is kept at no slip adiabatic conditions. Both top and outlet boundary conditions are obtained by linear extrapolation with the pressure kept at P_∞. The flow is tripped using the forcing function given by Schlatter and Orlu [209] for their baseline case. The tripping method uses a weak random volume forcing in the wall-normal direction. It includes three main parameters, amplitude A_t, spanwise length scale z_s and temporal scale t_s. The forcing function is given by

$$
\begin{aligned}
F_y &= \exp\left[\left\{(x-x_0)/l_x\right\}^2 - \left\{y/l_y\right\}^2\right] g(z,t) \\
g(z,t) &= A_t\left[\left\{1-b(t)\right\}h^i(z) + b(t)h^{i+1}(z)\right] \\
b(t) &= 3p^2 - 2p^3;\; p = t/t_s - i;\; i = \mathrm{int}(t/t_s)
\end{aligned}
\tag{5-7}
$$

In Eq. (5-7) x_0 is the streamwise location of the forcing which is set to $10\delta_i^*$, l_x and l_y are the spatial extent of the forcing and are set to $4\delta_i^*$ and δ_i^* respectively. The function $h^i(z)$ is a combination of random unit amplitude harmonic signals with wavenumber modes only below $2\pi/z_s$ and the random amplitude obtained by using *i* as the seeding value to pseudo-random generator. For the present study, six modes are taken in the spanwise direction. The temporal scale $t_s = 4\delta_i^*/U_\infty$ and the spanwise length scale $z_s = 1.7\delta_i^*$. The author recommends the reader to refer to the paper by Schlatter and Orlu [209] for a detailed explanation.

For all the cases, the non-dimensional time step is $\Delta t^+ = u_{\tau,i}^2 \Delta t/\nu = 0.0048$. The flow was allowed to convect two times over the entire streamwise length at a convective speed of around $0.75U_\infty$, before the mean flow calculations were started. This corresponds to about $3100\nu/u_\tau^2$ and the mean flow calculations were carried out over a period of $1200\nu/u_\tau^2$.

5.2.4 Mesh Convergence

The mesh sizes tested showed that the mean velocity scaled by viscous units, $U^+ = \overline{U}/u_\tau$, where $\overline{U}$ is the time and spanwise averaged solution, has minor variations due to mesh size as depicted in Figure 5-7. Only the coarse mesh overpredicts the log layer region. The skin friction, c_f shows good agreement with published DNS data [209]. In Figure 5-8, the normalized root mean square (RMS) streamwise fluctuating velocity $u'^+_{rms} = \sqrt{\overline{u'^2}/u_\tau^2}$, wall-normal fluctuating velocity $v'^+_{rms} = \sqrt{\overline{u'^2}/u_\tau^2}$, spanwise fluctuating velocity $w'^+_{rms} = \sqrt{\overline{u'^2}/u_\tau^2}$, and mean Reynolds stress $\overline{u'v'}^+$, where u', v' and w' are the instantaneous fluctuating components, are plotted. Coarse mesh is not suitable to resolve the perturbations. Doubling the mesh density in the spanwise direction solves this issue. Therefore, the mesh sizes equal or more than the z_fine case are adequate to resolve the fluctuations. The medium mesh case is used for rest of the visualizations and comparisons of case I. However, it should be noted that for the present study higher than second order moments were not compared, as suggested by Spalart [197]. For the current study, medium mesh case was considered adequate. From next section, all the results presented will be for the medium mesh case.

To test whether the spanwise domain is adequate, two-point correlations are plotted for different y – planes in Figure 5-9. The wall-normal and spanwise correlations are plotted against normalized half span length. The structures quickly decorrelate within $2z/L_z = 0.4$. Therefore, the spanwise domain size is enough to capture all the flow structures. It should be noted that the planes farther from the wall take longer to decorrelate than the ones closer. This is because the flow structures close to the wall, which is within the viscous sublayer and the buffer layer, are lot smaller than those in the outer region.

5.2.5 Instantaneous Flow Field

To look at the flow structures, Q – criterion iso-surfaces are shown in Figure 5-10. The flow turbulizes rapidly through bypass transition mechanism. For better visualization, the plate is divided into three parts based on the Re_θ values with the plate starting at Re_θ = 330 and the domain is duplicated three times in the spanwise direction. Near the tripping location, there are some quasi-streamwise vortices (ω_x) along with few lambda vortices which become hairpin vortices. The hairpin vortices create turbulent spots and finally generate a fully developed turbulent flow. As the Re_θ increases, the coherent hairpin structures become less prominent and turn into either cane vortices or just have tubular structures. This has been observed in various DNS studies [210], [209].

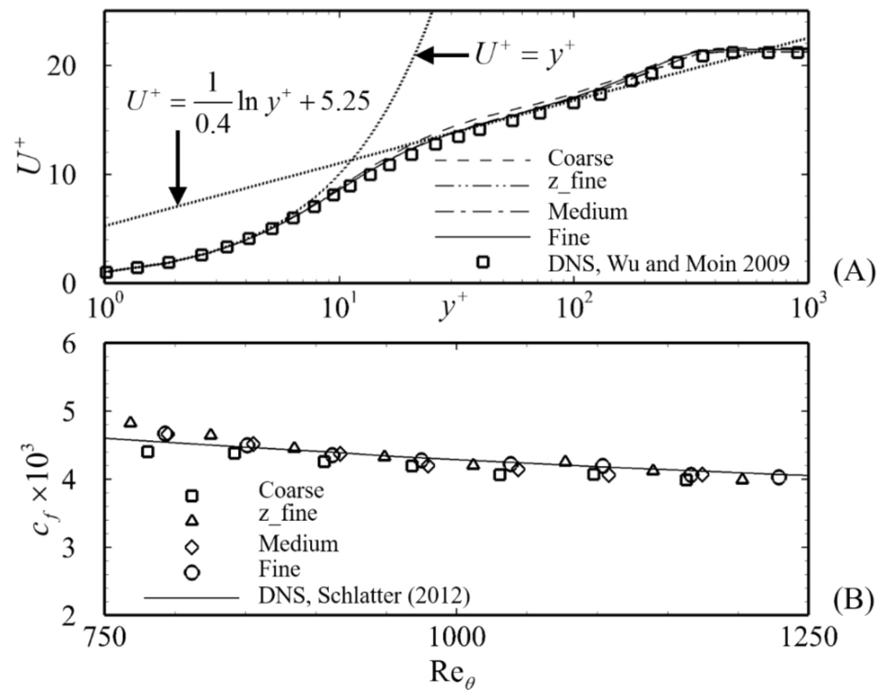

Figure 5-7. Mesh convergence study at $\mathrm{Re}_\theta = 900$ compared to DNS data [210]. Variation of (A) mean velocity profile with inner wall coordinates and (B) skin friction with Re_θ.

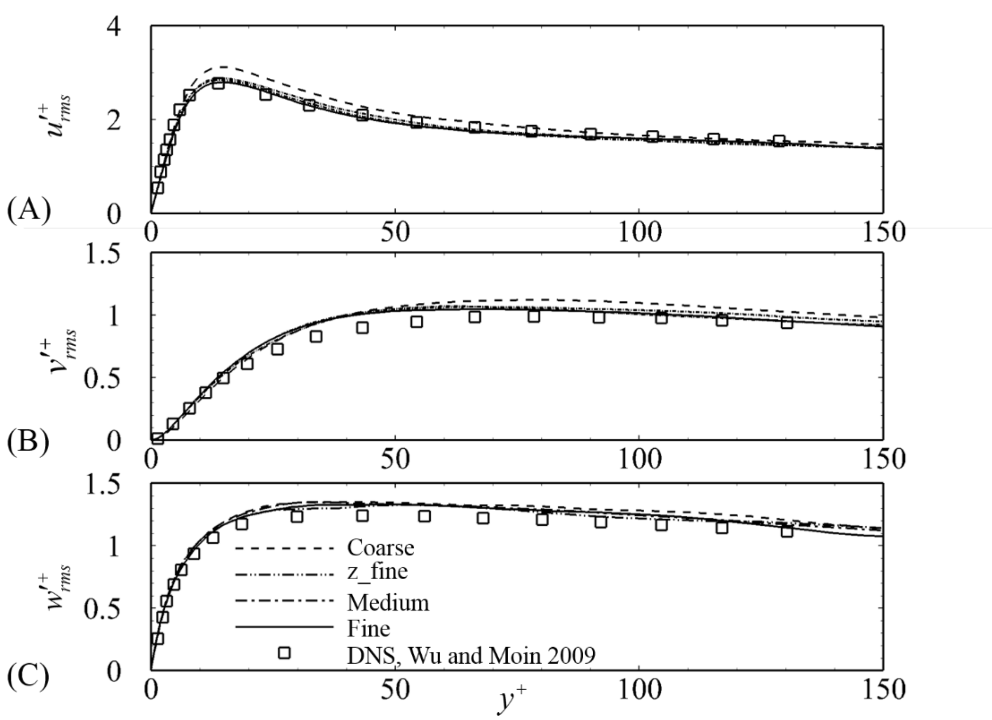

Figure 5-8. Mesh convergence study at $\mathrm{Re}_\theta = 900$ for Reynolds stresses compared with DNS data [210]. Variation of (A) streamwise, (B) wall-normal, (C) spanwise RMS fluctuations and (D) Reynolds shear stress.

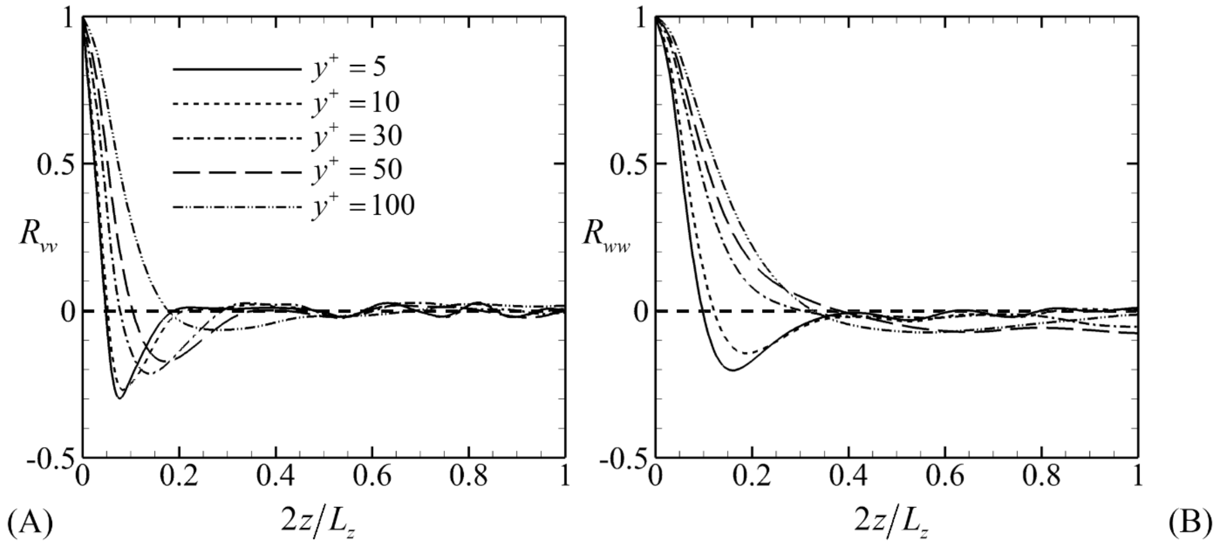

Figure 5-9. Variation of two-point correlation at different y^+ locations along the spanwise direction. (A) Wall-normal velocity correlations and (B) spanwise velocity correlations at $\mathrm{Re}_\theta = 900$.

Instantaneous details of density, streamwise velocity and pressure contours at the mid spanwise plane are shown in Figure 5-11. The density contours in Figure 5-11 show the distinct flow features such as large-scale bulges and valleys, the streamwise velocity contours show how the turbulent boundary grows and the pressure contours show the alternate low and high-pressure regions arising due to turbulent eddies.

The streaklines for $y_i^+ = 5$ plane with the domain duplicated three times is shown in Figure 5-12. It clearly shows the initial localized turbulent spots, which finally spread over the entire span of the plate. On an average, there are about seven to nine streaks in the spanwise direction which means that for a spanwise domain of $L_z^+ = 750$, the streaklines are separated by $z^+ \approx 80$ to 110 which is common for a turbulent boundary layer.

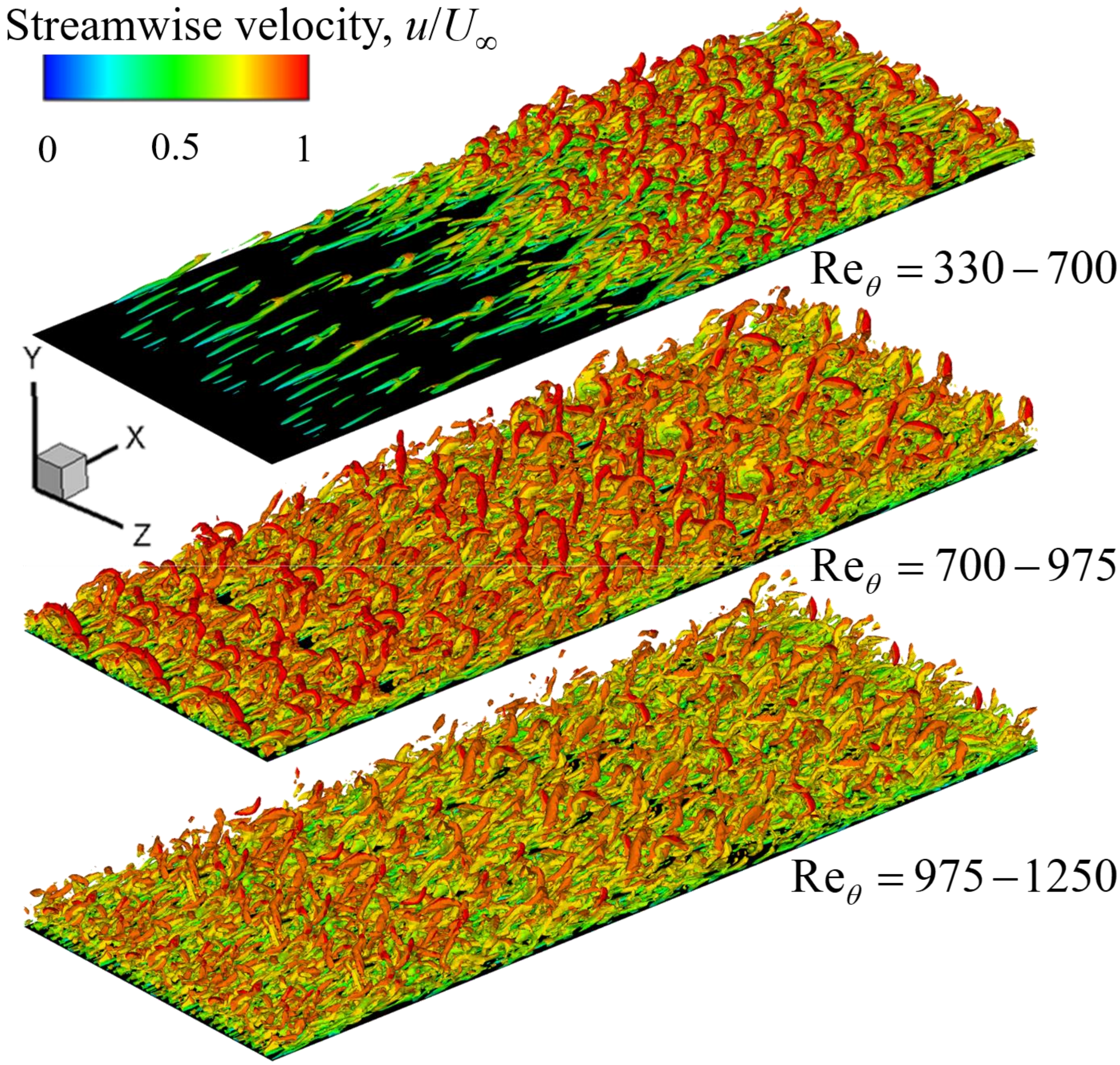

Figure 5-10. Instantaneous iso-surfaces of normalized Q – criterion (Q = 2) colored with normalized streamwise velocity at different Re_θ.

Instantaneous details of streamwise, wall-normal and spanwise velocity fluctuations at the mid spanwise plane are shown in Figure 5-13. The streamwise fluctuations u' show large positive and negative regions which denote sweeping and bursting events. The wall-normal velocity fluctuations v' and spanwise fluctuations w' show alternate positive and negative regions which are a representation of the turbulent eddies exchanging momentum inside the turbulent boundary layer.

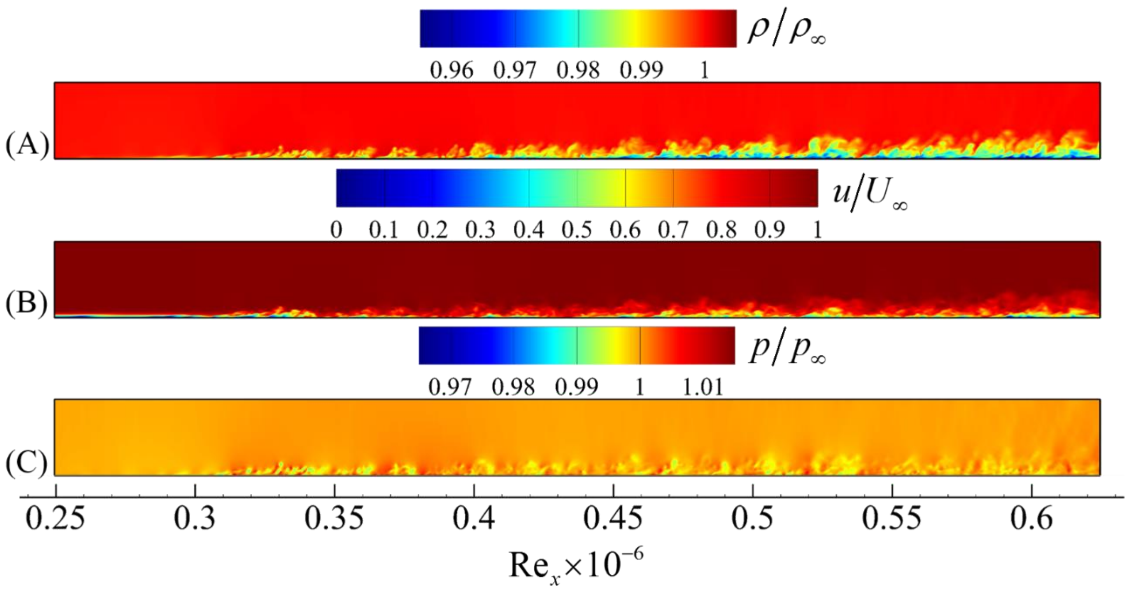

Figure 5-11. Instantaneous contours normalized with freestream conditions at middle span plane. (A) Density, (B) streamwise velocity and (C) pressure contours.

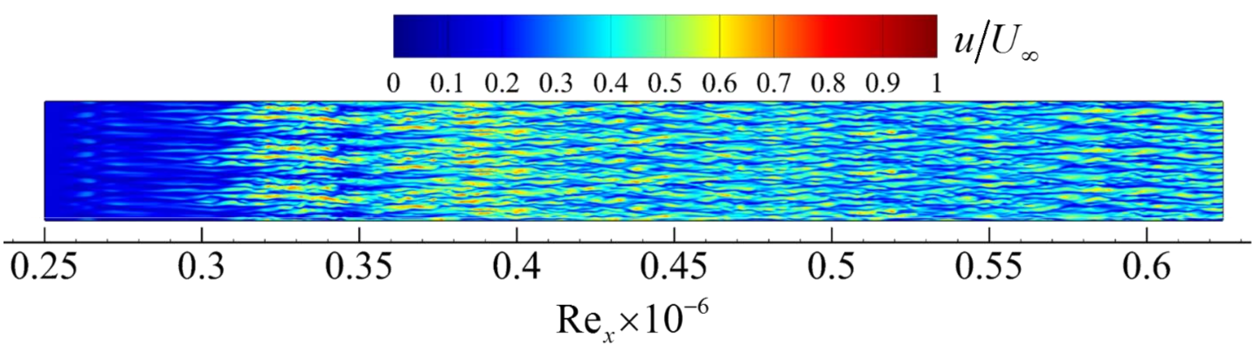

Figure 5-12. Normalized streamwise velocity streaklines over the $y_i^+ = 5$ plane.

5.2.6 Turbulent Statistics

All the mean flow data including the integral quantities are obtained using a spanwise and time-averaged solution. In Figure 5-14, the variation of the wall-scaled mean streamwise velocity with viscous wall units and velocity defect profile $\left(U_\infty - \overline{U}\right)/u_\tau$ with the outer coordinates are plotted. The defect profile corresponds to $\mathrm{Re}_\theta = 900$. The results slightly overpredict the solution in the buffer layer. However, the viscous sublayer and the log layer are accurately captured for all the Reynolds numbers. The slope of log layer is found to be 0.4 and the constant as 5.25, as shown in Figure 5-7 (A).

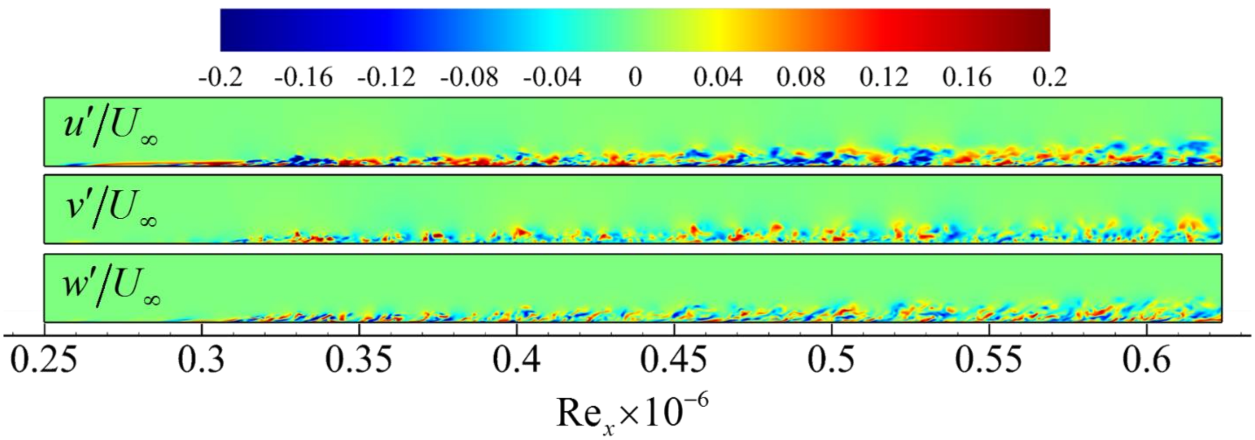

Figure 5-13. Instantaneous perturbation velocities at middle *z* plane.

The second order statistics involving Reynolds stress profiles compare well with the DNS results as shown in Figure 5-15. Data is plotted against wall distance scaled with wall parameters as well as boundary layer thickness. The peak value for u'^{+}_{rms} is 2.82 and it occurs at $y^+ = 14$ $(y/\delta = 0.04)$ for $\mathrm{Re}_\theta = 900$. The wall-normal and spanwise fluctuations have peak values of 1.09 and 1.33 respectively. These values are closer to Spalart's [197] data at $\mathrm{Re}_\theta = 670$ than Wu and Moin's data. Large variations in fluctuating components have not only been seen experimentally but also numerically at similar Reynolds numbers. Factors such as the spatial resolution of probes, measuring apparatus, tripping mechanism, etc. can affect the experimental data while grid resolution, inflow length, tripping method, domain size, etc. can impact the fluctuating components.

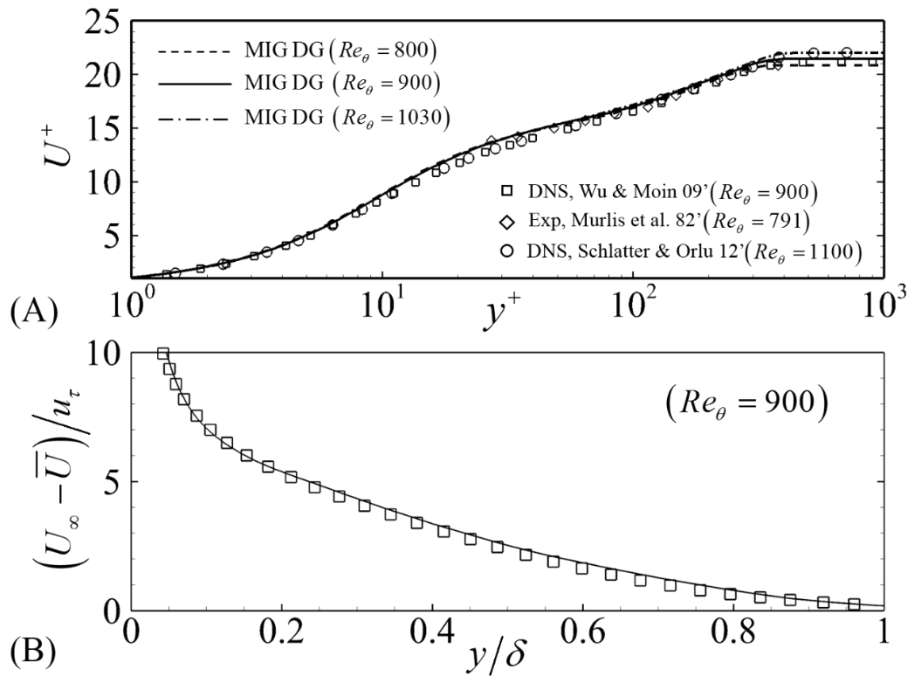

Figure 5-14. Comparison of mean flow velocity with experimental and numerical results. Variation of (A) mean velocity profile with inner wall coordinates and (B) mean velocity defect profile with outer coordinates.

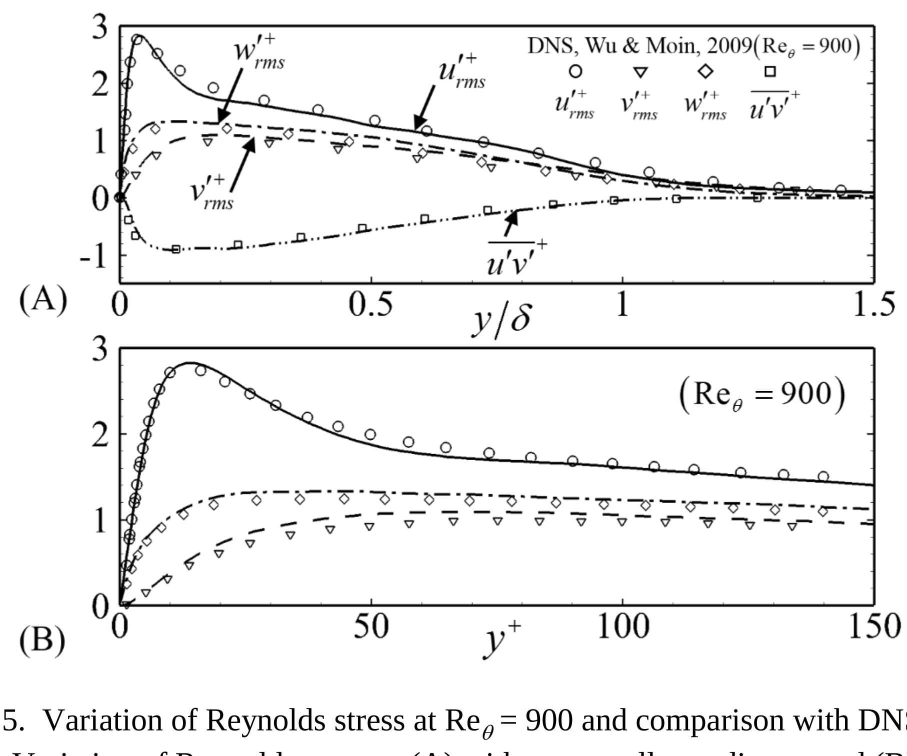

Figure 5-15. Variation of Reynolds stress at $\mathrm{Re}_\theta = 900$ and comparison with DNS data [210]. Variation of Reynolds stresses (A) with outer wall coordinates and (B) with inner wall coordinates.

In Figure 5-16, the total shear stress $\tau^{+} = \left(\nu\,\partial\overline{U}/\partial y\right)^{+} - u'v'^{+}$ is plotted against outer coordinates at $\mathrm{Re}_{\theta} = 1030$. Similar to Wu and Moin [210], the data shows that the maximum shear stress $\tau^{+} = 1.025$ does not occur at the wall, but at around $y/\delta = 0.03$ or $y^{+} = 12$ (see inlay). This is the same location where u'^{+}_{rms} is maximum. This behavior is observed throughout the turbulent boundary layer ranging from $\mathrm{Re}_{\theta} = 670$ to 1030. This has not been seen by other authors [197], [209] and for channel flow cases where the stress is linear.

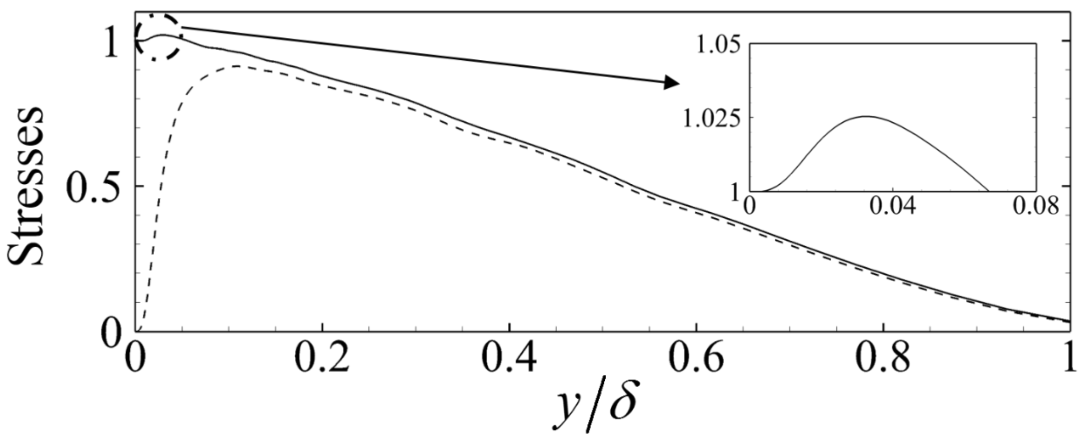

Figure 5-16. Variation of total shear stress (solid line) and Reynolds shear stress (dashed line), with outer coordinates at $\mathrm{Re}_{\theta} = 1030$.

The integral quantities shown in Figure 5-17, depict the variation of displacement thickness γ and the shape factor H with Re_{θ}. Both displacement thickness and shape factor show the deviation from the Blasius laminar solution to the turbulent solution. The shape factor shown in Figure 5-17 (B) is in good agreement with the DNS results of Sayadi, Hamman, and Moin [165] for a K-type transition. Present data shows a similar slope of shape factor in the transitional region when compared to results obtained by Sayadi et al. [165].

The Reynolds stress budget terms are plotted at $\mathrm{Re}_{\theta} = 900$ near the wall in Figure 5-18. The equations to determine these parameters are given below [211]

$$
\begin{aligned}
P_{ij} &= -\left(\overline{u_i'u_k'}\bar{U}_{j,k} + \overline{u_j'u_k'}\bar{U}_{i,k}\right)\nu/u_\tau^4, && \text{Production rate} \\
\varepsilon_{ij} &= -2\left(\overline{u_{i,k}'u_{j,k}'}\right)\nu^2/u_\tau^4, && \text{Dissipation rate} \\
T_{ij} &= -\left(\overline{u_i'u_j'u_k'}\right)_{,k}\nu/u_\tau^4, && \text{Turbulent transport rate} \\
D_{ij} &= \left(\overline{u_i'u_j'}\right)_{,kk}\nu^2/u_\tau^4, && \text{Viscous diffusion rate} \\
\Pi_{ij} &= -\left(\overline{u_i'p_{,j}' + u_j'p_{,i}'}\right)\nu/\rho u_\tau^4, && \text{Velocity pressure-gradient term}
\end{aligned}
\tag{5-8}
$$

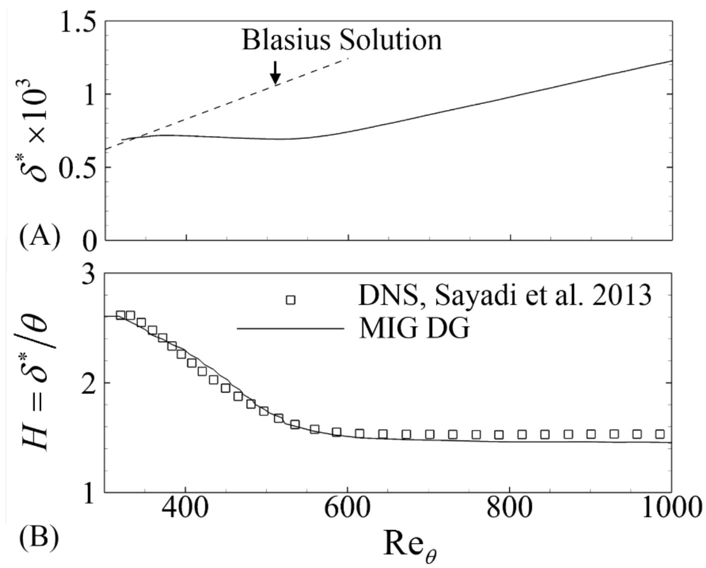

Figure 5-17. Variation of integral quantities with Re_θ. Variation of (A) displacement thickness and (B) shape factor profile showing the transition from laminar to turbulent flow.

The subscripts i, j and k to u' in Eq. (5-8) correspond to the streamwise, wall-normal and spanwise fluctuating velocity. All the terms are scaled using wall parameters. The budget terms show that the Reynolds stresses are predominant in the $\overline{u'^2}$ and $\overline{u'v'}$ components. The terms also balance out showing that the mean flow quantities have reached steady state. These results show similar behavior and trends when compared to the data by Spalart [197].

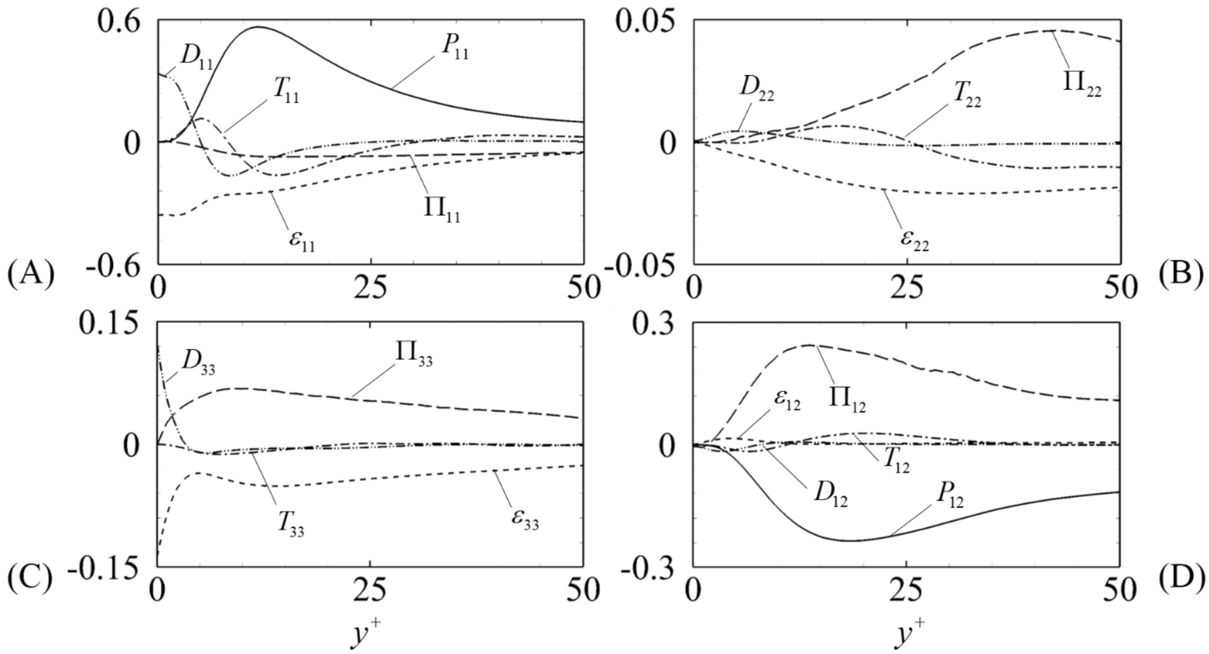

Figure 5-18. Variation of wall-scaled Reynolds stress budget terms with inner wall coordinates at $\mathrm{Re}_\theta = 900$. (A) $\overline{u'^2}$, (B) $\overline{v'^2}$, (C) $\overline{w'^2}$ and (D) $\overline{u'v'}$.

The probability density function (PDF) of velocity fluctuation gives an idea of whether the turbulent structures follow the normal distribution. The pdfs of channel flow and ZPGTBL are very similar. Unlike homogeneous shear flows, which follow the Gaussian distribution, ZPGTBL has some skewness at the tail ends as depicted in the PDF of fluctuating velocity components in Figure 5-19. It was found by Dinavahi, Breuer, and Sirovich [212] that for channel flows the pdf is independent of the wall-normal location and Re_θ when outside the buffer layer. Therefore, the pdf for the region $30 < y^+ < 50$ is plotted instead of different y locations. It should be noted that the pdf is generated using 40 bins, and the bin for mean value is not plotted. The mean for all pdfs is zero and the standard deviation of the fluctuating velocity is used to construct the Gaussian curve. The w' pdf follows the Gaussian distribution more closely than u' and v' pdfs.

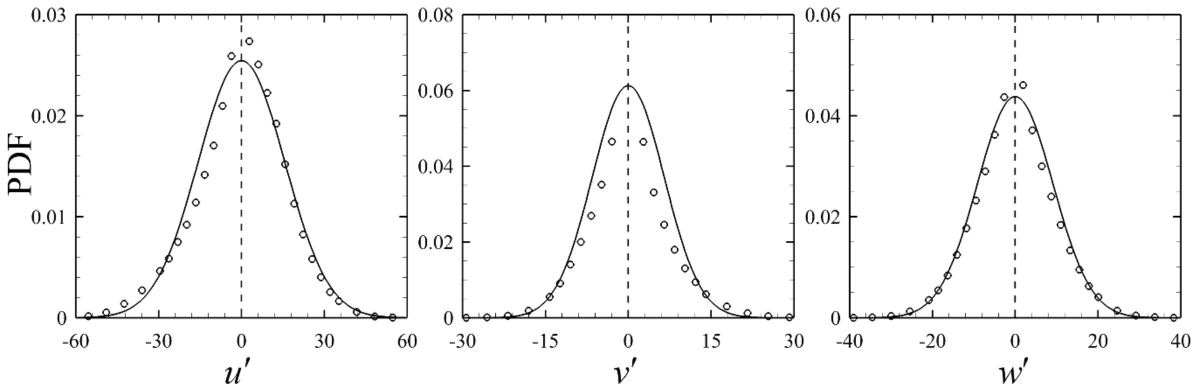

Figure 5-19. Probability density function for the fluctuating components of velocity over a region of $30 < y^+ < 50$ using 40 bins. Symbols represent present results and solid line represents the normal distribution.

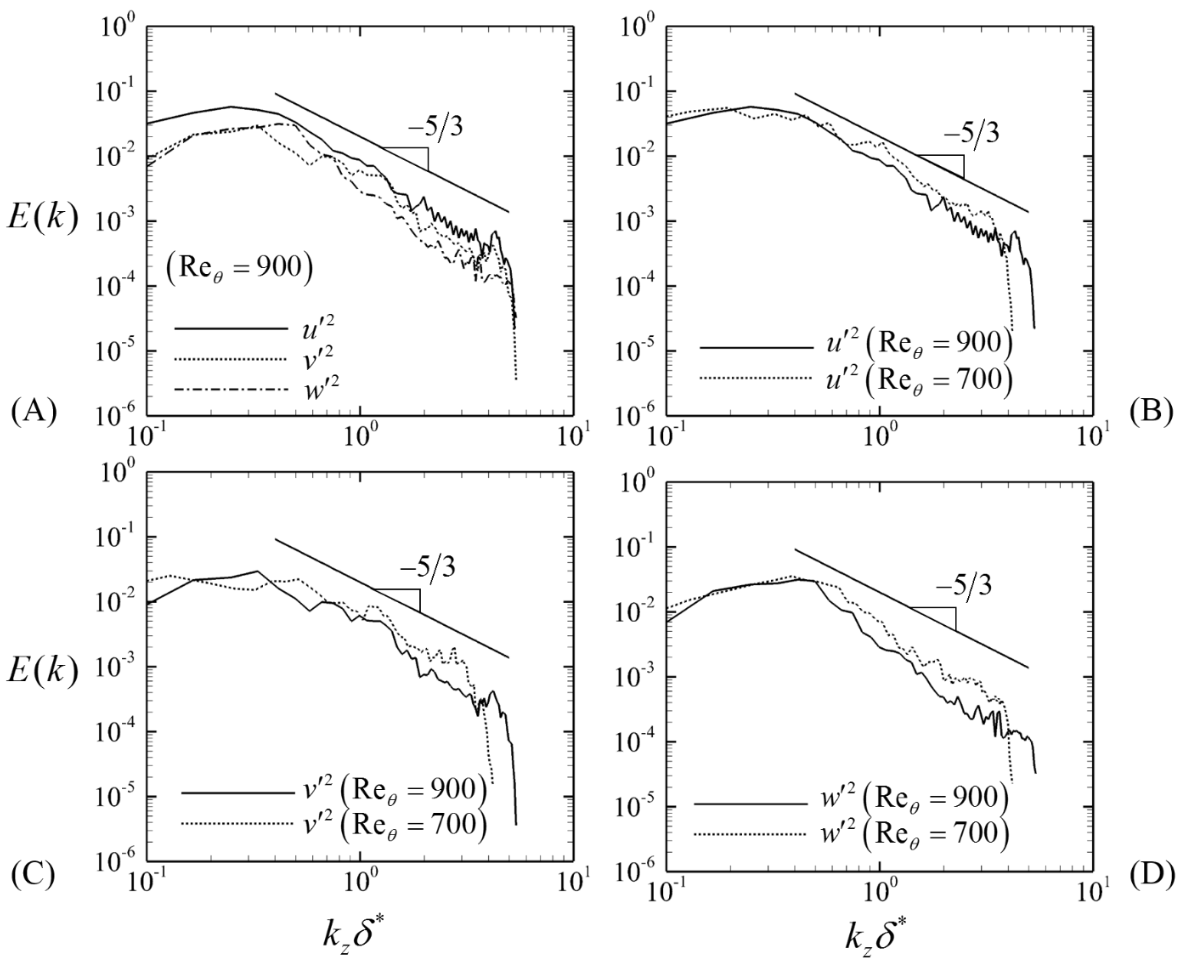

Figure 5-20. The energy spectrum of fluctuating components in the spanwise direction at $y = \delta^*$. (A) Spectrum at $Re_\theta = 900$ and comparison of spectrum at $Re_\theta = 700$ and 900 for (B) streamwise, (C) wall-normal and (D) spanwise fluctuations.

The energy spectrum is plotted in Figure 5-20 for the instantaneous fluctuating velocity components. The energy levels in the inertial region for all the perturbations are similar, which indicates the flow is isotropic in nature. There is a minor decrease in energy as the Re_{θ} increases from 700 to 900. It can also be seen that as the Reynolds number is increased, the wavenumbers grow higher due to the reduction in eddy size. The $-5/3$ slope line is also shown for reference in all the Figures 5-20 (A) through Figures 5-20 (D).

CHAPTER 6
INFLUENCING TRANSITION USING SERPENTINE PLASMA ACTUATORS

6.1 Surface Dielectric Barrier Discharge (SDBD) Plasma Actuators

The current work studies plasma actuators as a flow control device by conducting implicit large eddy simulation of transition to turbulence due to three-dimensional actuation on a zero-pressure gradient laminar boundary layer flow over a flat plate. The three-dimensional actuation resembles the effect from a surface dielectric barrier discharge (SDBD) actuator. Depending on the input signal and the configuration of the actuator electrodes, different types of plasma actuators can be designed. Some of the designs include SDBD actuators [34], plasma synthetic jet actuators [59], arc discharge actuators [44], and corona discharge actuators [41]. The focus of this research is on investigating a special case of SDBD actuators called the square serpentine plasma actuator [57], [84]. Numerical and experimental studies have shown plasma actuators can be used to either suppress [213], [214], [215] or raise [216], [217] the growth of Tollmien-Schlichting (TS) waves and thereby delaying or advancing the transition to turbulence. The transition can be manipulated by applying actuators at different locations and voltages [213]. To conduct this fundamental study, the influence of plasma actuators on a zero-pressure gradient laminar boundary layer for a flat plate is chosen due to its simple and frequently encountered geometry. Both experimental [57] and numerical [84] work has shown the benefits of serpentine actuators over the standard linear SDBD actuators for flow control applications due to their three-dimensional flow structures. Therefore, investigating these types of actuators can provide useful insight on efficient flow control applications. The impact of plasma actuators on laminar to turbulent transition depends on different factors such as the ratio of the plasma jet velocity to freestream velocity, the frequency of perturbation and the geometry of the actuator [84], [218].

To understand the functioning of a plasma actuator, a brief description of their design and operation is discussed here. To obtain a better understanding of these actuators the author recommends the reader to refer to published literature by Moreau [219], Corke et al. [33] and Enloe et al. [220]. The standard SDBD plasma actuators are constructed using two asymmetrically placed electrodes separated using a dielectric material. A high voltage (~ kV) alternating current is applied to the electrodes across the dielectric material. Radio frequencies are generally used for the applied voltage. One of the electrodes is exposed to the surrounding air while the other is encapsulated. A simple depiction of the actuator is shown in Figure 6-1. The plasma forms at the edge of the exposed electrode as shown in the Figure 6-1 (B) [33].

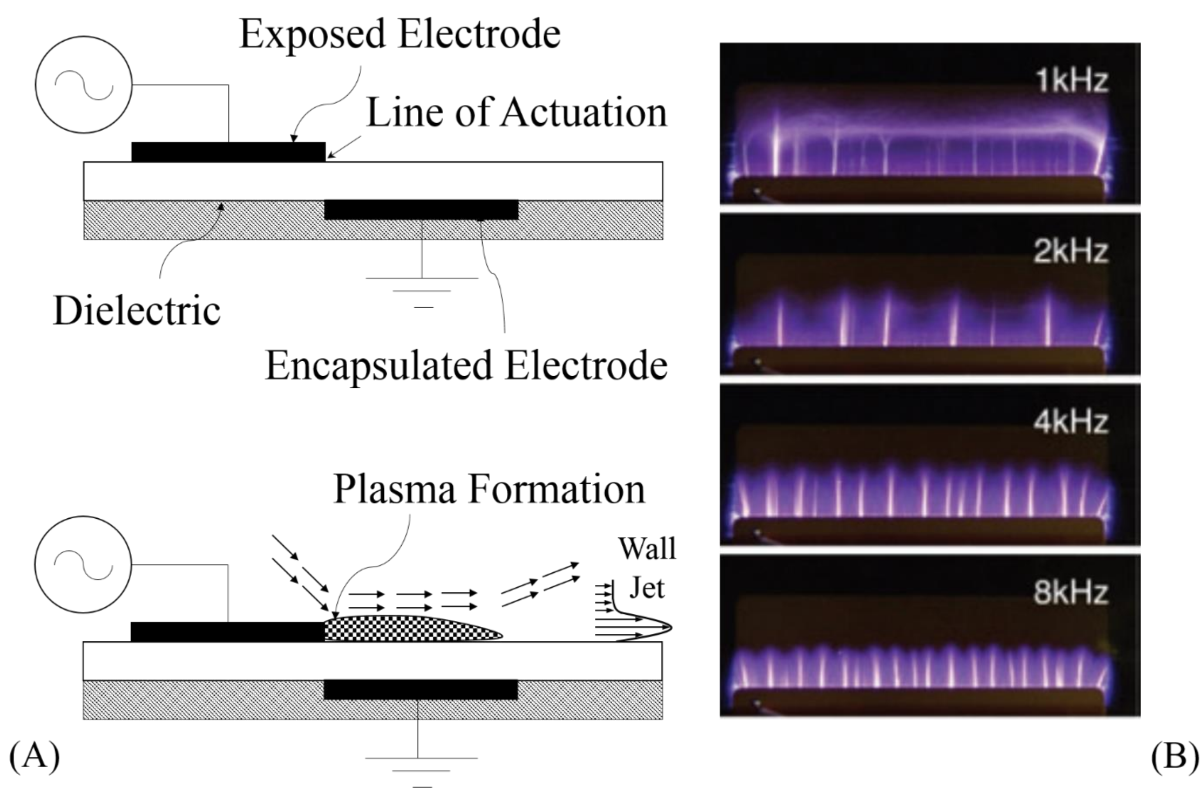

Figure 6-1. Schematic of the operation of SDBD actuator and plasma formation. (A) Parts of SDBD actuator and wall jet created by the plasma and (B) plasma formation at different frequencies [33].

Schematic of one of the methods of powering the actuator is shown in Figure 6-2. The encapsulated electrode is grounded and the exposed electrode is powered using high voltage Trek (model 30/20A) power amplifier. The power amplifier usually contains a high voltage transformer which can step up the wall supply voltage to ± 30 kV. A controlled input signal is provided using a function generator. Current and voltage probes are connected to an oscilloscope to collect and visualize the electrical characteristics.

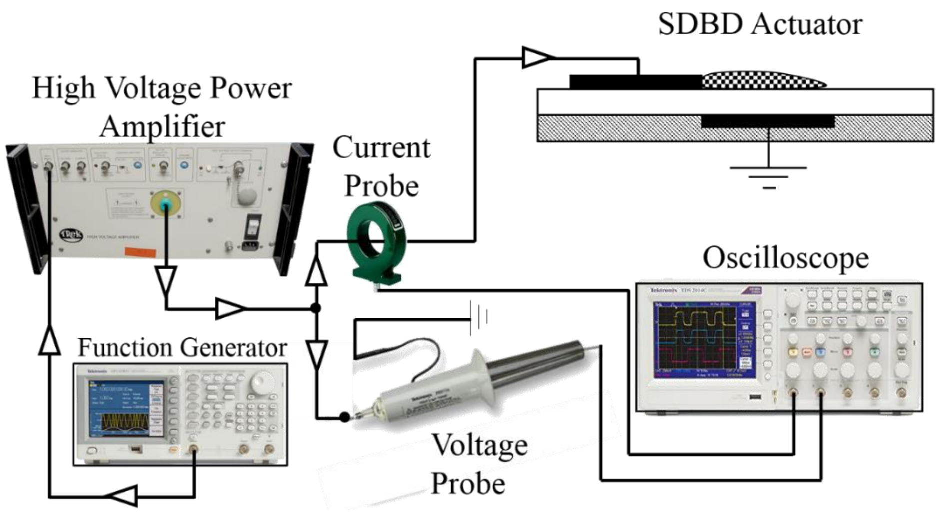

Figure 6-2. Schematic of SDBD power supply and voltage and current measurement.

When the high voltage is applied across the electrodes, the gas surrounding the exposed electrode ionizes and creates electrons, positive ions, and negative ions. Due to the asymmetrically placed electrodes, the electric field directs the ions in its direction which in turn impacts the neutral gas molecules and creates a flow. There is still some ambiguity on the exact mechanism of the flow generation, however, the details of different conjectures are considered outside the scope of this work. Here the focus is on the numerical approach of simulating actuators.

6.2 Numerical Approach

6.2.1 Mesh Details

Three different mesh sizes were tested and have been tabulated in Table 6-1. The mesh is created using similar procedure mentioned in Chapter 5 for the turbulent flat plate boundary layer. The boundary conditions and flow field parameters are also similar to the flat plate case in Chapter 5. This study involves a transition to turbulence using square serpentine actuator. For all the cases hereon, the Reynolds number based on plate length, Re_x ranges from 3.75×10^5 to 8×10^5 and the minimum to maximum Re_θ ranges from 400 to 1250. The same numerical approach is taken here as in flat plate validation case in Chapter 5. The medium mesh was found to be adequate to resolve the flow based on the convergence shown in Figure 6-3. The actuator forcing details are provided in Section 6.2.2. It should be noted that the DNS results are for $\mathrm{Re}_\theta = 900$ whereas the MIG DG data corresponds to $\mathrm{Re}_\theta = 1000$ due to which there are some differences in the maximum amplitude of the fluctuating components.

Table 6-1. Computational mesh details

Case	N_x	N_y	N_z	Δx_i^+	Δy_i^+	Δz_i^+	L_x^+	L_y^+	L_z^+
coarse	750	48	32	26.5	0.9	24	18 600	4200	750
medium	750	48	64	26.5	0.9	12	18 600	4200	750
fine	750	64	64	26.5	0.9	12	18 600	4200	750

6.2.2 Actuator Forcing Mechanism

The approach here is to use a body force model formulated by Singh and Roy [74] to simulate the effect of plasma actuators. The body force distribution for the actuators used in the current study is obtained using Eq. (6-1).

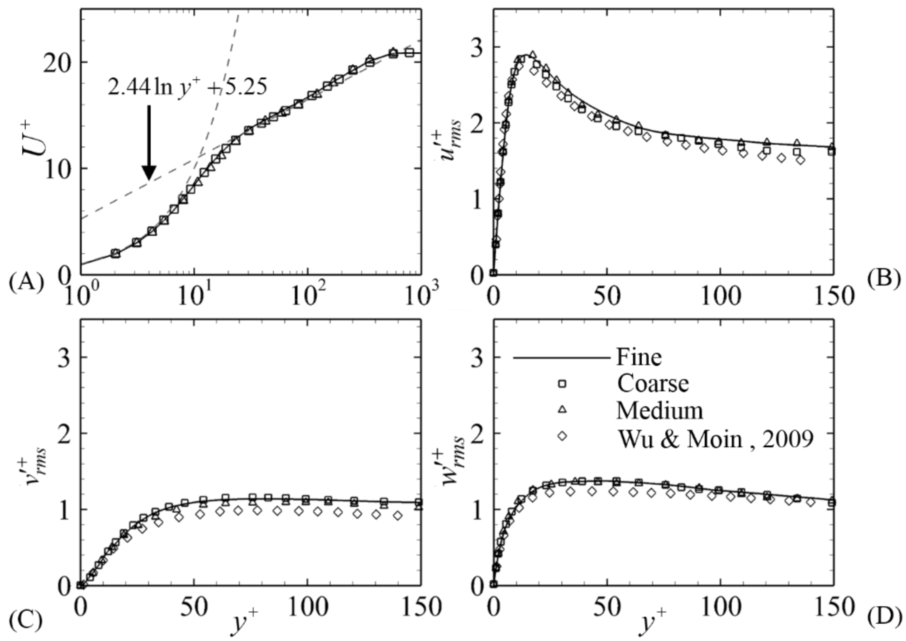

Figure 6-3. Mesh comparison of turbulent mean statistics at $Re_\theta = 1000$ with DNS results [210] at $Re_\theta = 900$ (A) Mean velocity profile, (B) streamwise, (C) wall-normal, (D) spanwise RMS fluctuations.

$$F_\varsigma = \frac{F_{\varsigma_0}}{\sqrt{F_{\varsigma_0}^2 + F_{y_0}^2}} \exp\left\{-\left[\frac{(\varsigma-\varsigma_0)-(y-y_0)}{y-y_0+y_b}\right]^2 - \beta_\varsigma (y-y_0)^2\right\}$$
$$F_y = \frac{F_{y_0}}{\sqrt{F_{\varsigma_0}^2 + F_{y_0}^2}} \exp\left\{-\left[\frac{(\varsigma-\varsigma_0)}{y-y_0+y_b}\right]^2 - \beta_y (y-y_0)^2\right\} \tag{6-1}$$

In Eq. (6-1) $F_{\varsigma_0} = 2.6, F_{y_0} = 2.0, \beta_\varsigma = 1.44\times10^5, \beta_y = 1.8\times10^6$ and $y_b = 0.001665$. The last three parameters provide the extent of the exponential function. The location of the actuation is given by ς_0 and y_0 which correspond to the points along the line of actuation which varies depending on the actuator being studied. This is depicted in Figure 6-4 along with the force distribution from Eq. (6-1) for a center z – plane. The body force terms are applied such that F_y is always directed in the negative wall-normal direction. The forcing terms are modulated with a sinusoidal frequency ω_0, and an amplitude, A given by

$$F_{b_\varsigma} = AF_\varsigma \left|\sin(\omega_0 t)\right|$$
$$F_{b_y} = AF_y \left|\sin(\omega_0 t)\right| \tag{6-2}$$

Both F_{b_ς} and F_{b_y} are implemented as body force terms in the momentum and energy equations of Navier-Stokes equations. The amplitude *A* was determined by conducting simulations of the actuator in quiescent conditions for different values of *A*, to obtain the maximum velocity generated, u_p and consequently the velocity ratio $\gamma = u_p/U_\infty$. The relationship between *A* and γ is depicted in Figure 6-5. To avoid symmetry in the spanwise direction, an additional normally distributed random perturbation of amplitude 0.1*A* was added to the amplitude *A*. It should be noted that since an absolute value of the sine wave is used, the forcing occurs at a frequency $2\omega_0$. All the simulation details provided in this chapter have γ = 0.1 and $\mathrm{St} = 2\omega_0\delta_i/U_\infty = 0.584$. The effect of γ and ω_0 is discussed in Chapter 7. The RMS fluctuation due to this forcing is around 5% of the free stream velocity.

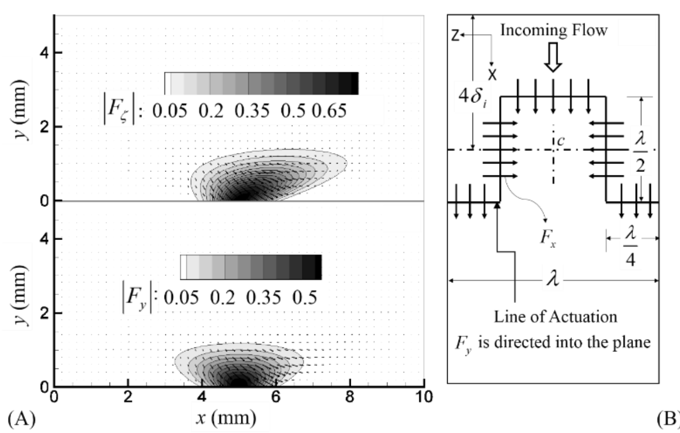

Figure 6-4. Plasma body force contours and square serpentine plasma actuator schematic. (A) Body force distribution for a linear SDBD actuator and (B) schematic of the square serpentine actuator with different parameters and force directions.

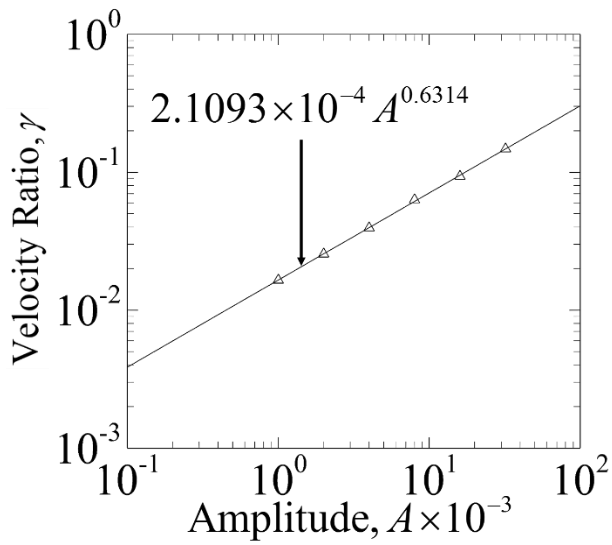

Figure 6-5. Effect on velocity ratio based on different forcing amplitudes for a linear actuator.

The three-dimensional forcing due to the actuator creates two kinds of regions, namely the pinching region (center z – plane), where the forces are directed towards each other and the spreading region (spanwise boundary planes) where the forces are directed away from each other as shown in Figure 6-4. For reference, Figure 6-6 gives a depiction of the pinch plane and the spread plane of the actuator. It should be noted that only one wavelength of the actuator is simulated and for better depiction the domain is duplicated three times for Figures 6-6 to 6-13.

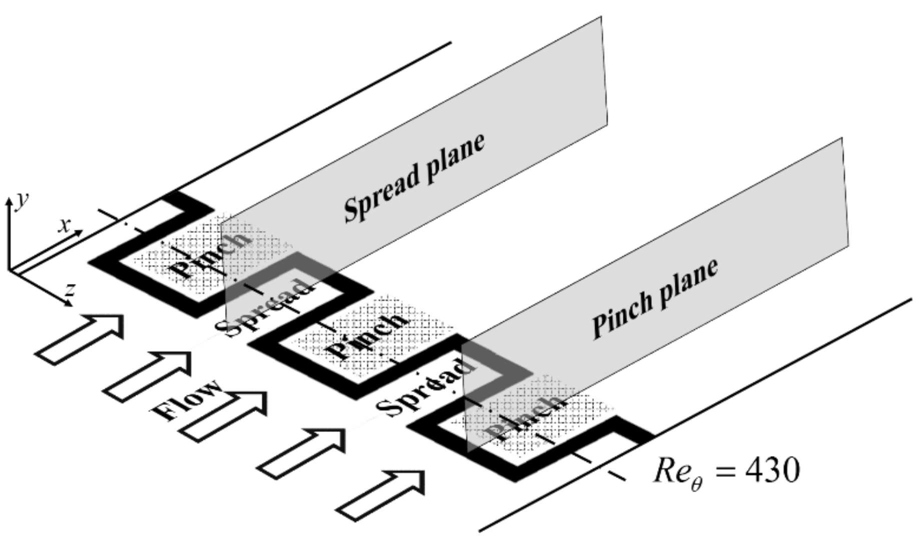

Figure 6-6. Schematic of the actuation pinch plane and spread plane.

6.2.3 Instantaneous Flow Field

To visualize the turbulent structures, Q – criterion iso-surface is shown in Figure 6-7. The flow turbulizes faster downstream of the pinch region compared to the spread region. The serpentine actuator creates 'X' like structures which have been found in the experimental and numerical study of oblique wave transition [174], [177], [179], [221]. The pinching region turbulizes before the spreading region due to its lifted streak nature. This can be clearly seen in the spanwise planes of pinching and spreading region shown in Figure 6-8. Different slices are plotted in Figure 6-8 to show contours of normalized velocity magnitude, streamwise vorticity, and density. The density variations are less than 4%, due to which the flow is assumed incompressible. All the parameters are nondimensionalized using freestream and inlet parameters. The serpentine actuator shows strong streamwise oriented vortices at the wall. Two streamwise oriented counter-rotating vortices shown by the black and white regions are created immediately downstream of the actuator. Their combined effect pushes the flow in between them upwards, as can be seen in the x – planes. The density variations shown in the pinch and spread planes are minimal but give a good representation of the flow turbulizing.

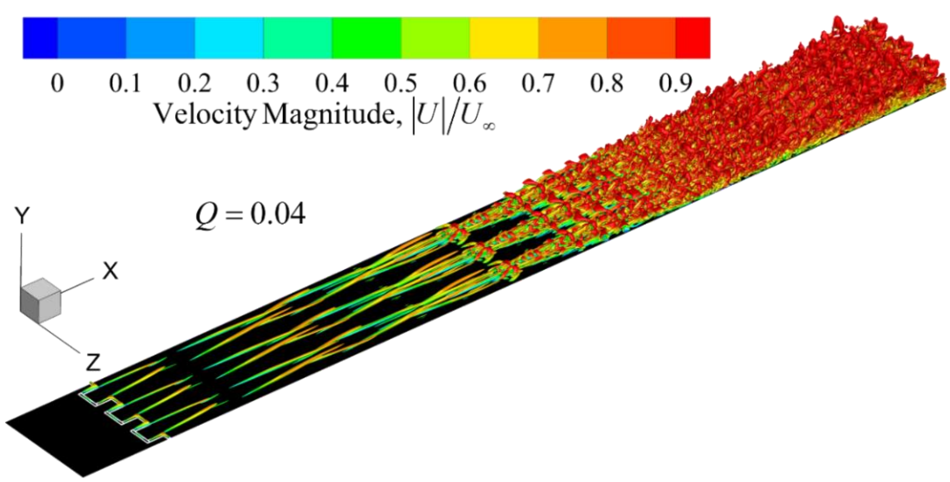

Figure 6-7. Instantaneous Q – criterion colored with velocity magnitude showing breakdown of coherent structures for the square serpentine actuator.

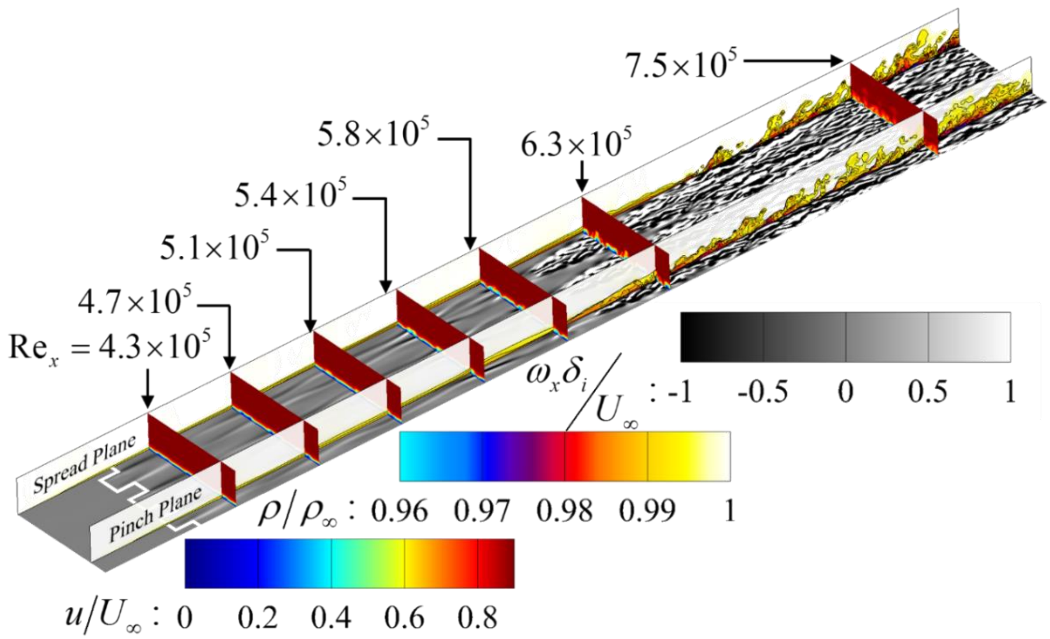

Figure 6-8. Instantaneous contours of velocity magnitude, vorticity and density variation for different planes.

The contour of streamwise velocity on a wall-normal plane inside the buffer layer, $y^+ = 10$ is shown in Figure 6-9. The low-speed streaklines for the serpentine actuators occur at the pinching regions where the flow gets lifted up. The pair of opposite angle oblique waves is indicated using dashed white lines. The wavy streak pattern observed in Figure 6-9 are similar to subharmonic sinuous streaks [85]. This type of pattern was also observed by Elofsson and Alfredsson [174] in their experimental study of oblique wave transition.

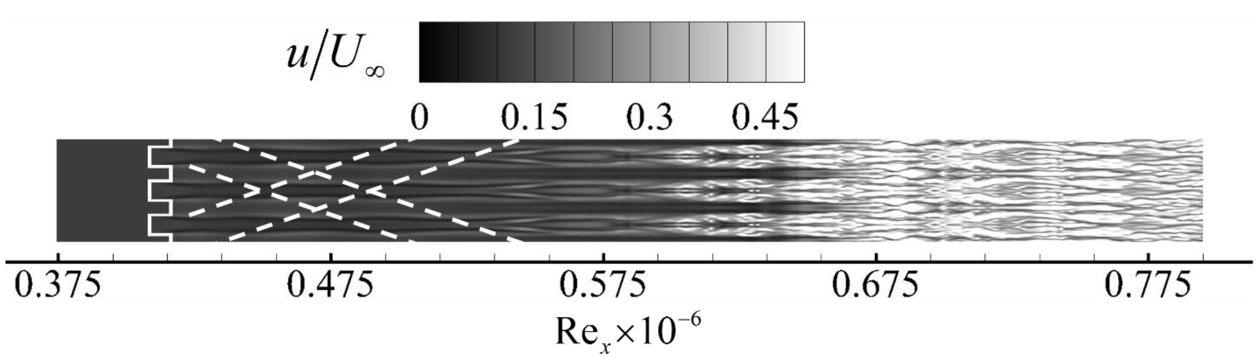

Figure 6-9. Instantaneous velocity streaklines at $y^+ = 10$ with the oblique waves shown using dashed white lines.

To investigate the growth of vortical structures generated by the actuation, Q – criterion iso-surfaces (Q = 0.1) are plotted in Figure 6-10 for the square serpentine actuator. It shows the time evolution of the quasi-streamwise oriented vortices generated by the actuator into three-dimensional structures. The lambda shaped vortices interact with the structures downstream as well as upstream to create a staggered set of harmonic and subharmonic lambda vortices similar to an oblique wave transition. These have been experimentally and numerically tested using speakers and ribbons [174], [175] and with a pair of oblique waves [176], [222]. Although the frequency of actuation is kept at St = 0.584, the transition occurs through the subharmonic mode which involves a fundamental mode and a subharmonic mode with a frequency half of the fundamental mode. The lambda structures are lifted from the plate due to which their tail end moves slower compared to the front, and consequently, they grow in time. The growth is shown by the increase in spacing between the dashed white lines. Since a periodic sine wave forcing is used, similar structures are generated every t^+ = 241.12 which is also equal to $u_\tau^2 / 2\omega_0 \nu$ (here ω_0 is the forcing frequency of the actuation in hertz).

As the structures grow in time, they form staggered patterns of positive and negative fluctuations. In Figure 6-11, two time periods based on the time period $T = 1/2\omega$ of the actuator are plotted for the spanwise fluctuations at different y^+ locations for Re_θ = 500. The spanwise domain is duplicated three times. The flow is from top to bottom since the y-axis is time. The dashed lines are negative fluctuations and solid lines are positive fluctuations. As the structures grow in time they form staggered patterns of positive and negative spanwise fluctuations. As the y^+ value increases the staggered patterns have different behavior in time. From careful inspection, it can be seen that the positive and negative fluctuations switch places as the distance from the wall increases. This is due to the oblique and lifted shear layer in the flow as well as the presence of two modes.

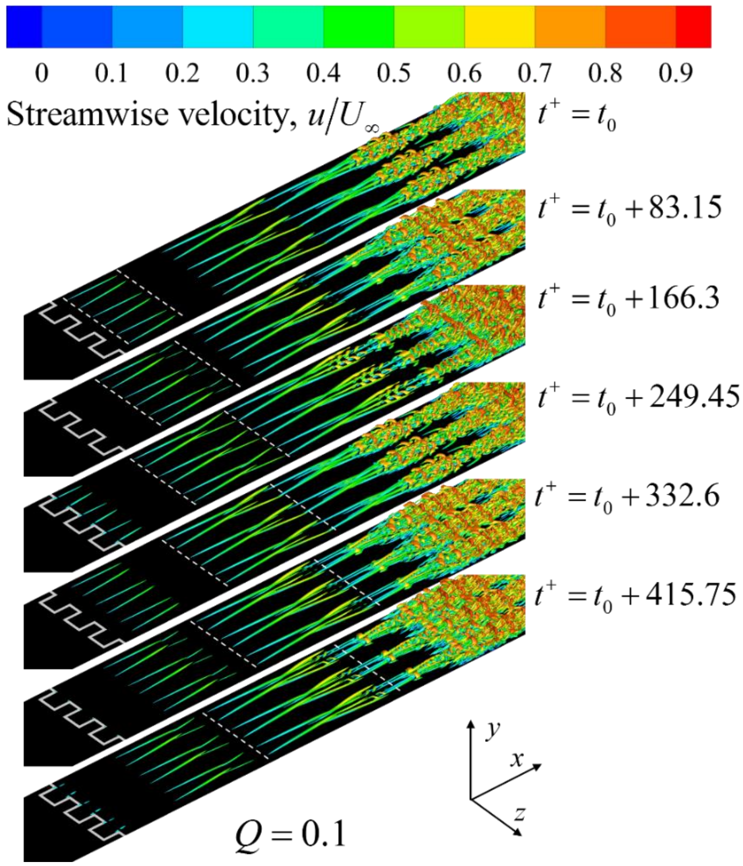

Figure 6-10. Instantaneous normalized Q – criterion iso-surfaces (Q = 0.1) shown at different instances in time depicting the growth of turbulent structures.

This behavior is unlike most of the controlled forcing functions which require the input of a fundamental and a subharmonic frequency [165], [223] or an oblique wave [174], [170]. For supersonic flat plate boundary layer, the most unstable mode is oblique so suction and blowing [179] can create this type of transition. Also, to confirm whether the combined effect of pinching and spreading created this type of transition, horseshoe geometry was simulated (results not shown here) and similar type of transition was obtained. Therefore, the serpentine geometry forcing does not need to operate on different frequencies to achieve the oblique transition and the pinching effect is the major contributor of this type of transition. Also, the oblique transition is known to transition faster compared to the standard secondary instability mechanism with similar disturbance amplitude [170]. Therefore, we conclude that serpentine shaped surface compliant plasma actuation can induce a faster transition to turbulence.

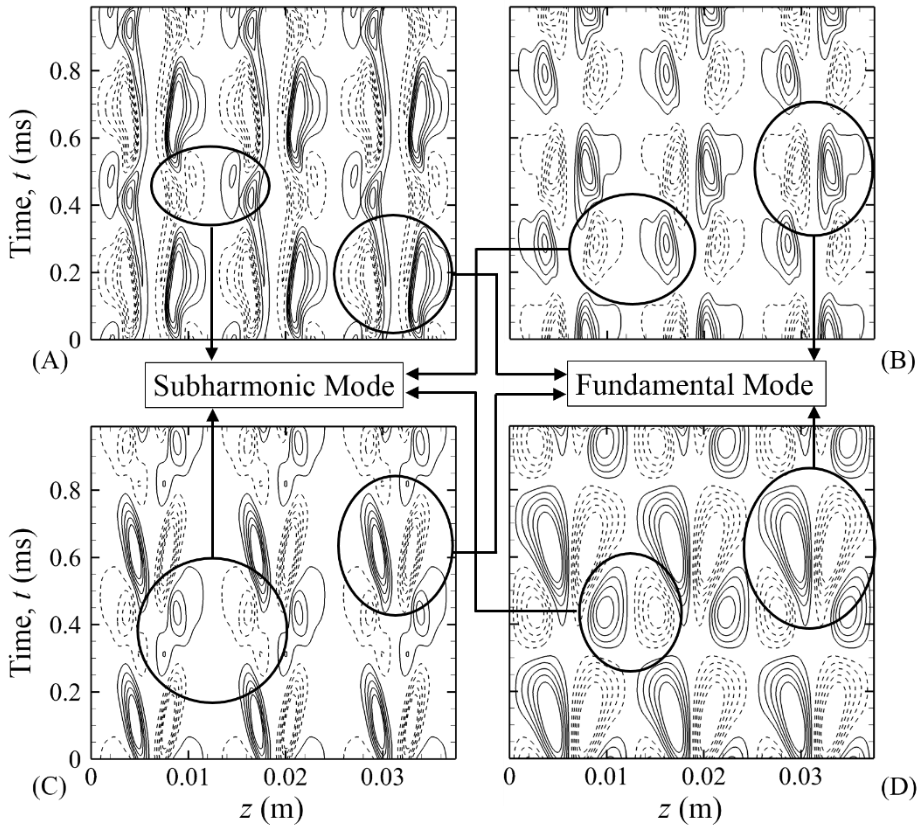

Figure 6-11. Variations of instantaneous spanwise fluctuations over time depicting staggered pattern of oblique wave transition at $Re_\theta = 500$. Variations at (A) $y^+ = 10$, (B) $y^+ = 30$, (C) $y^+ = 50$ and (D) $y^+ = 100$ plane.

To study the structures in more detail two instances in time are picked from Figure 6-10, that is at $t^+ = t_0$ and $t^+ = t_0 + 415.75$. Figure 6-12 (A) shows approximate depiction of the initial structure at $t^+ = t_0$ while Figure 6-12 (B) shows the structures at $t^+ = t_0 + 415.75$. The lift angle on the $x - y$ plane of the structure is denoted as φ and the polar angle on the $x - z$ plane is α. The length of the structure is given by L and the spacing between the front ends is B. It should be noted that the structures in black have anticlockwise rotation while the structures in grey have clockwise rotation. When Figures 6-12 (A) and (B) are compared, it was found that φ and α barely change while L grows to $2L$ and B reduces to $B/2$. The development of these vortices is dependent mainly on the proximity of the front end of the lambda structures and the distance from the upstream lambda vortices of the fundamental harmonic mode. Unlike the fundamental harmonic lambda vortices, the subharmonic vortices generated are not inclined and their growth is attributed to the growth in strength of their interaction with the upstream fundamental mode. The lambda structures start breaking down once the pair of purely spanwise oriented vortices starts to develop at the two front ends. The pair of spanwise oriented vortices coalesce together and turn into hairpin vortices, to generate fully turbulent flow.

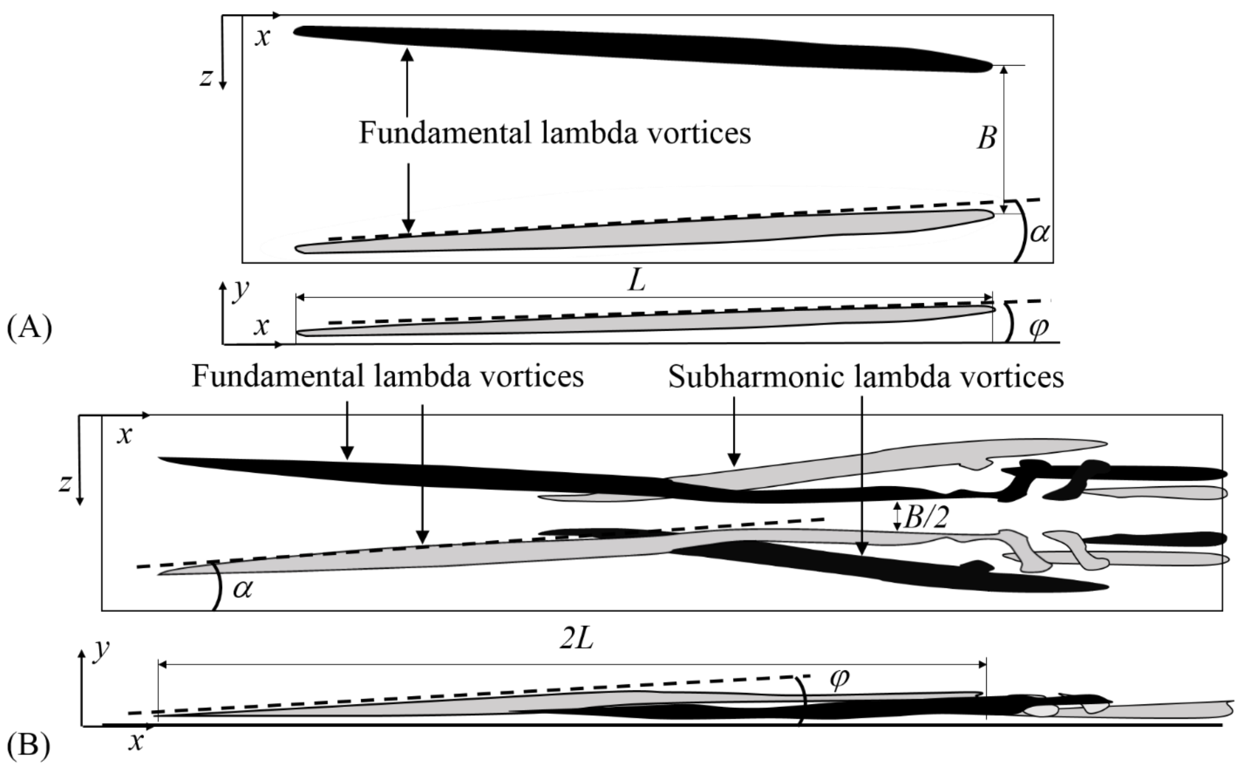

Figure 6-12. Approximate representation of vortical structures at different instances in time. (A) $t^+ = t_0$ and (B) $t^+ = t_0 + 415.75$. The shaded grey structures have clockwise rotation and the shaded black structures have anticlockwise rotation.

Figure 6-13 shows the structures at an instant $t^+ = t_0 + 166.3$, where the shaded regions depict lifting of the flow structures due to pinching effect of the counter-rotating vortices. The streamwise velocity perturbations have been represented by dashed arrows in the Figure. The arrows are an approximate representation of the streamwise perturbations. The regions between a pair of lambda vortices for both the fundamental harmonic and subharmonic modes have the perturbation vectors pointing in the streamwise direction which is similar to a Q4 (sweeping) event. The region between the legs of individual lambda vortices has the perturbation vectors pointing opposite to the streamwise direction which is like a Q2 (bursting) event.

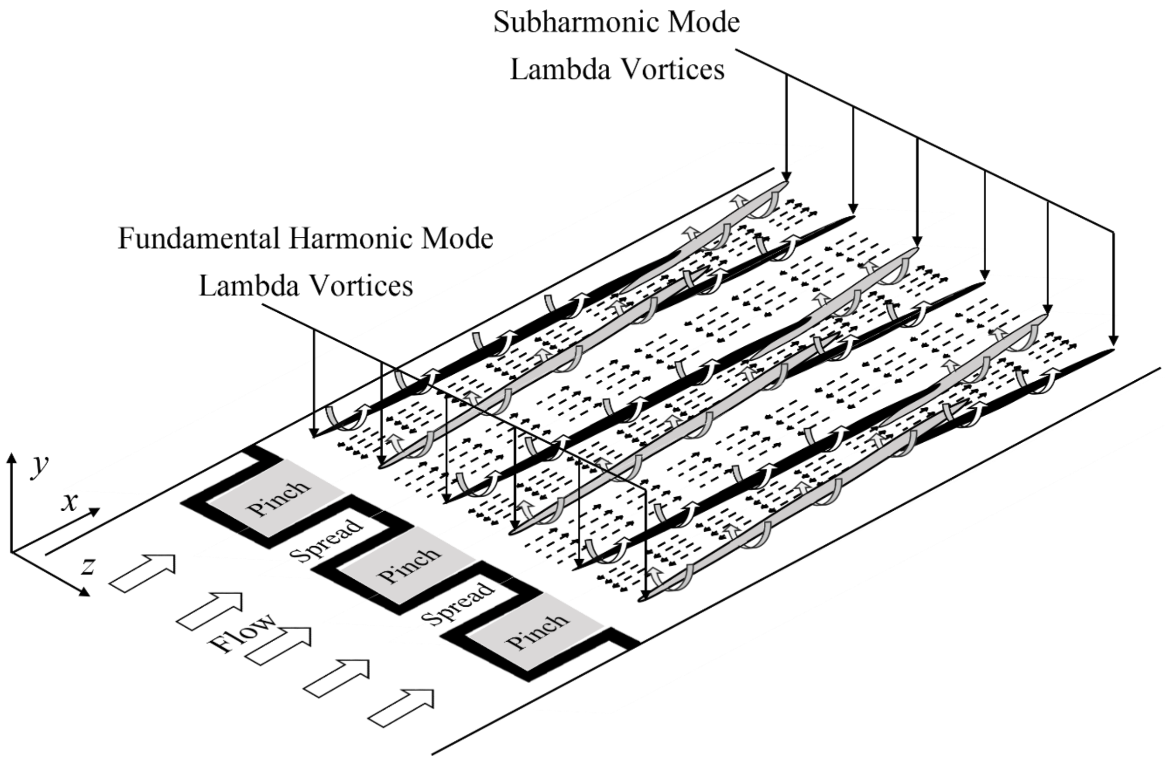

Figure 6-13. Schematic of the vortical structures generated by the actuation depicting the direction of streamwise perturbation vector at $t^+ = t_0 + 166.3$.

Since the actuator creates different modes, a proper orthogonal decomposition (POD) on the velocity flow field is conducted to look at the most energetic modes and the coherent structures in the spanwise direction. The POD method was first proposed by Lumley [224] to study turbulent structures and an in-depth analysis and procedure can be found in Berkooz et al. [225]. The snapshot method proposed by Sirovich [226] is used here. Four planes are recorded in the transition region corresponding to Re_θ = 450, 500, 550 and 600. A total of N = 132 equally spaced snapshots were chosen over a time period of $T = 3/2\omega$. For details on the POD analysis please refer to Appendix A. Figure 6-14 shows the relative energy content for first 13 modes at different locations in the transitional region. At $\mathrm{Re}_\theta \leq 550$, most of the energy is in the first three modes. There is some energy in the fourth and fifth mode at Re_θ = 500 which is not present at Re_θ = 550. In the y^+ planes, the energy content in the dominant mode is below 20% and the second and third dominant modes also have similar as well as significant energy in comparison. This can also be seen in the pinch and spread planes. The pinch plane has about 4% more energy content than the spread plane.

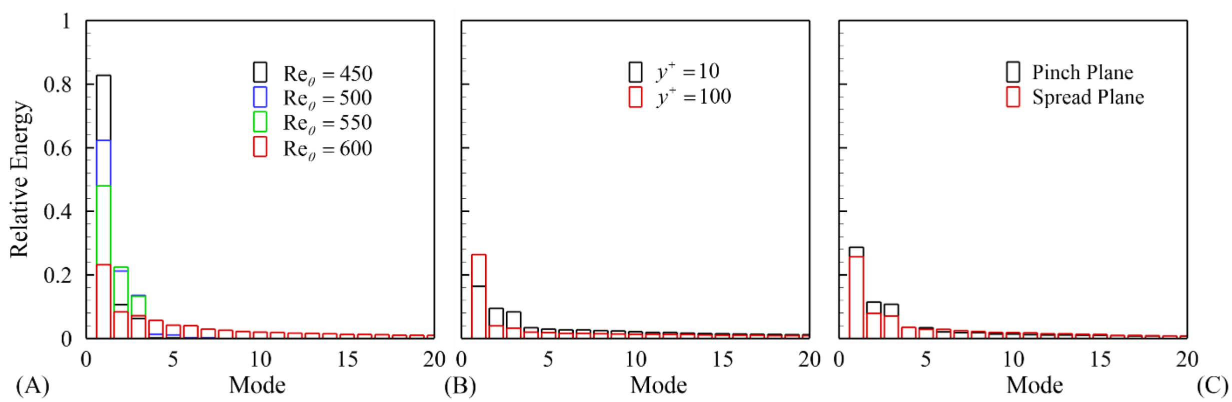

Figure 6-14. Relative energy content for different modes. Relative energy at different (A) Re_θ locations, (B) y^+ planes and (C) pinch and spread planes.

The coherent structures are further investigated by looking at the different modes obtained using POD analysis. Figure 6-15 shows the first four modal structures at Re_θ = 450, 500, 550 and 600. The contours are colored with POD modes for spanwise velocity fluctuations and the overlaid vectors are based on the wall-normal and spanwise velocity fluctuation POD modes. The first four modes at $Re_\theta = 450$ show two structures in the spanwise direction and wall-normal direction. However, at $Re_\theta = 500$ the second mode shows an additional structure in the wall-normal direction. This is due to the formation of the subharmonic lambda vortices which begin appearing after $Re_\theta \approx 480$. The influence of subharmonic mode (mode 2) at $Re_\theta = 500$ appears on the dominant mode at $Re_\theta = 550$. Figure 6-16 shows the streamwise POD modes for two y – planes. The subharmonic mode (mode 2) appears closer to the wall. Away from the wall, the mode is two-dimensional in nature. This behavior is seen for higher modes also. In Figure 6-17, the staggered pattern of the oblique mode in the spanwise fluctuations is clearly visible. The positive (solid lines) and negative (dashed lines) fluctuations have a spanwise wavenumber same as the actuation and are shifted by a phase angle of 45 degrees. Unlike the streamwise mode, the spanwise modes are not two-dimensional away from the wall at $y^+ = 100$. They one order of magnitude lower than the fluctuation modes near the wall. The nonlinear effects near the wall from mode 4, increase the wavenumber in the spanwise direction in mode 1.

6.2.4 Turbulent Statistics

The mean flow characteristics are plotted for different Re_θ values to depict the transition process from laminar to fully turbulent region in Figure 6-18. At the later stages of transition, the log layer region has a lower velocity compared to the fully turbulent region. The Reynolds stresses depicted in Figure 6-19 show that the peak streamwise fluctuations, first increases and then starts decaying till it reaches fully turbulent region.

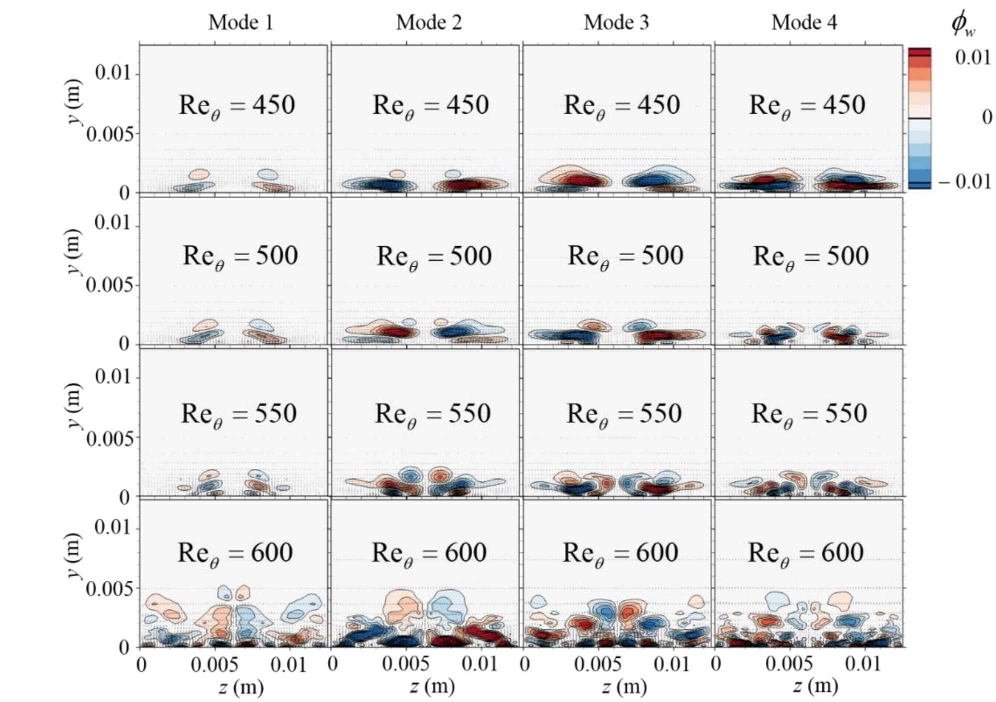

Figure 6-15. Relative energy content for different POD modes at different Re_θ locations.

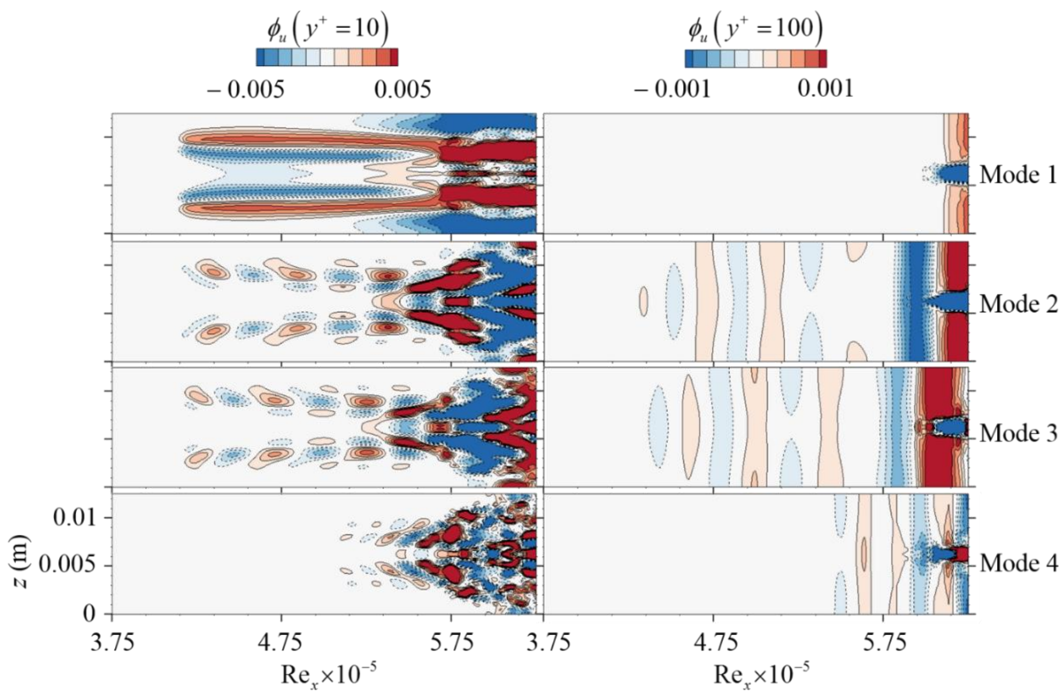

Figure 6-16. Relative energy content for different streamwise modes along two y - planes.

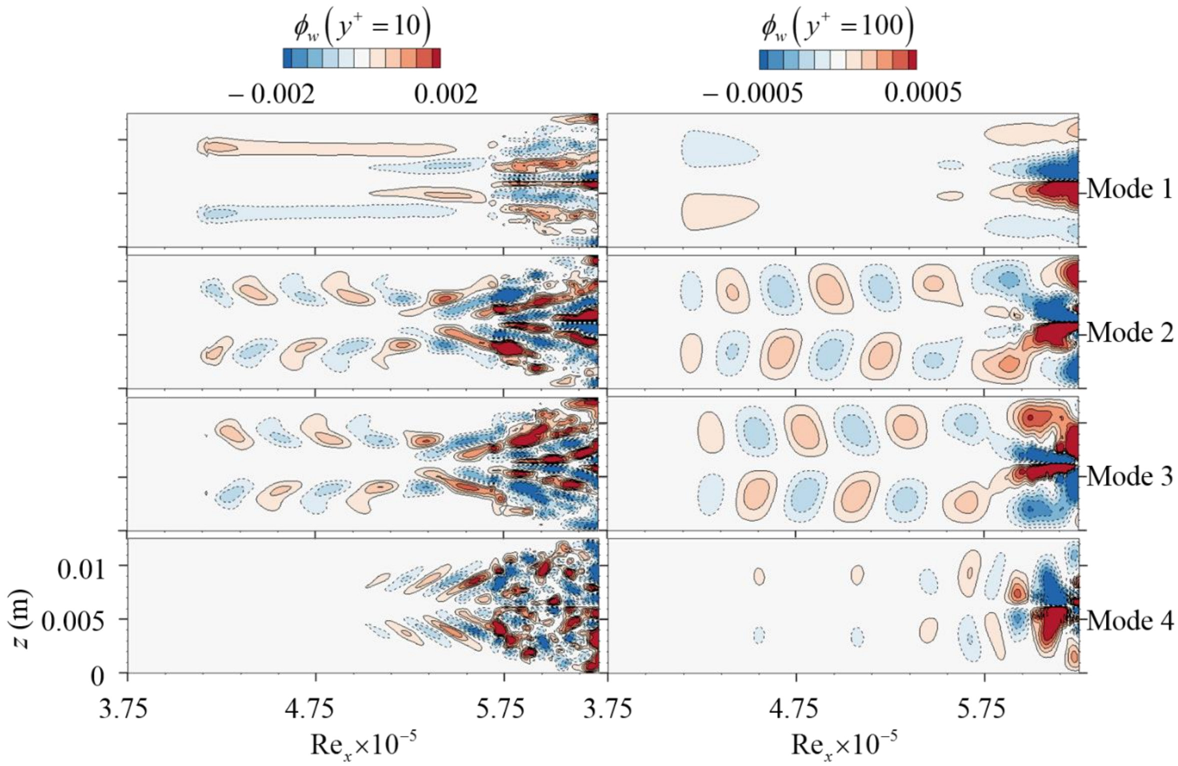

Figure 6-17. Relative energy content for different spanwise modes along two *y* - planes.

Like the bypass transition case in Section 5.2, the peak value of total shear stress shown in Figure 6-20 does not occur at the wall, but at around $y/\delta = 0.03$ or $y^+ = 12$ (see inlay). The transition occurs over the region $\mathrm{Re}_\theta = 420 – 780$ after which the flow becomes fully turbulent. This can be clearly seen in Figure 6-21 (A) for the skin friction. Since the forcing is of large magnitude $\gamma = 0.1$, the flow quickly transitions to turbulence. The shape factor shown in Figure 6-21 (B) has a value of around 1.38 in the fully turbulent region. The displacement thickness plateaus in the later stages of transition while the momentum thickness increases at a higher rate as depicted in Figure 6-21 (C).

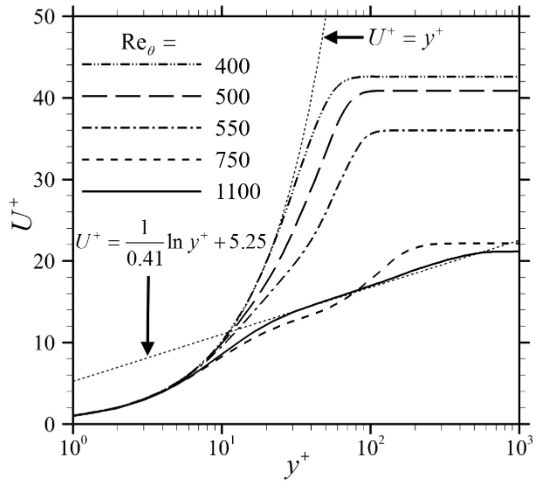

Figure 6-18. Time and span averaged mean velocity profile variation with inner coordinates scaled with wall parameters at different Re_θ.

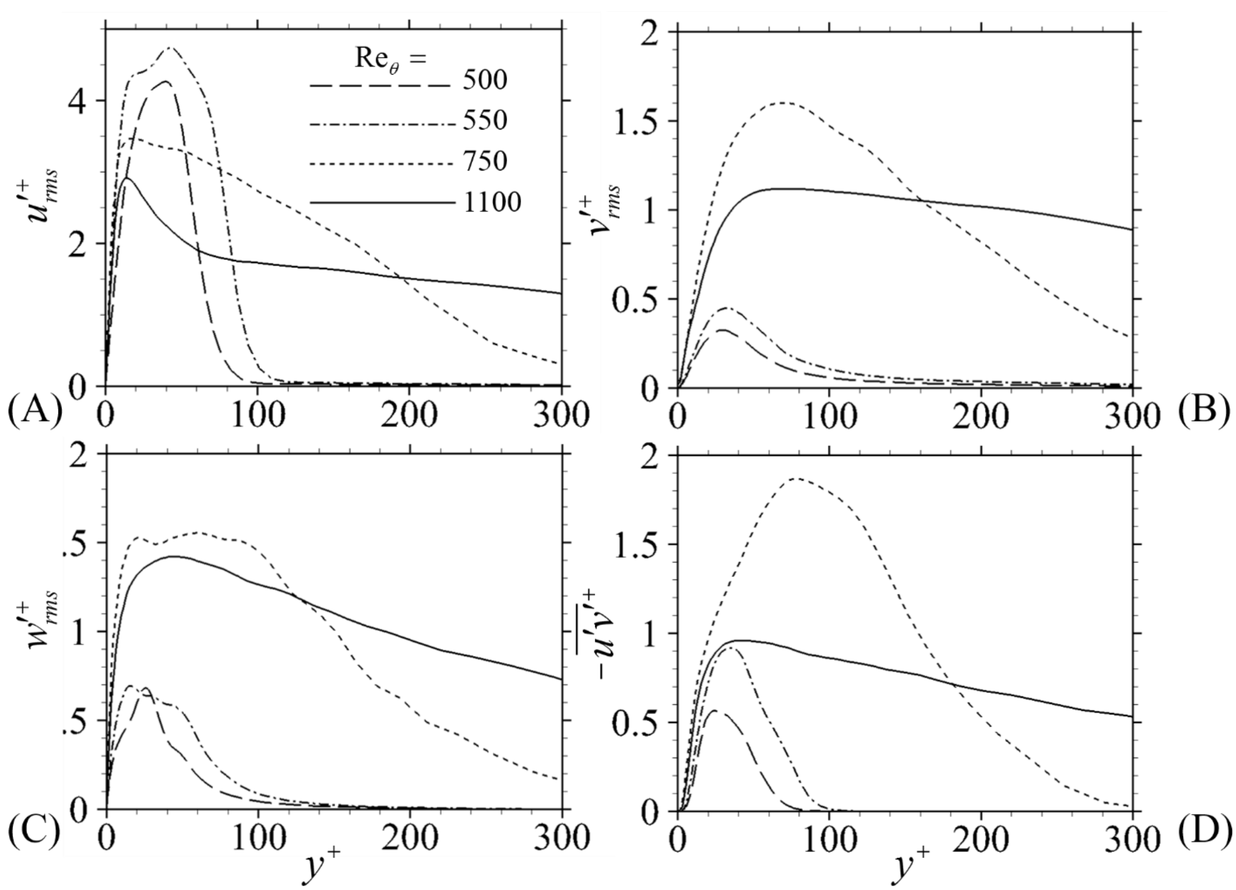

Figure 6-19. Wall-scaled variation of Reynolds stresses at different Re_θ values. (A) Streamwise, (B) wall-normal, (C) spanwise RMS fluctuations and (D) Reynolds shear stress variation with inner wall coordinates.

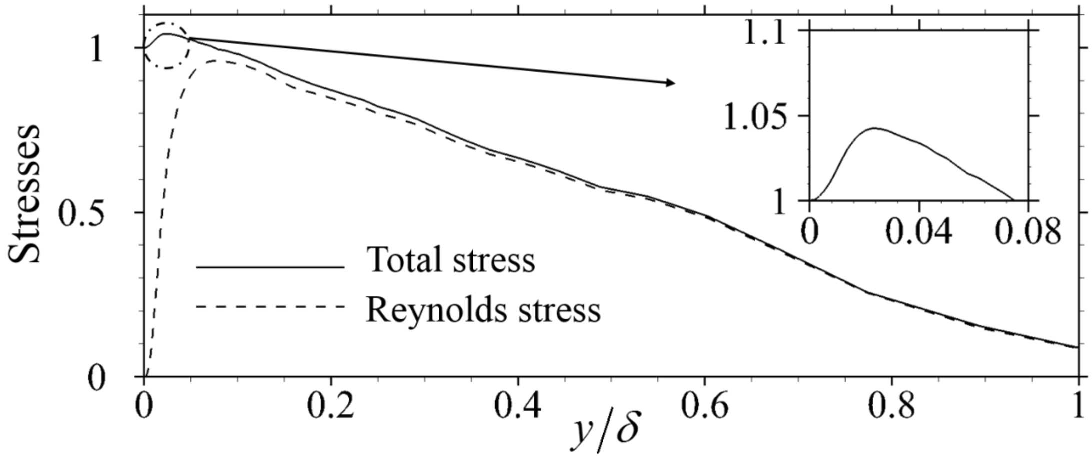

Figure 6-20. Variation of wall-scaled total shear stress and Reynolds shear stress with outer coordinates at $\mathrm{Re}_\theta = 1100$.

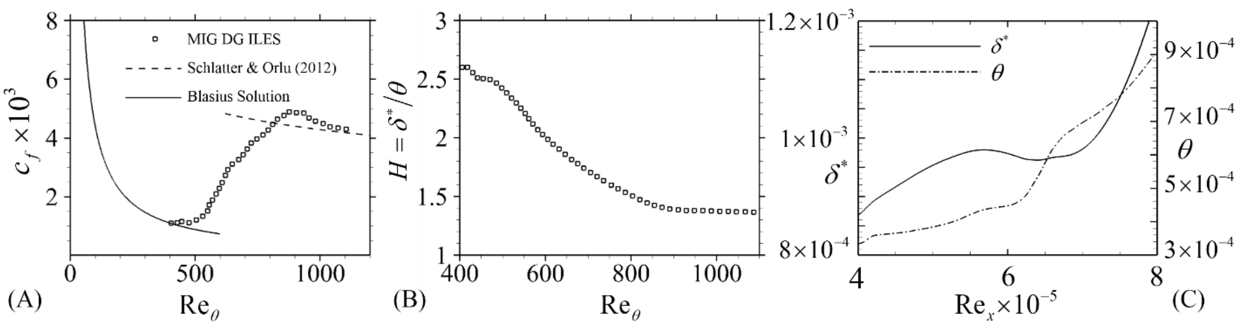

Figure 6-21. Variation of skin friction and integral quantities. Variation of (A) skin friction and (B) shape factor with Re_θ and (C) displacement and momentum thickness with Re_x.

To investigate the growth of fluctuations a growth parameter A_ψ is defined as

$$A_\psi(x,z) = \int_0^\infty \psi(x,y,z)\,dy \tag{6-3}$$

In Eq. (6-3), ψ is the variable for which the growth parameter is being evaluated, for example, wall-scaled root mean square streamwise velocity fluctuations u'^+_{rms}. The growth parameters can also be averaged in the homogeneous spanwise direction, but for Figure 6-22 only temporal averaging is done to show the differences in the growth parameter for pinch and spread plane.

The spread plane shows the transition to be at $\mathrm{Re}_x \approx 6.5\times10^5$ based on the streamwise and wall-normal fluctuation growth as well as Reynolds shear stress growth parameter. However, the spanwise fluctuations do not transition up to $\mathrm{Re}_x \approx 7\times10^5$. The spanwise perturbations on the spread plane occur when hairpin vortices start forming and interacting with each other in the later stages of transition. From close inspection, this can be observed in the $u'v'^+$ growth parameter of the spread plane in Figure 6-22 (D) which shows a slope change at $\mathrm{Re}_x \approx 7\times10^5$ indicative of the flow crossing the transitional region and reaching fully developed turbulence.

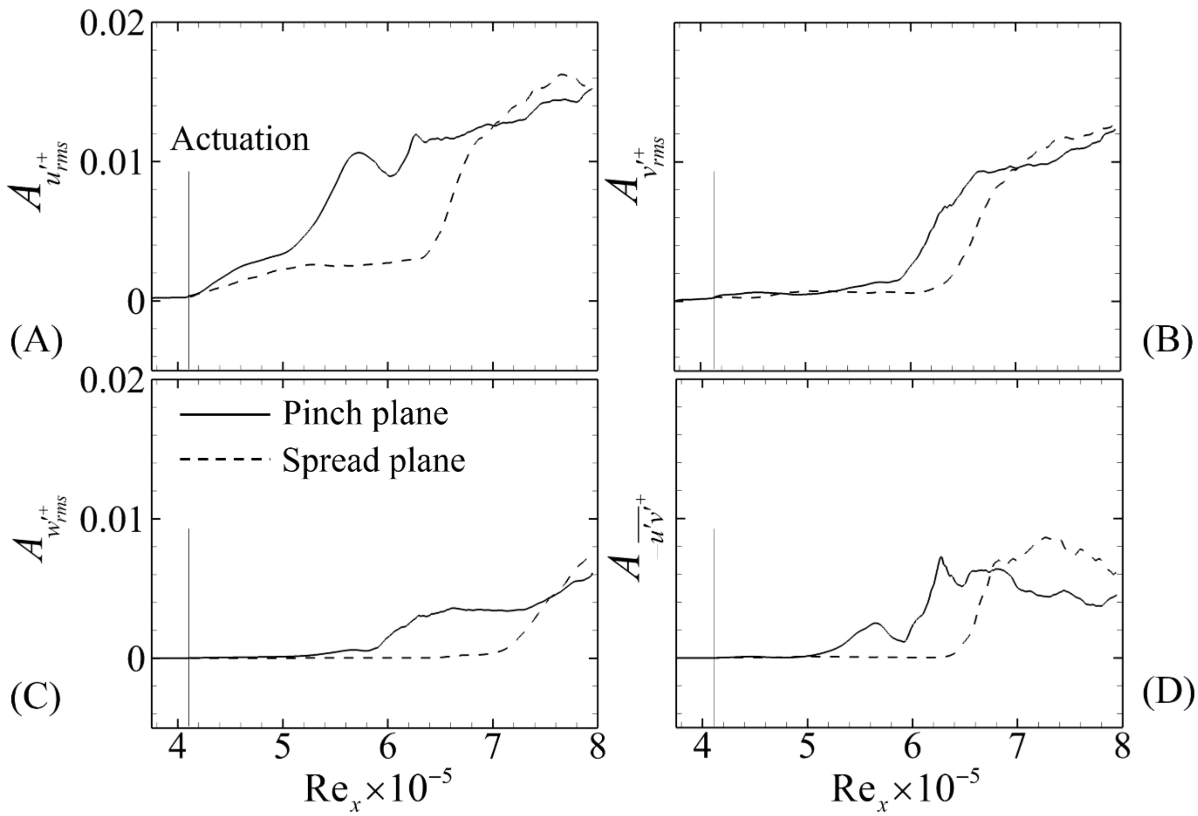

Figure 6-22. Variation of growth parameter for pinch and spread planes with Re_x. Wall-scaled (A) streamwise, (B) wall-normal, (C) spanwise RMS fluctuating component and (D) Reynolds shear stress growth parameters.

The skewness, S and kurtosis, K shown in Figure 6-23 are given by

$$S(u') = \frac{\overline{u'^3}}{\left(\overline{u'^2}\right)^{3/2}};\ K(u') = \frac{\overline{u'^4}}{\left(\overline{u'^2}\right)^2} \tag{6-4}$$

Both S and K are plotted at $Re_\theta = 1100$ and compared to experimental data for a flat plate boundary layer by Barlow and Johnston [227] and numerical data for channel flow by Kim et al. [228]. The data from experimental results correspond to $Re_\theta = 1100$. The results show good agreement with the published data. For reference, the normal distribution values for skewness ($S = 0$) and kurtosis ($K = 3$) are also shown in solid line. The large positive flatness of v' shows the highly intermittent nature of fluctuations occurring near the wall.

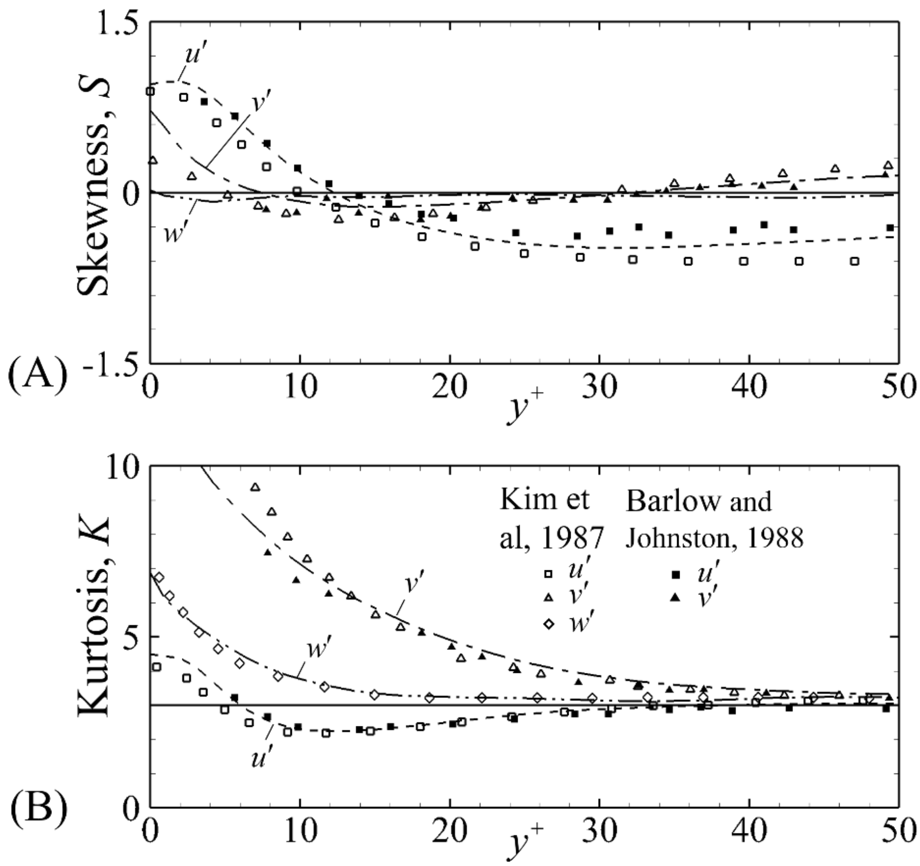

Figure 6-23. Variation of higher moments of velocity fluctuations with inner wall coordinates at $Re_\theta = 1100$. (A) Skewness and (B) Kurtosis compared with published results [227], [228]

In Figure 6-24, the variation of skewness and kurtosis (flatness) is shown at different regions of transition. Closer to the actuation the skewness is negligible near the wall for u', but v' has similar skewness to that of the fully turbulent region. In Figure 6-24 (A), a larger skewness near the wall is seen for u' at the later stages of transition where the breakdown of lambda vortices occurs ($\mathrm{Re}_\theta \approx 550$ to 780) whereas v' has a larger value near the early transitional region ($\mathrm{Re}_\theta \approx 450$ to 550). The large intermittency shown in the kurtosis plots takes place at the later stages of transition which drops down to almost half the value in the fully turbulent region.

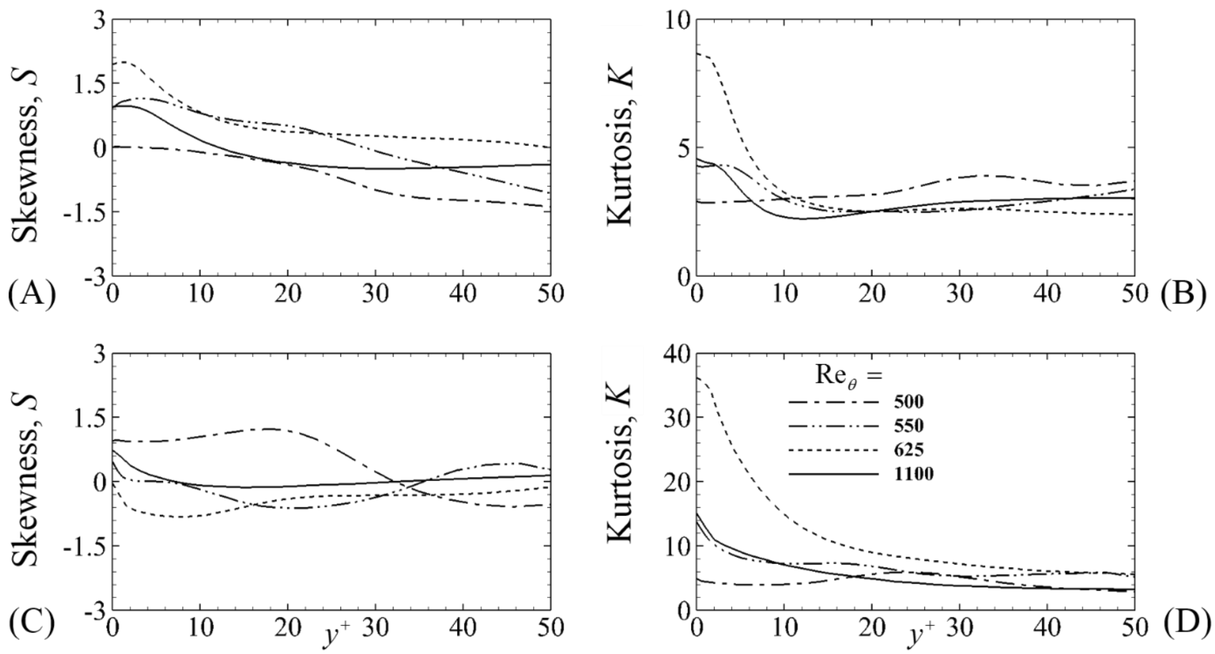

Figure 6-24. Variation of higher moments of velocity fluctuations with inner wall coordinates at different Re_θ values. Skewness and Kurtosis of (A) and (B) streamwise and (C) and (D) wall-normal velocity fluctuations.

The energy spectrum at different Re_θ values for the $y = \delta^*$ plane is shown in Figure 6-25. Please note that the plots are shifted by a factor of 1000 between consecutive Re_θ values and

$Re_\theta = 500$ is at the right scale. The −5/3 slope is also shown with a solid line. The different velocity fluctuations in the inertial zone have large differences in energy for the transitional region. For $Re_\theta = 1100$ this disappears due to isotropy. The streamwise fluctuations have the highest energy compared to the wall-normal and spanwise fluctuations but as Reynolds number increases the difference decreases until the inertial region becomes isotropic.

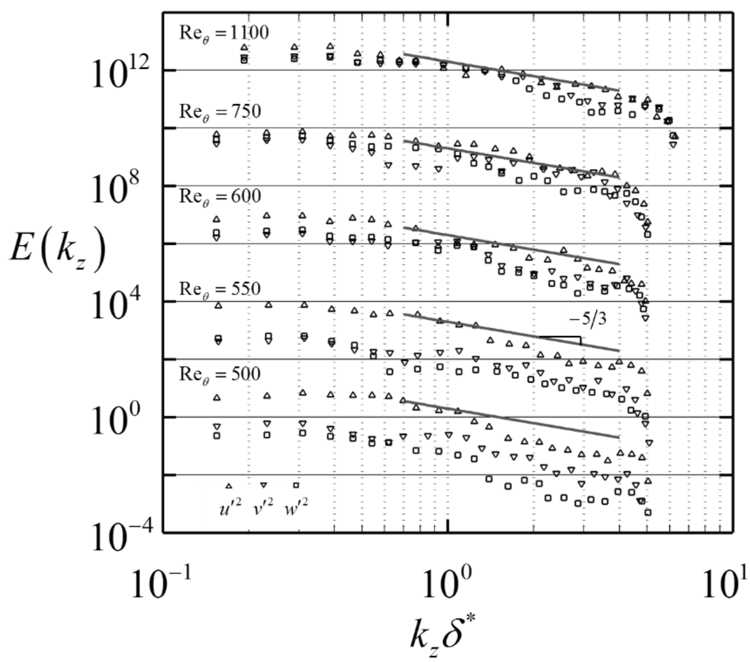

Figure 6-25. The energy spectrum of fluctuating components in the spanwise direction at $y = \delta^*$.

6.2.5 Modal Analysis

In Figure 6-26, Figure 6-27 and Figure 6-28 comparison of energy content in different excited Fourier components of the normalized streamwise, wall-normal and spanwise fluctuations are depicted respectively. The plots are constructed using twenty one *x*-planes in the transitional region. Discrete Fourier transform of the fluctuations in an *x*-plane, provides the maximum energy component for a specific spanwise mode β. The variation in time of this particular β mode provides the frequency ω. The combination ω, β is normalized with the actuator frequency ω_0 and wavenumber $\beta_0 = 2\pi/\lambda$ respectively. The oblique mode corresponds to the (1, 1)-mode. The (0, 1)-mode has higher amplitude than the (0, 2)-mode for $\mathrm{Re}_x < 5.25\times10^5$, after which the nonlinear effects add energy to the higher wavenumber modes and causes the amplitude of (0, 2), (0, 4), (1, 4), (2, 2), (2, 4) and (3,4)-modes to be higher than $\beta = 1$ modes as seen in Figure 6-26. For the wall-normal and spanwise fluctuations shown in Figure 6-27 and Figure 6-28 most of the modes have an initial peak at the actuator location after which they start decreasing in amplitude. The wall-normal and spanwise fluctuation modes with higher wavenumbers $(\beta > 1)$ start growing after $\mathrm{Re}_x \approx 4.5\times10^5$. The amplitudes of the streamwise fluctuations modes are an order of magnitude higher than the wall-normal and spanwise fluctuation modes for the same (ω, β)-mode.

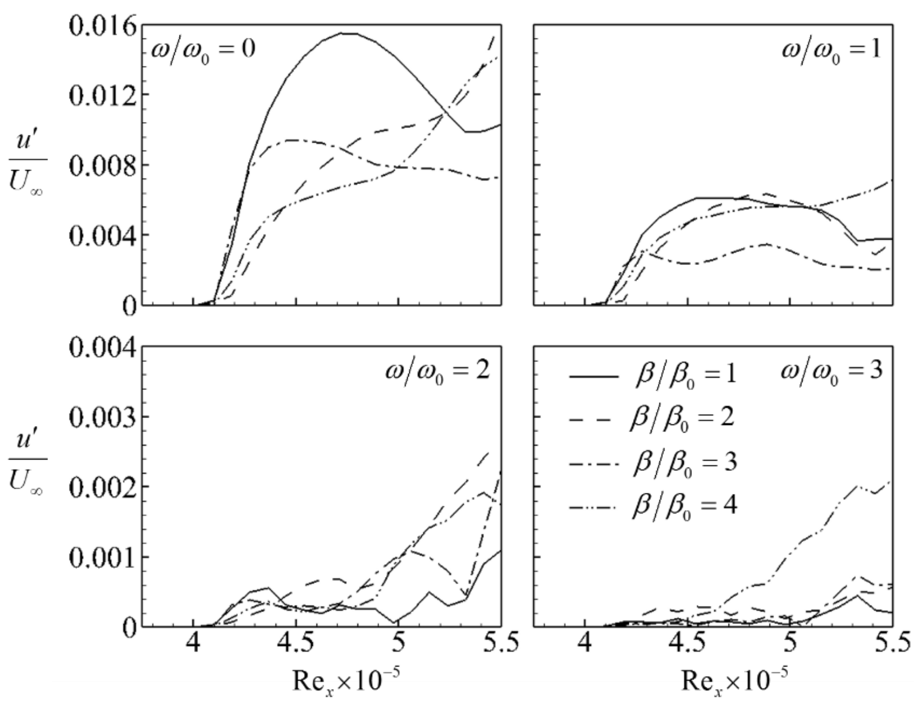

Figure 6-26. Comparison of normalized streamwise fluctuation amplitude for different (ω, β)-modes.

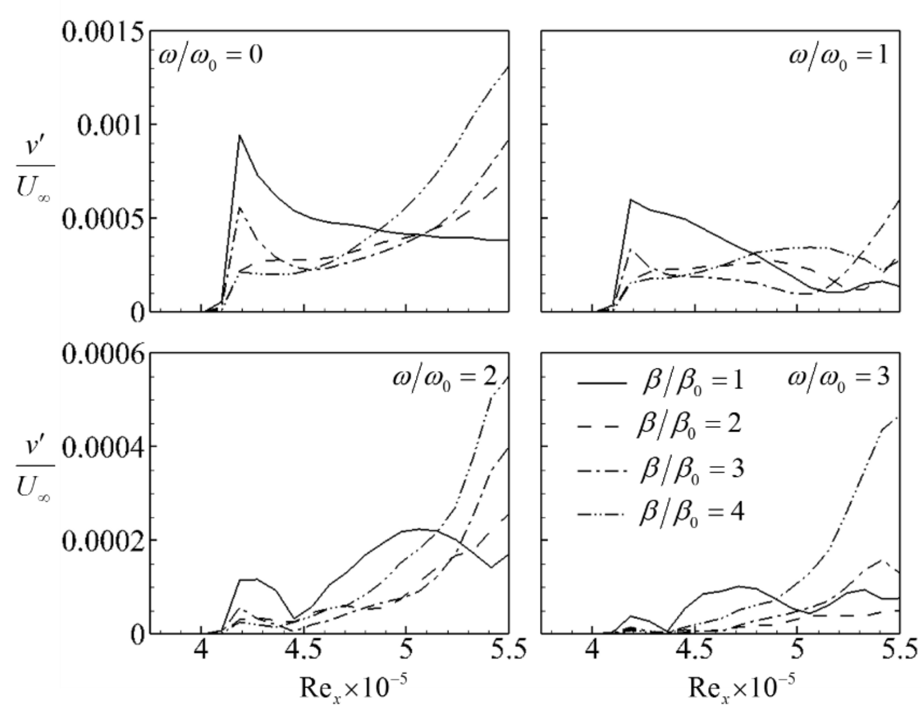

Figure 6-27. Comparison of normalized wall-normal fluctuation amplitude for different (ω, β)-modes.

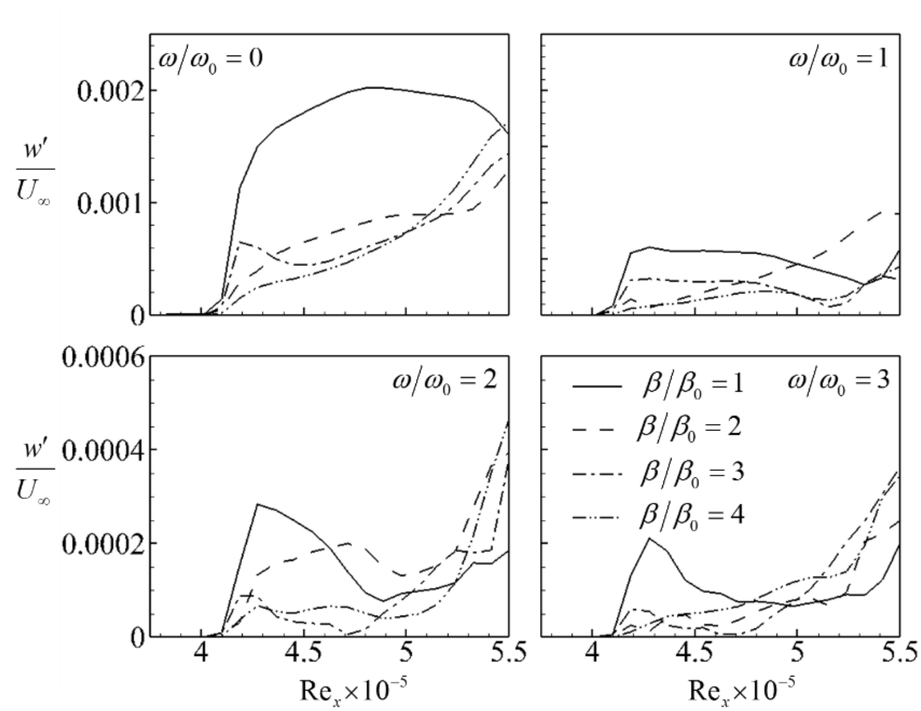

Figure 6-28. Comparison of normalized spanwise fluctuation amplitude for different (ω, β)-modes.

CHAPTER 7
EFFECT OF ACTUATOR PARAMETERS ON TRANSITION

7.1 Background

Various actuator parameters are investigated here. The parameters include the geometry of the actuator, frequency of actuation, the amplitude of actuator perturbation and thermal effects of the actuator. All the simulations in this chapter are conducted using the medium or fine mesh mentioned in Chapter 6 with all other flow field parameters kept identical.

7.2 Effect of Geometry

Three types of geometry for the actuator were tested. These include the standard linear SDBD actuator, circular serpentine actuator and the square serpentine actuator [57]. For the numerical study, the plasma body force mentioned in Chapter 6 is applied along the line of actuation provided in Figure 7-1. For this study γ = 0.1 and ω_0 = 1 kHz. Three-dimensional flow field data is depicted with the domain duplicated three times in spanwise direction. The simulations here are conducted using the fine mesh.

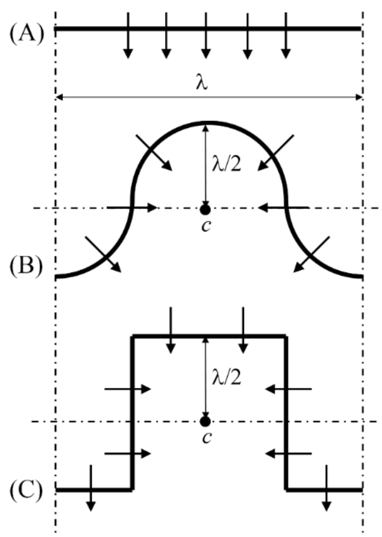

Figure 7-1. Schematic of the line of actuation for different actuator geometries with force vectors. (A) Linear, (B) circular serpentine and (C) square serpentine actuator.

7.2.1 Instantaneous Flow Field

The flow does not transition to fully developed turbulence for the linear and circular serpentine actuator case in the domain size chosen. However, the square serpentine actuator case reaches fully turbulent flow. This can be observed in the normalized instantaneous wall-normal velocity contours at the middle spanwise plane shown in Figure 7-2. The linear actuator creates TS waves which grow with Reynolds number, but they remain coherent and tubular. However, for the same forcing amplitude, the square serpentine actuator transitions earlier compared to the other actuators. For both the serpentine actuators, the initial contours look similar (elongated contour) but due to the difference in strength of the structures generated, the square serpentine transitions faster than the circular serpentine actuator geometry.

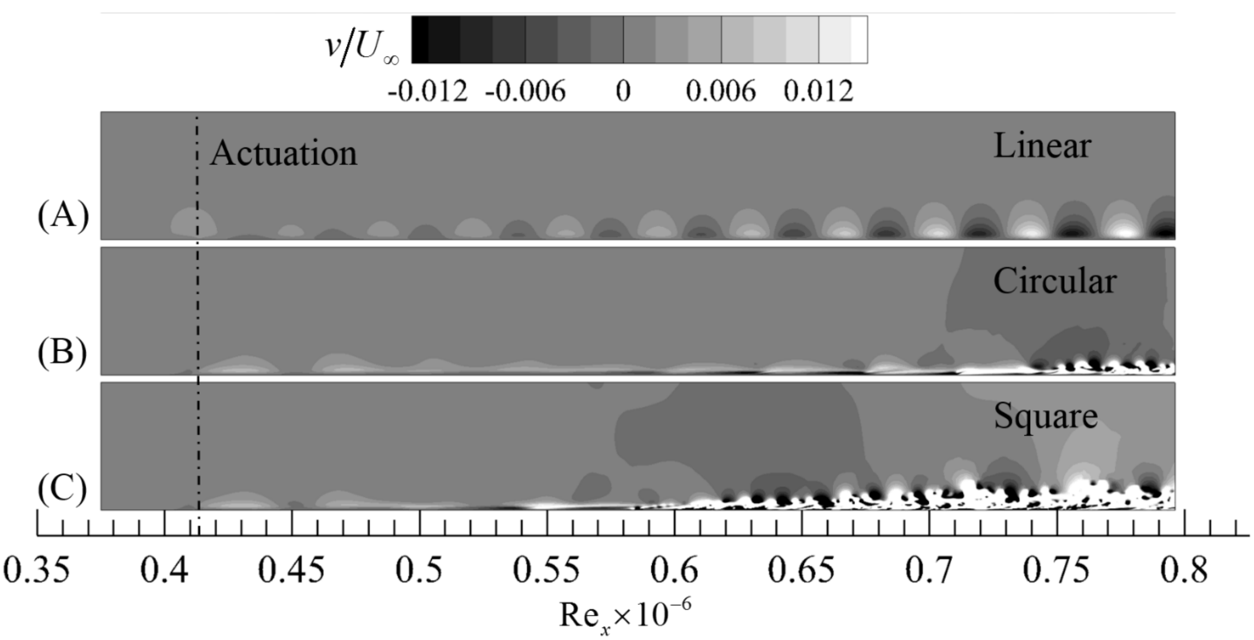

Figure 7-2. Instantaneous wall-normal velocity contours for different actuators at middle spanwise plane showing transition. (A) Linear, (B) circular serpentine and (C) square serpentine SDBD actuator.

The *y*-plane shown in Figure 7-3 depicts the instantaneous positive spanwise vortices for the different actuator geometries at $y^+ = 10$ plane. The two-dimensional nature of the vortical structures for the linear actuator can be clearly seen. Although the contours of both the serpentine actuators look similar, downstream of the pinch regions is darker (weaker vorticity) for the circular serpentine actuator. The oblique waves created by both the serpentine actuators, shown in Figure 7-3 with dashed-dotted lines, have similar angles. Therefore, the structures generated by serpentine actuators have similar behavior and shape but different magnitudes.

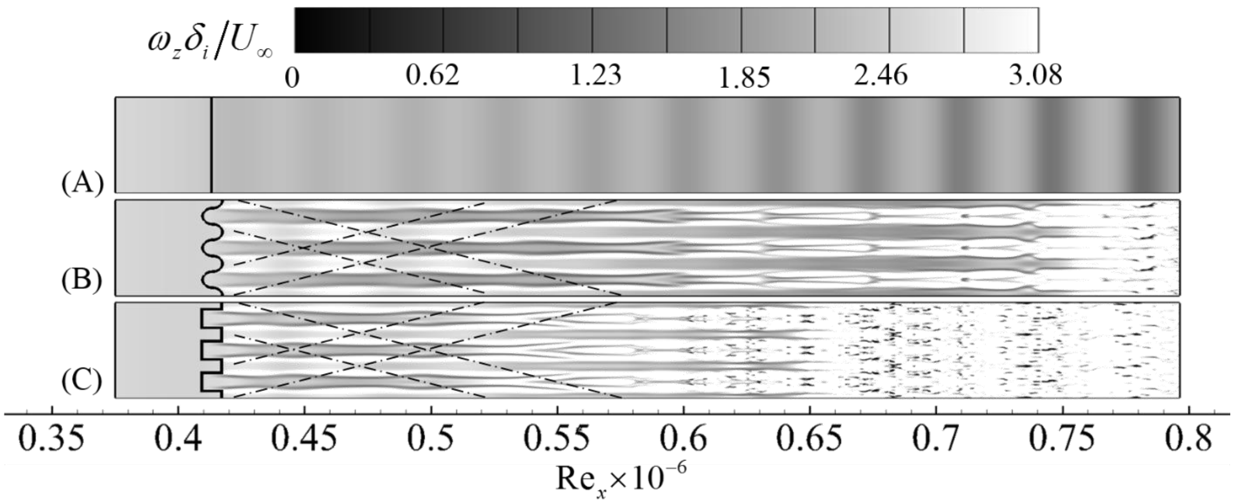

Figure 7-3. Instantaneous spanwise vorticity contours for different actuators at $y^+ = 10$ plane. (A) Linear, (B) circular serpentine and (C) square serpentine SDBD actuator. The dashed-dotted lines depict the directions of oblique waves.

To visualize the vortical structures, Q – criterion is plotted in Figure 7-4 for the different actuator geometries. The linear actuator does not show any streamwise oriented vortices but creates one-dimensional spanwise oriented vortices. The serpentine actuators create similar vortical structures, however, their strengths are different. Similar 'X' like structures have been found in the experimental and numerical study of oblique wave transition [174], [179], [221]. The lifted nature of the structures is evident by the change in velocity magnitude from the tail to the head of the lambda structures.

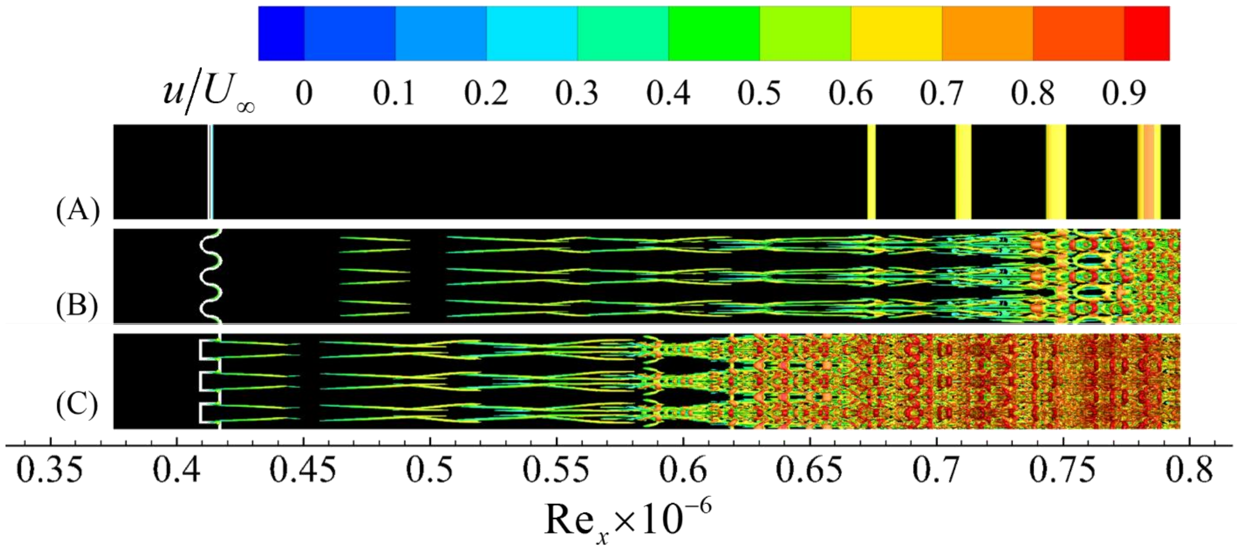

Figure 7-4. Instantaneous Q – criterion (Q = 0.04) iso-surface colored with velocity magnitude for different geometries. (A) Linear, (B) circular serpentine and (C) square serpentine SDBD actuator.

7.2.2 Turbulent Statistics

The mean flow velocities for the different geometries are shown in Figure 7-5. The wall-scaled velocities are plotted at different Re_x values to show the effect of transition. For the linear actuator, the velocity profile remains laminar throughout due to which the maximum U^+ keeps increasing due to the decrease in friction velocity. However, after $\mathrm{Re}_x = 7.75\times10^5$ ($\mathrm{Re}_\theta = 583$) there is a decrease in maximum U^+. This difference is insignificant and the flow is still in early stages of transition as can be seen in the momentum thickness shown in Figure 7-6 (A). The circular serpentine stays in the early stages of transition for $\mathrm{Re}_x < 5.87\times10^5$ ($\mathrm{Re}_\theta = 550$) and then starts deviating from the laminar behavior. This is also observable in Figure 7-6 (A). The square serpentine in comparison to the other actuators quickly reaches fully turbulent flow.

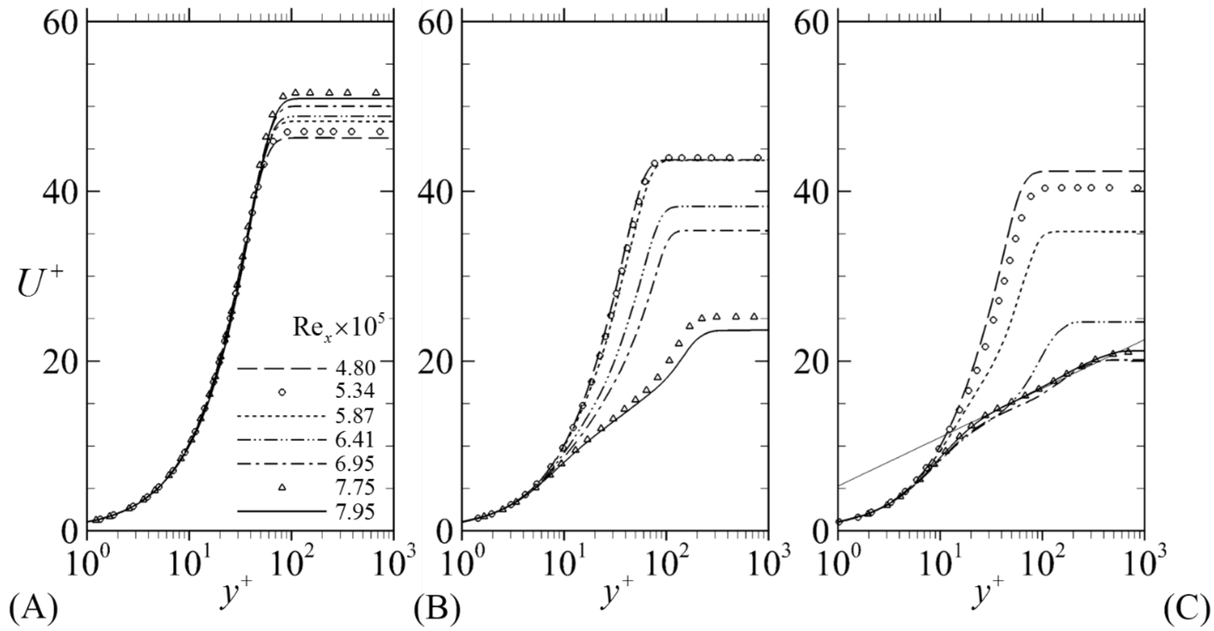

Figure 7-5. Time and span averaged mean velocity profile variation with inner coordinates scaled with wall parameters at different Re_x. (A) Linear, (B) circular serpentine and (C) square serpentine SDBD actuator.

The shape factor *H*, shown in Figure 7-6 (A) stays at a laminar value of 2.65 for the linear actuator throughout the domain. There is an initial increase in shape factor at the actuator location for the linear actuator, whereas the serpentine actuators show a decrease in shape factor at the same location. This is due to the pinching effect of the serpentine actuator which pushes the fluid away from the wall and thus increasing the momentum thickness as depicted in Figure 7-6 (B). The displacement thickness does not show a difference between the actuators at the actuation location. At the later stages of transition, both the serpentine actuators have a similar slope in shape factor and momentum thickness. However, in the skin friction plots the flow transitions at different rates for the serpentine actuators. The serpentine actuators deviate from the laminar profile at $\mathrm{Re}_x \approx 4.12\times10^5$ (actuator location) and the later stages of transition start at $\mathrm{Re}_x \approx 7.75\times10^5$ for the circular serpentine actuator and $\mathrm{Re}_x \approx 6\times10^5$ for the square serpentine actuator.

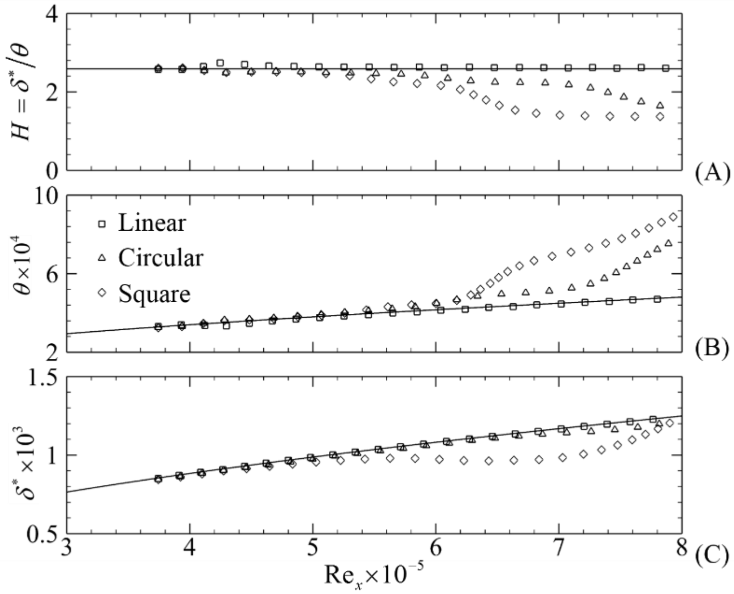

Figure 7-6. Variation of integral quantities with Re_x for linear, circular serpentine and square serpentine SDBD actuator. (A) Shape factor, (B) momentum thickness and (C) displacement thickness. The solid line represents a laminar solution.

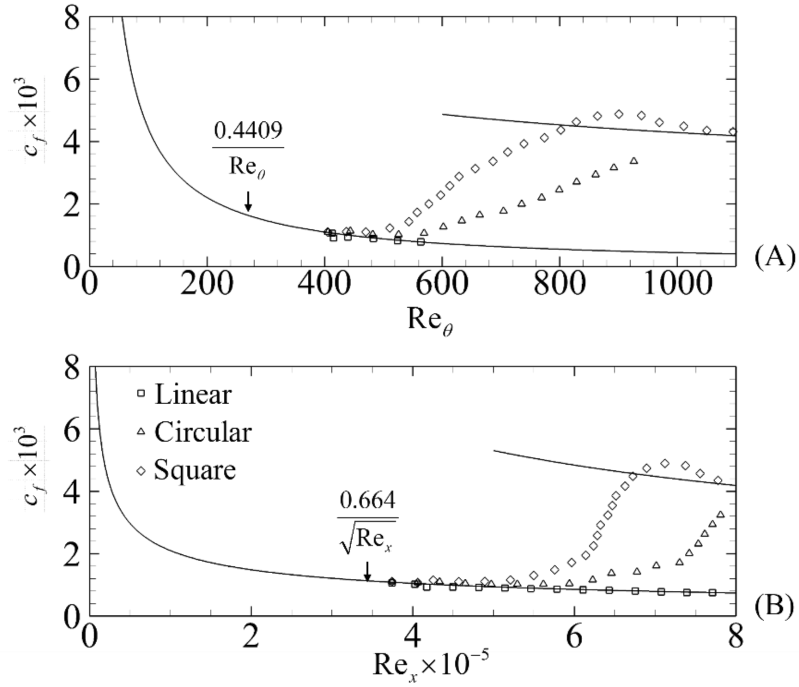

Figure 7-7. Variation of skin friction for linear, circular serpentine and square serpentine SDBD actuator. Variation of skin friction with (A) Re_θ and (B) Re_x. Turbulent skin friction is compared with DNS results [209].

The variation of wall-scaled RMS fluctuations is depicted in Figure 7-8. The linear actuator shows a different transition mechanism compared to the serpentine actuators. The streamwise fluctuations behave like a fundamental transition mechanism [223], [165] for the linear actuator while it behaves similarly to subharmonic transition mechanism [223], [165] for the serpentine actuators. The spanwise fluctuations are negligible for the linear actuator case since the flow is still in the two-dimensional TS wave region with no spanwise variation. For the square serpentine case, the maximum streamwise fluctuations in the transitional region are always higher than in the fully turbulent region $\left(u'^{+}_{rms} = 2.85\right)$. This is not the case when the transition goes through the linear instability region [223], [165] or weakly nonlinear region where the wall-scaled streamwise fluctuations are higher. This can also be observed in the linear actuator case where the maximum amplitudes are below 1.5. Although the circular serpentine actuator has not reached the fully turbulent region the RMS fluctuations are above 2.85. This is mainly attributed to the geometry of the square serpentine actuators which creates strong streamwise perturbation and avoids the entire linear instability region. Therefore, this allows the serpentine actuators to transition faster compared to the linear actuators with the same amount of input perturbations.

To investigate the growth of fluctuations, the growth parameter given by Eq. (6-3) is plotted for the Reynolds stresses in Figure 7-9. There is an initial jump at the actuator location and a second jump for the serpentine actuation cases indicating highly nonlinear stages of transition to turbulence. For the linear actuation case, the streamwise and wall-normal fluctuations grow steadily but the domain is not long enough for it to reach fully developed turbulence. For the wall-normal and spanwise fluctuation growth, the serpentine actuation cases show an abrupt increase in the growth parameter at later stages of transition where it diverges from the linear actuation case. Both the serpentine actuators have similar growth rates (shown by dotted lines in wall-normal and spanwise fluctuation growth rate) for wall-normal and spanwise fluctuations in this region. The streamwise fluctuation growth parameter for the serpentine actuators have similar amplitude and slope in the transitional region as shown in Figure 7-10. Interestingly the wall-normal fluctuations for the linear actuation have a higher growth parameter than the circular serpentine for the same momentum Reynolds number, in the transitional region. Also, right after $Re_\theta \approx 500$ the square serpentine actuator dips in amplitude for the wall-normal fluctuation growth parameter compared to the linear actuator and goes back up to similar amplitude in the later stages of transition.

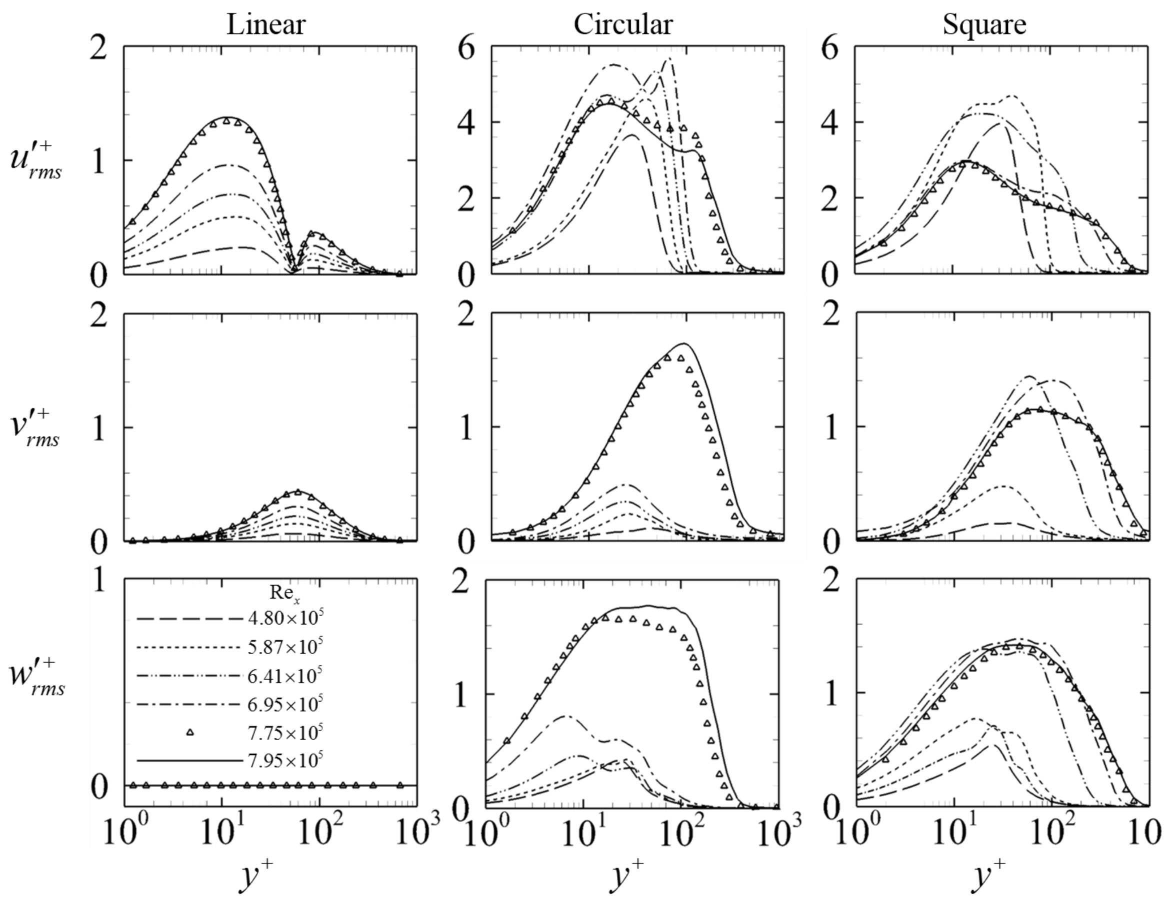

Figure 7-8. Variation of wall-scaled RMS velocity fluctuations variation with inner coordinates at different Re_x values.

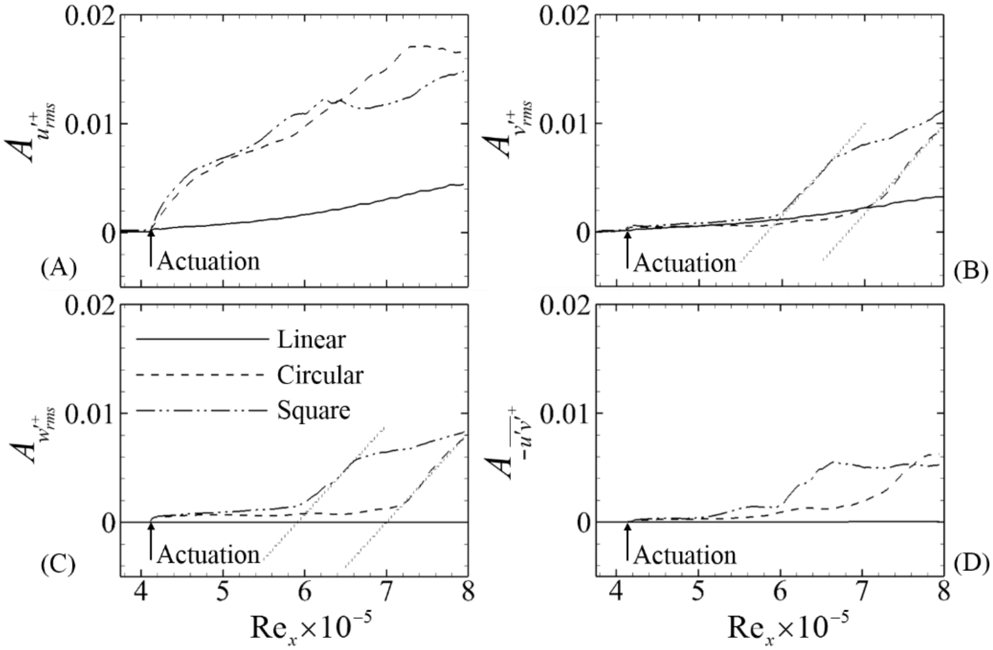

Figure 7-9. Variation of growth parameter with Re_x for wall-scaled Reynolds stresses. Growth parameter of (A) streamwise, (B) wall-normal and (C) spanwise RMS fluctuations and (D) Reynolds shear stress.

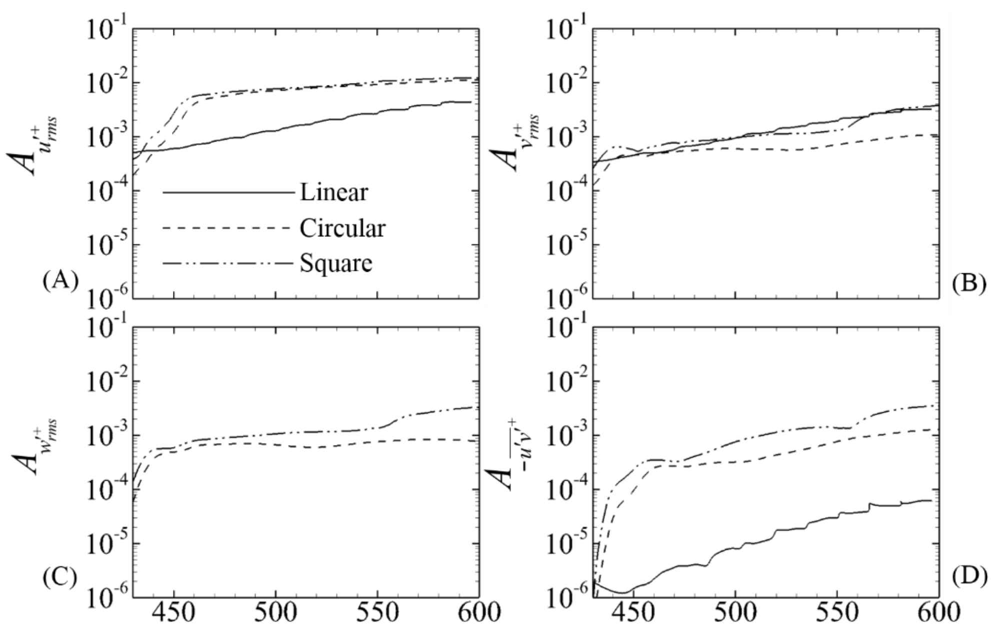

Figure 7-10. Variation of growth parameter with Re_θ in the transitional region for wall-scaled Reynolds stresses. Growth parameter of (A) streamwise, (B) wall-normal and (C) spanwise RMS fluctuations and (D) Reynolds shear stress.

7.3 Effect of Frequency

To study the impact of frequency of actuation three different frequencies were chosen. The frequency ω_0 in Eq. (6-2) is set to 500 Hz, 1000 Hz and 2000 Hz which gives a Strouhal number of 0.292, 0.584 and 1.168 respectively. These frequencies are chosen because they are typical for an SDBD actuator. A case with a continuous signal is also studied. The γ value for all the cases is set to 0.1. The simulations are performed for the square serpentine actuator using the medium mesh given in Table 6-1. All other flow field parameters are kept identical.

7.3.1 Instantaneous Flow Field

The continuous signal and the 500 Hz cases do not turbulize in the chosen domain. This can be observed in Figure 7-11 and Figure 7-12. The transition occurs earlier for higher frequencies since they have lower critical Reynolds number based on the neutral stability curve [229]. The oblique structures in the later stages of transition in Figure 7-11 (C) are regions of high shear which break down via Kelvin Helmholtz free shear layer instability mechanism. These oblique structures are also a characteristic of oblique wave transition and have been observed in numerical studies [173]. When comparing streamwise velocities for two different y planes in Figure 7-12, it is found that except the continuous signal case all the other cases have a similar wavy pattern, created by the fundamental and subharmonic lambda vortices in the transitional region. It can also be seen that for both 1 kHz and 2 kHz cases, the lambda vortices break down after about three wavelengths. For the 500 Hz, the lambda structures are more elongated and have a smaller angle compared to the 1 kHz and 2 kHz cases, which makes them weaker and in the far downstream region, it becomes like the continuous signal case. The vortical structures are depicted using Q – criterion iso-surface shown in Figure 7-13. The lambda structures quickly decay for the continuous signal and the spacing between them reduces as the frequencies increase.

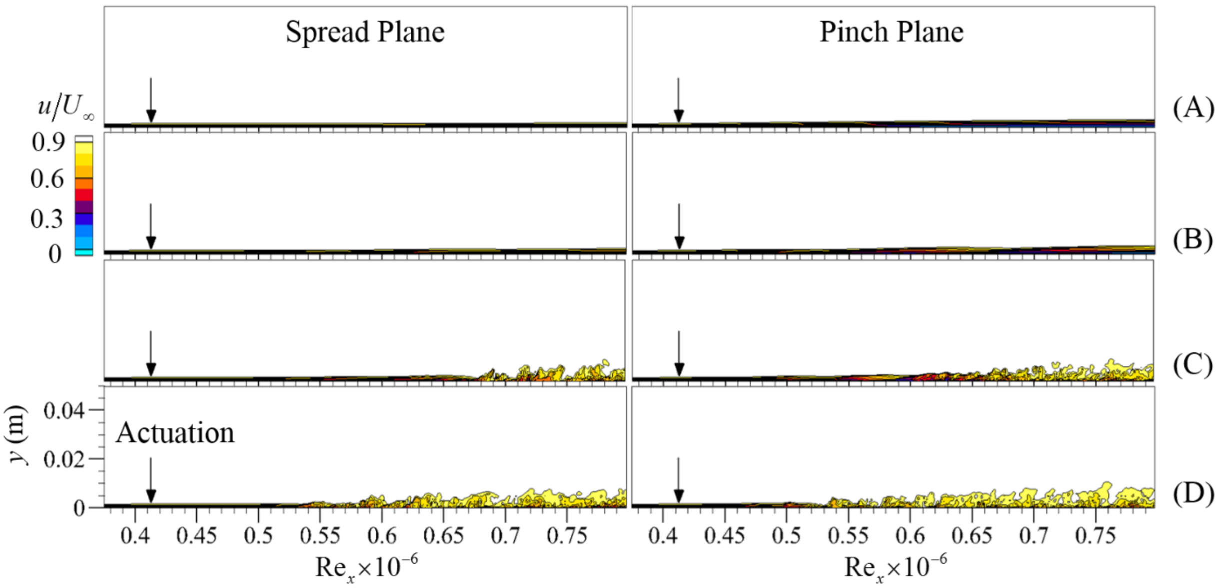

Figure 7-11. Variation of normalized streamwise velocity for spread and pinch plane. (A) Continuous, (B) 500 Hz, (C) 1 kHz, (D) 2 kHz actuation signal.

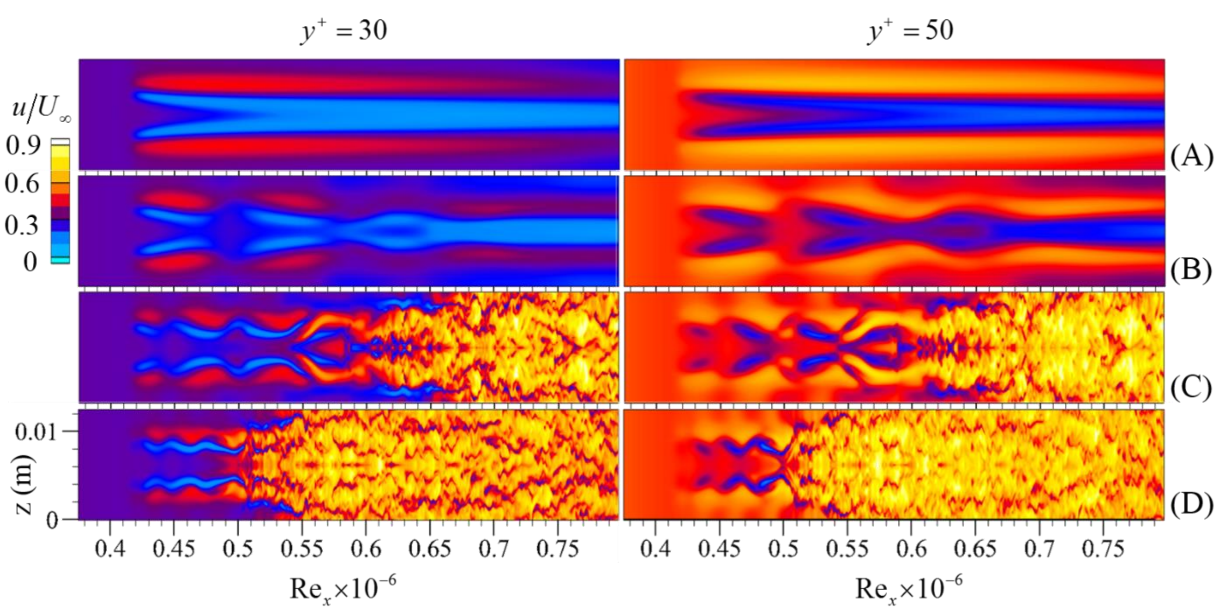

Figure 7-12. Variation of normalized streamwise velocity at different y – planes. (A) Continuous, (B) 500 Hz, (C) 1 kHz, (D) 2 kHz actuation signal.

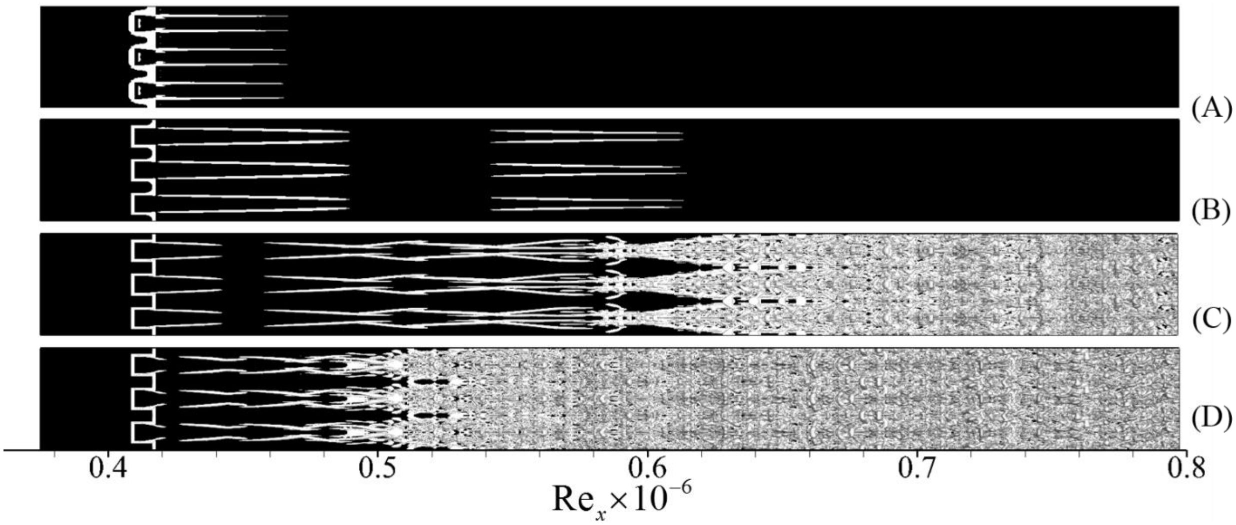

Figure 7-13. Top view of Q – criterion iso-surface at different frequencies. (A) Continuous, (B) 500 Hz, (C) 1 kHz, (D) 2 kHz actuation signal. The domain is duplicated three times.

7.3.2 Turbulent Statistics

The turbulent statistics of the 500 Hz, 1 kHz, and 2 kHz are presented in this section for comparison. The mean velocity profiles are shown in Figure 7-14. At the lowest Re_x shown in the Figure 7-14, the 2 kHz case already shows deviations from the laminar behavior due to which the transitional region is extremely short. The shape factor shown in Figure 7-15 (A) shows the transitional region for the 1 kHz case ends around $Re_x = 6.75\times10^5$ while for the 2 kHz case it ends around $Re_x = 5.5\times10^5$. In the turbulent region, the shape factor converges to a value to 1.38 for both the 1 kHz and 2 kHz cases. There is a slight reduction from the laminar shape factor for the 500 Hz case due to boundary layer thickening in the pinch region. The momentum and displacement thickness also show similar behavior. Both 1 kHz and 2 kHz cases have a similar slope in shape factor and momentum thickness in the later stages of transition as well as in the turbulent region.

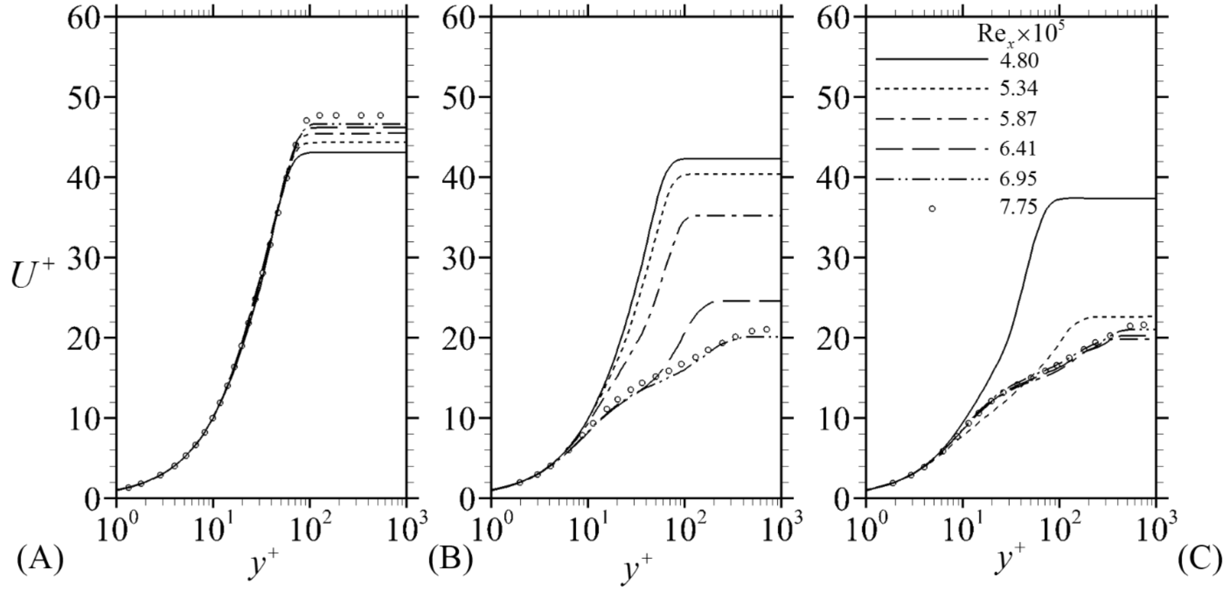

Figure 7-14. Time and span averaged mean velocity profile variation with inner coordinates scaled with wall parameters at different Re_x. (A) 500 Hz, (B) 1 kHz and (C) 2 kHz signal.

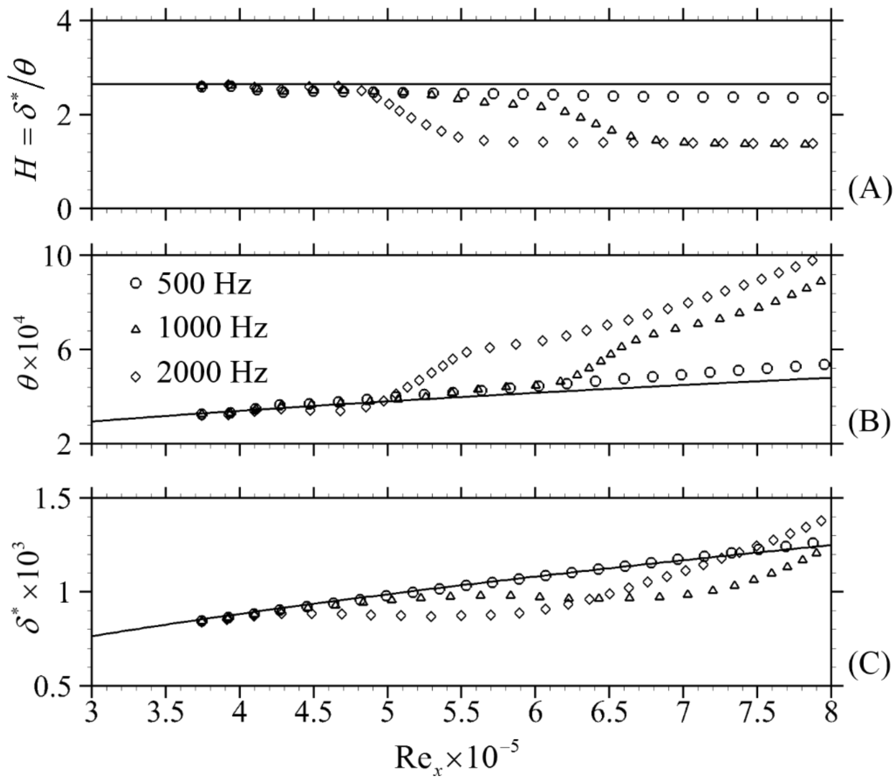

Figure 7-15. Variation of integral quantities with Re_x at different frequencies for the square serpentine SDBD actuator. (A) Shape factor, (B) momentum thickness and (C) displacement thickness. The solid line represents the laminar solution.

The skin friction plots shown in Figure 7-16 show the difference in location of transition to turbulence when the frequency of perturbation is varied. The overshoot in skin friction before the flow becomes fully turbulent is lower for the 2 kHz case when plotted against Re_x but it becomes comparable for similar Re_θ. Both the 1 kHz and 2 kHz cases converge to the published turbulent skin friction data [209]. The wall-scaled RMS fluctuations are shown in Figure 7-17. For the 2 kHz case, the fluctuations show fully developed turbulent profile for $\mathrm{Re}_x \geq 5.87\times10^5$.

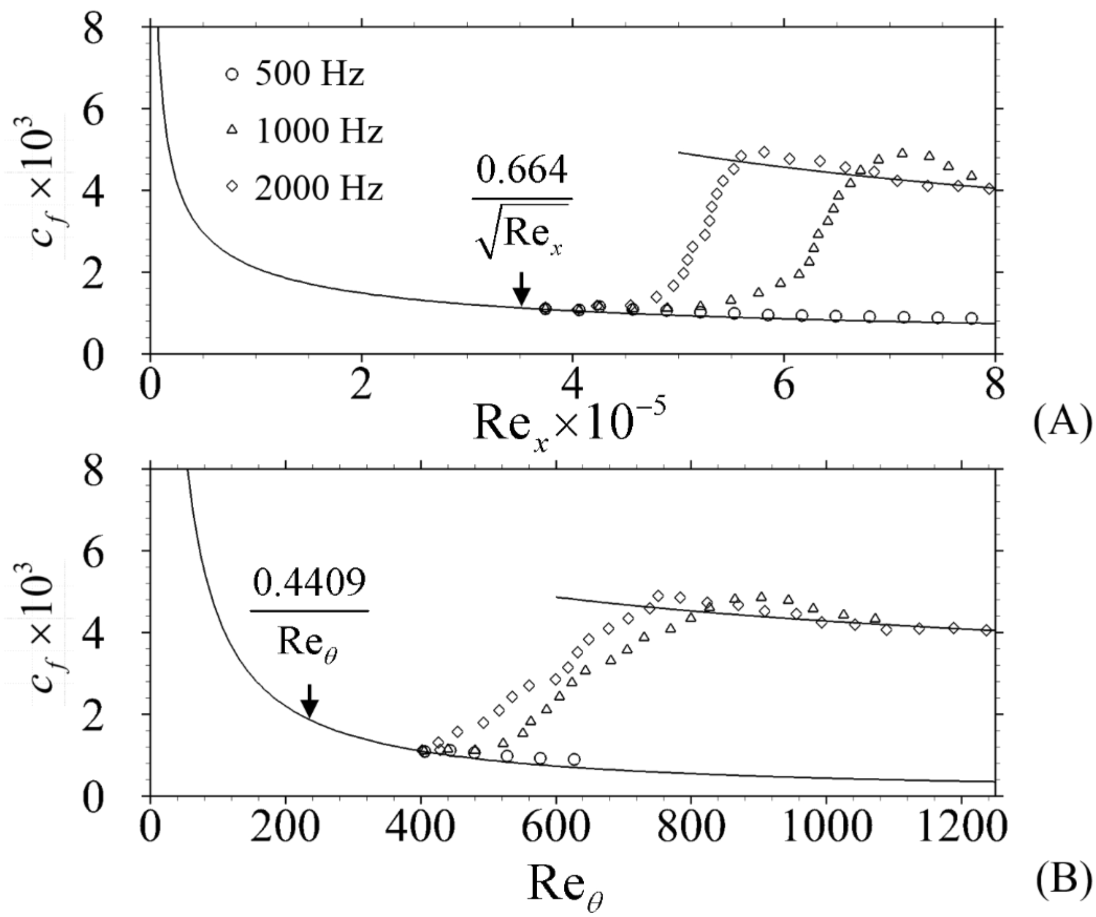

Figure 7-16. Variation of skin friction for different frequencies of actuation of the square serpentine actuator. Variation of skin friction with (A) Re_θ and (B) Re_x. Turbulent skin friction is compared with DNS results [209].

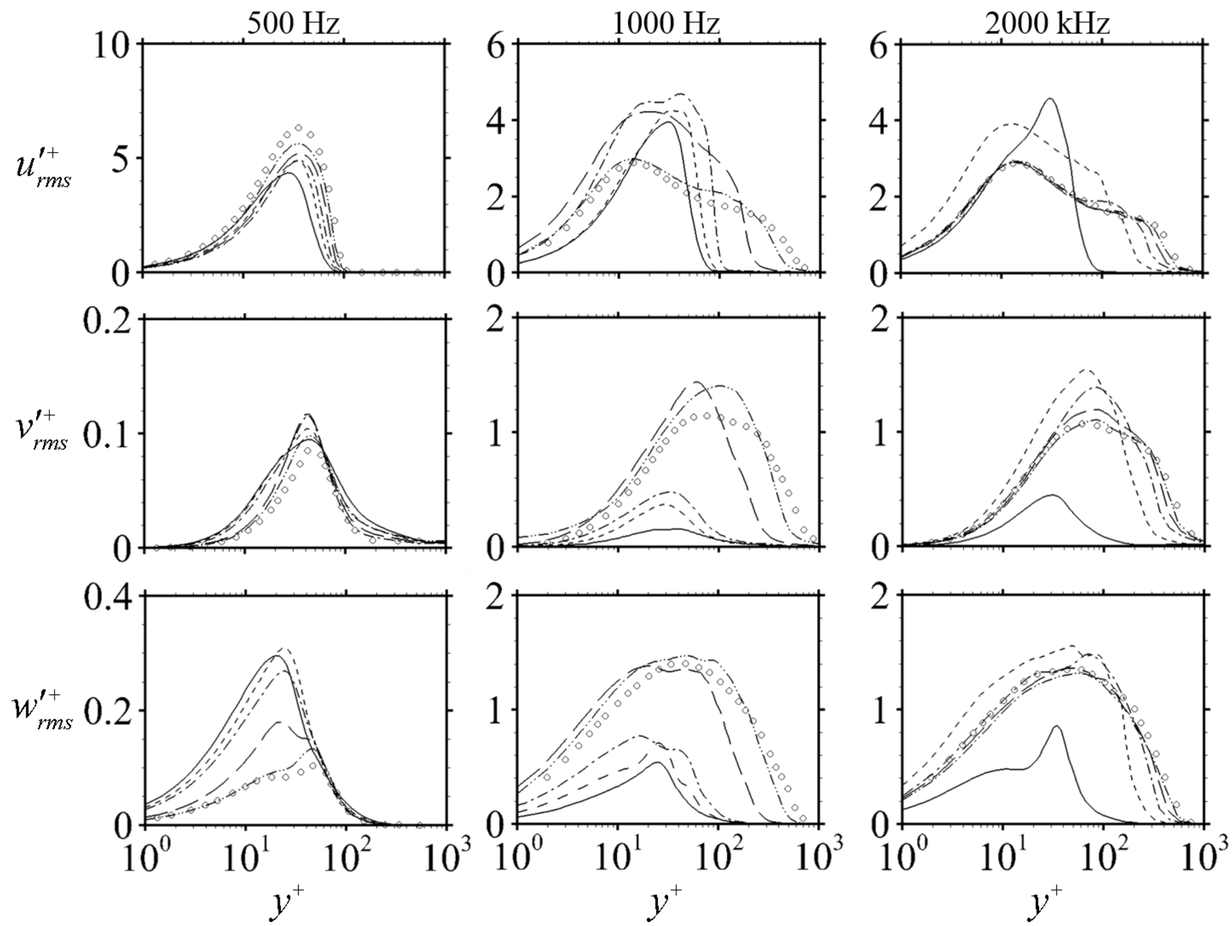

Figure 7-17. Variation of wall-scaled RMS velocity fluctuations with inner coordinates at different Re_x values. Please refer to Figure 7-14 for the legend.

The growth parameters for the fluctuating components are plotted in Figure 7-18 and Figure 7-19. The growth parameters for streamwise fluctuations have similar amplitude for all the three cases however they have different slopes when plotted against Re_θ. The 500 Hz case has growth only in the streamwise fluctuations which inhibits the transition to turbulence. Both the 1 kHz and 2 kHz cases show similar growth rate in the later stages of transition.

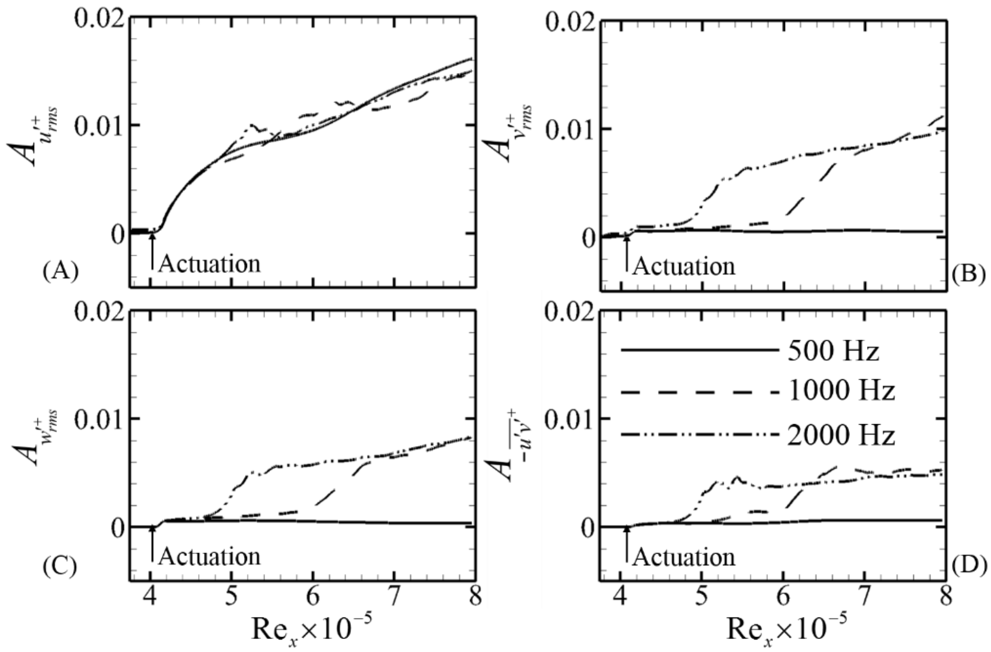

Figure 7-18. Variation of growth parameter with Re_x for wall-scaled Reynolds stresses. Growth parameter of (A) streamwise, (B) wall-normal and (C) spanwise RMS fluctuations and (D) Reynolds shear stress.

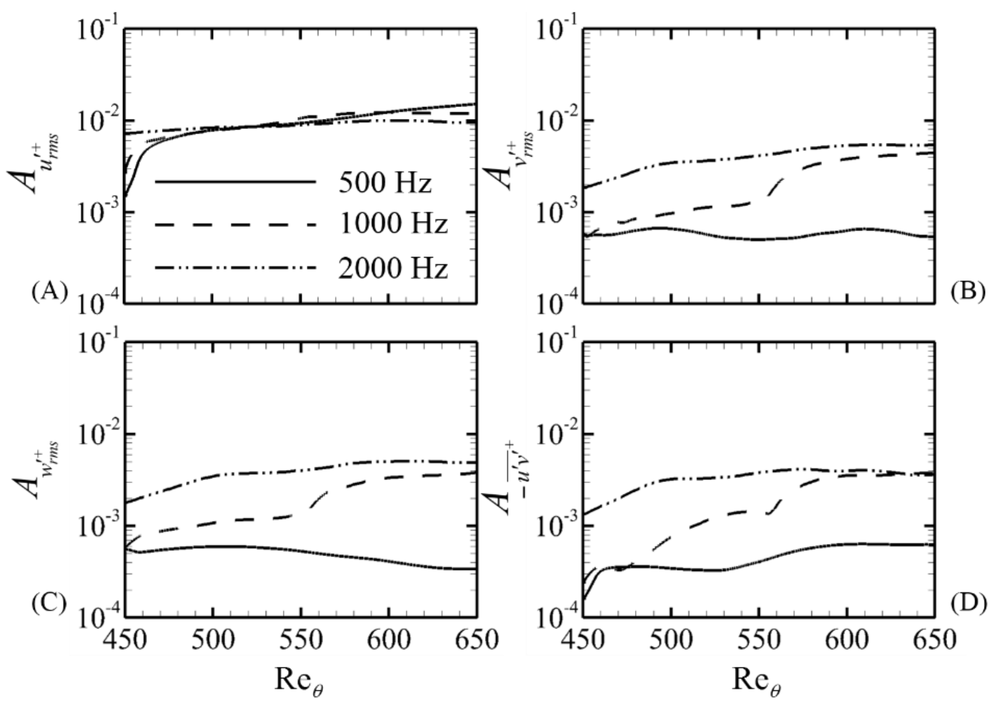

Figure 7-19. Variation of growth parameter with Re_θ in the transitional region for wall-scaled Reynolds stresses. Growth parameter of (A) streamwise, (B) wall-normal and (C) spanwise RMS fluctuations and (D) Reynolds shear stress.

7.4 Effect of Amplitude

The effect of forcing amplitude is investigated for three velocity ratios namely, γ = 0.05, 0.10 and 0.14. The perturbation frequency was kept constant at 1 kHz. It should be noted that the velocity ratio also relates to the amplitude of perturbation through Figure 6-5. From an experimental point of view, this is related to the fourth power of potential difference [74] across the electrodes. This test is only performed for the square serpentine actuator. The medium mesh given in Table 6-1 is used for this study.

7.4.1 Instantaneous Flow Field

The vortical structures created using different velocity ratios are depicted using instantaneous Q – criterion iso-surface in Figure 7-20.The initial effect of the serpentine actuator is similar for all the velocity ratios where it creates streamwise oriented vortices. However, for γ = 0.05 these structures dissipate quickly. The cases with γ = 0.10 and 0.14 have similar behavior in the later stages of transition. The structures are weaker at lower velocity ratios. Interestingly, new vortical structures appear downstream of the γ = 0.05 case. These vortices have spanwise orientation and also vary in strength in the spanwise direction. This variation has the same wavenumber as the initial upstream region. The elongated structures upstream get compressed into globular shapes which reduces their streamwise extent and increases the spanwise width.

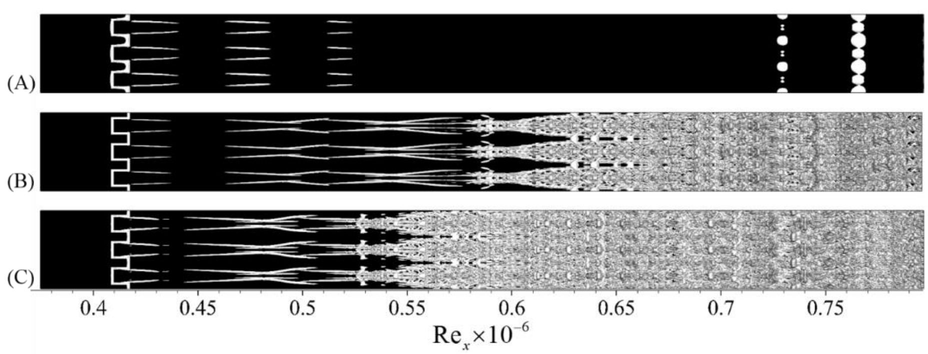

Figure 7-20. Iso-surface of instantaneous normalized Q - criterion (Q = 0.01) at different velocity ratios. Velocity ratio of (A) 0.05, (B) 0.10 and (C) 0.14.

The streaklines depicted in Figure 7-21 show that the $\gamma = 0.05$ case loses its wavy nature and the low-speed streaklines keep getting thinner downstream. The two-dimensional nature of these structures can be seen in the wall pressure contours shown in Figure 7-22. The wall pressure grows in strength in streamwise direction but decreases spanwise variation.

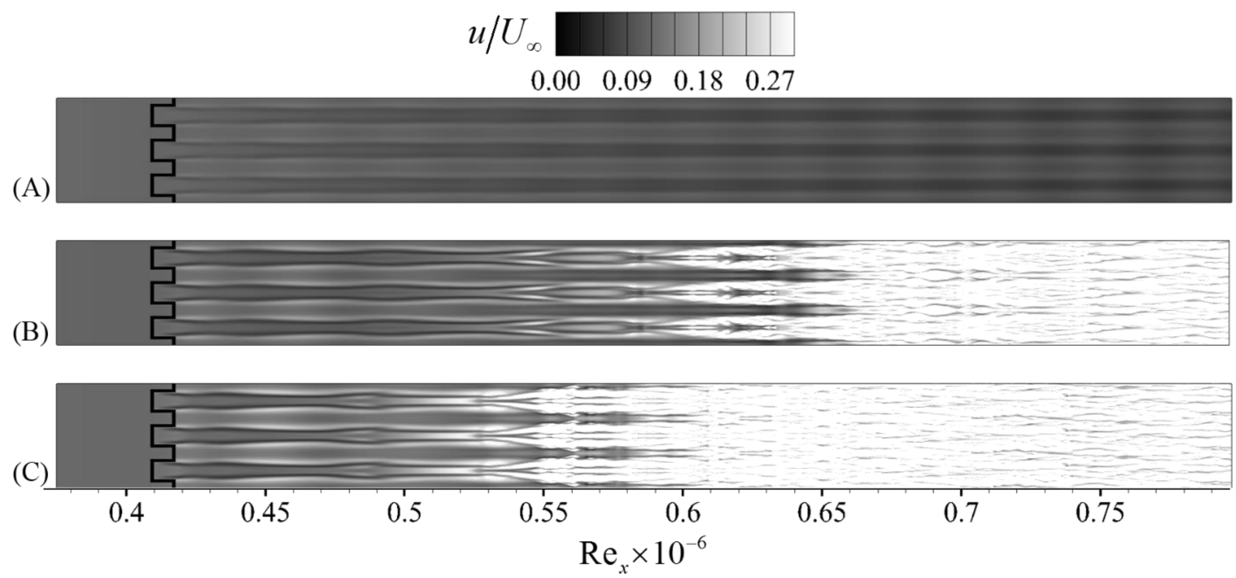

Figure 7-21. Instantaneous velocity streaklines at different velocity ratios. Velocity ratio of (A) 0.05, (B) 0.10 and (C) 0.14.

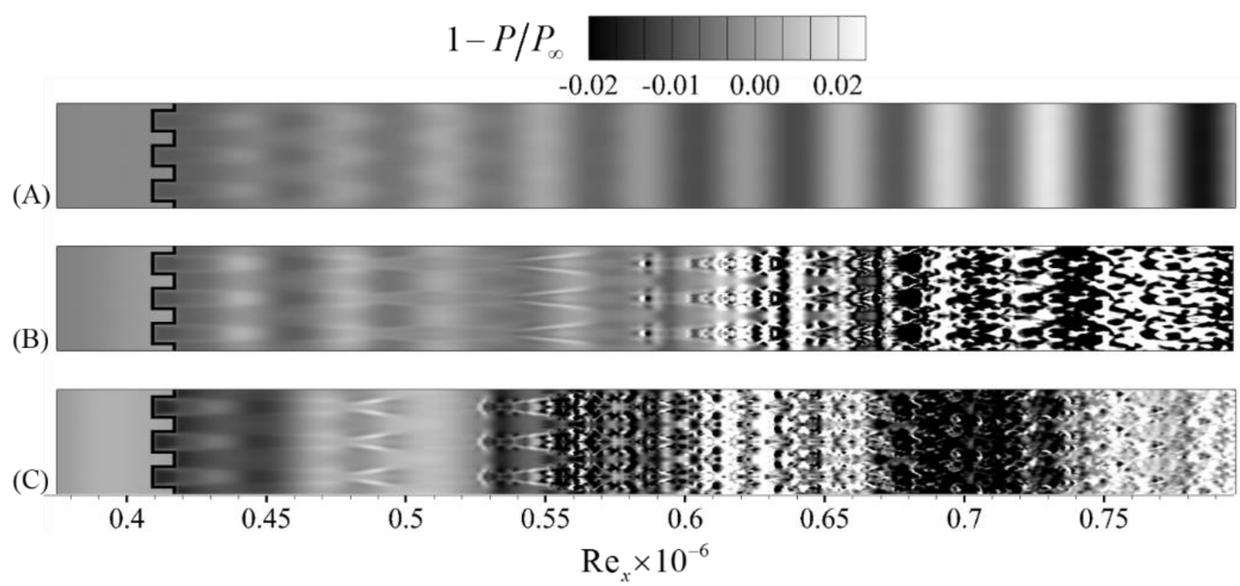

Figure 7-22. Instantaneous wall pressure at different velocity ratios. Velocity ratio of (A) 0.05, (B) 0.10 and (C) 0.14.

7.4.2 Turbulent Statistics

The mean velocity profiles at different Re_x locations are plotted in Figure 7-23. The gradual decrease in friction velocity keeps increasing the maximum U^+ for the $\gamma = 0.05$ case and the flow remains laminar for the entire domain. The short transition region for the $\gamma = 0.14$ case shows that the flow shows a fully developed turbulent profile at $Re_\theta = 6.95\times10^5$.

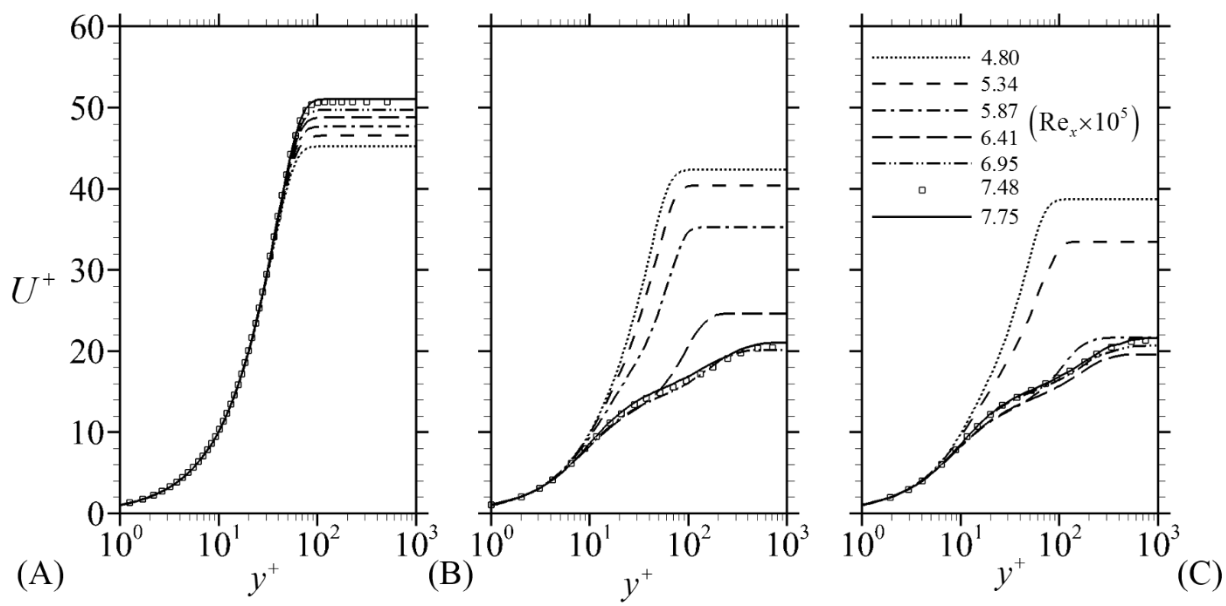

Figure 7-23. Time and span averaged mean velocity profile variation with inner coordinates scaled with wall parameters at different Re_x. Velocity ratio of (A) 0.05, (B) 0.10 and (C) 0.14.

To determine the location where the transition ends skin friction variation is plotted in Figure 7-24. Due to similar behavior between the $\gamma = 0.10$ and 0.14 cases, the skin friction collapses to similar values when plotted against Re_x. The $\gamma = 0.05$ shows a laminar profile throughout the domain without any deviation. Although the skin friction shows an overshoot for the $\gamma = 0.10$ and 0.14 cases it finally matches with the fully developed turbulent profile. The integral quantities shown in Figure 7-25 also provide similar observations.

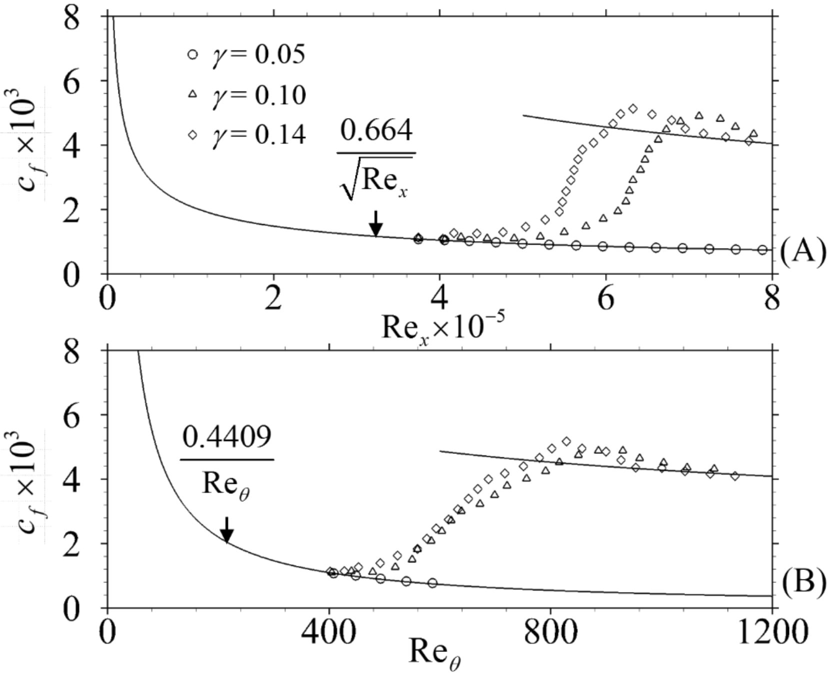

Figure 7-24. Variation of skin friction at different velocity ratios. Variation of skin friction with (A) Re_x and (B) Re_θ. Turbulent skin friction is compared to published data [209].

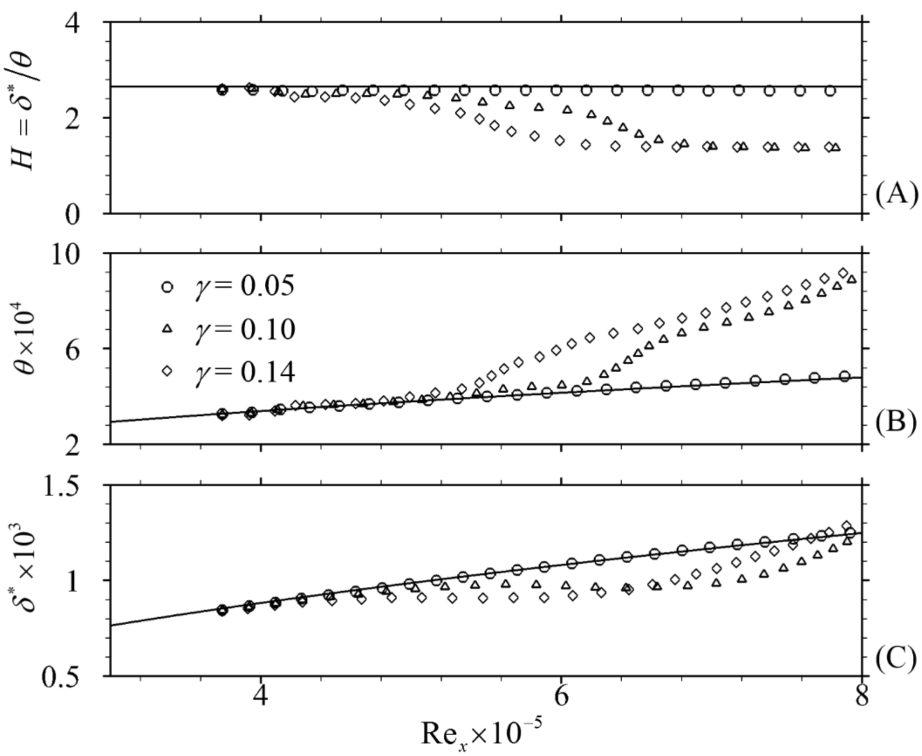

Figure 7-25. Variation of integral quantities with Reynolds number for different velocity ratios. (A) Shape factor, (B) momentum thickness and (C) displacement thickness. The solid line represents the laminar solution.

The velocity fluctuations shown in Figure 7-26 are relatively similar in behavior for the higher velocity ratio cases. The spanwise fluctuations for the $\gamma = 0.05$ case show two peaks. Also, while the streamwise and wall-normal fluctuations steadily grow in magnitude, the spanwise fluctuations first drop abruptly and then start gradually increasing. This behavior of dual peaks has been reported to be an optimal initial perturbation in spanwise direction for the wavenumber at maximum amplification [230]. Therefore, due to the gradual increase in perturbation in the downstream region along with the optimal perturbation behavior, it can be concluded that the flow will turbulize at a further downstream location.

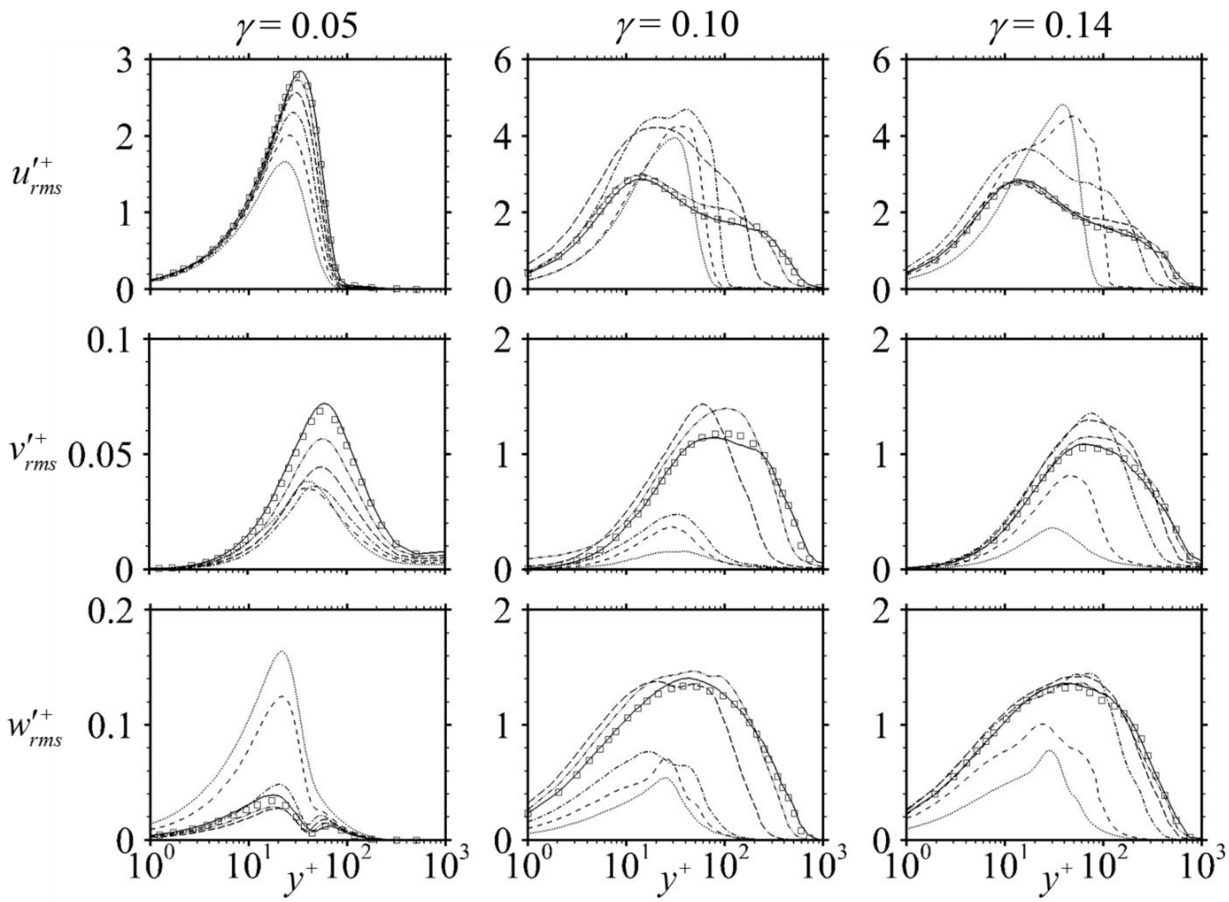

Figure 7-26. Variation of wall-scaled RMS velocity fluctuations with inner coordinates at different Re_x values. Please refer to Figure 7-23 for line legend.

The growth parameter is depicted in Figure 7-27. The variation of growth parameter for the streamwise oscillations shows that the growth rates gradually increase as velocity ratio increases. After the initial increase in spanwise fluctuation growth parameter for $\gamma = 0.05$ at the actuator location, the growth parameter reaches a maximum around $Re_\theta \approx 470$ and then starts dropping until $Re_\theta \approx 540$. Finally, the growth parameter shows a gradual increase. This behavior was not found in the transitional region for any of the other cases wherein, the spanwise growth parameter either monotonically increased or decreased after the actuator location. The second jump seen in the growth parameter for $\gamma = 0.10$ corresponds to the final transitional stage where the skin friction abruptly rises.

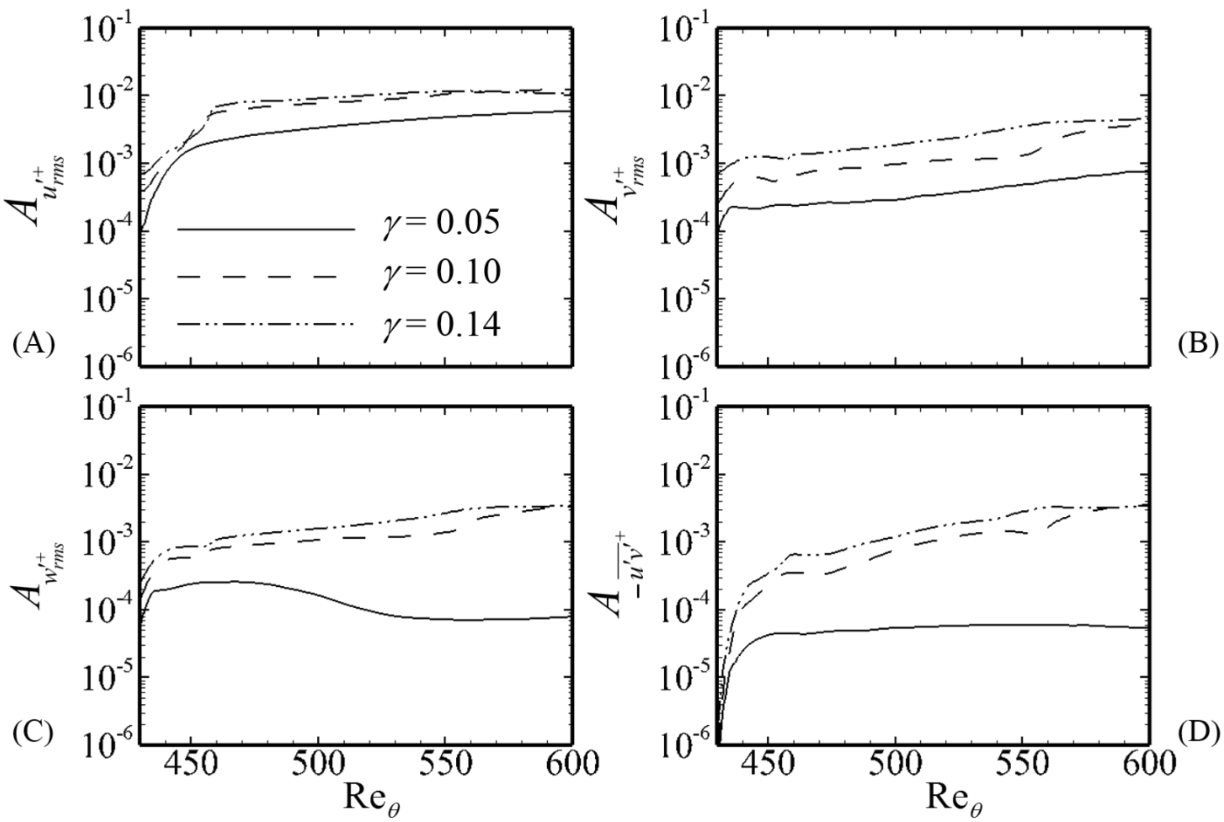

Figure 7-27. Variation of growth parameter for fluctuations and Reynolds stress with Re_θ. Growth parameter of (A) streamwise, (B) wall-normal and (C) spanwise RMS fluctuations and (D) Reynolds shear stress.

7.5 Thermal Effects

Although SDBD actuators operate in the cold plasma regime, the surface of the dielectric material gets heated up [94], [231], [232]. Temperatures have been shown to reach up to 200 °C for some dielectrics [232]. A lot of factors impact the surface temperature including operating voltage, frequency, and dielectric material. IR measurements on comb serpentine actuators showed temperatures of around 50 °C at locations with high plasma concentration [94]. Therefore, the impact of actuator temperature on the transitional flow was investigated using an approximate heating element applied as a thermal boundary condition. This analysis was done using the fine mesh given in Table 6-1. Three temperatures were tested with the actuator temperature T_A shown in Figure 7-28 at 273 K, 323 K and 373 K. The heating element is applied as a boundary condition only in the pinch location since it has the maximum concentration of plasma. The temperature is uniform across the square heating element and it spans a wall-scaled distance of 252 units in streamwise and spanwise direction with the center coinciding with the pinch region center.

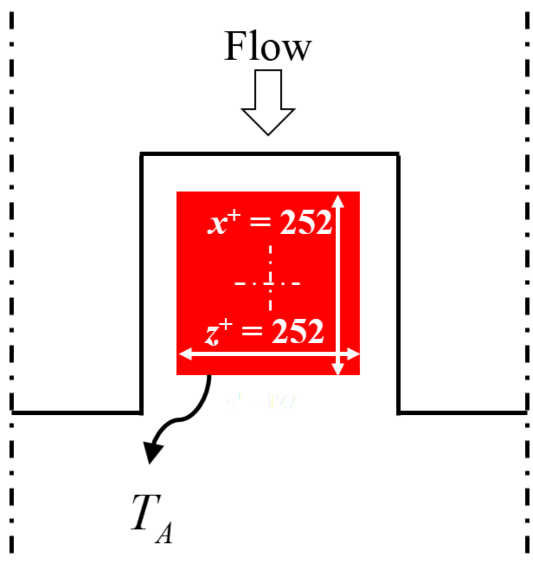

Figure 7-28. Schematic of the heating element applied at the pinch location of the actuator.

7.5.1 Instantaneous Flow Field

The heating element does not show a significant impact on the flow field for the current Mach number. This can be observed in the Q – criterion plotted in Figure 7-29. Only local effects can be seen at the actuator location. However, at the later stages of transition, the structures have different behavior as shown in Figure 7-30. Adding heat lifts the hairpin structures formed at the later stages of transition further away from the wall. The vortical structures are almost indistinguishable up to $\mathrm{Re}_x \approx 5.9\times10^5$ and then the differences start appearing. Since the hairpin structures are more lifted at higher temperatures, they tend to break down faster as observed in the velocity streaklines shown in Figure 7-31. It should be noted that since the flow regime is weakly compressible, the temperature effects might not be affecting the flow in the transitional region where the temperature effects have not amplified enough to be observed. Wall heating is known to significantly impact the streamwise vortical structures as well as flow instability [233], [234]. However, these studies involve uniform or non-uniform heating of the entire plate. The effect of localized heating is observed in supersonic flows [235] where it can create localized shocks which interact and manipulate the boundary layer.

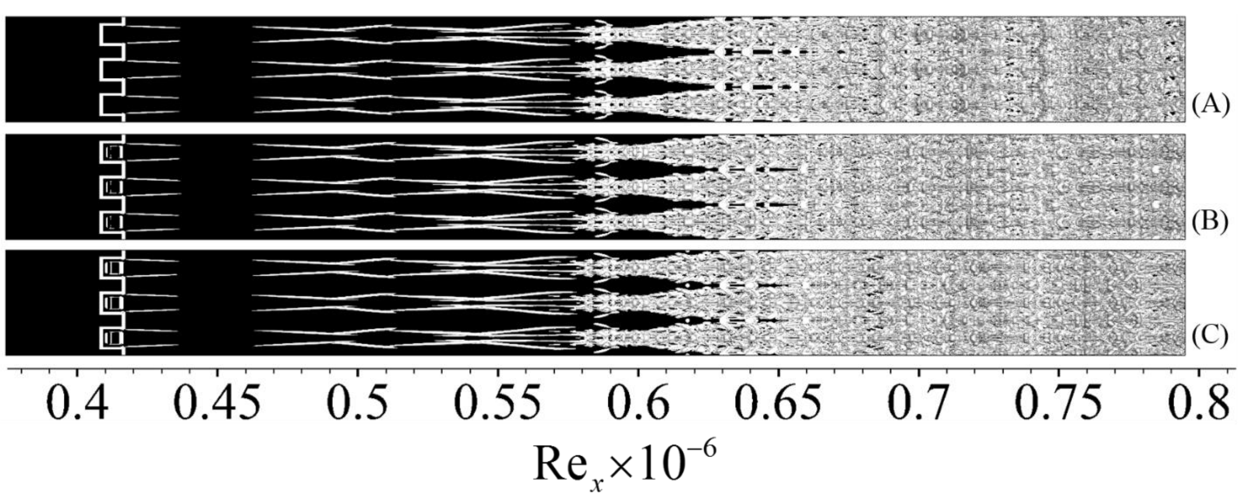

Figure 7-29. Instantaneous normalized Q – criterion for different heating element temperatures. The temperature of the heating element at (A) 273 K, (B) 323 K and (C) 373 K.

The impact of temperature on the velocity streaklines at $y^+ = 10$ plane is shown in Figure 7-31. Although no discernable difference is seen in the transitional region, large differences are observed for the turbulent region. At higher temperatures, the streaklines in the region $Re_x \approx 7\times10^5$ to 7.7×10^5 appear to have broken down into smaller structures with higher spanwise wavenumbers. Therefore, even though the temperature has an insignificant impact on the transitional region, it does impact the flow structures in the turbulent region. The high temperatures of the heating element dissipate over the transitional region and reach similar magnitudes in the turbulent region for all the cases as shown in Figure 7-32.

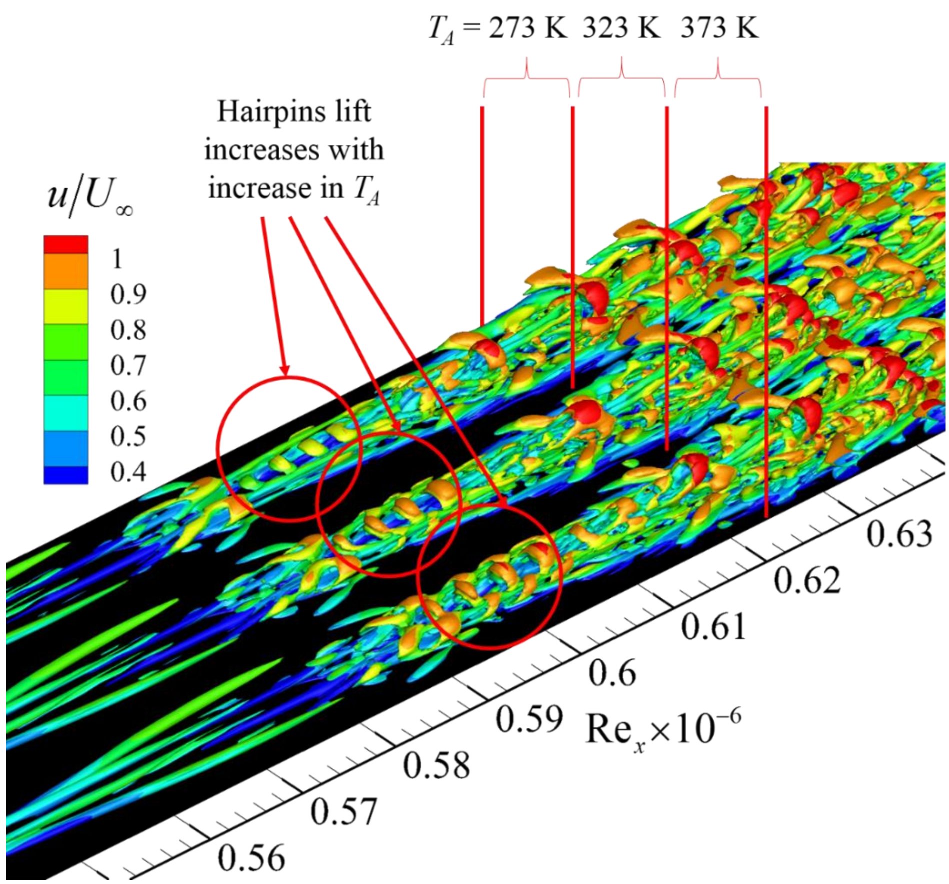

Figure 7-30. Instantaneous normalized Q – criterion for different heating element temperatures at later stages of transition. The regions between the vertical red lines mark the region for each case.

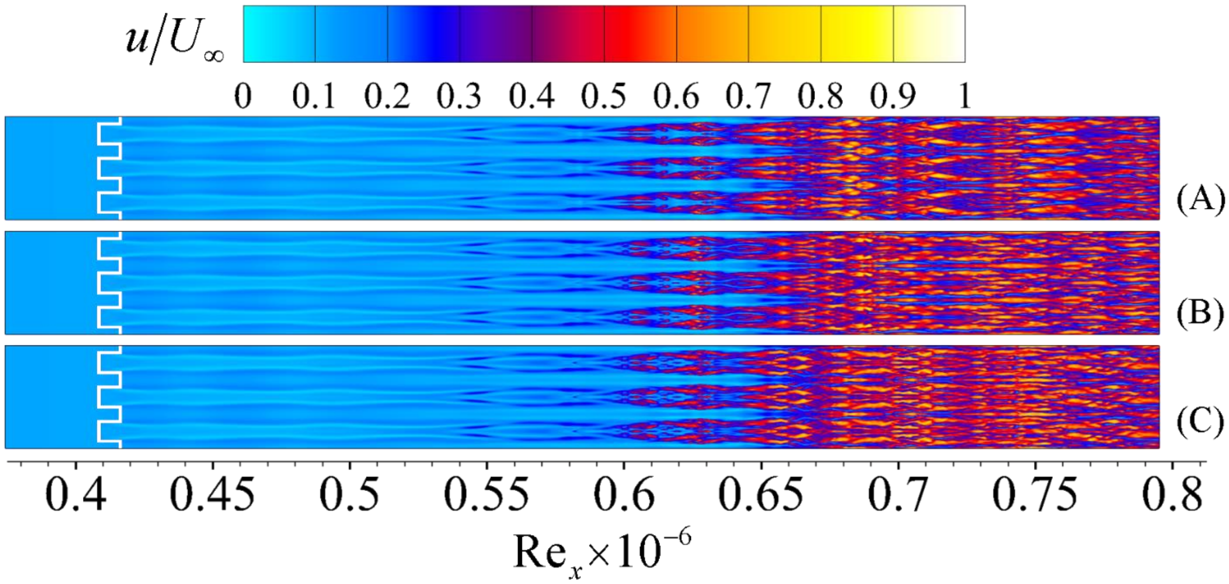

Figure 7-31. Instantaneous velocity streaklines for different heating element temperatures at y^+ = 10. The temperature of the heating element at (A) 273 K, (B) 323 K and (C) 373 K.

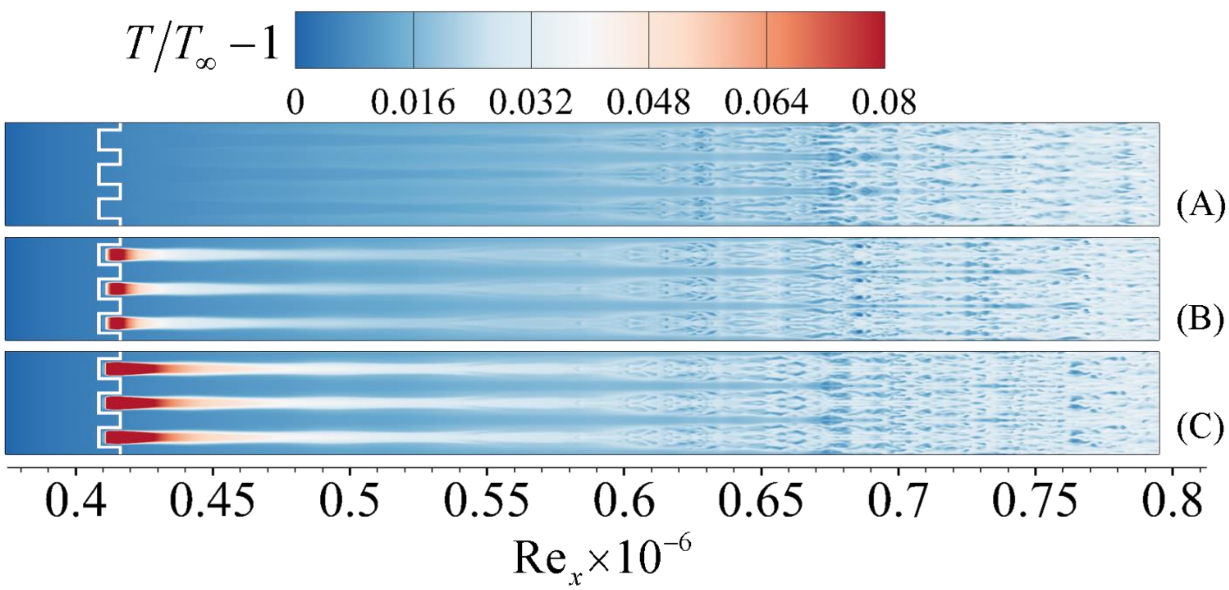

Figure 7-32. Instantaneous temperature contours for different heating element temperatures at y^+ = 10. The temperature of the heating element at (A) 273 K, (B) 323 K and (C) 373 K.

7.5.2 Turbulent Statistics

To assess the impact of the heating element, mean flow properties, as well as fluctuation profiles, are investigated. Lee et al. [234] showed that uniform wall heating reduced skin friction by almost 26%. This behavior was however not observed for localized wall heating as shown in Figure 7-33. The impact is mainly in the later stages of transition as observed in Figure 7-30. The mean velocity profiles are compared for the three temperature cases at the later transitional region in Figure 7-34. The heating element shows no impact on the mean velocity at Re_θ = 700 as well as in the fully developed turbulent region (Re_θ = 1000). The variations due to heating are observed in the log layer due to differences in friction velocity at Re_θ = 775 and 850. Since this difference is over a very small region, the impact on the overall flow remains insignificant.

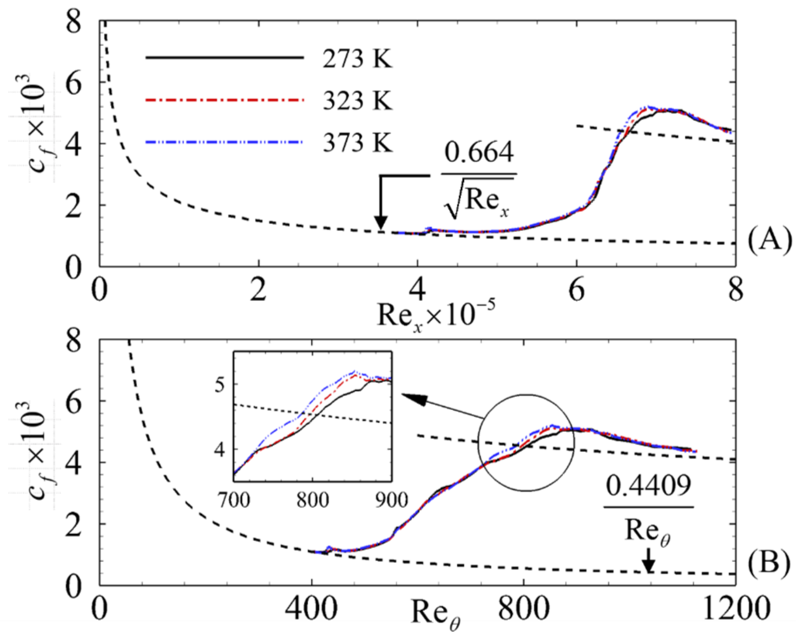

Figure 7-33. Variation of skin friction at different heating element temperatures. Variation of skin friction with (A) Re_x and (B) Re_θ. Turbulent skin friction is compared to published data [209].

The temperature profiles are shown in Figure 7-35. Overall temperature variations (~ 3%) are negligible since the flow is weakly compressible. The effect of localized wall heating increases the wall temperature for the entire domain. Interestingly, wall temperature of the 323 K case slowly deviates from the 273 K case and gets aligned with the 373 K case. The variations in the log layer dissipate due to mixing as Re_θ increases and the variations only remain in $y^+ < 10$.

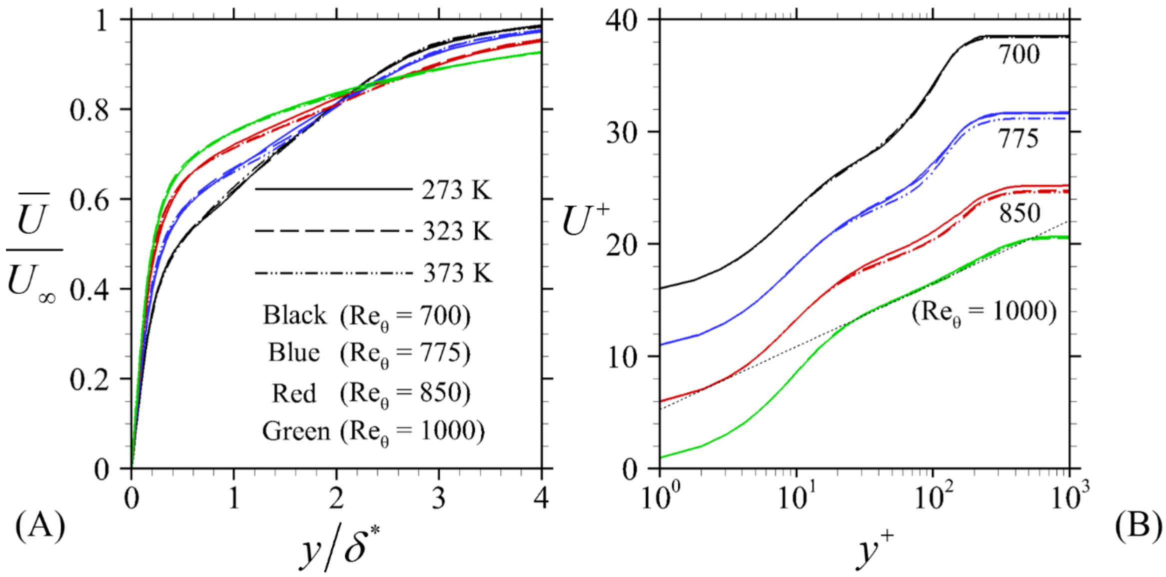

Figure 7-34. Variation of mean velocity profiles for different heating element temperatures and Reynolds numbers. Variation of (A) mean velocity with outer coordinates and (B) wall-scaled mean velocity (velocities are successively shifted by 5 units, with the green curves at the right scale) with inner coordinates.

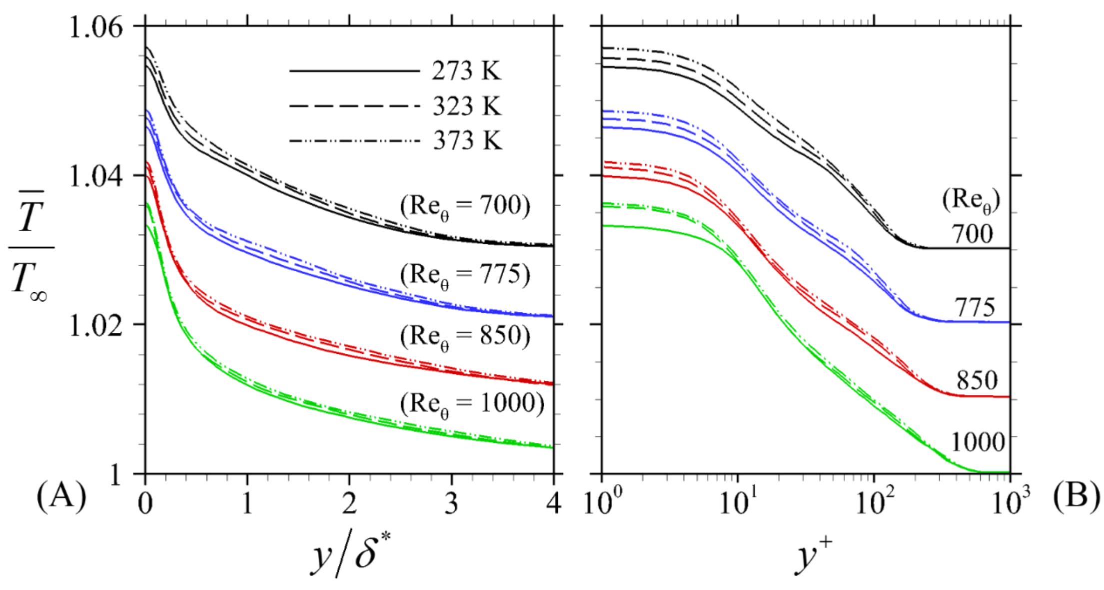

Figure 7-35. Variation of mean temperature profiles at different heating element temperatures and Reynolds numbers. Variation of mean temperature (A) with outer coordinates and (B) inner coordinates. The temperatures are successively shifted by 0.01 units for better depiction, with the green curves at the right scale.

The comparisons of the fluctuating components and Reynolds shear stress at the later stages of transition are depicted in Figure 7-36. The streamwise fluctuating components show almost insignificant impact due to localized heating. However, significant differences are observed for wall-normal and spanwise fluctuations. The maximum impact due to heating is on the Reynolds shear stress where the curves shift more towards the wall. This indicates better mixing and transfer of energy from the inner region to the outer region of the boundary layer.

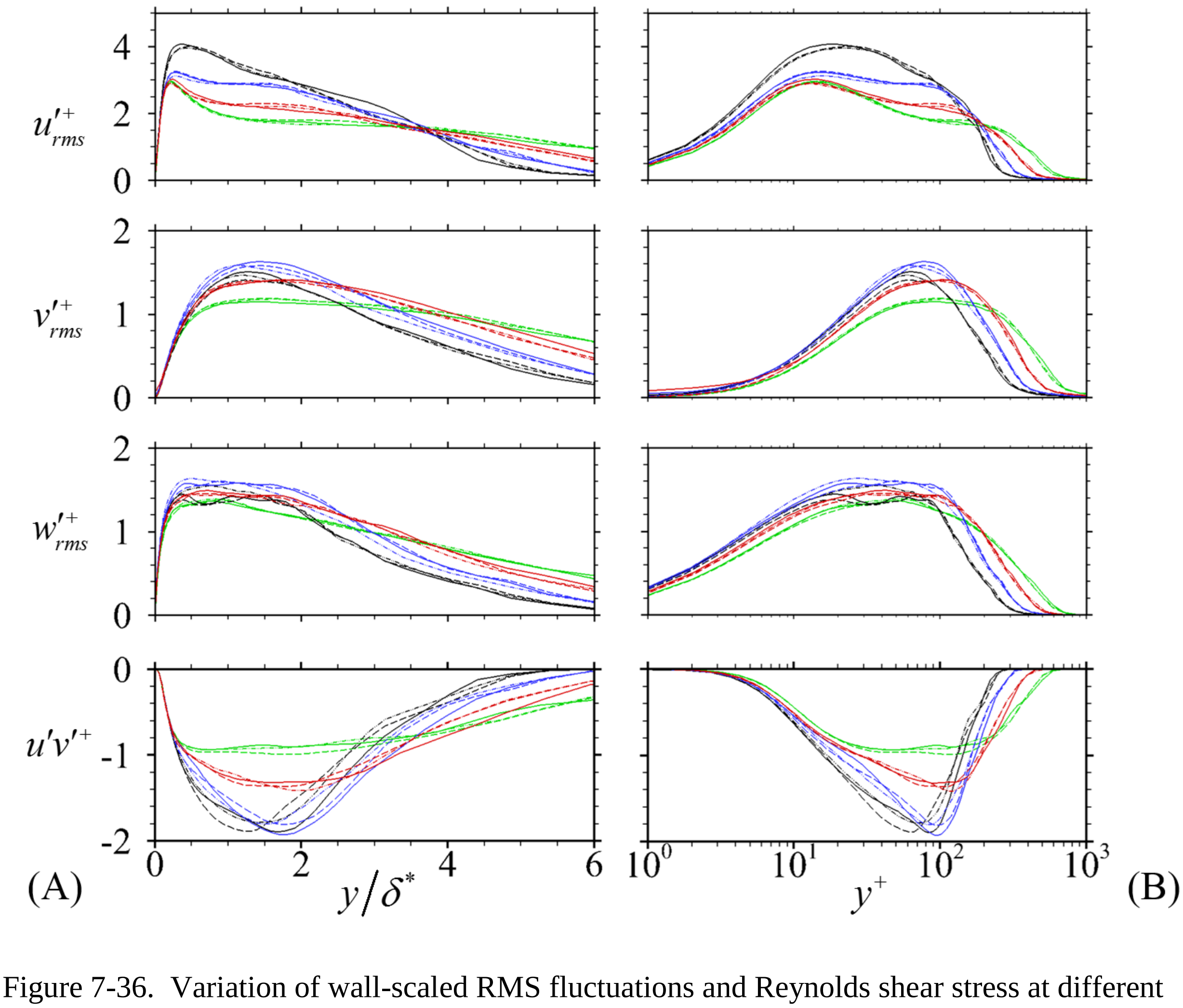

Figure 7-36. Variation of wall-scaled RMS fluctuations and Reynolds shear stress at different heating element temperatures and Reynolds number. Variation of wall-scaled RMS fluctuations and Reynolds shear stress with (A) outer coordinates and (B) inner coordinates. Please refer to Figure 7-34 for line legend.

The growth parameter in Figure 7-37 shows small variations in the wall-normal growth. These variations are absent in the streamwise, spanwise and Reynolds shear stress growth parameter. The impact on the difference in growth of Reynolds shear stress is not evident here since the Reynolds shear stress only shifts towards the wall. However, the changes seen in the growth of wall-normal fluctuations impact the Reynolds stress as seen in Figure 7-36.

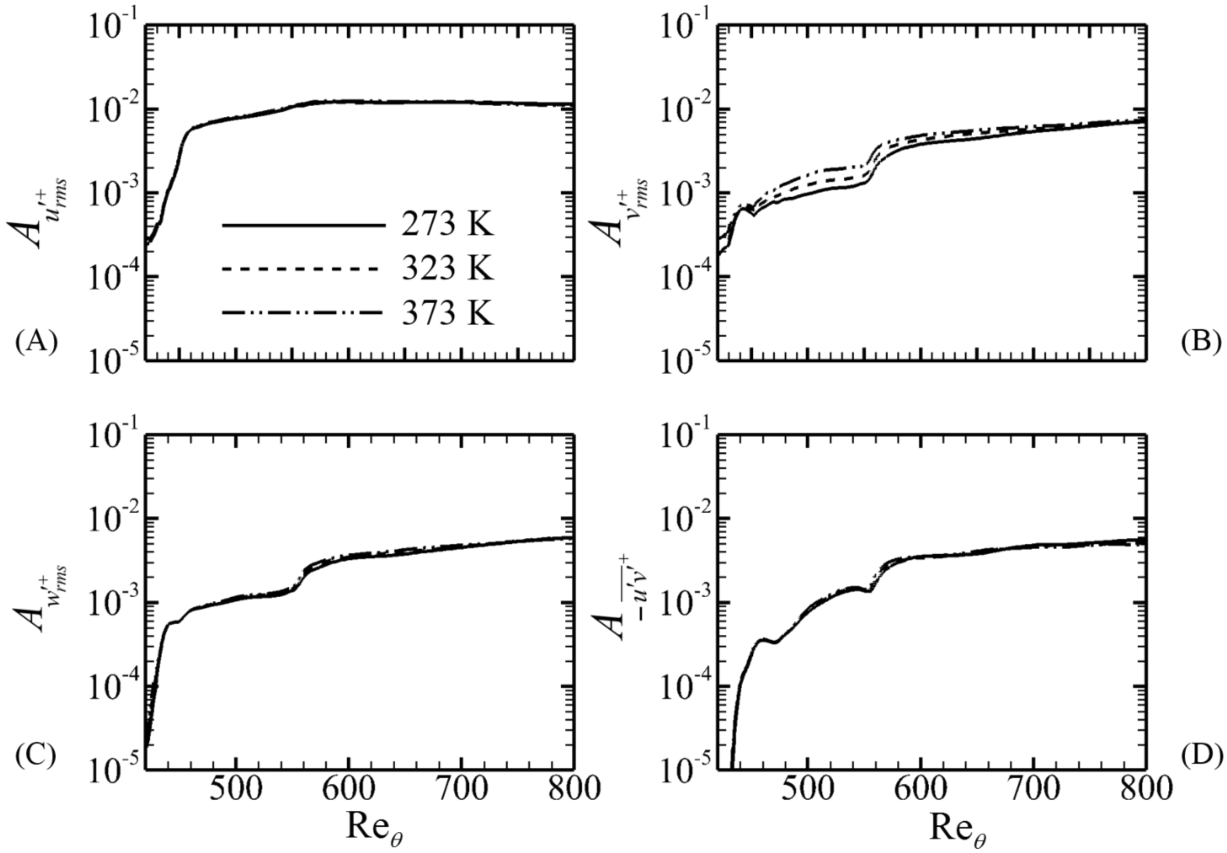

Figure 7-37. Variation of wall-scaled RMS fluctuations and Reynolds shear stress growth parameter with Reynolds number for different heating element temperatures. Growth parameter of (A) streamwise, (B) wall-normal and (C) spanwise RMS fluctuations and (D) Reynolds shear stress.

CHAPTER 8
COLLOCATION OF ACTUATORS

8.1 Background

Most plasma flow control applications involve a single actuator or an array of actuators being placed along the spanwise direction [80], [236], [237]. Experimental study on the impact of actuators placed with streamwise separation has also shown a delay in transition [214], [238]. Grundmann and Tropea [214] used two sets of steady operating plasma actuators to damp TS waves created by a plasma actuator acting as a tripping mechanism. They showed a reduction in freestream disturbances by almost 50%. They further studied the impact of pulsed actuation on TS waves [238] and found similar reduction using only 12% of the power consumed compared to the steady operation. Barckmann et al. [239] used four sets of cascaded arrays of spanwise oriented actuators along the streamwise direction. They showed the capability of using these actuators to actively energize the streamwise streaks. The approach here involves, the use of a pair of square serpentine actuators to manipulate the laminar flow to delay or advance the transition to turbulence. Plasma actuators can be operated in both co-flow and counter-flow orientations, where the latter has been shown to always increase the TS wave amplitudes [240]. Therefore, effects of actuator orientations, as well as locations, are investigated.

8.2 Tripping Actuator Configurations

In order to operate the actuators in co-flow and counter-flow arrangement with the pinch plane at the center of the plate, the square serpentine actuators are setup as shown in Figure 8-1. Both the actuators are run with the same conditions of ω_0 = 1 kHz and γ = 0.10. All the flow field conditions are kept same as the conditions for the M = 0.5 square serpentine cases given in Chapter 6. The medium mesh case given in Table 6-1 is used to compare the co-flow and counter flow tripping configurations. These two configurations were tested to find whether they generate different vortical structures or have similar behavior. Since counter-flow configurations are known to be more unstable than their co-flow counterpart [240], it is expected that the flow will turbulize faster in the counter-flow arrangement.

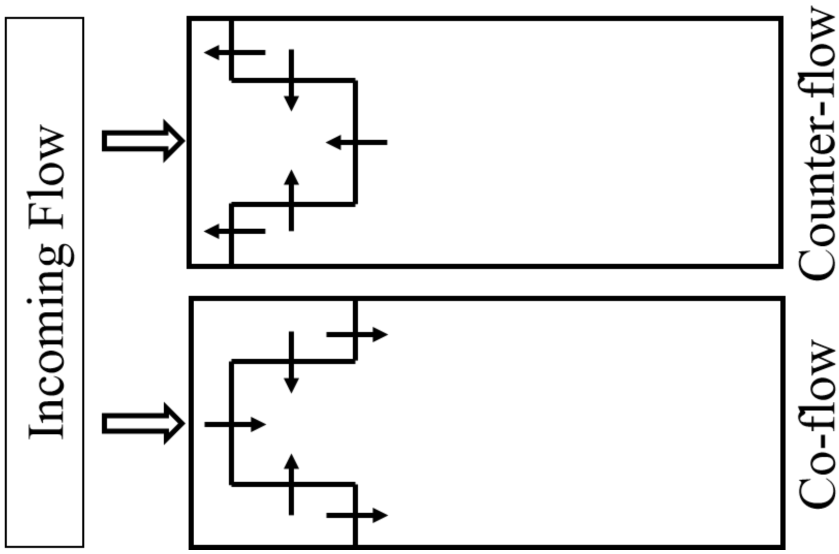

Figure 8-1. Schematic of actuators for co-flow and counter-flow orientations with arrows depicting force direction.

8.2.1 Impact on Instantaneous Flow Field

Looking at the instantaneous vortical structures shown by Q – criterion iso-surface in Figure 8-2, it is clear that both the arrangements create similar quasi-streamwise vortical structures. However, there are differences in strength of the vortices in the early stages of transition as well as the shape of structures in the later stages of transition between the counter-flow and co-flow arrangement. The structures formed in the early stages of transition have longer relative streamwise extent for the counter-flow arrangement since the vortices are stronger and do not dissipate as quickly as the co-flow case. Since the later stages of transition are highly nonlinear and dependent on the forcing mechanism, large differences in flow structures are observed in the Q – criterion iso-surface depicted in Figure 8-3. It shows that the hairpin structures are formed early ($Re_x \approx 5.35\times10^5$) for the counter-flow case. The two configurations show similar behavior after $Re_x \approx 6.1\times10^5$.

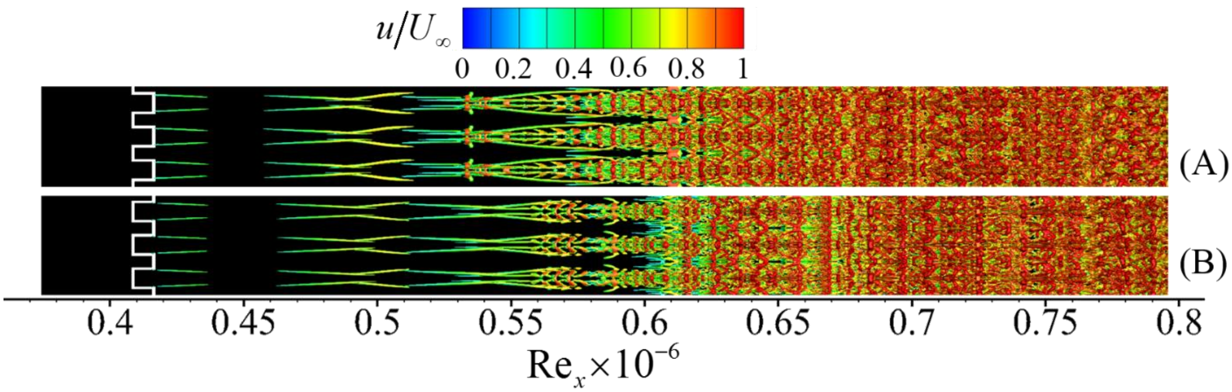

Figure 8-2. Instantaneous normalized Q – criterion (Q = 0.1) iso-surface colored with streamwise velocity. Actuator in (A) counter-flow and (B) co-flow arrangement.

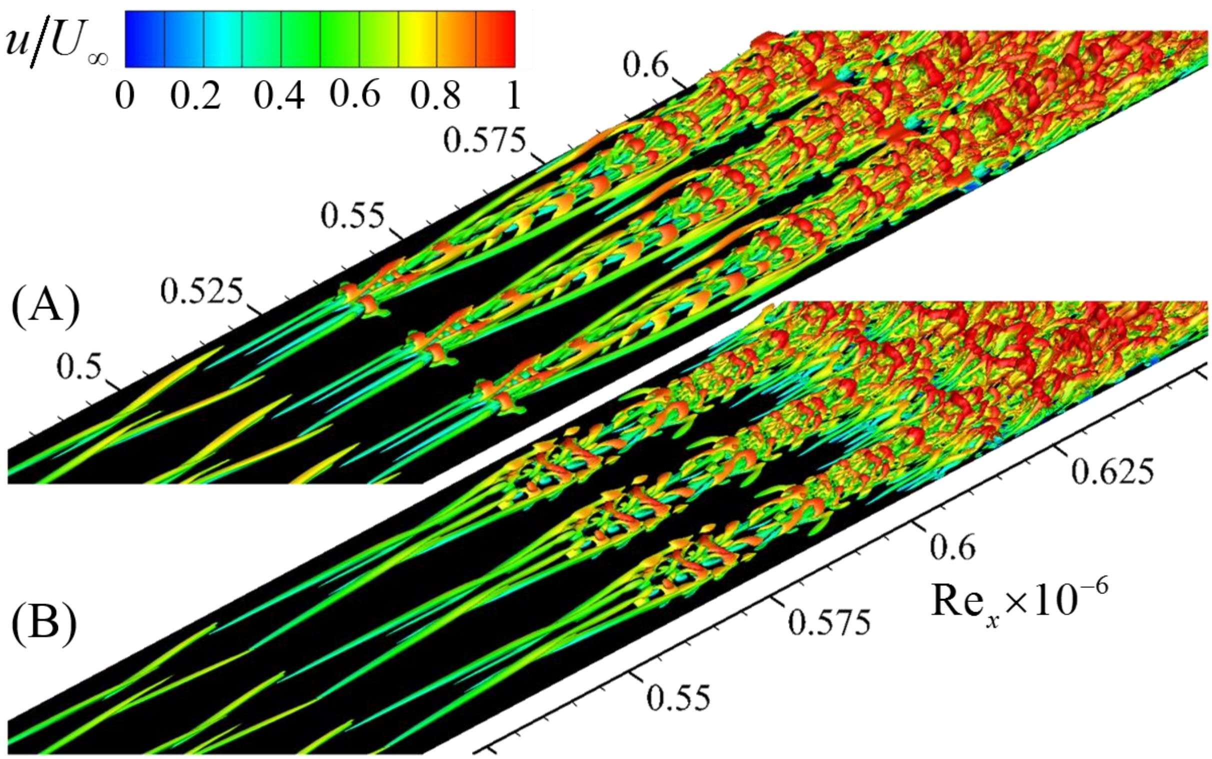

Figure 8-3. Instantaneous normalized Q – criterion (Q = 0.1) iso-surface colored with streamwise velocity at the later stage of transitional region. Actuator in (A) counter-flow and (B) co-flow arrangement.

The streaklines shown in Figure 8-4 clearly depict the difference in strength of the streamwise vortices. The difference in value between the low-speed and high-speed streaklines is amplified for the counter-flow arrangement.

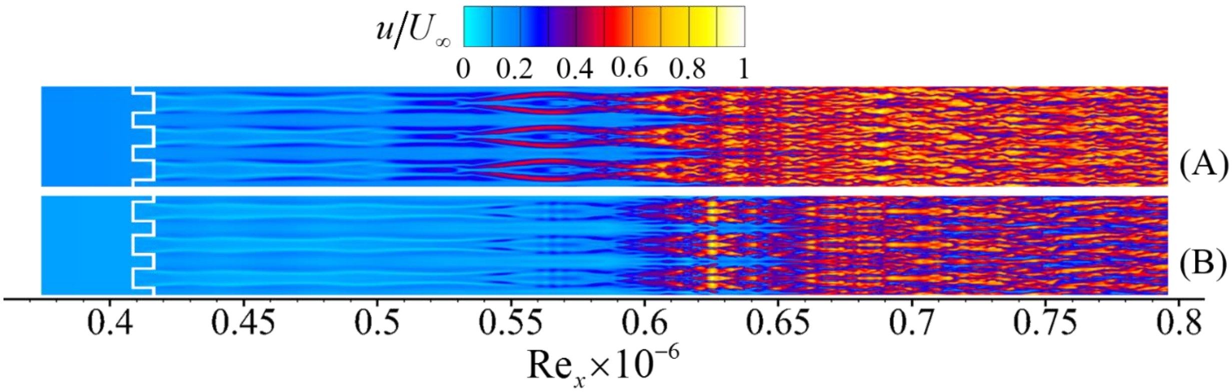

Figure 8-4. Instantaneous normalized streamwise velocity streaklines at $y^+ = 10$ plane. Actuator in (A) counter-flow and (B) co-flow arrangement.

8.2.2 Impact on Mean Flow

The skin friction comparison shown in Figure 8-5 shows minor differences between the two configurations. The counter-flow transitions at an earlier location but the difference is insignificant. Even the integral quantities shown in Figure 8-6 provide a similar picture of the transition location. The impact of configuration is negligible on the displacement thickness. However, compared to a laminar Blasius profile, the counter-flow arrangement increases the shape factor since it reduces the momentum in the boundary layer, while co-flow reduces shape factor due to increase in momentum. For the fully turbulent flow field, both arrangements reach a value of 1.38 for the shape factor. Looking at all the instantaneous structures and the integral quantities, it can be concluded that the counter-flow arrangement turbulizes the flow faster than the co-flow arrangement for the same input perturbation. However, both the arrangements have a similar footprint and exhibit transient growth, which is the property of oblique wave transition.

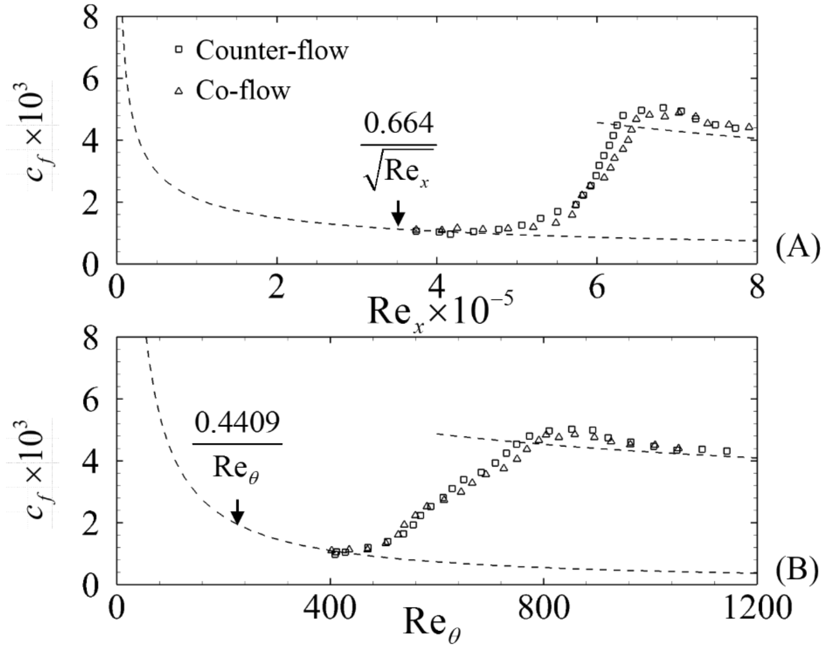

Figure 8-5. Variation of skin friction for different tripping actuator configuration. Variation of skin friction with (A) Re_x and (B) Re_θ. Turbulent skin friction is compared to published data [209].

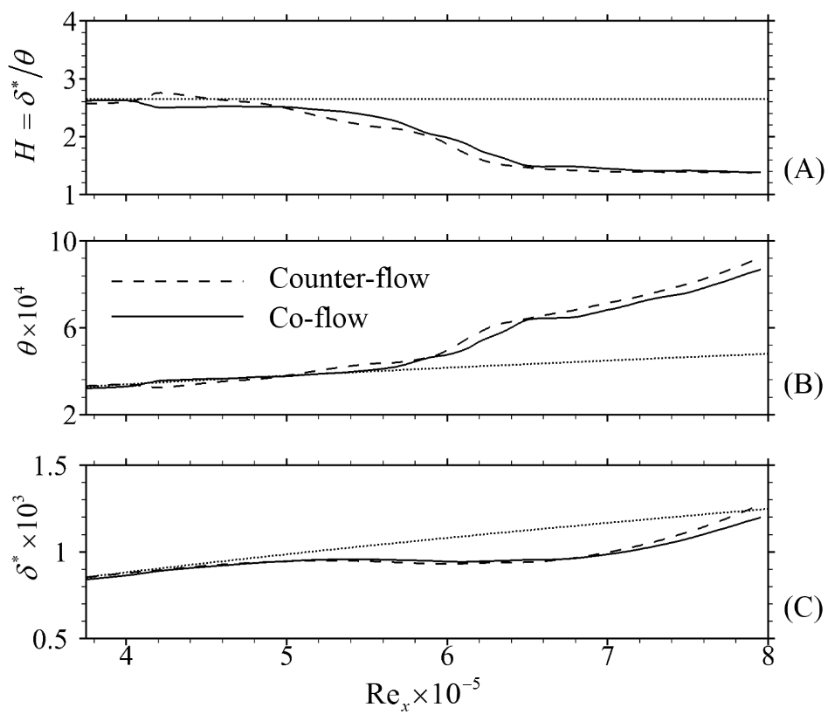

Figure 8-6. Variation of integral quantities with Reynolds number for different tripping actuator configuration. (A) Shape factor, (B) momentum thickness and (C) displacement thickness. The dotted line represents a laminar solution.

8.3 Actuator Collocation

Since counter-flow and co-flow arrangements of the tripping actuator do not fundamentally change the nature of the transition, from here on the co-flow arrangement will be used as the tripping actuator. A second actuator placed downstream of the tripping actuator is introduced and is called the control actuator. The control actuator is placed in different orientations and locations to investigate its impact on the transitional flow. The different control actuator orientations are shown in Figure 8-7. For cases A and D, the tripping and control actuators have the pinch location aligned with each other while for cases B and C, the control actuator has the spreading region aligned with the pinch region of the tripping actuator. Also for cases A and B the control actuator has a co-flow arrangement while for cases C and D, it has a counter-flow arrangement. The distance in wall units between the tripping and control actuator is given by L_A which has a value of 2500 for all the cases. For case B, three values of L_A are studied, viz., 2500, 5000 and 7500.

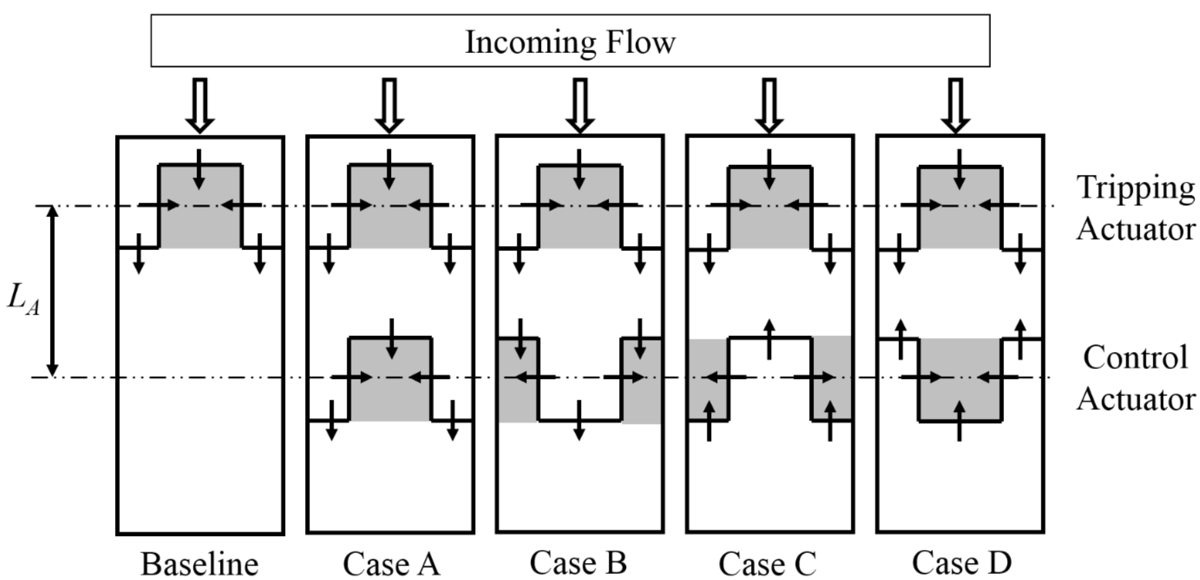

Figure 8-7. Schematic of various control actuator configurations showing the distance between the tripping and control actuator. The shaded grey regions are the pinching region of the actuators and the arrows show the actuator force direction.

In a generalized transitional flow, the turbulent low-speed streak locations are random. Serpentine actuators such as spanwise array actuators [80] can bundle the streaklines in a predictable arrangement, allowing a control actuator to selectively manipulate them. Therefore, it is assumed that the tripping actuator shown in Figure 8-7 will bundle the incoming random streaklines, which can then be manipulated by the control actuator to control transition.

8.3.1 Effect of Actuator Configuration

Instantaneous structures: To compare the impact of actuator orientation on the vortical structures, Q – criterion iso-surface is plotted in Figure 8-8. The control actuators placed in counter-flow arrangement are colored red. The control actuator is placed at L_A = 2500. For cases A and D, the pinch planes are aligned for the tripping and control actuator which causes the strengthening of vortical structures downstream of the control actuator. Since for case D, the control actuator is placed in a counter-flow arrangement, it has a higher impact on the structures than case A. However, as discussed earlier the difference in arrangement does not impact the solution significantly. Both case A and case D advance the transition to turbulence by adding energy to both the fundamental and subharmonic mode lambda vortices.

The maximum impact on the flow is observed for case B. Although case C shows a significant impact, it delays the transition by a similar amount as the cases A and D advance the transition as observed in Figure 8-8. Both cases B and C have the pinch location of the control actuator aligned with the spread location of the tripping actuator and vice versa. Unlike cases A and D, cases B and C reduce the strength of the fundamental lambda vortices but increase the strength of subharmonic vortices. The transition still occurs through the similar process described in Chapter 6 where the front ends of the subharmonic lambda vortices interact with the tail end of the lambda vortices to create the hairpin structures. However, irrespective of the control actuator orientation, the transitioning of the flow is still faster at the pinch plane versus the spread plane of the tripping actuator.

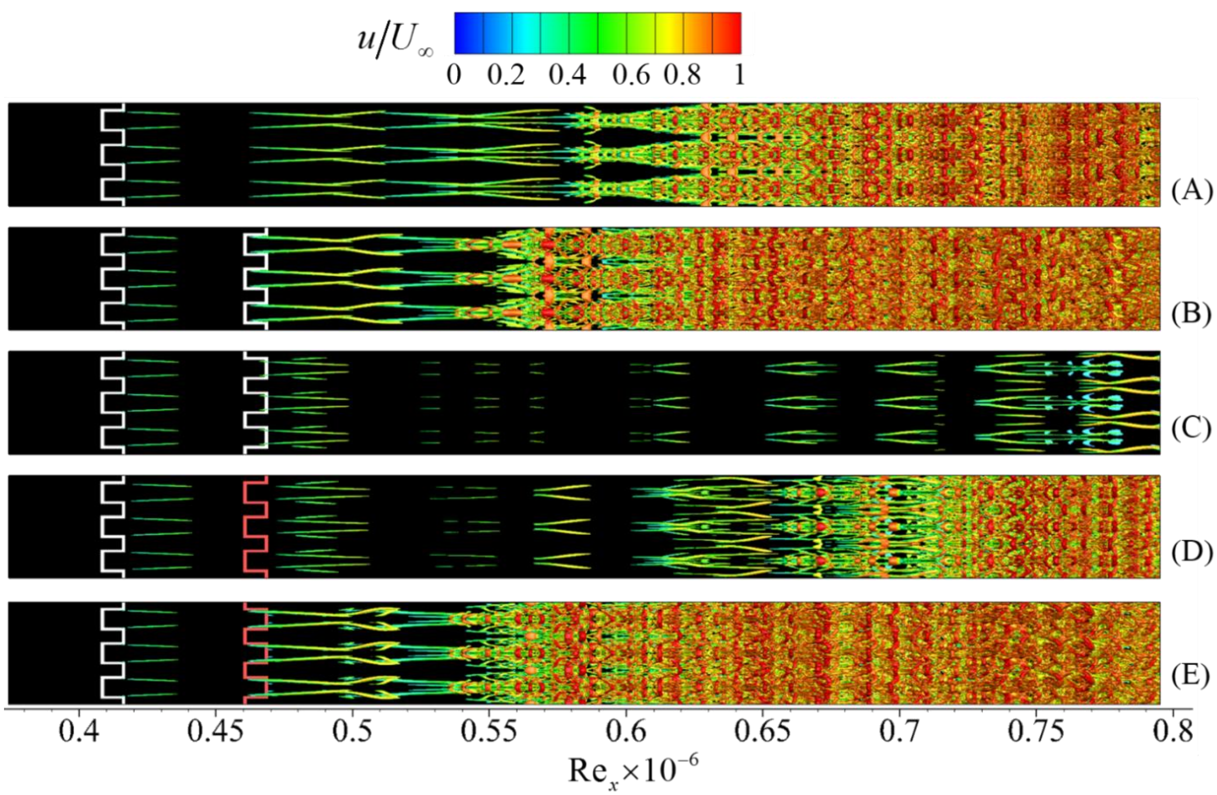

Figure 8-8. Instantaneous normalized Q – criterion (Q = 0.1) iso-surface colored with the normalized streamwise velocity with the control actuator placed at L_A = 2500. (A) Baseline, (B) case A, (C) case B, (D) case C and (E) case D. The counter-flow actuators are colored red and domain is duplicated three times.

The streamwise velocity contours for y^+ = 25 plane depicted in Figure 8-9 show the impact of control actuator on the spanwise and streamwise variation of streaklines. The counter-flow actuators are colored in white. For cases A and D, the region downstream of the pinch location of the tripping actuator remains at lower velocity (lower velocity streaklines) than the spread region (higher velocity streaklines) even after the application of the control actuator.

However, cases B and C show an additional low-speed streak which reduces the spanwise thickness of the low-velocity regions downstream of the pinch region for the tripping actuator. The wavy streak pattern representative of an oblique wave transition still governs the transition mechanism. At a higher *y* plane shown in Figure 8-10, the strengthened (darker gray) fundamental and subharmonic lambda vortices after the control actuator are clearly visible. For cases B and C, the lambda structures observed in the other case within the region $Re_x = 5\times10^5$ to 5.5×10^5, have increased in number but reduced in strength.

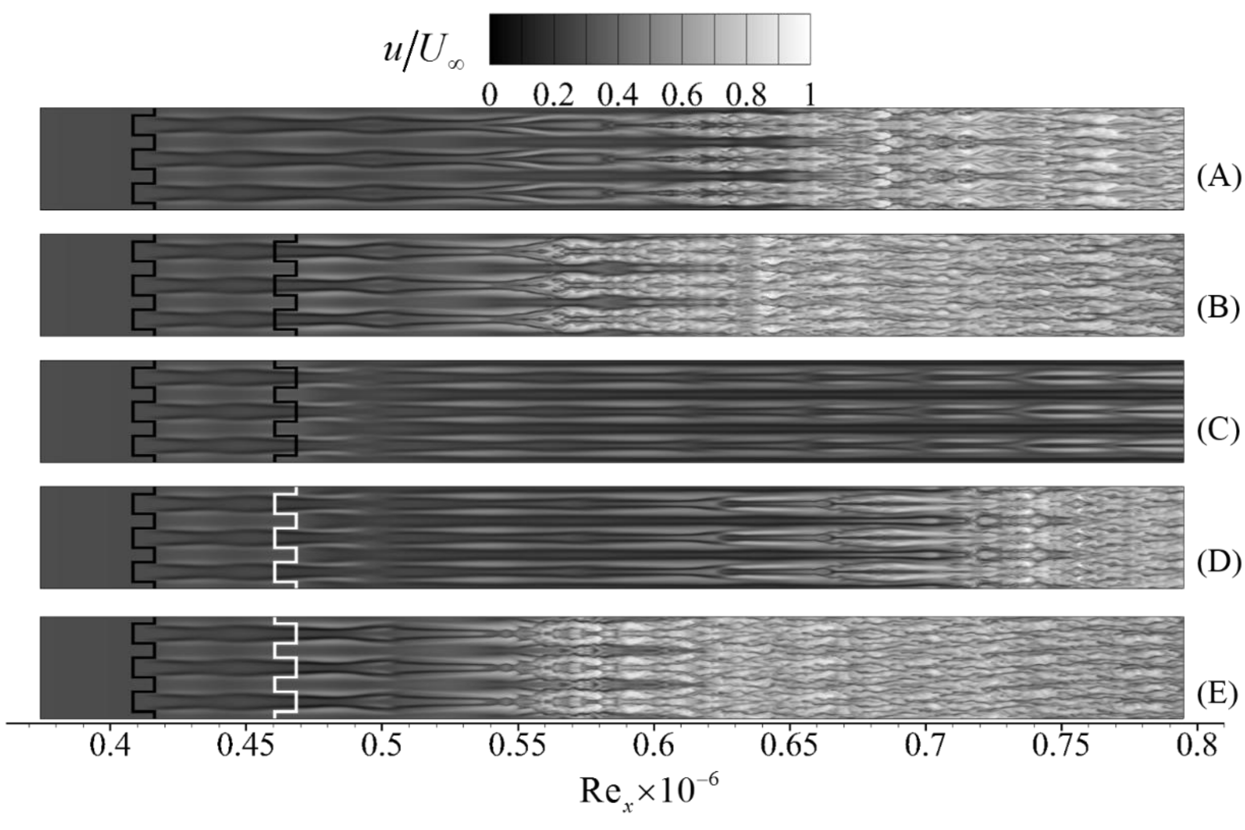

Figure 8-9. Instantaneous streamwise velocity with the control actuator placed at $L_A = 2500$ showing velocity streaklines at $y^+ = 25$. (A) Baseline, (B) case A, (C) case B, (D) case C and (E) case D. The counter-flow actuators are colored white.

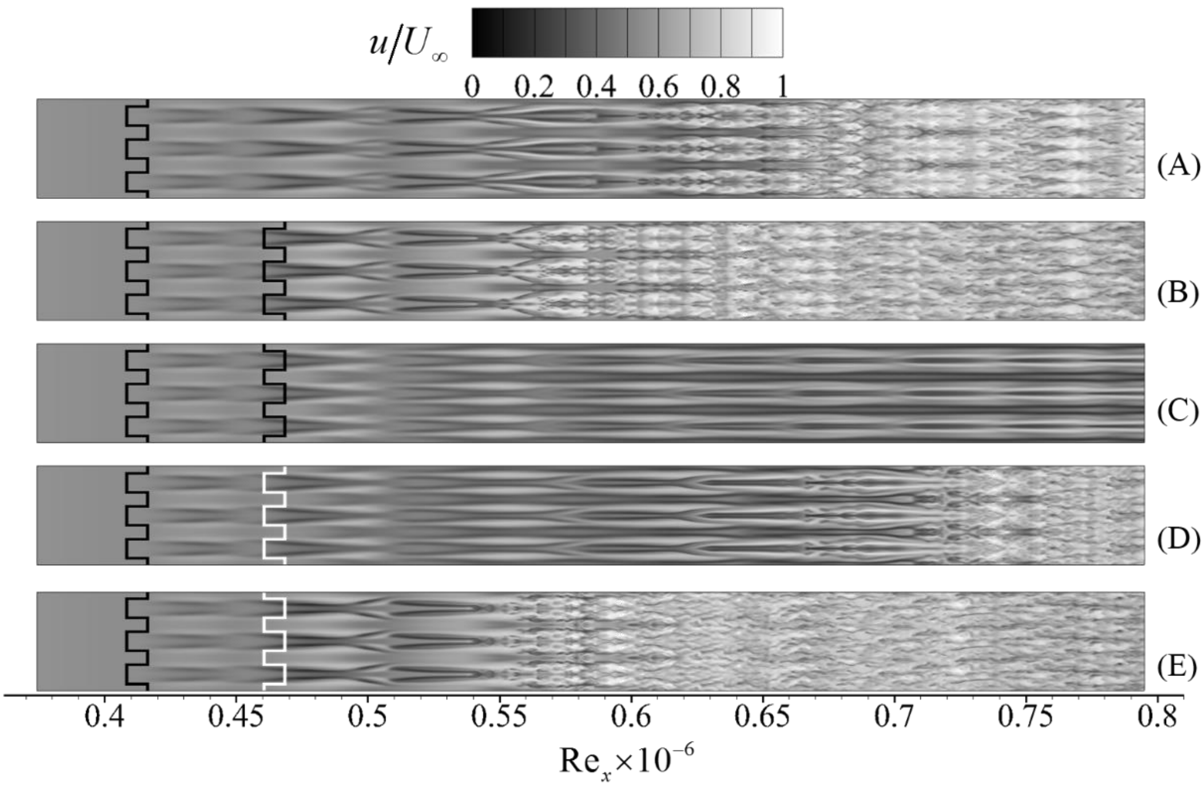

Figure 8-10. Instantaneous streamwise velocity with the control actuator placed at L_A = 2500 showing velocity streaklines at y^+ = 30. (A) Baseline, (B) case A, (C) case B, (D) case C and (E) case D. The counter-flow actuators are colored white.

The wall-normal and spanwise fluctuations depicted in Figure 8-11 and Figure 8-12 show that for case A and case D there is more turbulent mixing due to a significant increase in the spanwise fluctuations compared to the baseline case. For case B, the fluctuations are negligible in comparison and do not appear in the depicted range. For case A and D in Figure 8-11, the wall-normal fluctuations begin from $\mathrm{Re}_x \approx 5.4\times10^5$ and in Figure 8-12, the spanwise fluctuations begin from $\mathrm{Re}_x \approx 6.2\times10^5$. However, these two locations for baseline case are larger showing that the flow takes longer to become fully developed.

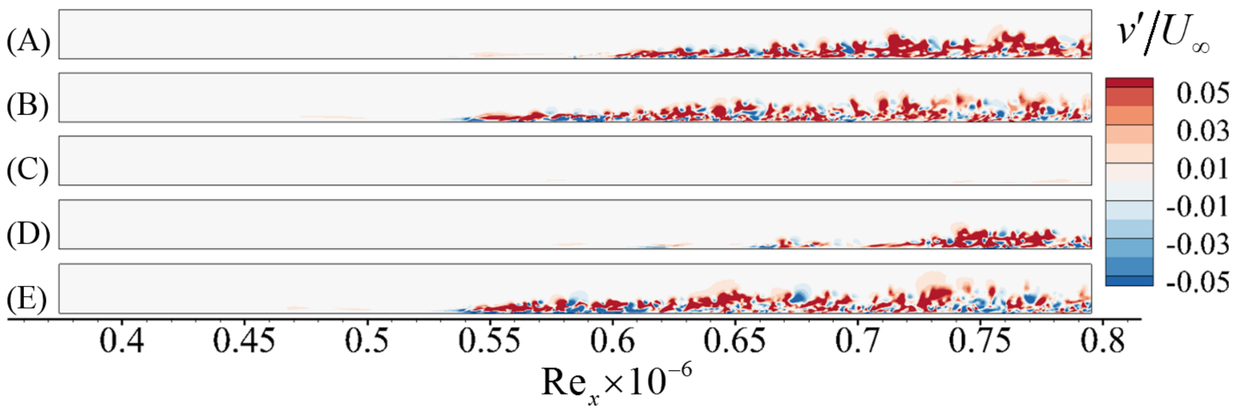

Figure 8-11. Instantaneous wall-normal fluctuating velocity contours at mid *z* plane with the control actuator placed at L_A = 2500. (A) Baseline, (B) case A, (C) case B, (D) case C and (E) case D.

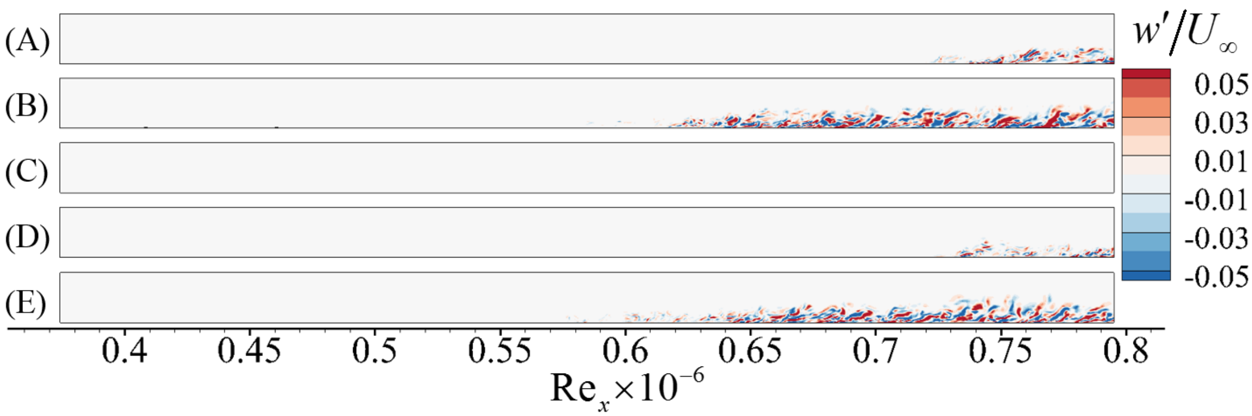

Figure 8-12. Instantaneous spanwise fluctuating velocity contours at mid *z* plane with the control actuator placed at L_A = 2500. (A) Baseline, (B) case A, (C) case B, (D) case C and (E) case D.

Turbulent statistics: The effect on transition location due to the actuator configuration is shown by the skin friction plots depicted in Figure 8-13. The transition location is highly dependent on the control actuator configuration. For cases A, C and D the difference in transition location compared to the baseline are similar when plotted against Re_x. Case B does not transition to fully developed turbulence. From Figure 8-13 (B), case A and D have similar skin friction as the baseline case for the same Re_θ values. Interestingly, all the cases show lower skin friction than the baseline case in the fully developed turbulence region after the skin friction overshoot.

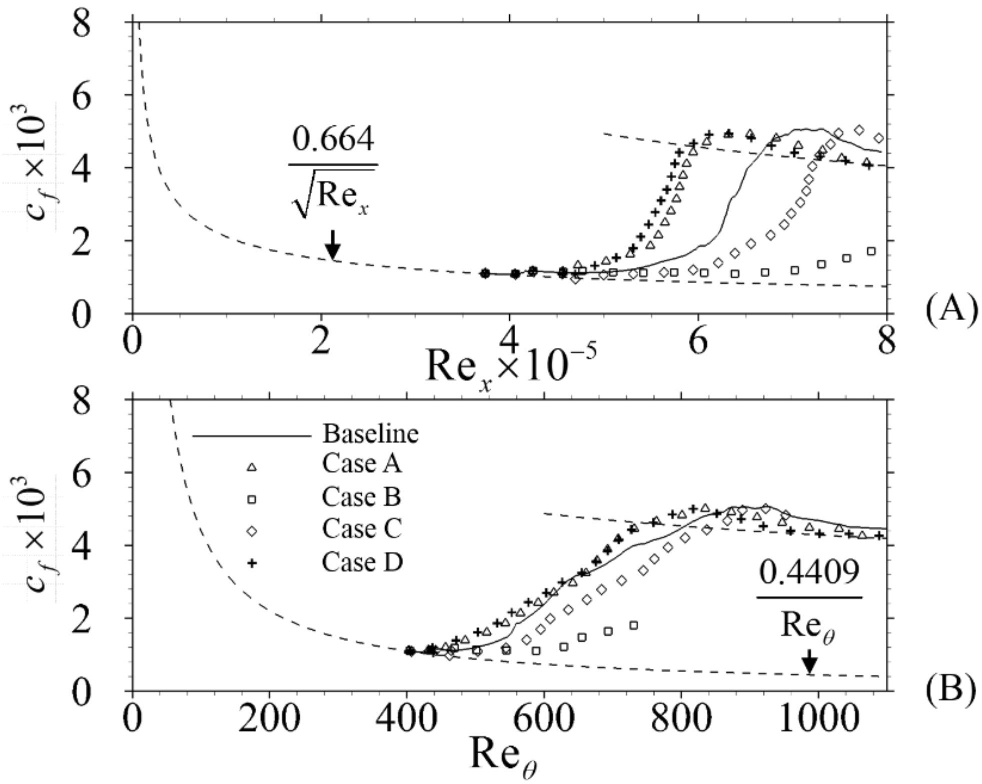

Figure 8-13. Variation of skin friction for different control actuator configuration. Variation of skin friction with (A) Re_x and (B) Re_θ. Turbulent skin friction is compared to published data [209].

The comparison of mean velocity profiles at different locations in the transitional region of the plate is depicted in Figure 8-14. The control actuator for case D impacts the boundary layer at $\mathrm{Re}_\theta = 450$ since it has the highest growth in boundary layer thickness. This allows it to have a similar momentum thickness at an earlier location compared to the baseline case. Similar behavior is seen for case A. For case B and C which have relatively low friction velocity show large U^+ values. From Figure 8-14 (B), for case B and C, the control actuator pushes the higher velocity structures away from the wall while cases A and D pull them closer to the wall.

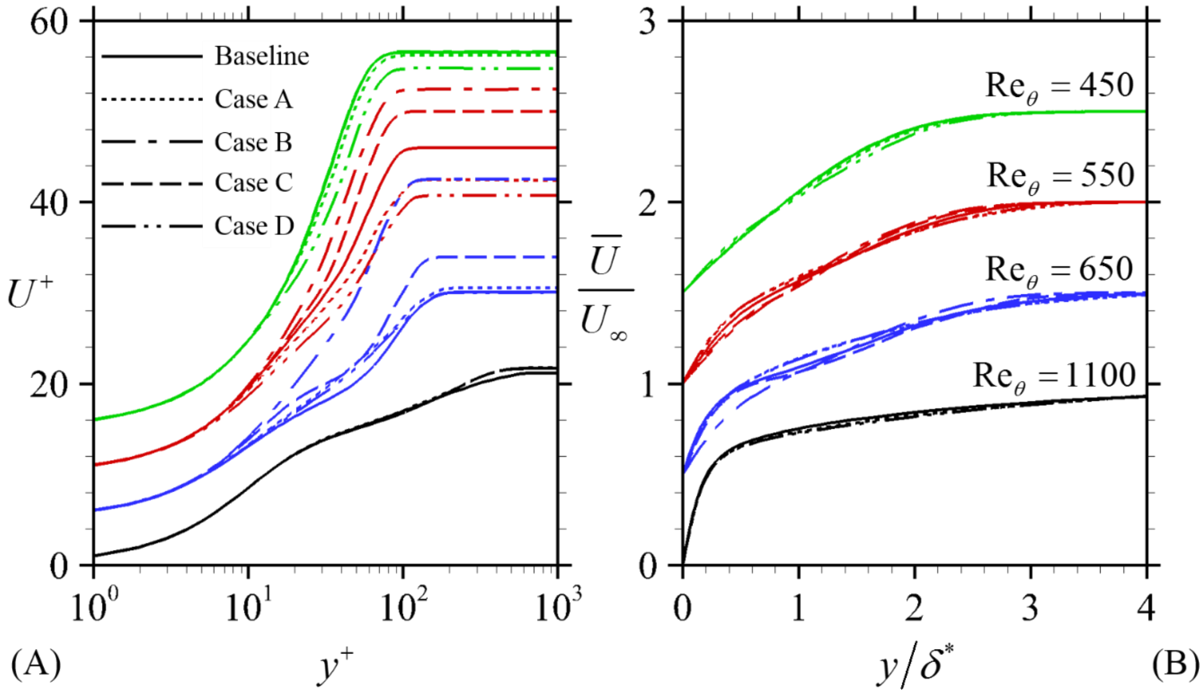

Figure 8-14. Variation of mean velocity profiles for different actuator configuration and Reynolds number. Variation of (A) wall-scaled mean velocity with inner coordinates and (B) mean velocity with outer coordinates. U^+ is successively shifted by 5 units and $\overline{U}/U_\infty$ by 0.5 units with the black curves at the right scale.

The integral quantities shown in Figure 8-15 provide the impact of actuator configuration on the transition to turbulence. For both case A and case D the integral quantities almost overlap with each other, confirming that cases A and D do not have a significant difference in impact on the transition. However, for cases B and C, the counter-flow arranged control actuator (case C) in comparison to the co-flow arranged control actuator (case B) has a significant difference in impact on the transition. In the momentum thickness plots shown in Figure 8-15, the point after which the thickness abruptly deviates from the laminar profile indicates the onset of nonlinearity before the flow becomes fully turbulent. For cases A and D this location is around $\mathrm{Re}_x \approx 5.5\times10^5$ and for case C it is $\mathrm{Re}_x \approx 7\times10^5$. For the case B, this location is difficult to determine, since the flow does not transition to fully developed turbulence in the chosen domain.

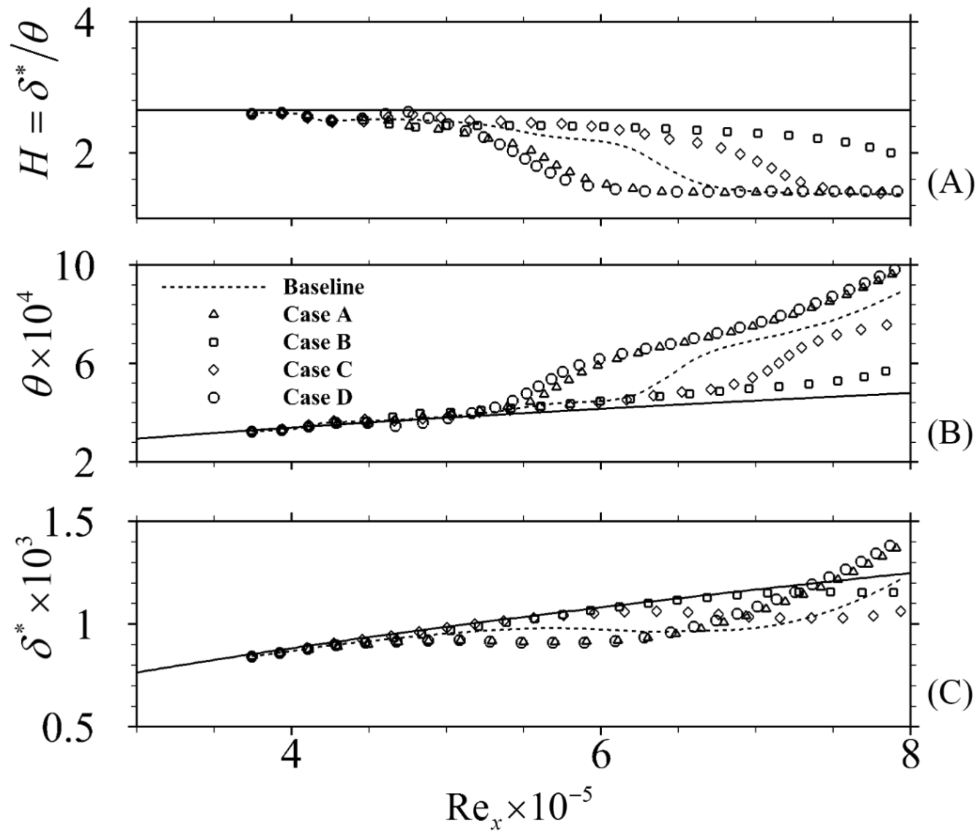

Figure 8-15. Variation of integral quantities with Reynolds number for different control actuator configuration. (A) Shape factor, (B) momentum thickness and (C) displacement thickness. The solid line represents a laminar solution.

The growth parameter given in Eq. (6-3) is plotted for the fluctuations and Reynolds shear stress for different cases in Figure 8-16 and Figure 8-17. Cases A and D have higher growth rates than the baseline case and the growth rates are lower than the baseline for case B and C. In Figure 8-16, the Reynolds shear stress is decreased by almost two orders of magnitude for case B. The growth rate bifurcates at the control actuator location, which is clearly seen in the streamwise fluctuation growth in Figure 8-17. Although the wall-normal growth shows a change in the rate at $Re_x \approx 7{\times}10^5$, the spanwise fluctuations change the rate at $Re_x \approx 7.6{\times}10^5$. This behavior was also observed in the growth rates of pinch and spread plane for the baseline case in Figure 6-22.

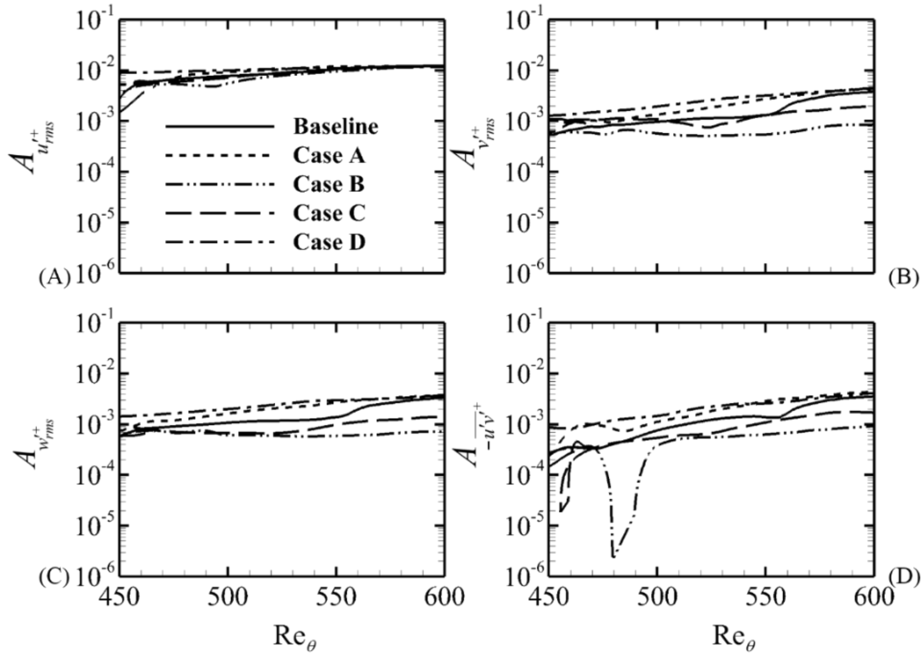

Figure 8-16. Variation of growth parameter with Re_θ for wall-scaled fluctuations and Reynolds shear stress. Growth parameter of (A) streamwise, (B) wall-normal and (C) spanwise RMS fluctuations and (D) Reynolds shear stress.

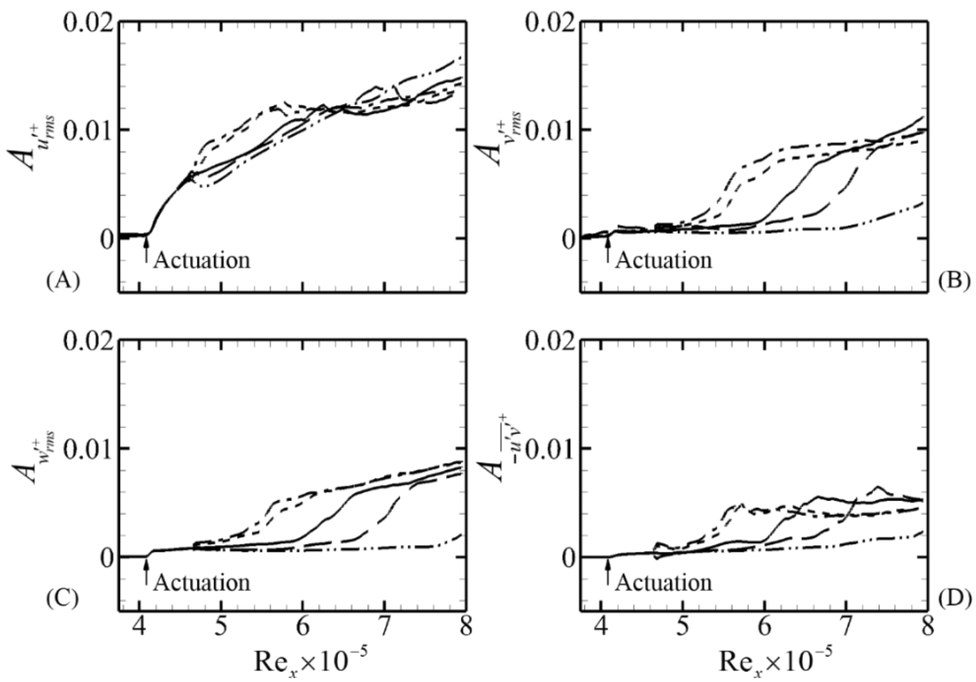

Figure 8-17. Variation of growth parameter with Re_x in transitional region for wall-scaled fluctuations and Reynolds shear stress. Growth parameter of (A) streamwise, (B) wall-normal and (C) spanwise RMS fluctuations and (D) Reynolds shear stress. For the line legend refer to Figure 8-16.

The Reynolds stress budget terms given by Eq. (5-8) are shown in Figure 8-18, Figure 8-19, Figure 8-20 and Figure 8-21. It should be noted that the terms are scaled using freestream conditions to have a better relative magnitude comparison. The production rate plotted in Figure 8-18 shows that the turbulent production is higher for case D than case A for the entire transitional region and is lower after the skin friction overshoot where the flow becomes fully developed. The baseline case has a higher production rate than case A and case D in the fully developed turbulent region. Cases B and C show a gradual increase in production rate. In the fully developed turbulent region for cases A and case D, the production rate peaks at $y \approx 0.2\delta^*$ and the maximum production is observed around $\mathrm{Re}_x \approx 6.41\times10^5$. Similar behavior is seen for production rate when compared at same Re_θ values in Figure 8-19.

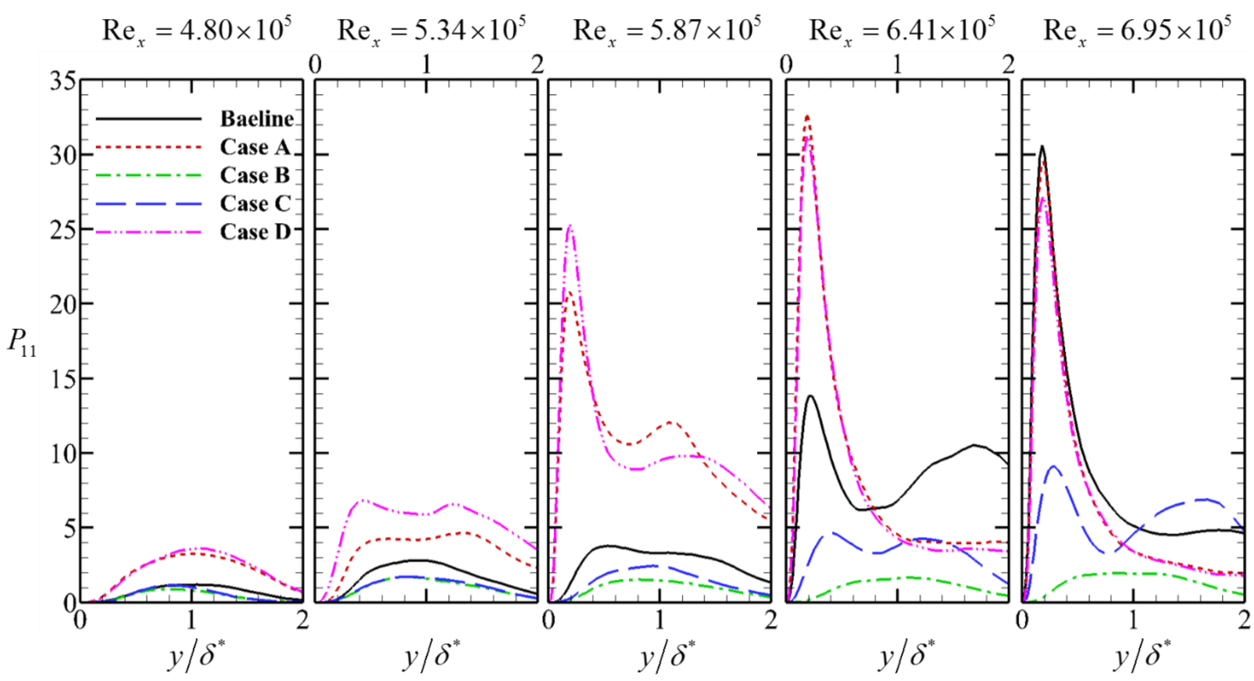

Figure 8-18. Variation of $\overline{u'^2}$ production rate at various Re_x locations in the transitional region for different control actuator configuration.

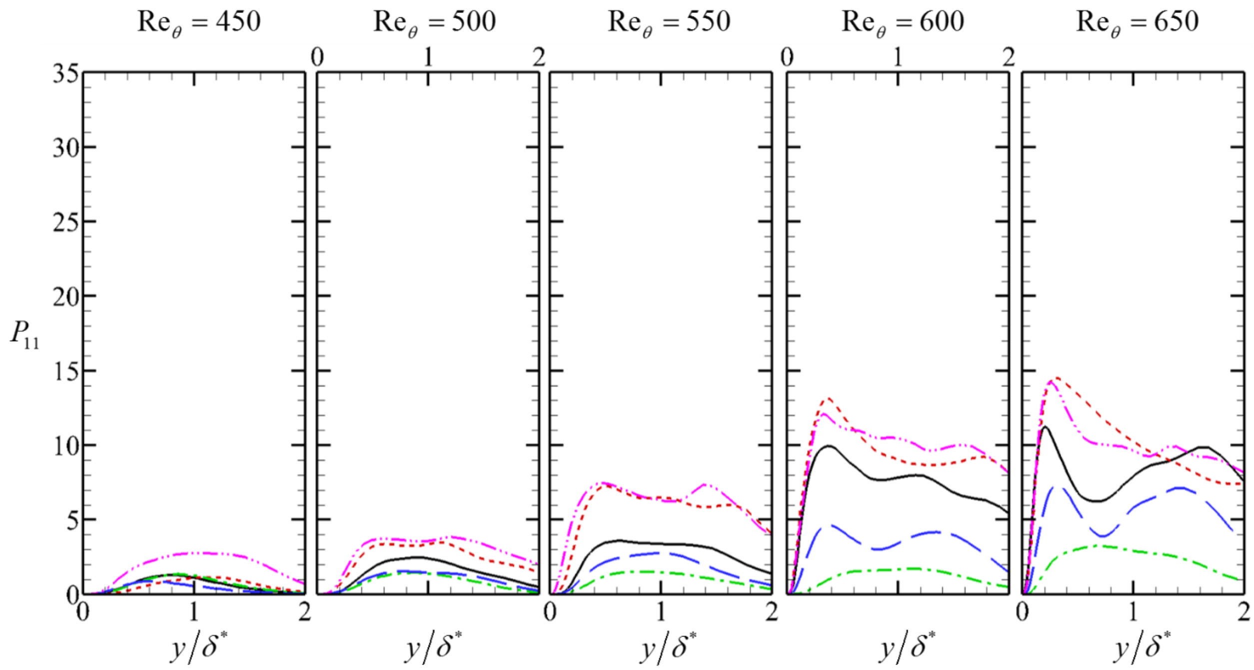

Figure 8-19. Variation of $\overline{u'^2}$ production rate at various Re_θ locations in the transitional region for different control actuator configuration. For line legend, refer to Figure 8-18.

The turbulent dissipation rate, as well as viscous diffusion rate, are shown in Figure 8-19 and Figure 8-20 respectively. Similar trends are observed in comparison to the production rate. However, peak dissipation and diffusion for case A and case D does not occur around $\mathrm{Re}_x = 6.41\times10^5$ and rather occurs around $\mathrm{Re}_x = 5.87\times10^5$. This is at a slightly earlier location to the peak skin friction location. The production rate peaks at the maximum skin friction location. After the dissipation and diffusion rates reach their maximum values, they start dropping. This behavior is also observed for the baseline case where the peak production rate occurs at the maximum skin friction location and the peak dissipation and diffusion occurs at a slightly earlier location to the peak skin friction location.

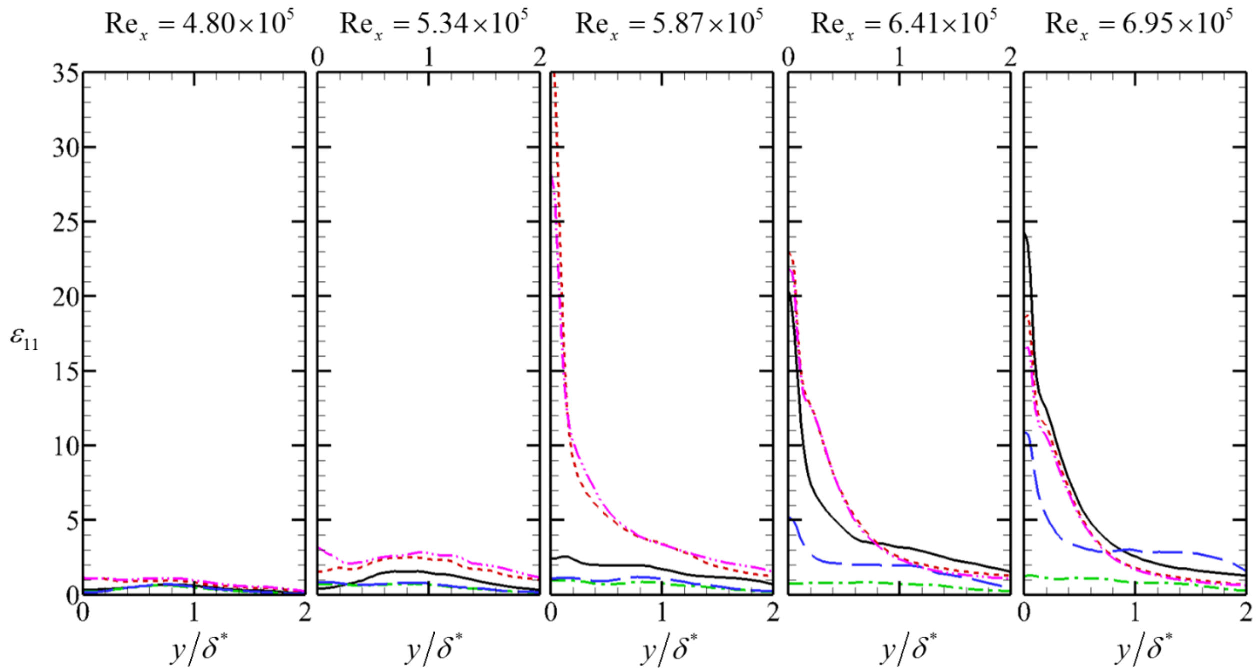

Figure 8-20. Variation of $\overline{u'^2}$ dissipation rate at various Re_x locations in the transitional region for different control actuator configuration. For the line legend, refer to Figure 8-18.

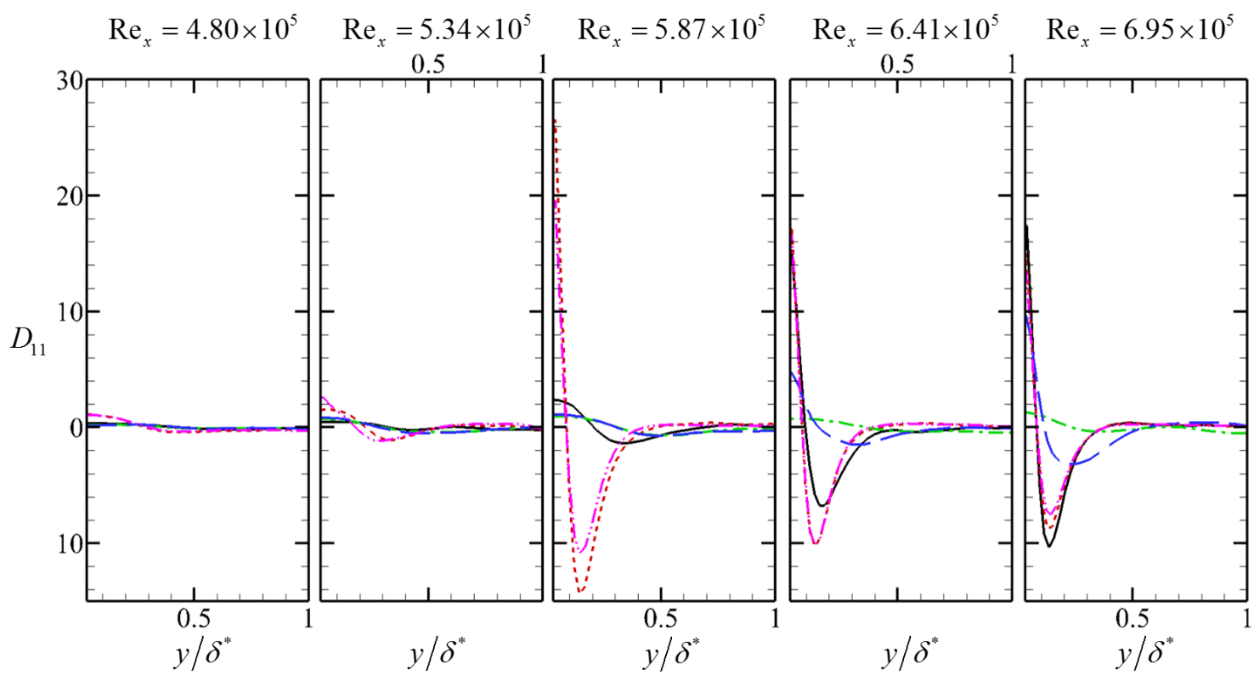

Figure 8-21. Variation of $\overline{u'^2}$ diffusion rate at various Re_x locations in the transitional region for different control actuator configuration. For the line legend, refer to Figure 8-18.

Therefore, the control actuator placed in an arrangement where its pinch planes align with the tripping actuator pinch planes, will enhance turbulent mixing as well as advance the transition to turbulence. When the control actuator is placed in an arrangement where its pinch planes align with the tripping actuator pinch planes, it will suppress turbulent mixing and delay transition.

8.3.2 Effect of Control Actuator Location

From the control actuator configuration study, case B has the maximum impact on the boundary layer. Therefore, to investigate further, the location of control actuator specifically for case B is tested. As mentioned earlier three locations of the control actuator are studied, namely L_A = 2500, 5000 and 7500. Based on the baseline flow, these locations correspond to $Re_x = 4.65 \times 10^5$ ($Re_\theta = 460$), 5.17×10^5 ($Re_\theta = 490$) and 5.7×10^5 ($Re_\theta = 545$).

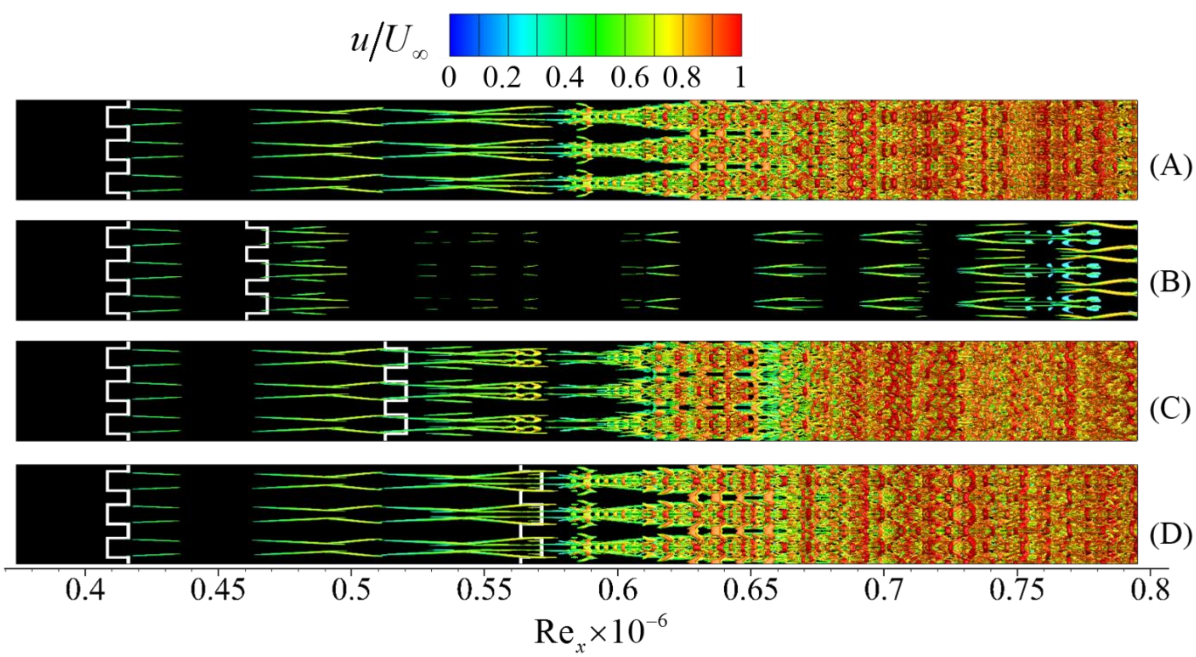

Figure 8-22. Instantaneous normalized Q – criterion (Q = 0.1) iso-surface colored with streamwise velocity for case B. (A) Baseline and the control actuator placed at (B) L_A = 2500 (C) L_A = 5000 and (D) L_A = 7500. The domain is duplicated three times.

Instantaneous structures: The Q –criterion iso-surface depicted in Figure 8-22 shows that the transition control by the control actuator is very sensitive to its location. The impact of control actuator on the transition to turbulence becomes negligible when the actuators are placed beyond L_A = 5000. Although the vortical structures are different at the later stages of transition for L_A = 5000 case, the fully developed turbulence starts at the same location as the baseline case. From Figure 8-23 it is evident that the incoming lambda structures for the control actuator cannot be significantly altered after the strength of subharmonic vortical structures has reached a threshold amplitude.

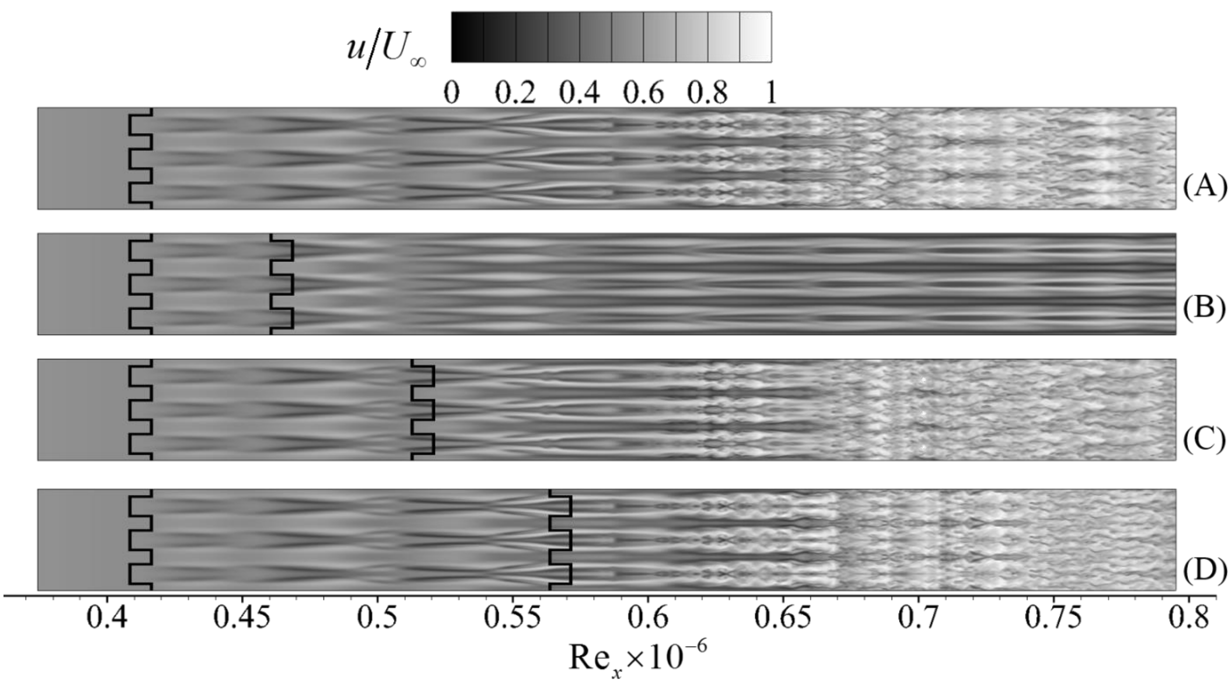

Figure 8-23. Instantaneous streamwise velocity streaklines at y^+ = 30 with the control actuator placed at different locations. (A) Baseline and the control actuator placed at (B) L_A = 2500 (C) L_A = 5000 and (D) L_A = 7500.

Looking at the wall-normal velocity fluctuations in Figure 8-24, both L_A = 5000 and 7500 do not have any significant impact compared to the baseline case. However, significant differences in spanwise fluctuations can be observed in Figure 8-25. Placing the control actuator at L_A = 5000 significantly increases the spanwise fluctuations indicating better mixing. When the control actuator is placed at L_A = 7500, the spanwise fluctuations increase compared to the baseline case, but they decrease compared to the case where control actuator is placed at L_A = 5000. For the location L_A = 2500, spanwise fluctuations are negligible in comparison and do not appear in the depicted range.

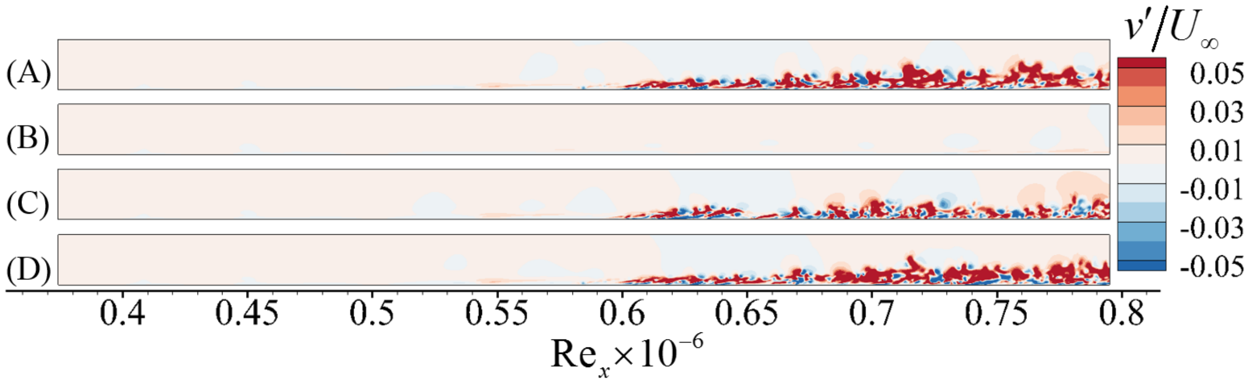

Figure 8-24. Instantaneous wall-normal velocity fluctuations at mid z plane with the control actuator placed at different locations. (A) Baseline and the control actuator placed at (B) L_A = 2500 (C) L_A = 5000 and (D) L_A = 7500.

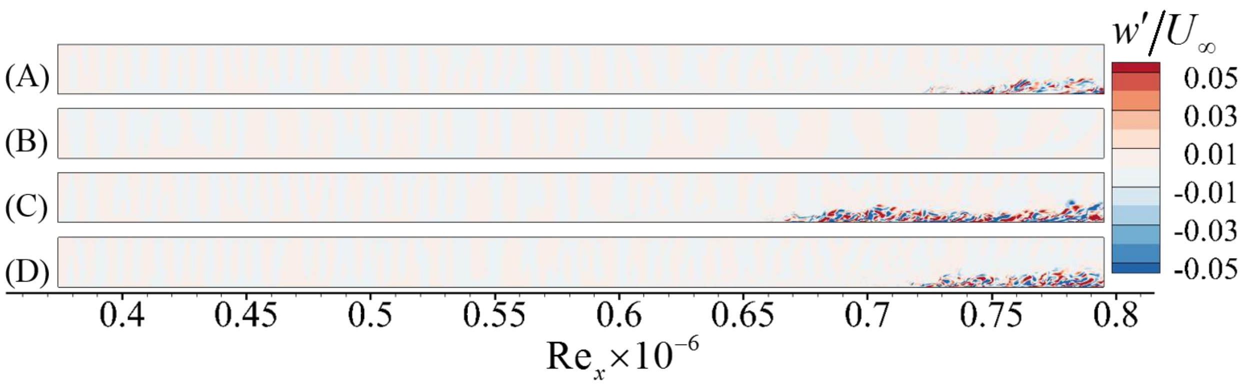

Figure 8-25. Instantaneous spanwise velocity fluctuations at mid z plane with the control actuator placed at different locations. (A) Baseline and the control actuator placed at (B) L_A = 2500 (C) L_A = 5000 and (D) L_A = 7500.

Turbulent statistics: The skin friction plots in Figure 8-26 show that unlike L_A = 2500, both L_A = 5000 and 7500 have no significant difference compared to the baseline case for the entire transitional region. For L_A = 5000, there is a reduction in skin friction in the fully developed turbulent region. This behavior indicates that although the transitional region is not affected, the impact of control actuator can extend to a further downstream region.

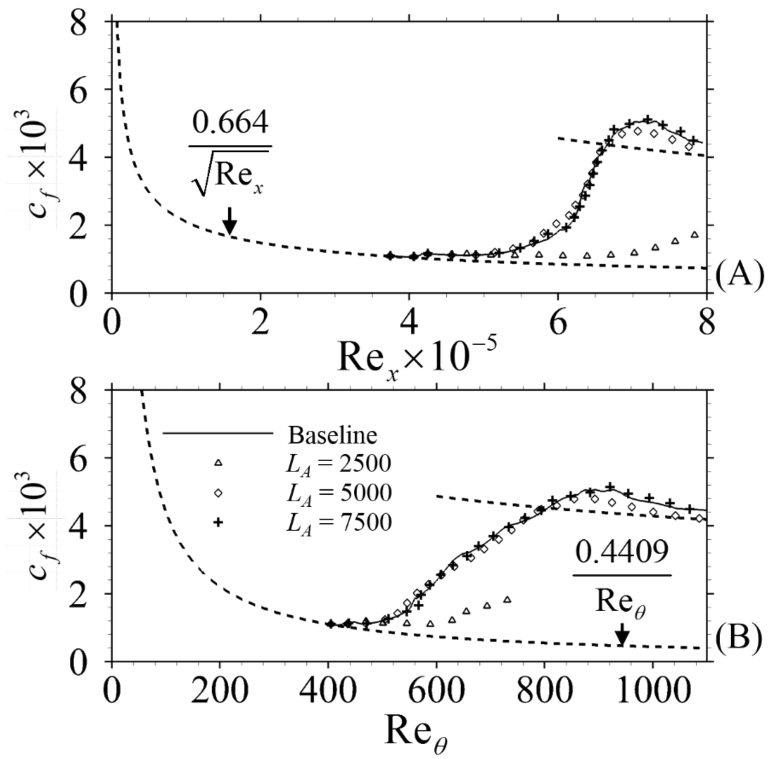

Figure 8-26. Variation of skin friction for different control actuator locations. Variation of skin friction with (A) Re_x and (B) Re_θ. Turbulent skin friction is compared to published data [209].

The mean velocity profiles are plotted in Figure 8-27 with inner and outer coordinates. The wall-scaled mean velocity shows large deviations from the baseline case at $\mathrm{Re}_x = 5.87\times10^5$ for all the control actuator locations. At $\mathrm{Re}_\theta = 550$, control actuator at L_A = 5000 shows a significant impact on the wall-scaled mean velocity profile. This behavior is not evident from Figure 8-27 (C) where the mean velocity is scaled with freestream velocity. This implies that although skin friction plots in Figure 8-26 did not show significant changes in the transitional region for L_A = 5000 and 7500, minor changes in friction velocity can alter the log layer and wake region wall-scaled mean velocity profiles.

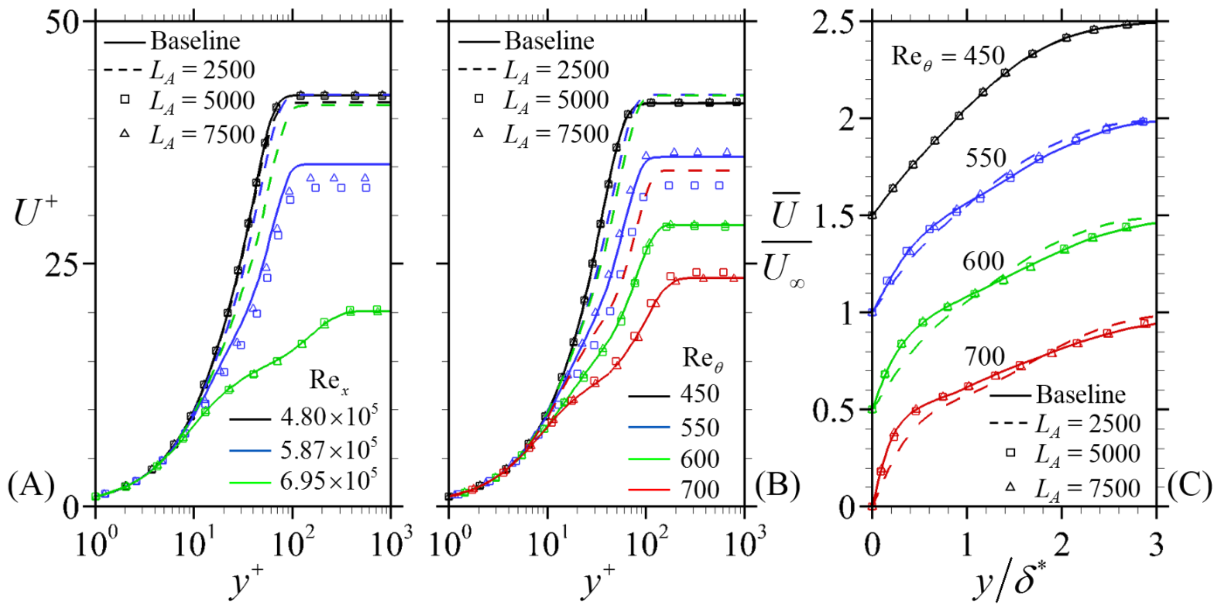

Figure 8-27. Variation of mean velocity profiles for different control actuator locations. Variation of (A) wall-scaled mean velocity with inner coordinates at different Re_x, (B) wall-scaled mean velocity with inner coordinates at different Re_θ and (C) mean velocity with outer coordinates ($\overline{U}/U_\infty$ is successively shifted by 0.5 units with the red curves at the right scale).

The RMS velocity fluctuations and Reynolds shear stress are plotted in Figure 8-28. When the control actuator is placed at L_A = 7500, there is negligible impact on the fluctuations when compared to the baseline case. When L_A = 5000, there are significant differences at Re_θ = 550 and Re_θ = 600, although mean velocity profiles in Figure 8-27 (C) does not show any difference. Therefore, the control actuator location has far greater impact on the second order characteristics than the mean velocity profiles. The peak RMS fluctuations for L_A = 5000 case are higher in comparison to the baseline case at Re_θ = 550 and are lower at Re_θ = 600. Due to the higher fluctuation amplitude, the production rate at $\mathrm{Re}_\theta = 550$ shown in Figure 8-29 is higher than the baseline and the other cases. This implies that if the current configuration control actuator is placed at a location around $L_A = 5000$, it will enhance the turbulent mixing in the later transitional stages even though it is expected to reduce it like the $L_A = 2500$ and 7500 cases. It should be noted that near the control actuator location, each of these cases reduces the turbulence production level. The growth parameters plotted in Figure 8-30 show that the turbulent kinetic energy falls below the baseline case at the control actuator location, but for $L_A = 5000$, it is higher over a range of $\mathrm{Re}_x = 6\times10^5$ to 7.3×10^5. The application of control actuator has the maximum impact on the Reynolds shear stress and the impact varies by two orders of magnitude, depending on its location.

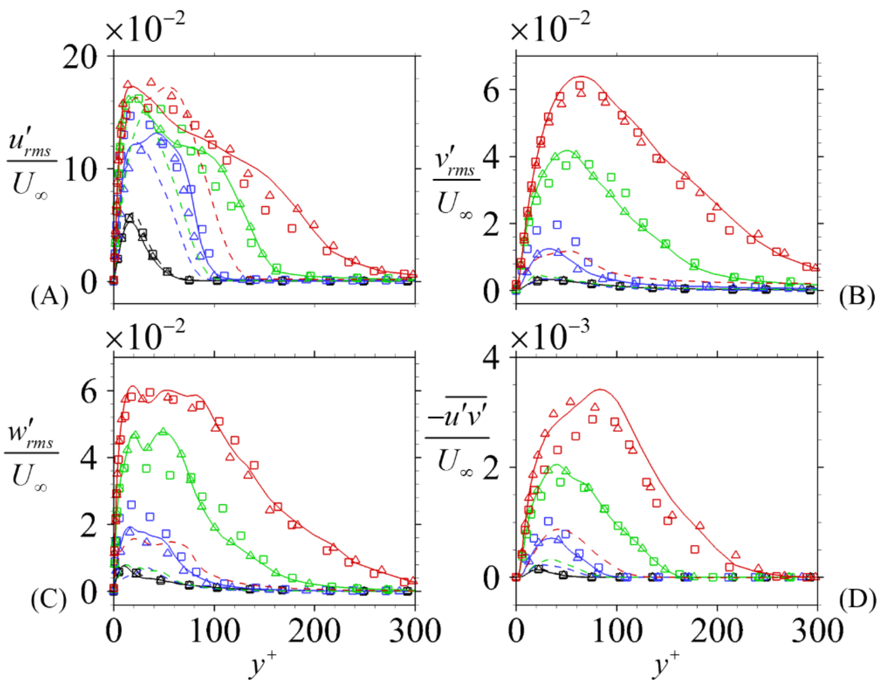

Figure 8-28. Variation of RMS velocity fluctuations and mean Reynolds shear stress with inner coordinates at various Re_θ values for different locations of control actuator. Variation of (A) streamwise, (B) wall-normal, (C) spanwise RMS fluctuations and (D) Reynolds shear stress. For the line legend, refer to Figure 8-27 (B).

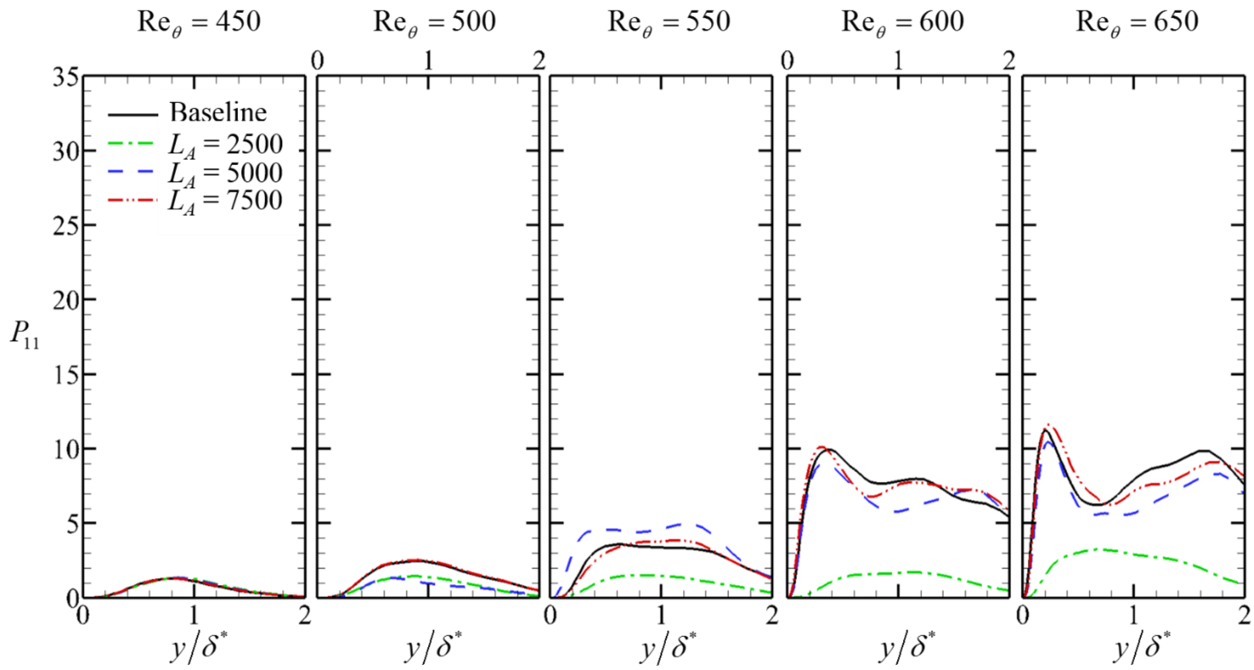

Figure 8-29. Variation of $\overline{u'^2}$ production rate at various Re_θ locations in the transitional region for different control actuator location.

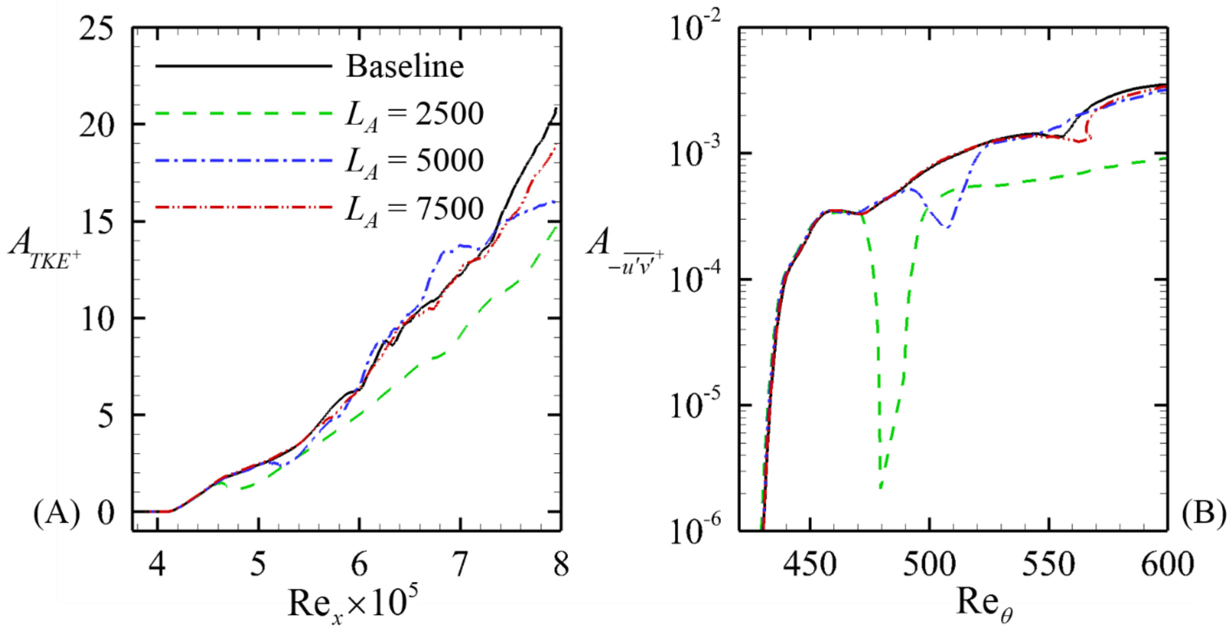

Figure 8-30. Variation of growth parameter for different control actuator locations. Variation of (A) wall-scaled turbulent kinetic energy growth parameter with Re_x and (B) Reynolds shear stress growth parameter with Re_θ.

8.3.3 Modal Analysis

In Figure 8-31, comparison of the excited Fourier components of the normalized streamwise fluctuations u'/U_∞ between baseline, case A, and case B are depicted. The plots are constructed using the same method given in Section 6.2.5. Case A increases the amplitude for all the (ω, β)-modes after the control actuator location. Case B reduces the amplitude for (0, 1) and (1, 1)-mode but increases it for (0, 2) and (1, 2)-mode. For all the cases, the (0, 1)-mode has higher amplitude than the (0, 2)-mode for $\mathrm{Re}_x < 5.25\times10^5$, after which the nonlinear effects add energy to the higher wavenumber mode and causes the amplitude of (0, 2)-mode to be higher than (0, 1)-mode. This location is advanced for cases A to $\mathrm{Re}_x \approx 5.1\times10^5$ and case B to $\mathrm{Re}_x \approx 4.75\times10^5$. Since case A increases the fluctuation amplitude for all the (ω, β)-modes, the transition location is advanced. However, case B reduces the amplitude for the most energetic mode (0, 1) as well as the oblique mode (1, 1) which results in transition delay. Case B increases the amplitude for (0, 2) and (1, 2)-modes, supporting the doubling of the spanwise streak wavenumber observed in Figure 8-23(C). For case B, the (ω, β)-modes for $\beta > 2$ have lower or similar amplitude in comparison to the baseline. Therefore, distributing energy between different modes results in transition delay for case B.

The streamwise (ϕ_u) and spanwise (ϕ_w) POD mode contours for a wall normal plane in the buffer layer is shown in Figure 8-32. It should be noted that POD modes are comprised of multiple (ω, β)-modes. The highest energy containing mode $(M = 1)$ has the same spanwise wavenumber as the actuation but the streamwise wavenumber is zero indicating a steady mode. The strength of the ϕ_w $(M \geq 1)$ and ϕ_u $(M > 1)$ increases after the control actuator for case A and decreases for case B. The increase or reduction in energy of the POD modes relative to the baseline case results in advance or delay in transition respectively. In case A, the lambda structures are stronger and the spacing between the legs of the structures decreases near the tip, while case B does the opposite. This phenomenon manipulates the spanwise oriented vortices near the tip of the lambda structures, where the streaks have maximum lift and are unstable, and contribute to advance or delay in transition. For case A, the sum of the relative energy for the all the modes greater than 5 is around 10% more than the baseline. This suggests that the collocation of actuators in case A amplifies the energy of the higher modes by reducing it for the lower modes. For M =1 in case B, strength of ϕ_u is increased since majority of the energy from higher modes $(M > 1)$ are transferred into M = 1, reducing the nonlinear interaction between the modes. The staggered pattern of positive and negative ϕ_w observed in $M = 2$, corresponds to the oblique mode. For case A, the lambda vortices $(M = 2,\ \phi_u)$ strengthen and grow in size. However, Case B creates weak lambda structures $(M = 2,\ \phi_u)$ between the strong ones after $\mathrm{Re}_x \approx 5.25 \times 10^5$ thereby doubling the spanwise wavenumber. These weak structures gradually become stronger relative to the upstream lambda vortices as the Reynolds number increases. This exchange of energy between the structures and increase in spanwise wavenumber, leads to transition delay for case B.

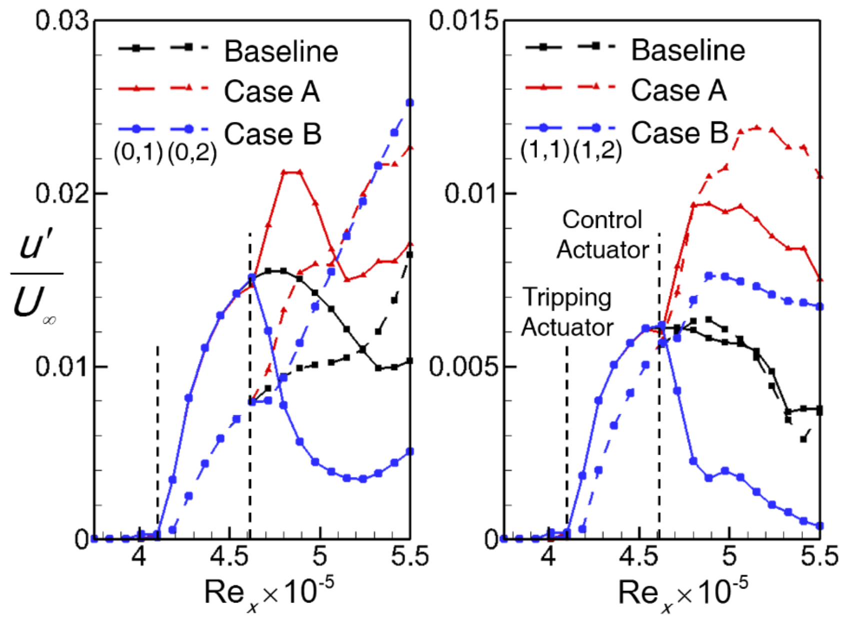

Figure 8-31. Comparison of normalized streamwise fluctuation amplitude for different (ω, β)-modes.

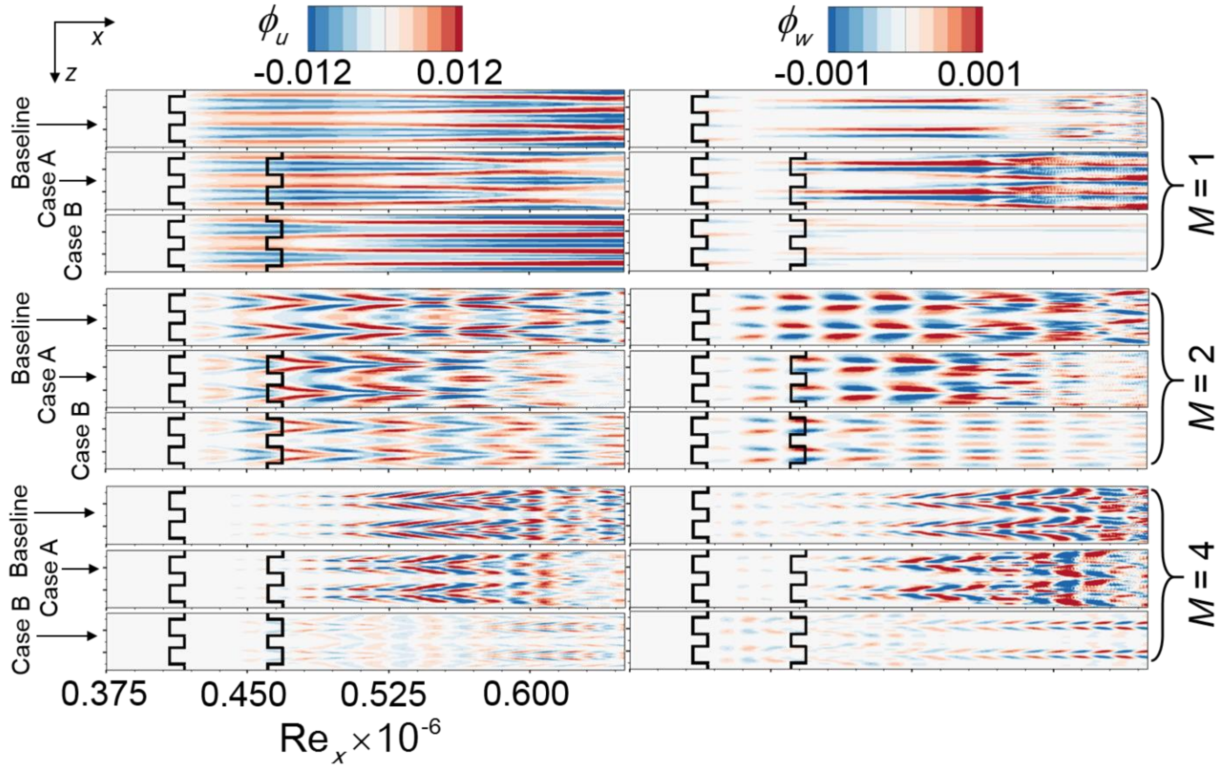

Figure 8-32. Relative energy content for different energetic modes based on POD analysis. The contours are plotted for $y/\delta^* \approx 1$.

CHAPTER 9
CONCLUSIONS AND EXPECTED IMPACT

9.1 Parallel Discontinuous Galerkin Method

The benefits of applying modal DG method in simulating turbulent flows are its ease of parallelization and extension to higher order accuracy. A three-dimensional DG method has been implemented in an in-house code called the Multiscale Ionized Gas (MIG) flow code to simulate turbulent flow physics. The code incorporates both Euler implicit and two-step Runge Kutta time discretization scheme with spatial order of accuracy up to $P = 4$. The parallelization has been done using open MPI with a lexicographic domain decomposition. For inviscid numerical fluxes both Godunov and local Lax-Friedrichs flux have been investigated. For the viscous numerical fluxes, LDG method, BR1 scheme, and BR2 scheme have been implemented [113].

To validate and benchmark the code, the Taylor-Green vortex problem has been studied using implicit large eddy simulation (ILES). Extensive analysis using different inviscid fluxes, spatial accuracy, and mesh sizes show that DG ILES can capture the relevant length scales and maintain the $-5/3$ slope in the inertial region. The findings from this study have been utilized to simulate a zero-pressure gradient turbulent boundary layer flow over a flat plate using both bypass and controlled transition mechanisms. One of the key findings of this study involved the overshoot of total shear stress near the wall, which is not observed in most published literature. Future studies can involve the use of high order approximation, with larger domain size and a wider range of Reynolds numbers to investigate whether the shear stress overshoot holds, over the entire range. All other parameters are found to match well with the published literature.

9.2 Serpentine Plasma Actuator for Turbulent Transition

A controlled transition method utilizing serpentine plasma actuators as a tripping mechanism has been studied. The transition mechanism initiated by a serpentine plasma actuator has been found to occur via a non-modal oblique wave transition mechanism. This involves a fundamental as well as subharmonic mode. A proper orthogonal decomposition study showed that the subharmonic mode has almost half the energy of the fundamental mode. The growth of disturbances showed that the pinch plane has a higher growth rate than the spread plane. At the final stages of transition, the legs of the subharmonic lambda vortices interact with the front end of the fundamental lambda vortices to create hairpin structures and finally turbulize the flow.

Different actuator parameters such as actuator geometry, frequency, amplitude, and temperature have also been investigated. For the actuator geometry, linear, circular serpentine and square serpentine actuators were tested. The linear actuator undergoes TS wave transition while both the serpentine geometry actuators show oblique wave transition. The square serpentine actuator has a faster transition than the circular serpentine actuator for the same amplitude of perturbation. Although the linear actuator has lower streamwise and wall-normal growth parameter amplitude than the serpentine actuators, it has a higher slope. This was mainly due to the absence of spanwise fluctuations for the linear actuator, which resulted in the distribution of energy only in the streamwise and wall-normal directions. The increase in frequency and amplitude of actuation advanced the transition process. However, for the low frequencies, the flow does not turbulize and the disturbances decay. The thermal effects have been investigated using a heating element placed in the center of the pinching region of the square serpentine actuator. The heating element lifted the flow structures at the later stages of transition and increased the shifted the Reynolds shear stress closer to the wall. Its maximum influence was on the wall-normal fluctuation growth parameter.

9.3 Collocation of Serpentine Plasma Actuators

An investigation on the influence of collocation of square serpentine actuators has been conducted. It has been found that when the turbulent tripping actuator is placed in counter-flow or co-flow arrangement, turbulent structures in the transitional region did not have a significant impact. Although the strength of the vortical structures increases in counter-flow arrangement, the flow structures have differences mainly in the highly nonlinear region of the later stages of transition. This behavior was further investigated by placing a control actuator downstream of the co-flow arranged tripping actuator.

The study of collocation of two square serpentine actuators involved the effect of the configuration of the control actuator as well as its location with respect to the tripping actuator. For the configuration study, the control actuator is placed in co-flow and counter-flow arrangements with respect to the tripping actuator as well as the spreading and pinching planes are shifted or aligned to the tripping actuator. To advance the transition to turbulence, the pinch planes or the spread planes of the tripping and control actuator should be aligned while to delay the transition, the pinch and spread planes should be aligned. Counter-flow arrangement of the control actuator destabilizes the flow more than the co-flow arrangement, which results in an earlier transition than its co-flow counterpart. The transition delay due to control actuator configuration occurs due to a large reduction in strength of incoming vortices which in turn reduces the local Reynolds shear stress at the control actuator.

To investigate further different locations of the control actuator has been studied. Apart from the configuration, the location of the control actuator plays a very important role. This location depends on different parameters such as, the frequency at which the tripping actuator perturbs the flow, the convective velocity, and relevant length scale. These parameters can be collectively defined using a Strouhal number. Although, an optimization study has not been performed, it can be concluded that for transition delay, the control actuator cannot be placed very close to the tripping actuator since it would behave like a tripping actuator and it cannot be placed too far since the perturbations would have grown to an amplitude which cannot be effectively manipulated. Therefore, an optimal location will exist in the transitional region where the control actuator can have the maximum impact in transition delay. Future studies can investigate the optimal location of the control actuator for which the transition delay is maximum.

9.4 Future Work

Future studies in this area can be conducted using fully resolved direct numerical simulations. Extending the study to larger Reynolds number flows can provide extensive knowledge for practical applications. A major advancement in this area would be to improve the design of the plasma actuators (both in terms of power supply and actuator geometry) such that they consume lower power and provide higher control authority. Chapter 8 shows the benefit of collocated serpentine plasma actuators to predictably control the streak growth in a turbulent boundary layer. This can be further investigated for incoming random turbulent streaks to provide a broader application. Since it has been shown that collocation can control different instability modal growth, investigating it for controlling secondary crossflow instabilities, generally found in swept-wings, can provide additional know-how on delaying the transition. As the control parameters of the plasma actuator are crucial to obtain optimum flow control, receptivity studies can be conducted for adept positioning, operation, and design of these actuators. This can involve both numerical and analytical studies to show which flow field parameters are impacted by small changes in actuator forcing methodology.

Since this study is based on a numerical investigation, an experimental analysis of all the cases will provide validation to the behavior observed numerically. Since experimentally the plasma actuators do not need any approximation, added information can be obtained on its impact on the background flow field. Extensive wind tunnel tests can show whether the numerically predicted transition scenarios of serpentine shaped plasma actuators are accurate. Flow visualization studies can show the instantaneous structures generated by the serpentine actuator operating in a background flow field. Apart from qualitative analysis, quantitative studies, both intrusive and non-intrusive, can provide extensive data for validation.

9.5 Expected Impact

The scientific knowledge obtained from this research will create an understanding of accurately actuated turbulent flow control capability which in turn would provide better design solutions. The efficient control of the hairpin structures generated in wall-bounded turbulence will have a large impact on energy efficiency of an aircraft. Understanding these inherent flow structures will allow efficient control over drag which plays a crucial role in aircraft industry. For example, on a Concorde, a reduction of one count of drag ($\Delta C_D = 0.0001$) can allow it to carry two extra passengers [241]. Controlling drag can also have a huge environmental impact. Emissions can be reduced significantly with the efficient use of fuel. For every percentage reduction in drag, almost one million gallons of fuel can be saved throughout the lifetime of a military transport aircraft [242]. Since almost 50% of the drag on aircraft is due to skin friction drag, reducing it would have a huge impact in the aircraft industry. Even for road vehicles skin friction drag can contribute up to 25% of the total drag. In the U.S. for single unit trucks, approximately 54.1 billion liters of diesel fuel is consumed, producing 144 million metric tons of CO_2 annually [243]. Future studies can be performed using the serpentine plasma actuators for high-speed flow ($M > 1$). At these flow regimes, fuel is approximately one-half of the gross weight and 1% reduction in drag can increase the payload by 5% to 10% [244]. Thus, use of serpentine plasma actuators can have a significant impact on both environmental issues and fuel economy.

APPENDIX
PROPER ORTHOGONAL DECOMPOSITION

Proper orthogonal decomposition (POD) is obtained using the following procedure [245].

Step 1. Collect N number of snapshots instantaneous fluctuating velocity field $\left(u_i'^{j}, v_i'^{j}, w_i'^{j}\right)$ data over a specified period of time for the plane (M grid points) to be investigated. N should be large to check whether varying number of snapshots impacts the POD analysis. The subscript i is for the nodal value and superscript j is for the snapshot value.

Step 2. Arrange the fluctuating velocities for the chosen N snapshots as specified by Eq. (A-1).

$$\boldsymbol{A} = \begin{bmatrix} u_1'^{1} & u_1'^{2} & \dots & u_1'^{N} \\ \vdots & \vdots & \vdots & \vdots \\ u_M'^{1} & u_M'^{1} & \dots & u_M'^{N} \\ v_1'^{1} & v_1'^{1} & \dots & v_1'^{N} \\ \vdots & \vdots & \vdots & \vdots \\ v_M'^{1} & v_M'^{1} & \dots & v_M'^{N} \\ w_1'^{1} & w_1'^{1} & \dots & w_1'^{N} \\ \vdots & \vdots & \vdots & \vdots \\ w_M'^{1} & w_M'^{1} & \dots & w_M'^{N} \end{bmatrix} \tag{A-1}$$

Step 3. Calculate the correlation matrix using Eq. (A-2).

$$C = \boldsymbol{A}^T \boldsymbol{A} \tag{A-2}$$

Step 4. Evaluate the Eigenvalues (λ) and Eigenvectors (υ) of C. The Eigen values are arranged in descending order with last Eigenvalue $\lambda_N = 0$ and the Eigenvectors associated with each Eigenvalue also gets sorted accordingly. The Eigenvalues will provide the energy content in each mode starting with the dominant mode. The relative energy associated with each mode is obtained using Eq. (A-3).

$$E_j = \frac{\lambda_j}{\sum_{n=1}^{N} \lambda_n} \tag{A-3}$$

Step 5. The POD modes for the different fluctuating velocity components $\left(\boldsymbol{u}'^n = \left[u_1'^n \ldots u_M'^n\right]\right)$ are found using Eq. (A-4).

$$\phi_u^i = \frac{\sum_{n=1}^{N} \upsilon_n^i \boldsymbol{u}'^n}{\left\| \sum_{n=1}^{N} \upsilon_n^i \boldsymbol{u}'^n \right\|};\ \phi_v^i = \frac{\sum_{n=1}^{N} \upsilon_n^i \boldsymbol{v}'^n}{\left\| \sum_{n=1}^{N} \upsilon_n^i \boldsymbol{v}'^n \right\|};\ \phi_w^i = \frac{\sum_{n=1}^{N} \upsilon_n^i \boldsymbol{w}'}{\left\| \sum_{n=1}^{N} \upsilon_n^i \boldsymbol{w}'^n \right\|} \tag{A-4}$$

LIST OF REFERENCES

[1] R. Osborne, "An experimental investigation of the circumstances which determine whether the motion of water shall be direct or sinuous, and of the law of resistance in parallel channels," *Proceedings of the royal society of London,* vol. 35, no. 224-226, pp. 84-99, 1883.

[2] L. Prandtl, "Motion of fluids with very little viscosity," in *Proceedings in Third International Mathemtical Congress (N.A.C.A. Rep. TM 452, March 1928),* Heidelberg, Germany, 1904.

[3] M. Gad-el-Hak, "Modern developments in flow control," *Applied Mechanics Reviews,* vol. 49, pp. 365-380, 1996.

[4] L. N. Cattafesta and M. Sheplak, "Actuators for Active Flow Control," *Annual Review of Fluid Mechanics,* vol. 43, pp. 247-272, 2011.

[5] L. Cattafesta, Q. Song, D. R. Williams, C. W. Rowley and F. S. Alvi, "Active control of flow-induced cavity oscillations," *Progress in Aerospace Sciences,* vol. 44, no. 7, pp. 479-502, 2008.

[6] J. E. Rossiter, "Wind Tunnel Experiments On the Flow Over Rectangular Cavities for Subsonic and Transonic Speeds," Ministry of Aviation; Royal Aircraft Establishment, RAE Farnborough, 1964.

[7] H. H. Heller and D. B. Bliss, "Aerodynamically Induced Pressure Oscillations In Cavities - Physical Mechanisms and Suppression Concepts," in *No. BBN-2884, Bolt Beranek and Newman Inc.*, Cambridge, MA, 1975.

[8] R. L. Sarno and M. E. Franke, "Suppression of Flow-Induced Pressure Oscillations in Cavities," *Journal of Aircraft,* vol. 31, no. 1, pp. 90-96, 1994.

[9] R. J. Englar and G. G. Huson, "Development of Advanced Circulation Control Wing High-Lift Airfoils," *Journal of Aircraft,* vol. 21, no. 7, pp. 476-483, 1984.

[10] M. J. Walsh, "Riblets as a viscous drag reduction technique," *AIAA journal,* vol. 21, no. 4, pp. 485-486, 1983.

[11] D. W. Bechert, M. Bruse, W. Hage, J. Van Der Hoeven and G. Hoppe, "Experiments on drag-reducing surfaces and their optimization with an adjustable geometry," *Journal of Fluid Mechanics,* vol. 338, pp. 59-87, 1997.

[12] Y. Suzuki and N. Kasagi, "Turbulent Drag Reduction Mechanism Above a Riblet Surface," *AIAA Journal,* vol. 32, no. 9, pp. 1781-1790, 1994.

[13] J. C. Lin, F. G. Howard and G. V. Selby, "Small submerged vortex generators for turbulent flow separation control," *Journal of Spacecraft and Rockets,* vol. 27, no. 5, pp. 503-507, 1990.

[14] D. McCormick, "Shock-boundary layer interation control with low-profile vortex generators and passive cavity," in *30th Aerospace Sciences Meeting and Exhibit*, Reno, NV, 1992.

[15] P. R. Ashill, J. L. Fulker and K. C. Hackett, "Studies of flow induced by sub boundary layer vortex generators (SBVGs)," *AIAA paper,* vol. 968, p. 2002, 2002.

[16] C. S. Yao, J. C. Lin and B. G. Allan, "Flowfield measurement of device-induced embedded streamwise vortex on a flat plate," in *1st AIAA Flow Control Conference*, St. Louis, MO, 2002.

[17] J. Lin, "Control of Turbulent boundary layer separation using micro-vortex generators," in *30th Fluid Dynamics Conference*, Norfolk,VA, 1999.

[18] R. E. Dix and C. Butler, "Cavity aeroacoustics," AFATL-TP-90-08, AFATL, FL, 1990.

[19] M. Amitay, A. Honohan, M. Trautman and A. Glezer, "Modification of the aerodynamic characteristics of bluff bodies using fluidic actuators," in *28th Fluid Dynamics Conference, AIAA*, Snowmass,Co, 1997.

[20] M. Amitay, V. Kibens, D. Parekh and A. Glezer, "The dynamics of flow reattachment over ia thick airfoil controlled by synthetic jet actuators," in *37th AIAA Aerospace Sciences Meeting and Exhibit*, Reno,NV, 1999.

[21] L. D. Kral, J. F. Donovan, A. B. Cain and A. W. Cary, "Numerical Simulation of synthetic jet actuators," in *AIAA Paper*, Reno, NV, 1997.

[22] T. Lorkowski, R. Rathnasingham and K. Breuer, "Small scale forcing of a turbulent boundary layer," Department of Aeronautics and Astronautics, MIT, Cambridge, MA, 1997.

[23] A. Glezer and M. Amitay, "Synthetic Jets," *Annual Review of Fluid Mechanics,* vol. 34, no. 1, pp. 503-529, 2002.

[24] A. Seifert, T. Bachar, D. Koss, M. Shepshelovich and I. Wygnanskil, "Oscillatory Blowing: A Tool to Delay Boundary-Layer Separation," *AIAA Journal,* vol. 31, no. 11, pp. 2052-2060, 1993.

[25] A. Seifert, S. Eliahu, D. Greenblatt and I. Wygnanski, "Use of Piezoelectric actuators for airfoil separation control," *AIAA Journal,* vol. 36, no. 8, pp. 1535-1537, 1998.

[26] D. Fabris and D. Williams, "Experimental measurements of cavity and shear layer response to unsteady bleed forcing," in *AIAA Paper : Aerospace Sciences Meeting and Exhibit*, Reno, NV, 1999.

[27] A. M. Lamp and N. Chokani, "Control of cavity resonance using steady and oscillatory blowing," in *AIAA paper: 37th Aerospace Sciences Meeting and Exhibit*, Reno,NV, 1999.

[28] L. N. Cattafesta, S. Garg and D. Shukla, "Development of Piezoelectric Actuators for Active Flow Control," *AIAA Journal,* vol. 39, no. 8, pp. 1562-1568, 2001.

[29] M. Debiasi and M. Samimy, "Logic-Based Active Control of Subsonic Cavity Flow Resonance," *AIAA journal,* vol. 42, no. 9, pp. 1901-1909, 2004.

[30] A. D. Gupta and S. Roy, "Noise Control of Subsonic Cavity flows using Plasma Actuated Receptive Channels," *Journal of Physics D: Applied Physics,* vol. 47, no. 50, p. 502002, 2014.

[31] J. S. Shang and S. T. Surzhikov, "Magnetoaerodynamic actuator for hypersonic flow control," *AIAA Journal,* vol. 43, no. 8, pp. 1633-1652, 2005.

[32] B. L. Smith and A. Glezer, "The formation and evolution of synthetic jets," *Physics of Fluids,* vol. 10, no. 9, pp. 2281-2297, 1998.

[33] T. C. Corke, C. L. Enloe and S. P. Wilkinson, "Dielectric barrier discharge plasma actuators for flow control," *Annual review of fluid mechanics,* vol. 42, pp. 505-529, 2010.

[34] J. R. Roth, D. M. Sherman and S. P. Wilkinson, "Electrohydrodynamic flow control with a glow discharge surface plasma," *AIAA Journal,* vol. 38, no. 7, pp. 1166-1172, 2000.

[35] J.-J. Wang, K.-S. Choi, L.-H. Feng, T. N. Jukes and R. D. Whalley, "Recent developments in DBD plasma flow control," *Progress in Aerospace Sciences,* vol. 62, pp. 52-78, 2013.

[36] J. R. Roth, Industrial Plasma Engineering: Volume 1 - Principles, Bristol and Philadelphia: Institute of Physics Publishing, 1995.

[37] H. R. Velkoff and J. Ketcham, "Effect of electrostatic field on boundary layer transition," *AIAA Journal,* vol. 6, no. 7, pp. 1381-1383, 1968.

[38] H. R. Velkoff and R. Godfrey, "Low-velocity heat transfer to a flat plate in the presence of a corona discharge in air," *Journal of Heat Transfer,* vol. 101, pp. 157-163, 1979.

[39] J. R. Van Rosendale, M. R. Malik and M. Y. Hussaini, "Ion-wind effects on poiseuille and blasius flow," *AIAA Journal,* vol. 26, no. 8, pp. 961-968, 1988.

[40] L. Léger, E. Moreau, G. Artana and G. Touchard, "Influence of a DC corona discharge on the airflow along an inclined flat plate," *Journal of Electrostatics,* vol. 51, pp. 301-306, 2001.

[41] E. Moreau, L. Léger and G. Touchard, " Effect of a DC surface-corona discharge on a flat plate boundary layer for air flow velocity up to 25m/s," *Journal of electrostatics,* vol. 64, no. 3, pp. 215-225, 2006.

[42] E. Moreau, N. Benard, F. Alicalapa and A. Douyère, "Electrohydrodynamic force produced by a corona discharge between a wire active electrode and several cylinder electrodes – Application to electric propulsion," *Journal of Electrostatics,* vol. 76, pp. 194-200, 2015.

[43] P. Zhao, S. Portugal and S. Roy, "Efficient needle plasma actuators for flow control and surface cooling," *Applied Physics Letters,* vol. 107, no. 3, p. 033501, 2015.

[44] M. Samimy, I. Adamovich, B. Webb, J. Kastner, J. Hileman, S. Keshav and P. Palm, "Development and characterization of plasma actuators for high-speed jet control," *Experiments in Fluids,* vol. 37, no. 4, pp. 577-588, 2004.

[45] K. R. Grossman, B. Z. Cybyk and D. M. VanWie, "Sparkjet Actuators for Flow Control," in *41st Aerospace Sciences Meeting and Exhibit*, *Aerospace Sciences Meetings*, Reno, NV, 2003.

[46] L. Wang, Z. X. Xia, Z. B. Luo and J. Chen, "Three-electrode plasma synthetic jet actuator for high-speed flow control," *AIAA Journal,* vol. 52, pp. 879-882, 2014.

[47] V. Narayanaswamy, L. L. Raja and N. T. Clemens, "Characterization of a High-Frequency Pulsed-Plasma Jet Actuator for Supersonic Flow Control," *AIAA Journal,* vol. 48, no. 2, pp. 297-305, 2010.

[48] S. Leonov, V. Bityurin, K. Savelkin and D. Yarantsev, "Effect of electrical discharge on separation processes and shocks position in supersonic airflow," in *40th AIAA Aerospace Sciences Meeting & Exhibit*, *Aerospace Sciences Meetings*, Reno, NV, 2002.

[49] Y. G. Utkin, S. Keshav, J. H. Kim, J. Kastner, I. V. Adamovich and M. Samimy, "Development and use of localized arc filament plasma actuators for high-speed flow control," *Journal of Physics D: Applied Physics,* vol. 40, no. 3, pp. 685-694, 2006.

[50] P. Sunka, V. Babický, M. Clupek, P. Lukes, M. Simek, J. Schmidt and M. Cernak, "Generation of chemically active species by electrical discharges in water," *Plasma Sources Science and Technology,* vol. 8, no. 2, p. 258, 1999.

[51] Y. Yang, H. Kim, A. Starikovskiy, A. Fridman and Y. I. Cho, "Application of pulsed spark discharge for calcium carbonate precipitation in hard water," *Water research,* vol. 44, no. 12, pp. 3659-3668, 2010.

[52] D. V. Roupassov, A. A. Nikipelov, M. M. Nudnova and A. Y. Starikovskii, "Flow separation control by plasma actuator with nanosecond pulsed periodic discharge," *AIAA Journal,* vol. 47, no. 1, pp. 168-185, 2009.

[53] G. Correale, T. Michelis, D. Ragni, M. Kotsonis and F. Scarano, "Nanosecond-pulsed plasma actuation in quiescent air and laminar boundary layer," *Journal of Physics D: Applied Physics,* vol. 47, no. 10, p. 105201, 2014.

[54] E. Moreau, C. Louste and G. Touchard, "Electric wind induced by sliding discharge in air at atmospheric pressure," *Journal of Electrostatics,* vol. 66, no. 1, pp. 107-114, 2008.

[55] R. Sosa, E. Arnaud, E. Memin and G. Artana, "Study of the flow induced by a sliding discharge," *IEEE Transactions on Dielectrics and Electrical Insulation,* vol. 16, no. 2, pp. 305-311, 2009.

[56] S. Roy and C. C. Wang, "Bulk flow modification with horseshoe and serpentine plasma actuators," *Journal of Physics D: Applied Physics,* vol. 42, no. 3, p. 032004, 2008.

[57] R. J. Durscher and S. Roy, "Three dimensional flow measurements Induced from serpentine plasma actuators in quiescent air," *Journal of Physics D: Applied Physics*, vol. 45, no. 3, pp. 035202-9, 2012.

[58] A. Dasgupta and S. Roy, "Three-dimensional plasma actuation for faster transition to turbulence," *Journal of Physics D: Applied Physics*, vol. 50, p. 425201, 2017.

[59] A. Santhanakrishnan and J. Jacob, "Flow Control with plasma synthetic jet actuators," *Journal of Physics D: Applied Physics*, vol. 40, no. 3, pp. 637-651, 2007.

[60] D. Caruana, P. Barricau and C. Gleyzes, "Separation control with plasma synthetic jet actuators," *International Journal of Aerodynamics*, vol. 3, no. 1-2-3, pp. 71-83, 2013.

[61] J. Little, K. Takashima, M. Nishihara, I. Adamovich and M. Samimy, "Separation control with nanosecond-pulse-driven dielectric barrier discharge plasma actuators," *AIAA journal*, vol. 50, no. 2, pp. 350-365, 2012.

[62] M. Nishihara, K. Takashima, J. W. Rich and I. V. Adamovich, "Mach 5 bow shock control by a nanosecond pulse surface dielectric barrier discharge," *Physics of Fluids*, vol. 23, no. 6, p. 066101, 2011.

[63] T. Unfer and J. P. Boeuf, "Modeling and comparison of sinusoidal and nanosecond pulsed surface dielectric barrier discharges for flow control," *Plasma Physics and Controlled Fusion*, vol. 52, no. 12, p. 124019, 2010.

[64] M. L. Post and T. C. Corke, "Separation Control Using Plasma Actuators: Dynamic Stall Vortex Control on Oscillating Airfoil," *AIAA Journal*, vol. 44, no. 12, pp. 3125-3135, 2006.

[65] M. L. Post and T. C. Corke, "Separation control on high angle of attack airfoil using plasma actuators," *AIAA Journal*, vol. 42, no. 11, pp. 2177-2184, 2004.

[66] A. N. Vorobiev, R. M. Rennie, E. J. Jumper and T. E. McLaughlin, "Experimental Investigation of Lift Enhancement and Roll Control Using Plasma Actuators," *Journal of Aircraft*, vol. 45, no. 4, pp. 1315-1321, 2008.

[67] C. He, T. C. Corke and M. P. Patel, "Plasma Flaps and Slats: An Application of Weakly Ionized Plasma Actuators," *Journal of Aircraft*, vol. 46, no. 3, pp. 864-873, 2009.

[68] M. P. Patel, T. T. Ng, S. Vasudevan, T. C. Corke and C. He, "Plasma Actuators for Hingeless Aerodynamic Control of an Unmanned Air Vehicle," *Journal of Aircraft*, vol. 44, no. 4, pp. 1264-1274, 2007.

[69] J. Huang, T. C. Corke and F. O. Thomas, "Plasma actuators for separation control of low-pressure turbine blades," *AIAA journal*, vol. 44, no. 1, pp. 51-57, 2006.

[70] J. List, A. R. Byerley, T. E. McLaughlin and R. D. Van Dyken, "Using a plasma actuator to control laminar separation on a linear cascade turbine blade," in *41st AIAA Aerospace Sciences Meeting and Exhibit* , Reno, Nevada, 2003.

[71] Y. Li, X. Zhang and X. Huang, "The use of plasma actuators for bluff body broadband noise control," *Experiments in Fluids,* vol. 49, no. 2, pp. 367-377, 2010.

[72] X. Huang and X. Zhang, "Streamwise and spanwise plasma actuators for flow-induced cavity noise control," *Physics of Fluids,* vol. 20, no. 3, p. 037101, 2008.

[73] D. M. Orlov and T. C. Corke, "Numerical simulation of aerodynamic plasma actuator effects," *AIAA paper,* vol. 1083, 2005.

[74] K. P. Singh and S. Roy, "Force approximation for a plasma actuator operating in atmospheric air," *Journal of Applied Physics,* vol. 103, no. 1, p. 013305, 2008.

[75] W. Shyy, B. Jayaraman and A. Andersson, "Modeling of glow discharge-induced fluid dynamics," *Journal of Applied Physics,* vol. 92, no. 11, pp. 6434-6443, 2002.

[76] M. R. Visbal and D. V. Gaitonde, "Control of vortical flows using plasma actuators," *AIAA paper,* vol. 505, 2006.

[77] M. Riherd, S. Roy and M. Visbal, "Numerical Investigation of Serpentine Plasma Actuators for Separation Control at Low Reynolds Number," in *41st AIAA fluid dynamics conference and exhibit,* Honolulu, Hawaii, 2011.

[78] Y. B. Suzen and P. J. Huang, "Simulation of flow separation control using Plasma actuators," in *44th AIAA Aerospace Sciences Meeting and Exhibit* , Reno, Nevada, 2006.

[79] D. P. Rizzetta and M. R. Visbal, "Numerical investigation of plasma-based flow control for transitional highly-loaded low-pressure turbine," *AIAA journal,* vol. 45, no. 10, pp. 2554-2564, 2007.

[80] K. S. Choi, T. Jukes and R. Whalley, "Turbulent boundary-layer control with plasma actuators," *Philosophical Transactions of the Royal Society of London A: Mathematical, Physical and Engineering Sciences,* vol. 369, no. 1940, pp. 1443-1458, 2011.

[81] N. Benard and E. Moreau, "Electrical and mechanical characteristics of surface AC dielectric barrier discharge plasma actuators applied to airflow control," *Experiments in Fluids,* vol. 55, no. 11, p. 1846, 2014.

[82] R. Joussot, A. Leroy, R. Weber, H. Rabat, S. Loyer and D. Hong, "Plasma morphology and induced airflow characterization of a DBD actuator with serrated electrode," *Journal of Physics D: Applied Physics,* vol. 46, no. 12, p. 125204, 2013.

[83] G. E. Elsinga and J. Westerweel, "Tomographic-PIV measurement of the flow around a zigzag boundary layer trip," *Experiments in fluids,* vol. 52, no. 4, pp. 865-876, 2012.

[84] M. Riherd and S. Roy, "Serpentine geometery plasma actuators for flow control," *Journal of Applied Physics,* vol. 114, no. 8, p. 083303, 2013.

[85] W. Schoppa and F. Hussain, "Coherent Structure generation in near-wall turbulence," *Journal of Fluid Mechanics,* vol. 453, pp. 57-108, 2002.

[86] J. M. Kendall, "Experimental study of disturbances produced in a pre-transitional laminar boundary layer by weak freestream turbulence," in *AIAA, 18th Fluid Dynamics and Plasmadynamics and Lasers Conference*, Cincinnati,OH, 1985.

[87] P. S. Klebanoff, "Effect of free-stream turbulence on a laminar boundary layer," vol. 16, 1971.

[88] M. E. Goldstein, "Effect of free-stream turbulence on boundary layer transition," *Philosophical Transactions of the Royal Society A*, vol. 372, no. 2020, p. 20130354, 2014.

[89] M. Matsubara and P. H. Alfredsson, "Disturbance growth in boundary layers subjected to free-stream turbulence," *Journal of Fluid Mechanics*, vol. 430, pp. 149-168, 2001.

[90] P. Andersson, M. Berggren and D. S. Henningson, "Optimal disturbances and bypass transition in boundary layers," *Physics of Fluids*, vol. 11, no. 1, pp. 134-150, 1999.

[91] X. Wu, P. Moin, R. J. Adrian and J. R. Baltzer, "Osborne Reynolds pipe flow: Direct simulation from laminar through gradual transition to fully developed turbulence," *Proceedings of the National Academy of Sciences*, vol. 112, no. 26, pp. 7920-7924, 2015.

[92] A. P. Wheeler, R. D. Sandberg, N. D. Sandham, R. Pichler, V. Michelassi and G. Laskowski, "Direct numerical simulations of a high-pressure turbine vane," *Journal of Turbomachinery*, vol. 138, no. 7, p. 071003, 2016.

[93] A. D. Gupta, P. Zhao and S. Roy, "Plasma assisted Turbulent Flow Separation control over a backward facing step," in *54th AIAA Aerospace Sciences Meeting*, San Diego, California, 2016.

[94] S. Roy, P. Zhao, A. DasGupta and J. Soni, "Dielectric barrier discharge actuator for vehicle drag reduction at highway speeds," *AIP Advances*, vol. 6, no. 2, p. 025322, 2016.

[95] W. H. Reed and T. R. Hill, "Triangular mesh methods for the Neutron Transport equation," LA-UR-73-479, Los Alamos, NM, 1973.

[96] B. Cockburn and C. W. Shu, "The Runge-Kutta local projection P1 - discontinuous Galerkin method for scalar conservation laws," *ESAIM: Mathematical Modelling and Numerical Analysis*, vol. 25, no. 3, pp. 337-361, 1991.

[97] B. Cockburn and C. W. Shu, "TVB Runge-Kutta local projection discontinuous Galerkin finite element method for conservation laws. II. General framework," *Mathematics of Computation*, vol. 52, no. 186, pp. 411-435, 1989.

[98] Z. Chen and B. Cockburn, "Analysis of a finite element method for the drift-diffusion semiconductor device equations," *Numerische Mathematik*, vol. 71, no. 1, pp. 1-28, 1995.

[99] Z. Chen, "A Finite element method for the quantum hydrodynamic model for semiconductor devices," *Computers & Mathematics with Applications*, vol. 31, no. 7, pp. 17-26, 1996.

[100] F. Bassi and S. Rebay, "A high-order accurate discontinuous finite element method for numerical solution of the compressible Navier-Stokes equations," *Journal of Computational Physics,* vol. 131, no. 2, pp. 267-279, 1997.

[101] F. Bassi, A. Crivellini, S. Rebay and M. Savini, "Discontinuous Galerkin solution of the Reynolds-averaged Navier-Stokes and k–ω turbulence model equations," *Computer and Fluids,* vol. 34, no. 4, pp. 507-540, 2005.

[102] D. N. Arnold, F. Brezzi, B. Cockburn and L. D. Marini, "Unified analysis of discontinuous Galerkin methods for elliptic problems," *SIAM Journal on Numerical Analysis,* vol. 39, no. 5, pp. 1749-1779, 2002.

[103] B. Cockburn and C. W. Shu, "The local discontinuous Galerkin method for time-dependent convection-diffusion systems," *SIAM Journal on Numerical Analysis,* vol. 35, no. 6, pp. 2440-2463, 1998.

[104] D. Funaro, "A multidomain spectral approximation of elliptic equations," *Numerical Methods for Partial Differential Equations,* vol. 2, no. 3, pp. 187-205, 1986.

[105] D. Funaro and D. Gottlieb, "Convergence results for pseudospectral approximations of hyperbolic systems by a penalty-type boundary treatment," *Mathematics of Computation,* vol. 57, no. 196, pp. 585-596, 1991.

[106] J. S. Hesthaven, " A Stable Penalty Method for the Compressible Navier--Stokes Equations: II. One-Dimensional Domain Decomposition Schemes," *SIAM Journal on Scientific Computing,* vol. 18, no. 3, pp. 658-685, 1997.

[107] J. S. Hesthaven and D. Gottlieb, " A stable penalty method for the compressible Navier–Stokes equations: I. Open boundary conditions," *SIAM Journal on Scientific Computing,* vol. 17, no. 3, pp. 579-612, 1996.

[108] J. S. Hesthaven, " A Stable Penalty Method for the Compressible Navier--Stokes Equations: III. Multidimensional Domain Decomposition Schemes," *SIAM Journal on Scientific Computing,* vol. 20, no. 1, pp. 62-93, 1998.

[109] K. S. Bey, T. J. Oden and A. Patra, "A parallel hp-adaptive discontinuous Galerkin method for hyperbolic conservation laws," *Applied Numerical Mathematics,* vol. 20, no. 4, pp. 321-336, 1996.

[110] C. E. Baumann and T. J. Oden, "A discontinuous hp finite element method for convection—diffusion problems," *Computer Methods in Applied Mechanics and Engineering,* vol. 175, no. 3-4, pp. 311-341, 1999.

[111] P. Houston, C. Schwab and E. Suli, "Discontinuous hp-finite element methods for advection-diffusion-reaction problems," *SIAM Journal on Numerical Analysis,* vol. 39, no. 6, pp. 2133-2163, 2002.

[112] S. Roy and D. Gaitonde, "Radio Frequency induced ionized collisional flow model for application at atmospheric pressures," *Journal of Applied Physics,* vol. 96, no. 5, pp. 2476-2481, 2004.

[113] A. Bhatia, S. Roy and R. Gosse, "Effect of dielectric barrier discharge plasma actuators on non-equilibrium hypersonic flows," *Journal of Applied Physics,* vol. 116, no. 16, p. 164904, 2014.

[114] A. Das Gupta and S. Roy, "Discontinuous Galerkin Method for Solving Magnetohydrodynamic Equations," in *53rd AIAA Aerospace Sciences Meeting*, Kissimmee, Florida, 2015.

[115] B. Cockburn, "Discontinuous Galerkin Methods for Convection-Diffusion Problems," in *High-Order Methods for Computational Physics*, T. J. Barth and H. Deconinck, Eds., Springer, 2001, pp. 69-224.

[116] C. W. Shu and S. Osher, "Efficient Implementation of Essentially Non-Oscillatory Shock-Capturing Schemes II," *Journal of Computational Physics,* vol. 83, no. 1, pp. 32-78, 1989.

[117] J. Douglas Jr. and T. Dupont, "Interior Penalty Procedures for Elliptic and Parabolic Galerkin Methods," *Computing Methods in Applied Sciences. Lecture Notes in Phys,* vol. 58, pp. 207-216, 1976.

[118] G. Chavent and G. Salzano, "A finite element method for the 1D water flooding problem with gravity," *Journal of Computational Physics,* vol. 45, no. 3, pp. 307-344, 1982.

[119] G. Chavent and B. Cockburn, "The local projection P0 P1 discontinuous-Galerkin finite element method for scalar conservation laws," *ESAIM: Mathematical Modelling and Numerical Analysis,* vol. 23, no. 4, pp. 565-592, 1989.

[120] P. LeSaint and P. A. Raviart, "On a finite element method for solving the neutron transport equation," in *Mathematical Aspects of Finite Elements in Partial Differential Equations, Proceedings of a Symposium Conducted by the Mathematics Research Center, the University of Wisconsin-Madison*, Madison, WI, 1974.

[121] Q. Lin and J. Zhou, "Superconvergence in high-order Galerkin finite element methods," *Computer methods in applied mechanics and engineering,* vol. 196, no. 37, pp. 3779-3784, 2007.

[122] B. Cockburn, M. Luskin, C. W. Shu and E. Suli, "Enhanced accuracy by post-processing for finite element methods for hyperbolic equations," *Mathematics of Computation,* vol. 72, no. 242, pp. 577-606, 2003.

[123] M. Leisieur, O. Metais and P. Comte, Large - Eddy Simulation of Turbulence, Cambridge University Press, 2008.

[124] S. B. Pope, Turbulent Flows, 8 ed., Cambridge University Press, 2011.

[125] L. F. Richardson, Weather Prediction by Numerical Process, Cambridge University Press, 2007.

[126] J. Smagorinsky, "General circulation experiments with the primitive equations: I. the basic experiment," *Monthly weather review,* vol. 91, no. 3, pp. 99-164, 1963.

[127] J. W. Deardorff, "A numerical study of three-dimensional turbulent channel flow at large Reynolds numbers," *Journal of Fluid Mechanics,* vol. 41, no. 02, pp. 453-480, 1970.

[128] M. Germano, U. Piolelli, P. Moin and W. H. Cabot , "A dynamic subgrid-scale eddy viscosity model," *Physics of Fluids A: Fluid Dynamics,* vol. 3, no. 7, pp. 1760-1765, 1991.

[129] P. Moin, W. Squires , W. Cabot and S. Lee, "A dynamic subgrid-scale model for compressible turbulence and scalar transport," *Physics of Fluids A: Fluid Dynamics,* vol. 3, no. 11, pp. 2746-2757, 1991.

[130] D. You and P. Moin, "A dynamic global-coefficient subgrid-scale eddy-viscosity model for large-eddy simulation in complex geometries," *Physics of Fluids,* vol. 19, no. 6, p. 065110, 2007.

[131] A. Favre, "Turbulence: Space-time statistical properties and behavior in supersonic flows," *Physics of Fluids,* vol. 26, no. 10, pp. 2851-2863, 1983.

[132] P. Moin and J. Kim, "Numerical Investigation of turbulent channel flow," *Journal of Fluid Mechanics*, vol. 118, pp. 341-377, 1982.

[133] D. Rizzetta and M. Visbal, "Large Eddy Simulation of Supersonic Boundary Layer flow by a High Order method," *Int. Journal of Computational Fluid Dynamics,* vol. 18, no. 1, pp. 15-27, 2004.

[134] J. P. Boris, "On large eddy simulation using subgrid turbulence models Comment 1," in *Whither Turbulence? Turbulence at the Crossroads. Lecture Notes in Physics*, vol. 357, Berlin, Heidelberg, Springer, 1990, pp. 344-353.

[135] J. P. Boris, F. F. Grinstein, E. S. Oran and R. L. Kolbe, "New Insights into large eddy simulation," *Journal of Fluid Dynamics,* vol. 10, no. 4-6, pp. 199-228, 1992.

[136] J. P. Boris and D. L. Book, "Flux-corrected transport. I. SHASTA, A fluid transport algorithm that works," *Journal of computational physics,* vol. 11, no. 1, pp. 38-69, 1973.

[137] E. Garnier, M. Mossi, P. Sagaut, P. Comte and M. Deville, "On the use of shock-capturing schemes for large-eddy simulation," *Journal of Computational Physics,* vol. 153, no. 2, pp. 273-311, 1999.

[138] C. W. Hirt, "Heuristic stability theory for finite-difference equations," *Journal of Computational Physics,* vol. 2, no. 4, pp. 339-355, 1968.

[139] C. Fureby and F. F. Grinstein, "Monotonically integrated large eddy simulation of free shear flows," *AIAA Journal,* vol. 37, no. 5, pp. 544-556, 1999.

[140] C. Fureby and F. F. Grinstein, "Large eddy simulation of high-Reynolds-number free and wall-bounded flows," *Journal of Computational Physics,* vol. 181, no. 1, pp. 68-97, 2002.

[141] P. Colella and P. R. Woodward, "The piecewise parabolic method (PPM) for gas-dynamical simulations," *Journal of Computational Physics,* vol. 54, no. 1, pp. 174-201, 1984.

[142] P. K. Smolarkiewicz and L. G. Margolin, "MPDATA: A finite-difference solver for geophysical flows," *Journal of Computational Physics,*, vol. 140, no. 2, pp. 459-480, 1998.

[143] F. Kuwahara, S. Komurasaki , J. Ooida and A. Betancourt, "Development of Implicit Large Eddy simulation," *New Developments in Computational Fluid Dynamics,* pp. 47-59, 2005.

[144] M. C. Galbraith, "Implicit Large Eddy Simulation of Low-Reynolds-Number Transitional Flow Past the SD7003 Airfoil," University of Cincinnati, Cincinnati, 2009.

[145] F. F. Grinstein, L. G. Margolin and W. J. Rider, Implicit large eddy simulation: computing turbulent fluid dynamics, 1st ed., Cambridge University Press, 2007.

[146] G. Comte-Bellot and S. Corrsin, "Simple Eulerian time correlation of full-and narrow-band velocity signals in grid-generated,'isotropic' turbulence," *Journal of Fluid Mechanics,* vol. 48, no. 2, pp. 273-337, 1971.

[147] D. H. Porter, A. Pouquet and P. R. Woodward, "Three Dimensional supersonic homogeneous turbulence: A numerical study," *Physics Review Letters,* vol. 68, pp. 3156-3159, 1992.

[148] S. A. Orszag and C. Tang, "Small Scale Structure of two-dimensional magnetohydrodynamic turbulence," *Journal of Fluid Mechanics,* vol. 90, no. 1, pp. 129-143, 1979.

[149] C. S. Scott, "The DG/VMS method for unified turbulence simulation," in *32nd AIAA Fluid Dynamics Conference and Exhibit,* St. Louis, MO, 2002.

[150] K. Sengupta, F. Mashayek and G. Jacobs, "Large-eddy simulation using a discontinuous Galerkin spectral element method," in *45th AIAA Aerospace Sciences Meeting and Exhibit*, Reno, NV, 2007.

[151] A. Uranga, P. O. Persson, M. Drela and J. Peraire, "Implicit large eddy simulation of transition to turbulence at low Reynolds numbers using a discontinuous Galerkin method," *International Journal for Numerical Methods,* vol. 87, no. 1-5, pp. 232-261, 2011.

[152] F. Q. Hu, M. Y. Hussaini and P. Rasetarinera, "An Analysis of the Discontinuous Galerkin Method for Wave Propagation Problems," *Journal of Computational Physics,* vol. 151, no. 2, pp. 921-946, 1999.

[153] K. Salari, "DOE's Effort to Improve Heavy Vehicle Fuel Efficiency through Improved Aerodynamics," DOE Annual Merit Review, Lawrence Livermore Nat. Lab. , 2014.

[154] M. Riherd, "The Control of Boundary Layers and Channel Flows Using Plasma Actuators," University of Florida, Gainesville, 2013.

[155] P. A. Monkewitz, K. A. Chauhan and H. M. Nagib, "Self-consistent high-reynolds-number asymptotics for zero-pressure-gradient turbulent boundary layers," *Physics of fluids,* vol. 19, no. 11, p. 115101, 2007.

[156] L. Trefethen, A. Trefethen, S. Reddy and T. Driscoll, "Hydrodynamic stability without eigenvalues," *Science,* vol. 261, no. 5121, pp. 578-584, 1993.

[157] B. F. Farrell, "Optimal excitations of perturbations in viscous shear flows," *Physics of Fluids,* vol. 31, no. 8, pp. 2093-2102, 1988.

[158] F. P. Bertolotti, T. Herbert and P. R. Spalart, "Linear and Nonlinear stability analysis of the Blasius boundary layer," *Journal of Fluid Mechanics,* vol. 242, pp. 441-474, 1992.

[159] M. V. Morkovin, "Critical evaluation of transition from laminar to turbulent shear layers with emphasis on hypersonically traveling bodies," No. RIAS-TR-68-13C. Martin Marietta Corp. Baltimore MD Research Institute for Advanced Studies, Baltimore, MD, 1969.

[160] M. V. Morkovin, E. Reshotko and T. Herbert, "Transition in Open flow systems - a reassessment," *Bulletin of the American Physical Society,* vol. 39, no. 9, p. 1882, 1994.

[161] A. R. Wazzan, C. Gazley and A. M. O. Smith, "Tollmien-schlichting waves and transition: heated and adiabatic wedge flows with applications to bodies of revolution," *Progress in Aerospace Sciences,* vol. 18, pp. 351-392, 1979.

[162] J. L. Van Ingen, "A suggested semi-empirical method for the calculation of the boundary layer transition region," Tech. Rep. Institute of Technology, Department of Aeronautics and Engineering. Report VTH74, Delft, 1956.

[163] N. A. Jaffe, T. T. Okamura and A. M. O. Smith, "Determination of spatial amplification factors and their application to predicting transition," *AIAA Journal,* vol. 8, no. 2, pp. 301-308, 1970.

[164] T. Herbert , "Secondary Instability of boundary layers," *Annual Review of Fluid Mechanics,* vol. 20, no. 1, pp. 487-526, 1988.

[165] T. Sayadi, C. W. Hamman and P. Moin, "Direct numerical simulation of complete H-type and K-type transitions with implications for the dynamics of turbulent boundary layers," *Journal of Fluid Mechanics,* vol. 724, pp. 480-509, 2013.

[166] P. Moin, A. Leonard and J. Kim, "Evolution of a curved vortex filament into a vortex ring," *The Physics of Fluids,* vol. 29, no. 4, pp. 955-963, 1986.

[167] B. A. Singer, "Characteristics of young turbulent spot," *Physics of Fluids,* vol. 8, p. 509, 1996.

[168] H. A. Haidari and C. R. Smith, "The generation and regeneration of single hairpin vortices," *Journal of Fluid Mechanics,* vol. 277, pp. 135-162, 1994.

[169] R. J. Adrain, C. D. Meinhart and C. D. Tomkins, "Vortex organisation in the outer region of the turbulent boundary layer," *Journal of Fluid Mechanics,* vol. 422, pp. 1-54, 2000.

[170] P. J. Schmid and D. S. Henningson, "A new mechanism for rapid transition involving a pair of oblique waves," *Physics of Fluids A: Fluid Dynamics,* vol. 4, no. 9, pp. 1986-1989, 1992.

[171] S. C. Reddy, P. J. Schmid, J. S. Baggett and D. S. Henningson, "On the stability of streamwise streaks and transition thresholds in plane channel flows," *Journal of Fluid Mechanics,* vol. 365, pp. 269-303, 1998.

[172] R. D. Joslin, C. L. Streett and C. L. Chang, "Spatial direct numerical simulation of boundary-layer transition mechanisms: Validation of PSE theory," *Theoretical and Computational Fluid Dynamics,* vol. 4, no. 6, pp. 271-288, 1993.

[173] S. Berlin, A. Lundbladh and D. Henningson, "Spatial simulations of oblique transition in a boundary layer," *Physics of Fluids,* vol. 6, no. 6, pp. 1949-1951, 1994.

[174] P. A. Elofsson and P. H. Alfredsson, "An experimental study of oblique transition in a Blasius boundary layer flow," *European Journal of Mechanics - B/Fluids,* vol. 19, no. 5, pp. 615-636, 2000.

[175] P. A. Elofsson and P. H. Alfredsson, "An experimental study of oblique transition in plane Poiseuille flow," *Journal of Fluid Mechanics,* vol. 358, pp. 177-202, 1998.

[176] S. Berlin, M. Wiegel and D. S. Henningson, "Numerical and experimental investigations of oblique boundary layer transition," *Journal of Fluid Mechanics,* vol. 393, pp. 23-57, 1999.

[177] P. Elofsson, "Experiments on oblique transition in wall bounded shear flows," Doctoral dissertation, Ph. D. thesis, Royal Institute of Technology, Stockholm, Sweden, 1998.

[178] C. S. Mayer, S. Wernz and H. F. Fasel, "Numerical investigation of the nonlinear transition regime in a Mach 2 boundary layer," *Journal of Fluid Mechanics,* vol. 668, pp. 113-149, 2011.

[179] S. Ryu, O. Marxen and G. Iaccarino, "A comparison of laminar-turbulent boundary-layer transitions induced by deterministic and random oblique waves at Mach 3," *International Journal of Heat and Fluid Flow,* vol. 56, pp. 218-232, 2015.

[180] M. T. Landahl, "A note on an algebraic instability of inviscid parallel shear flows," *Journal of Fluid Mechanics,* vol. 98, no. 2, pp. 243-251, 1980.

[181] S. A. Orszag, "Numerical simulation of the Taylor-Green vortex," in *Computing Methods in Applied Sciences and Engineering Part 2. Lecture Notes in Computer Science,* vol. 11, Berlin, Heidelberg, Springer, 1974, pp. 50-64.

[182] M. E. Brachet, "Direct simulation of three-dimensional turbulence in the Taylor—Green vortex," *Fluid dynamics research,* vol. 8, no. 1-4, pp. 1-8, 1991.

[183] M. E. Brachet, D. I. Meiron, S. A. Orszag, B. G. Nickel, R. H. Morf and U. Frisch, "Small-scale structure of the Taylor–Green vortex," *Journal of Fluid Mechanics,* vol. 130, pp. 411-452, 1983.

[184] J. DeBonis, "Solutions of the Taylor-Green vortex problem using high-resolution explicit finite difference methods," in *51st AIAA Aerospace Sciences Meeting including the New Horizons Forum and Aerospace Exposition*, Grapewine, Texas, 2013.

[185] S. Hickel, N. A. Adams and J. A. Domaradzki, "An adaptive local deconvolution method for implicit LES," *Journal of Computational Physics,* vol. 213, no. 1, pp. 413-436, 2006.

[186] G. J. Gassner and A. D. Beck, "On the accuracy of high-order discretizations for underresolved turbulence simulations," *Theoretical and Computational Fluid Dynamics,* vol. 27, no. 3-4, pp. 221-237, 2013.

[187] A. D. Beck, G. J. Gassner and C. D. Munz, "On the effect of flux functions in discontinuous Galerkin simulations of underresolved turbulence," in *Spectral and High Order Methods for Partial Differential Equations - ICOSAHOM 2012. Lecture Notes in Computational Science and Engineering*, vol. 95, Springer, Cham, 2014, pp. 145-155.

[188] J. B. Chapelier, M. De La Llave Plata, F. Renac and E. Lamballais, "Evaluation of a high-order discontinuous Galerkin method for the DNS of turbulent flows," *Computers & Fluids,* vol. 95, pp. 210-226, 2014.

[189] P. S. Klebanoff and Z. W. Diehl, "Some Features of Artificially Thickened Fully Developed Turbulent Boundary Layers with Zero Pressure Gradient," NACA-TR-1110, 1952.

[190] D. E. Coles, "The turbulent boundary layer in a compressible fluid," R-403-PR, 1962.

[191] S. J. Kline, W. C. Reynolds, F. A. Schraub and P. W. Runstadler, "The structure of turbulent boundary layers," *J. Fluid Mech,* vol. 30, no. 4, pp. 741-773, 1967.

[192] J. Murlis, H. M. Tsai and P. Bradshaw, "The structure of turbulent boundary layers at low Reynolds numbers," *Journal of Fluid Mechanics,* vol. 122, pp. 13-56, 1982.

[193] J. M. Österlund, Experimental studies of zero pressure-gradient turbulent boundary layer flow, Sweden: Royal Institute of Technology, Department of Mechanics, 1999.

[194] D. B. Degraaff and J. K. Eaton, "Reynolds-number scaling of the flat-plate turbulent boundary layer," *Journal of Fluid Mechanics,* vol. 422, pp. 319-346, 2000.

[195] P. Schlatter, R. Orlu, Q. Li, G. Brethouwer, J. H. M. Fransson, A. V. Johansson, P. H. Alfredsson and D. S. Henningson., "Turbulent boundary layers up to Re θ= 2500 studied through simulation and experiment," *Physics of fluids,* vol. 21, no. 5, p. 051702, 2009.

[196] N. Hutchins, K. Chauhan, I. Marusic, J. Monty and J. Klewicki, "Towards Reconciling the Large-Scale Structure of Turbulent Boundary Layers in the Atmosphere and Laboratory," *Boundary-layer meteorology,* vol. 145, no. 2, p. 273–306, 2012.

[197] P. Spalart, "Direct simulation of a turbulent boundary layer up to Rθ = 1410," *Journal of fluid mechanics,* vol. 187, pp. 61-98, 1988.

[198] P. Schlatter and R. Orlu, "Assessment of direct numerical simulation data of turbulent boundary layers," *Journal of Fluid Mechanics,* vol. 659, pp. 116-126, 2010.

[199] S. S. Collis and Y. Chang, "The DG/VMS method for unified turbulence simulation," *AIAA paper,* vol. 3124, pp. 24-27, 2002.

[200] L. Wei and A. Pollard, "Direct numerical simulation of compressible turbulent channel flows using the discontinuous Galerkin method," *Computers & Fluids,* vol. 47, no. 1, pp. 85-100, 2011.

[201] F. Bassi, L. Botti, A. Colombo, A. Crivellini, A. Ghidoni and F. Massa, "On the development of an implicit high-order Discontinuous Galerkin method for DNS and implicit LES of turbulent flows," *European Journal of Mechanics-B/Fluids,* vol. 55, pp. 367-379, 2016.

[202] P. Fernandez, N. C. Nguyen, X. Roca and J. Peraire, "Implicit large-eddy simulation of compressible flows using the Interior Embedded Discontinuous Galerkin method," in *54th AIAA Aerospace Sciences Meeting*, San Diego, 2016.

[203] C. C. Wiart, K. Hillewaert, L. Bricteux and G. Winckelmans, "Implicit LES of free and wall-bounded turbulent flows based on the discontinuous Galerkin/symmetric interior penalty method," *International Journal for Numerical Methods in Fluids,* vol. 78, no. 6, pp. 335-354, 2015.

[204] H. M. Nagib, K. A. Chauhan and P. A. Monkewitz, "Approach to an asymptotic state for zero pressure gradient turbulent boundary layers," *Philosophical Transactions of the Royal Society of London A: Mathematical, Physical and Engineering Sciences,* vol. 365, no. 1852, pp. 755-770, 2007.

[205] F. Ducros, P. Comte and M. Lesieur, "Large-eddy simulation of transition to turbulence in a boundary layer developing spatially over a flat plate," *Journal of Fluid Mechanics,* vol. 326, pp. 1-36, 1996.

[206] M. Israeli and S. A. Orszag, "Approximation of radiation boundary conditions," *Journal of computational physics*, vol. 41, no. 1, pp. 115-135, 1981.

[207] D. J. Bodony, "Analysis of sponge zones for computational fluid mechanics," *Journal of Computational Physics*, vol. 212, no. 2, pp. 681-702, 2006.

[208] H. Choi and P. Moin, "Grid-point requirements for large eddy simulation: Chapman's estimates revisited," *Physics of Fluids*, vol. 24, no. 1, p. 011702, 2012.

[209] P. Schlatter and R. Orlu, "Turbulent boundary layers at moderate Reynolds numbers: inflow length and tripping effects," *Journal of Fluid Mechanics,* vol. 710, pp. 5-34, 2012.

[210] X. Wu and P. Moin, "Direct numerical simulation of turbulence in a nominally zero-pressure-gradient flat-plate boundary layer," *J. Fluid Mech.*, vol. 630, pp. 5-41, 2009.

[211] N. N. Mansour, J. Kim and P. Moin, "Reynolds-stress and dissipation-rate budgets in a turbulent channel flow," *J. Fluid Mech.,* vol. 194, pp. 15-44, 1988.

[212] S. P. G. Dinavahi, K. S. Breuer and L. Sirovich, "Universality of probability density functions in turbulent channel flow," *Physics of Fluids,* vol. 7, no. 5, pp. 1122-1129, 1995.

[213] R. Joussot, R. Weber, A. Leroy and D. Hong, "Transition control using a single plasma actuator," *International Journal of Aerodynamics,* vol. 3, no. 1-2-3, pp. 26-46, 2013.

[214] S. Grundmann and C. Tropea, "Experimental transition delay using glow-discharge plasma actuators," *Experiments in Fluids,* vol. 42, no. 4, pp. 653-657, 2007.

[215] B. Simon, P. Schnabel and S. Grundmann, "IR measurements for quantification of laminar boundary layer stabilization with dbd plasma actuators," in *In New Results in Numerical and Experimental Fluid Mechanics X,* Springer, Cham, 2016, pp. 269-278.

[216] C. Porter, T. McLaughlin, C. F. G. Enloe, J. Roney and J. Baughn, "Boundary layer control using a DBD plasma actuator," in *45th AIAA Aerospace Sciences Meeting and Exhibit,* 2007.

[217] A. Seraudie, E. Aubert, N. Naudé and J. Cambronne, "Effect of plasma actuators on a flat plate laminar boundary layer in subsonic conditions," in *3rd AIAA Flow Control Conference,* 2006.

[218] N. Benard, P. Note, M. Caron and E. Moreau, "Highly time-resolved investigation of the electric wind caused by surface DBD at various ac frequencies," *Journal of Electrostatics,* vol. 88, pp. 41-48, 2017.

[219] E. Moreau, "Airflow control by non-thermal plasma actuators," *Journal of Physics D: Applied Physics,* vol. 40, no. 3, pp. 605-636, 2007.

[220] C. Enloe, T. McLaughlin, R. Van Dyken, K. Kachner, E. Jumper, T. Corke, M. Post and O. Haddad, "Mechanisms and responses of a dielectric barrier plasma actuator: Geometric effects," *AIAA journal,* vol. 42, no. 3, pp. 595-604, 2004.

[221] C. L. Chang and M. R. Malik, "Oblique-mode breakdown and secondary instability in supersonic boundary layers," *Journal of Fluid Mechanics,* vol. 273, pp. 323-360, 1994.

[222] E. Laurien and L. Kleiser, "Numerical simulation of boundary-layer transition and transition control," *Journal of Fluid Mechanics,* vol. 199, pp. 403-440, 1989.

[223] U. Rist and H. Fasel, "Direct numerical simulation of controlled transition in a flat-plate boundary layer," *Journal of Fluid Mechanics,* vol. 298, pp. 211-248, 1995.

[224] J. L. Lumley, "The Structure of Inhomogeneous Turbulent Flows," *Atmospheric Turbulence and Radio Wave Propagation,* vol. 790, pp. 166-178, 1967.

[225] G. Berkooz, P. Holmes and J. L. Lumley, "The proper orthogonal decomposition in the analysis of turbulent flows," *Annual review of fluid mechanics,* vol. 25, no. 1, pp. 539-575, 1993.

[226] L. Sirovich, "Turbulence and the dynamics of coherent structures. I. Coherent structures," *Quarterly of applied mathematics,* vol. 45, no. 3, pp. 561-571, 1987.

[227] R. S. Barlow and J. P. Johnston, "Structure of a turbulent boundary layer on a concave surface," *Journal of Fluid Mechanics,* vol. 191, pp. 137-176, 1988.

[228] J. Kim, P. Moin and R. Moser, "Turbulence statistics in fully developed channel flow at low Reynolds number," *Journal of Fluid Mechanics,* vol. 177, pp. 133-166, 1987.

[229] R. Jordinson, "The flat plate boundary layer. Part 1. Numerical integration of the Orr–-Sommerfeld equation," *Journal of Fluid Mechanics*, vol. 43, no. 4, pp. 801-811, 1970.

[230] P. Luchini, "Reynolds-number-independent instability of the boundary layer over a flat surface: optimal perturbations," *Journal of Fluid Mechanics,* vol. 404, pp. 289-309, 2000.

[231] R. Joussot, V. Boucinha, R. Weber-Rozenbaum, H. Rabat, A. Leroy-Chesneau and D. Hong, "Thermal characterization of a dbd plasma actuator: dielectric temperature measurements using infrared thermography," in *40th Fluid Dynamics Conference and Exhibit*, 5102, 2010.

[232] R. Durscher and S. Roy, "Aerogel and ferroelectric dielectric materials for plasma actuators," *Journal of Physics D: Applied Physics,* vol. 45, no. 1, p. 012001, 2011.

[233] L. D. Kral and H. F. Fasel, "Direct numerical simulation of passive control of three-dimensional phenomena in boundary-layer transition using wall heating," *Journal of Fluid Mechanics,* vol. 264, pp. 213-254, 1994.

[234] J. Lee, S. Y. Jung, H. J. Sung and T. A. Zaki, "Effect of wall heating on turbulent boundary layers with temperature-dependent viscosity," *Journal of Fluid Mechanics,* vol. 726, pp. 196-225, 2013.

[235] H. Yan and D. Gaitonde, "Effect of thermally induced perturbation in supersonic boundary layers," *Physics of Fluids,* vol. 22, no. 6, p. 064101, 2010.

[236] T. N. Jukes, K. S. Choi, G. A. Johnson and S. J. Scott, "Turbulent drag reduction by surface plasma through spanwise flow oscillation," *AIAA paper,* vol. 3693, 2006.

[237] R. E. Hanson, P. Lavoie, A. M. Naguib and J. F. Morrison, "Transient growth instability cancelation by a plasma actuator array," *Experiments in fluids,* vol. 49, no. 6, pp. 1339-1348, 2010.

[238] S. Grundmann and C. Tropea, "Active cancellation of artificially introduced Tollmien–Schlichting waves using plasma actuators," *Experiments in Fluids,* vol. 44, no. 5, pp. 795-806, 2008.

[239] K. Barckmann, C. Tropea and S. Grundmann, "Attenuation of Tollmien–Schlichting waves using plasma actuator vortex generators," *AIAA Journal,* vol. 53, no. 5, pp. 1384-1388, 2015.

[240] M. Riherd, S. Roy and S. Balachandar, "Local stability effects of plasma actuation on a zero pressure gradient boundary layer," *Theoretical and Computational Fluid Dynamics,* vol. 28, no. 1, pp. 65-87, 2014.

[241] W. J. Strang and R. M. McKinlay, "Concorde in Service," *The Aeronautical Journal*, vol. 83, no. 818, pp. 39-52, Feb 1979.

[242] A. S. Thomas, W. S. Saric, A. L. Braslow, D. M. Bushnell, R. C. Lock and J. E. Hackett, "Aircraft Drag Prediction and Reduction," Advisory Group for Aerospace Research and Development NEUILLY-SUR-SEINE, France, 1985.

[243] J. Woodrooffe, "Reducing truck fuel use and emissions: tires, aerodynamics, engine efficiency, and size and weight regulations," UMTRI, 2014.

[244] M. Jahanmiri, "Aircraft Drag Reduction: An Overview," Dept. of Applied Mech. , Chalmers Univ. of Tech., Sweden, 2011.

[245] K. E. Meyer, J. M. Pedersen, O. Özcan, S. Haider and P. S. Larsen, " Identify flow structures with proper orthogonal decomposition (POD)," Departement of Mechanical Engineering Technical University of Danmark (DTU), 2008.

BIOGRAPHICAL SKETCH

Arnob Das Gupta was born in Asansol, India. He earned his bachelor's degree from National Institute of Calicut, Kerala in Production Engineering in 2009. He did internships in TATA motors and Kennametal Ltd. during his bachelor's degree. His area of research is in computational fluid dynamics and plasma flow control. His main research focus has been on numerical simulation and experimental study of turbulent transition using plasma actuators. He received his doctoral degree in mechanical engineering from University of Florida in the fall of 2017 under Dr. Subrata Roy at Applied Physics Research Group.